The University Of Sheffield.

Towards *Operando* Measurements of Li^+ Diffusion in Batteries using Muon Spectroscopy

Innes McClelland

Under the supervision of Serena A. Cussen and Peter J. Baker

A thesis submitted in partial fulfilment of the requirements for the degree of Doctor of Philosophy

Department of Chemical and Biological Engineering
Faculty of Engineering
The University of Sheffield
UK

July 2022

Abstract

Ionic movement through solids is one of the unseen operations which maintains the functionality of our technological lives; the most widespread example is Li^+ ion transfer, which underpins contemporary energy storage. High ionic conductivity is essential to enable efficient batteries, and such a macroscopic quality is derived from ionic diffusion at the atomic level. The kinetic limitations on diffusion have a crucial influence over a range of battery performance characteristics, such as fast-charging ability and capacity fade, and diffusion rates have been found to vary significantly during battery operation. As such, a fundamental understanding of the underlying mechanisms behind ionic diffusion, and the structural properties which act to regulate them, is vital for the design and application of next-generation energy materials.

A number of experimental techniques have recently been developed to study charge transfer in battery materials during the charge/discharge process: so-called "*operando*" measurements. This thesis describes a collection of experiments which develop a particle accelerator-based technique, muon spin relaxation spectroscopy (μSR), towards a consistent *operando* methodology for the advanced characterisation of energy materials during real battery operating conditions. μSR operates by using the time evolution of implanted muon spins to probe magnetic fields within materials, which can reveal information on the dynamics of Li^+ ions. To fully interpret the information learned from such experiments, the application of complementary techniques is essential; electrochemical impedance spectroscopy and X-ray absorption spectroscopy were thus employed to aid understanding over a range of length scales.

In this thesis, Chapter 1 introduces the underlying scientific motivation, before Chapter 2 reviews prior μSR studies of energy materials, and the experimental methods are outlined in Chapter 3. Chapter 4 demonstrates the possibility of *in situ* μSR, whereby a significantly hampered ionic diffusion rate is identified in an all-solid-state battery at low voltage, impeding cell cyclability. A garnet solid electrolyte is investigated in Chapter 5, uncovering a mechanism for interphase propagation through the grain surface regions. A custom-built cell for *operando* μSR experiments is given in Chapter 6, which provides reliable electrochemical performance and collection of high quality data. Chapter 7 describes the first *operando* μSR experiment, obtaining detailed information on the properties of commercially relevant cathode NMC811. Contrasting diffusivity behaviour in the particle surface and bulk was observed, with both regions significantly affected at a high state of charge. Finally, Chapter 8 provides the conclusions and future work; ultimately, a working methodology for *operando* measurements using μSR lays the foundations towards a variety of future opportunities in advanced material characterisation.

Acknowledgements

The first people to thank in a very long list are my supervisors, Serena Cussen and Peter Baker. A huge thank you to Serena, without whom I would not have even considered doing a PhD, for all your ideas, expertise, and determination to make this project successful. A huge thanks also to Peter, whose advice, feedback, and conversation have been invaluable. You have both led by example.

I would like to thank all members of the Corr/Cussen group, past and present, for all the help and the laughs. In particular, I extend my gratitude towards Sam Booth and Hany El-Shinawi, who have both improved this work immeasurably. Your willingness to share your expertise and to teach has been greatly appreciated. Special thanks to Sam for all the beamtimes, particularly the one with eight consecutive takeaways. Thanks to Quique, Seb, Beth, Sam, Jazz, Heather, Calum, Laurie, Marco, Tom, Laura, Kirstie, Peter, Katja, Chris, Dan, Ester, Otto, Naresh, Nirmalesh, and everyone else (sorry I can't name you all) for the coffees, pints, silly lunchtimes, and mutual despair. You are all great colleagues and friends and have made this experience what it was.

Many thanks of course to everyone who has helped along the way, both inside and outside of academia. I am very grateful to the University of Sheffield, the ISIS Neutron and Muon Source, and the Faraday Institution for the funding and the opportunities they have provided. Thanks to all collaborators and advisers over the course of this project: Adrian Hillier, Stéphanie Belin, Alan Chadwick, Anna Regoutz, and particularly Eddie Cussen for the expertise and guidance. To Ben, Cheryl, Odie, Nik, Peter, Hany, Simon, Sam, and everyone else for the patience to train me. To Beth for getting me interested in research during my undergrad. To all the engineering team at ISIS. To Michelle and everyone at Castleford Academy for such a fun teaching placement. To Gabriel for the lunchtimes, wisdom, and big blue. To Madeleine for our chats in the office at ISIS. To the Pickled Eggheads. To Charlie for the morning coffees, delicious dinners and all the rest. To all the gang in Sheffield, Glasgow, and everywhere else, who I won't name here, but are very much appreciated. Most of all to Helen, whose endless enthusiasm and awful puns have helped more than you know.

Finally, my deepest gratitude goes to all of my family, who have been my main inspiration and whose unwavering support has given me the opportunity to complete these studies in the first place. To my brother Rory, my parents Maureen and Pete, my grandparents Meta and Eppie, and everyone else. I am very grateful for you all.

Declaration

I, the author, confirm that the Thesis is my own work. I am aware of the University's Guidance on the Use of Unfair Means. This work has not been previously been presented for an award at this, or any other, university.

Signed: Innes McClelland

Table of Contents

Page Number

List of Figures

List of Tables

List of Abbreviations

LCO - $LiCoO_2$

LIB - Lithium-ion battery

NMC - $LiNi_xMn_yCo_zO_2$

OCV - Open circuit voltage

SEI - Solid electrolyte interface

SSB - Solid-state battery

SSE - Solid-state electrolyte

EV - Electric vehicle

CCD - Critical current density

NASICON - Sodium super ionic conductor

LLZO - $Li_7La_3Zr_2O_{12}$

μSR - Muon spin relaxation spectroscopy

NMR - Nuclear magnetic resonance

QENS - Quasi-elastic neutron scattering

DC/**AC** - Direct current/alternating current

LF - Longitudinal field

TF - Transverse field

ZF - Zero field

EIS - Electrochemical impedance spectroscopy

CV - Cyclic voltammetry

GITT - Galvanostatic intermittent titration technique

PITT - Potentiostatic intermittent titration technique

LFP - $Li_{1-x}FePO_4$

SPS/**FAST** - Spark plasma sintering/field assisted sintering technique

XRD - X-ray diffraction

SEM - Scanning electron microscopy

TEM - Transmission electron microscopy

EDX - Energy dispersive X-ray

GCPL - Galvanostatic cycling with potential limitation

CCCV - Constant current constant voltage

CPE - Constant phase element

BAM - Battery analysis by muon

XPS - X-ray photoelectron spectroscopy

XAS - X-ray absorption spectroscopy

XANES - X-ray absorption near-edge structure

EXAFS - Extended X-ray absorption fine structure

KT - Kubo-Toyabe

FFT - Fast fourier transform

LZP - $LiZr_2(PO_4)_3$

LTP - $LiTi_2(PO_4)_3$

LLZWO - $Li_{6.2}La_3Zr_{1.6}W_{0.4}O_{12}$

LNWO - $Li_3Nd_3W_2O12$

SOC - State of charge

PTFE - Polytetrafluoroethylene

TM - Transition metal

Thesis Structure and Author Contributions

This thesis is composed of both traditional style and publication format chapters. Chapters 1, 3, and 8 (the Introduction, Experimental Methods, and Conclusions), are written in the traditional thesis style. Chapter 2 is a review article which relates the introduction to the results. The results chapters (4 – 7) are written in the style of publishable research papers. These chapters are designed to stand alone as individual works of research, while together they are intended to form a coherent project of technique development and material research. Chapters 4, 5, and 7 are research papers while Chapter 6 is a technical paper. To date, Chapters 2, 4, and 5 are published in journals, Chapter 6 has not yet been submitted and Chapter 7 is under review. Copyright permissions for the published articles has been obtained. Provided below are the title, authors, and author contributions for each chapter.

Chapter 1 - Traditional Format

Introduction

Designed and written by IM, with corrections from PJB and SAC.

Chapter 2 - Review Paper

Muon Spectroscopy for Investigating Diffusion in Energy Storage Materials

Innes McClelland, Beth I. J. Johnston, Peter J. Baker, Marco Amores, Edmund J. Cussen, and Serena A. Corr. *Annu. Rev. Mater. Res.*, 50:15.1–15.23, 2020.

SAC was invited to write a review by Annual Reviews of Materials Research. Article research was done by IM; article was drafted by IM before refinement by SAC. Section contributions were provided from BJ, PJB, MA, and EJC.

Chapter 3 - Traditional Format

Experimental Methods

Designed and written by IM, with corrections from PJB and SAC.

Chapter 4 - Research Paper

***In Situ* Diffusion Measurements of a NASICON-Structured All-Solid-State Battery Using Muon Spin Relaxation**

Innes McClelland, Samuel G. Booth, Hany El-Shinawi, Beth I. J. Johnston, Jasmin Clough, Weimin Guo, Edmund J. Cussen, Peter J. Baker, and Serena A. Corr. *ACS Appl. Energy. Mater.*, 4:1527–1536, 2021.

Funding was provided by EJC, PJB, and SAC, who all also supervised the study. HES designed the solid-state-battery system in previous work, while the experiments were conceived

by IM, SGB, and HES with guidance from PJB and SAC. Material synthesis, cell preparation, and laboratory testing was completed by both IM and HES. The muon experiment was completed by IM *et al.*, supported by PJB. Data analysis for the muon experiment was done by IM with advice from PJB. The X-ray absorption spectroscopy experiment was completed by IM, SGB, and JC, with data analysis performed by IM, SGB, and WG. IM wrote the paper with corrections provided by all authors.

Chapter 5 - Research Paper

The Role of the Reducible Dopant in Solid Electrolyte-Lithium Metal Interfaces

Innes McClelland, Hany El-Shinawi, Samuel G. Booth, Anna Regoutz, Jasmin Clough, Sebastian Altus, Edmund J. Cussen, Peter J. Baker, and Serena A. Corr. *Chem. Mater.*, 34:5054–5064, 2022.

Funding was provided by EJC, PJB, and SAC, who all also supervised the study. The experiments were conceived by IM and HES with guidance from PJB and SAC. Material synthesis and cell preparation was completed by IM and HES. FAST processing was done by IM. IM and HES both designed, conducted, and analysed the electrochemical tests with help from SA. Imaging characterisation was done by IM. The muon experiment was completed by IM, HES, SGB, and JC, supported by PJB. Data analysis for the muon experiment was done by IM with advice from PJB. The X-ray absorption spectroscopy experiment was designed, completed at the Diamond Light Source by external collaborators, and analysed by IM and SGB. The X-ray photoelectron spectroscopy experiment was prepared by HES, before being conducted and analysed by AR. IM and HES co-wrote the paper with corrections provided by all authors.

Chapter 6 - Technical Paper

The BAM Cell: An Electrochemical Device for *Operando* Ionic Diffusion Measurements using Muon Spectroscopy

Innes McClelland, Samuel G. Booth, Beth I. J. Johnston, Laurence Middlemss, Edmund J. Cussen, Peter J. Baker, and Serena A. Cussen.

Manuscript not yet submitted.

Funding was provided by EJC, PJB, and SAC, who all also supervised the study. The cell was designed in collaboration between IM, SGB, and PJB. The cell was produced by the engineering team at the ISIS Neutron and Muon Source. Data were used from muon experiments outlined in other chapters which were analysed by IM with advice from PJB. Some data were used from an experiment designed by BIJ, completed by BIJ, IM, SGB, and supported by PJB. Electrochemical tests were designed by IM under supervision from PJB and SAC. LM prepared the thick electrode sheets. Preparation of cells for the *operando* methodology, electrochemical testing, and cycling analysis were done by IM supported by PJB and SAC. The paper was written by IM with corrections provided by other authors.

Chapter 7 - Research Paper

Direct Observation of the Dynamic Lithium Diffusion Properties in the First Cycle of $LiNi_{0.8}Mn_{0.1}Co_{0.1}O_2$ (NMC811) using *Operando* Muon Spectroscopy

Innes McClelland, Samuel G. Booth, Nirmalesh Anthonisamy, Laurence Middlemiss, Gabriel E. Pérez, Edmund J. Cussen, Peter J. Baker, and Serena A. Cussen.

Manuscript not yet submitted.

Funding was provided by EJC, PJB, and SAC, who all also supervised the study. The experiments were conceived by IM and SGB with guidance from PJB and SAC. Material synthesis was conducted by NA with help from IM. Imaging and diffraction analysis was done by IM. Electrochemical testing was done by IM with advice from all other authors. The muon experiment was completed by IM, SGB, and GEP, with support from PJB. Analysis was done by IM with advice from PJB. *Operando* XRD experiments were completed by LM with help from IM. The impedance experiment was designed, completed, and analysed by IM. The paper was written by IM with advice from SGB and corrections provided by other authors.

Chapter 8 - Traditional Format

Conclusions and Future Work

Designed and written by IM, with corrections from PJB and SAC.

1 Introduction

Recent scientific progress towards the efficient storage of energy in chemical form has facilitated the ubiquity of rechargeable batteries in today's technological market. The demand for suitable energy storage solutions which allow for a greater penetration of renewables into our society is in large part motivated by the alarming consequences of global warming. Such urgency has predicated a global research effort towards the discovery of high performing and sustainable battery technologies for the transportation sector.

Alessandro Volta was the first to demonstrate, in 1800, how materials could be arranged in a manner such that they produce a continuous flow of electrical energy. Volta's design, which used zinc and copper electrodes with a brine-soaked cloth electrolyte, catalysed the development of many further energy storage devices in the 19^{th} century. It was not until 1974 that M. Stanley Whittingham demonstrated the first use of lithium in an energy storage device by reversibly intercalating Li^+ ions into a layered TiS_2 structure. Lithium has the advantage of being the lightest solid element, resulting in an extremely low electrochemical potential of -3.04 V vs. the standard hydrogen electrode [1], and enabling fast transport across electroactive materials. Whittingham's design was developed by John B. Goodenough in 1980, who applied the same principle to a rock-salt structured $LiCoO_2$ (LCO) cathode [2]. To date, LCO remains the dominant cathode material used in lithium-ion batteries [3]. Seven years after the inception of LCO as an energy storage material by Goodenough, Akira Yoshino patented a device using LCO with a soft carbon anode. The device, termed a lithium-ion battery (LIB), was subsequently commercialised in 1991 by Sony. Lithium-ion batteries, to date in 2022, dominate the portable electronics market and look poised to gain a substantial foothold in the transportation sector as well. Whittingham, Goodenough, and Yoshino were awarded the 2019 Nobel Prize in Chemistry as recognition for their efforts towards the development of lithium-ion batteries.

This introductory chapter will cover the scientific background behind the experimental research conducted in this thesis, before a literature review on the use of muon spectroscopy for energy materials is presented in Chapter 2. Chapters 4-7 each possess a brief and targeted introduction.

1.1 The Lithium-Ion Battery

An LIB works *via* the principle of reversible Li^+ ion transport between two electrodes. Under an externally applied current, Li stored in the cathode will forfeit its outer shell electron to become a Li^+ ion. The Li^+ ions are transported *via* the electrolyte to the anode, while the electrons flow through the external circuit. The electrons then recombine with Li^+ ions in the anode to form Li atoms, which are stored as chemical energy (using

the example of a Li metal anode battery). When desirable, this process can be operated in reverse; Li^+ ions move back across the electrolyte to the cathode and simultaneously the electrons flow around the external circuit to do useful work.

This process is known as charging and discharging (cycling), for which the working principle is shown in Figure 1.1. Both electrodes must be different materials for this process to store energy, these are called the cathode (positive electrode) and the anode (negative electrode). Conventionally, these are separated by a porous membrane (called the separator) and are immersed in an electrolyte solution. The redox reactions which happen at either electrode are physically separated, meaning the electrons produced can be used externally. Crucial for efficient operation is thus that the electrolyte possesses a high ionic conductivity (to move Li^+ ions between the electrodes) and a minimal electronic conductivity (to ensure electrons move around the external circuit).

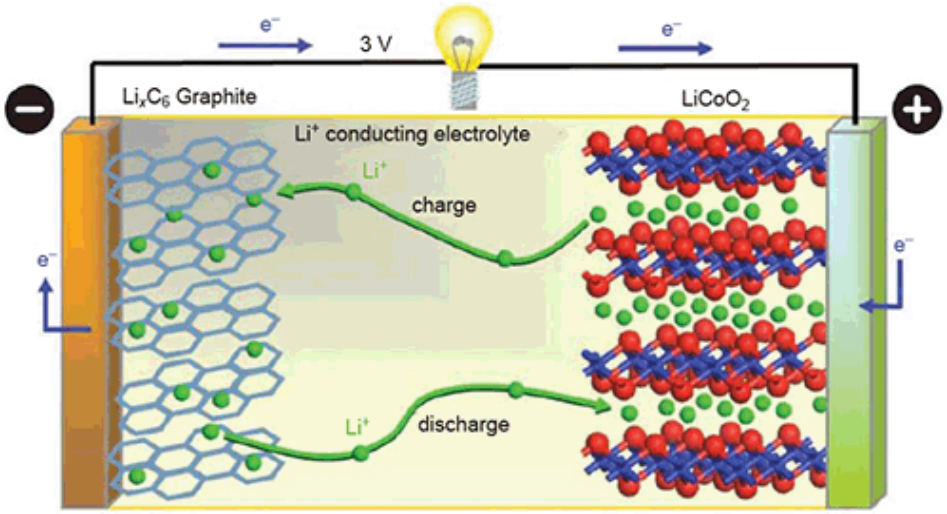

Figure 1.1: Schematic of a basic lithium-ion battery (LIB). Reproduced with permission from Johnson Matthey [4] under the CC BY-NC-ND 4.0 licence.

The materials used for the components in a LIB determine its performance characteristics. The specific battery capacity (given in mA hours g^{-1}), which is essentially a measure of how much charge can be stored under certain conditions, is restricted to the lower capacity of either electrode. Graphite is generally used in commercial LIBs and has a much higher capacity (theoretical specific capacity of 372 mA h g^{-1}) than most cathode materials; the cathode generally limits the overall battery capacity. Meanwhile, energy density (given in W h kg^{-1}) is the standard metric used to compare different cell types. Energy density is defined as the product of the specific capacity and the operating voltage. As such, one can see that two of the most important indicators of battery performance are the cathode capacity and the voltages between which it operates.

The reversibility of the charge transfer process largely depends on the structural changes of the host material which occur during cycling. Ideally, a material is unaffected by the insertion and removal of Li^+ ions, while in reality numerous degradation

processes occur [5]. For example, these include particle cracking due to repeated volume changes [6], reactions with the electrolyte at high transition metal redox states [7], and structural contraction of the unit cell caused by reduced electrostatic repulsion at low Li occupancy [8]. The structural stability of the cathode material is then an important factor in the lifetime of a battery; to extract the maximum capacity from a battery, this stability must also hold at high potential. Therefore, the desirability for high capacity and stability at high voltages remain outstanding challenges for battery cathode research.

Current cathode materials often take the form of layered oxides, such as $LiCoO_2$, $LiNiO_2$, and $LiMnO_2$ (space group $R\bar{3}m$). The rhombohedral symmetry of layered cathodes generally takes an $ABCABC$ stacking pattern with alternating layers of lithium, transition metal and oxygen [9]. Such materials offer a high theoretical capacity ($\geq$270 mAh g^{-1} [10]) and good capacity retention during cycling. To circumvent stability issues in these compounds, previous strategies have involved the partial replacement of Co with Mn and Ni: Co allows good rate capability, Mn provides structural stability, and Ni improves the practical capacity. This is in part motivated by lingering questions over the ethicality of the Co supply chain [11]. This class of cathodes, termed NMC, have become popular in recent battery research [12]. In NMC materials, the synthesis-controlled microstructure, structural changes during cycling, high potential stability, and sluggish diffusion rates are all pertinent to the electrochemical performance. Unfortunately, the cycle life of NMC materials tends to worsen with decreasing Co-content, limiting the practicality of desirable high Ni-content compositions [10]. The degradation mechanisms behind these limitations have become hotly debated topics in the literature [7]: such properties are investigated in Chapter 7.

Figure 1.2 explores the energy relationship between the electrochemical potential of the cathode (μ_C) and the anode (μ_A) in a typical cell set-up. Effectively, the electrochemical potential of a material defines how readily it will donate/accept an electron. For example, lithium has one loosely bound electron in the $2s^1$ molecular orbital, which it will readily donate. Conventionally for LIBs, the cathode is the oxidant and the anode is the reductant. The energy gap (E_g) between the electrochemical potentials of the anode and cathode can be used to define the open circuit voltage (V_{oc}) of the battery as:

$$V_{oc} = \frac{\mu_A - \mu_C}{e}, \tag{1.1}$$

where e is the electron's charge. As such, maximising E_g leads to a higher open circuit voltage across the cell. However, the chemical stability limits of the electrolyte act to constrain the choice of electrode material to a particular window. If μ_A is above the energy of the lowest unoccupied molecular orbital (LUMO) of the electrolyte, the electrolyte will be reduced at the anode surface. Similarly, if μ_C is below the highest occupied molecular orbital (HOMO), the electrolyte will be oxidised at the cathode surface. These limits are

not unremitting; a passivation layer, often known as a solid electrolyte interface (SEI), can effectively increase E_g by blocking the electron transfer processes between an electrode and the electrolyte. As such, the selection of materials used in a LIB is crucial.

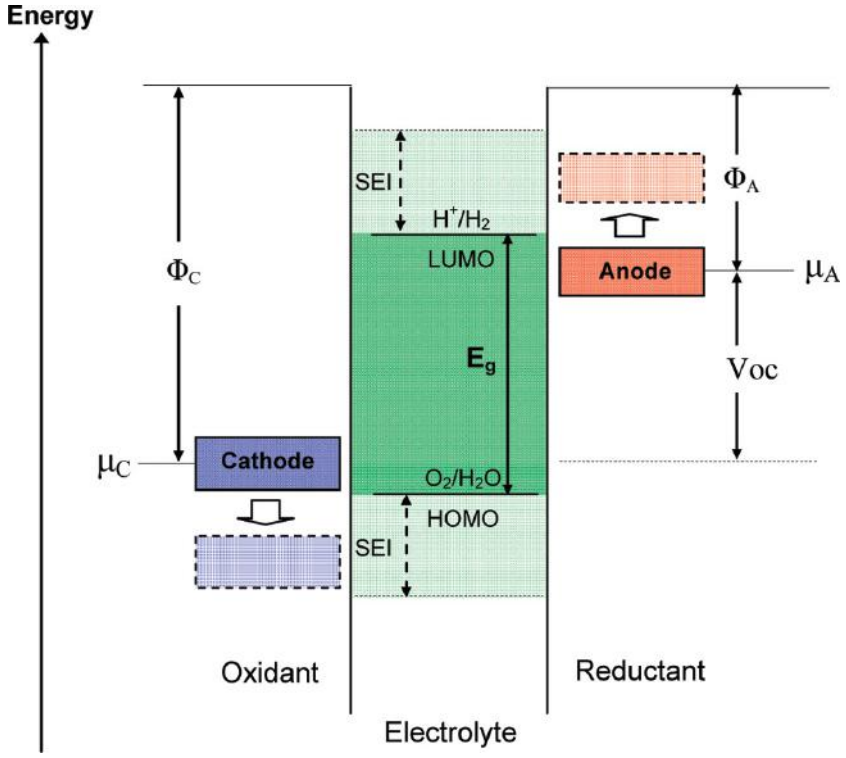

Figure 1.2: Electrochemical energy relationship between a cathode and an anode material separated between an electrolyte. E_g is the energy gap which represents the thermodynamic stability window of the electrolyte. Φ_A and Φ_C are the anode and cathode work functions, respectively. V_{oc} is the resultant open circuit voltage across the cell. Reprinted with permission from [13]. Copyright 2010 American Chemical Society.

As can be seen from Figure 1.2, the choice of electrolyte defines the electrochemical stability window. One of the most common electrolytes is $LiPF_6$ dissolved in carbonate solvents, which is an excellent ionic conductor and electronic insulator [14]. However, it possesses fast charging limitations ($\geq$0.7 mA cm^{-2}) when using a metallic Li anode, which restricts its practicality [15]. Metallic lithium has an extremely high theoretical capacity ($\sim$3860 mAh g^{-1} [16]), meaning its inclusion into battery research cells has become popular. However, sudden dendritic growth during cycling and detrimental SEI layer formation limit its implementation. Lithium dendrites are branch-like strands of lithium which grow from the metal anode across the electrolyte during cycling. They consume active material and can eventually cause a short circuit by forming a low resistance pathway for electrons between the electrodes. An SEI is formed on the anode-electrolyte interface when the electrochemical potential of metallic lithium dips below the LUMO energy level of the electrolyte. This is an electrochemically driven reaction which consumes both electrolyte and electrode active material. Furthermore, the SEI is generally more resistive to ionic motion than the other components, increasing both cell impedance

and overpotential [17]. While the SEI is generally detrimental to battery operation, its kinetic stabilisation effect and electron blocking nature may be used to an advantage in some cases.

Meanwhile, the toxicity and flammability of $LiPF_6$-based electrolytes have placed doubts over the safety of such devices, especially for automotive applications. Several high-profile incidents, such as the 2016 Samsung fires, have thrust battery safety into the public spotlight in recent years. These were in large part caused by the tiny margin for error in the highly competitive portable electronics market; the Samsung batteries were, on occasion, forced into too small a case, resulting in a short circuit and thermal runaway. Further dangerous incidents can occur at high operating voltages, where there is a danger that the HOMO energy level of the cathode will fall below the stable range of the electrolyte, causing a decomposition reaction. With common oxide cathode materials this can produce a variety of gaseous species, such as O_2, CO_2, H_2 and POF_3, depending on the cathode used [18]. In a contained system the accrual of these decomposition products poses a serious fire risk, while leakage of highly toxic PF_5, which can also be formed, creates a health risk. In tandem with high voltage electrochemical instability, the well-known thermal instability of carbonate electrolytes at higher temperatures (which accelerates decomposition reactions between 60 – 100 °C) has recently facilitated a push towards safer future technologies.

1.2 Solid-State Batteries

Solid-state-batteries (SSBs) have been widely tipped as the commercial successor to conventional liquid electrolyte chemistries for energy storage applications. Primarily, SSBs offer improved safety and reliability over their liquid-based counterparts as a consequence of the replacement of the flammable liquid electrolyte with a safer, solid material. An increased device safety presents a huge incentive to the battery sector, with the toxicity and flammability of current technologies under increasing public scrutiny as electric vehicle (EVs) numbers climb. Moreover, solid-state electrolytes (SSEs) can possess wide potential stability windows (≈6 V), allowing for the use of high voltage cathodes without debilitating capacity loss with cycling. To compete with conventional technologies, a solid electrolyte must possess a range of abilities, namely: fast ionic conductivity ($\geq 10^{-3}$ S cm^{-1}), compatibility with anode and cathode materials, stability in the interfacial regions, and crack resistance. Such a configuration is difficult to engineer, meaning a global research effort has endeavoured to develop the technology for SSBs in the last few decades.

A particular benefit of SSBs could be the realisation of a metallic Li anode which, as mentioned previously, has an extremely high theoretical capacity [16]. Uncontrolled dendrite growth, which has plagued the use of metallic lithium anodes in LIBs, remains similarly damaging for SSBs. The critical current density (CCD), defined as the threshold

at which a short circuit will occur, is often limited by dendrites, which can penetrate through a solid electrolyte to short circuit the cell. The CCD is observed for most garnets (a common solid electrolyte class described in Section 1.2.2) between 0.05 – 0.9 mA cm^{-2} [19]. To compete with current fast charging technologies available for LIBs, ideally the CCD for a solid electrolyte should be $\geq$5 mA cm^{-2}.

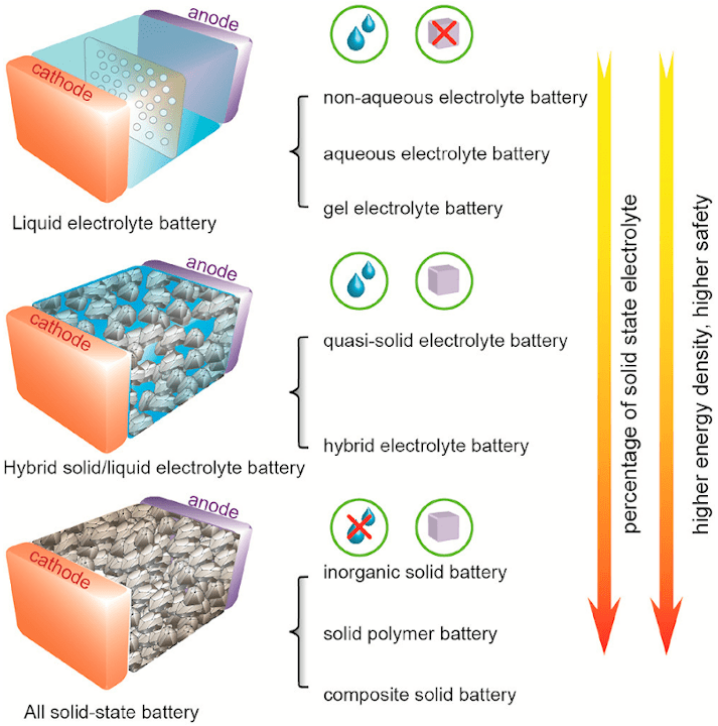

Figure 1.3: Schematic displaying the difference between liquid electrolyte, hybrid, and all-solid-state batteries. Reprinted and adapted with permission from [20]. Copyright 2020 American Chemical Society.

Dendrites are believed to propagate along grain boundaries and voids, motivating the desire for high relative density electrolytes [21–25]. In low density materials, large resistive differences between the grains and grain boundaries can result in an inhomogeneous current distribution, surpassing the CCD in certain "hot-spots" and expediting a short-circuit [26, 27]. Thus, the limiting region of solid electrolytes is often the grain boundaries, which display much lower conductivities than the bulk [27]. The development of efficient synthesis and processing procedures to enable high densities and grain boundary control are therefore imperative. One technique often used is the incorporation of aliovalent dopant elements during synthesis, which are well known to increase the density of ceramic materials [28–30]. For example, Li *et al.* have shown how dopants can help to reduce pores at the grain boundary, aiding contact between the grains [31]. Such microstructural control is key to maximising the performance of SSBs.

A further technique proposed to prevent dendritic growth is the choice of an electrolyte that possesses a high shear modulus and a maximal ionic transference number [32]. The transference number is the ratio of ionic charge carriers to the total number of mobile

charge carriers. Brissot *et al.* previously reported that dendritic growth was effectively stopped for perfect ionic conductors. This is because the time it takes for dendrites to begin to grow nears infinity as the transference number approaches unity [33]. The link between electronic conductivity in solid electrolytes and dendrite growth has grown more conclusive with a follow-up study by Han *et al.*, who identified a cause-and-effect relationship [25]. Characterisation of both charge carriers in SSBs is therefore important.

An obvious area of difference between solid- and liquid-based chemistries lies in the rate capability. That is, the ability of a battery to deliver a high amount of energy in a short amount of time (i.e., fast (dis)charging). This depends on the kinetic limitations for how fast ions can be physically transported across a device. The ionic conductivity of the best solid electrolytes is now $\geq 10^{-3}$ S cm^{-1} at room temperature, which is beginning to challenge liquid electrolytes such as $LiPF_6$ and LiTFSI in carbonate-based solvents ($\sim 3 \times 10^{-3}$ S cm^{-1} [34]). In solids, such macroscopic conductivity properties are intrinsically linked to the ionic diffusion rates at a microscopic level [35]. Furthermore, the charge transport processes on a fundamental site-site basis are highly dependent on the structural properties of a material, which change at a local level during cycling.

While fast charge transport across the bulk electrolyte is important, the rate capability of a SSB is often limited by the interfacial regions. In contrast to SSBs, liquid electrolytes possess excellent wettability properties, which effectively create a large contact area between a solid electrode material and a liquid electrolyte to enable efficient Li^+ ion removal/insertion. It is rather more difficult for SSBs, for which the extraction of charge from an electrode must occur across a solid-solid boundary. A highly resistive electrode-electrolyte interface can dominate a cell's impedance and hamper the rate capability [36–38]. The resistance across the boundary is known as the area specific resistance (given in Ω cm^{-2}). Various surface modifications have been shown to improve the wettability and reduce the area specific resistance of solid-state electrolytes. These include, but are not limited to lithium metal-alloy layers [36], metal layers (i.e., Au, Ge) [39, 40], carbon layers [41, 42], high external pressure [37, 43], additives [44, 45], hybrid polymer layers [46], and thin buffer layers such as Al_2O_3 [47]. However, the scalability and cost of these solutions remains a serious challenge, while dendritic issues over extended cycling persist [48]. Another potential route to improve the area specific resistance, particularly across the cathode-electrolyte boundary, is by 'matching' the crystal structures of both components. In other words, by joining two materials of the same structural class. This can provide uninterrupted diffusion pathways for ions to alleviate the bottleneck in charge transfer across the interfacial region.

In SSBs there is often an electrode-electrolyte reaction which occurs at the interface. This can form a layer, termed the interphase, which has a profound influence on the electrochemical performance of a cell [49]. The nature of the interphase formed between a solid electrolyte and a lithium anode is highly dependent on the electrolyte composition,

and its properties vary widely in the literature depending on the material [49]. Such a layer can be acceptable for battery functionality if it possesses a minimal resistance to ionic motion [46]; however, the maintenance of a robust physical electrolyte-electrode contact is often problematic due to the largely unavoidable volume changes in the electrode during cycling [50]. In some cases, the interphase can act to increase the contact area between the electrode and electrolyte, decreasing the area specific resistance, while in others it can become a bottleneck for ionic transport [26].

The relationship between dendritic growth and electronic conductivity [25] is apposite here, as any formed interphase alters both the ionic and electronic conductivity across a cell. As the growth of an interphase typically depends on the reaction of both ions and electrons, if it blocks electronic mobility the interphase can become kinetically stabilised. If not, and electronic mobility is allowed, the interphase may grow continuously during cycling and/or become increasingly resistive [51]. Unfortunately, highly conductive electrolytes appear to decompose most readily at the interface; two effects likely linked by the thermodynamic stability of mobile charge carriers [52]. To develop SSBs then, it is vital to understand the charge transport properties in both the bulk and the interphase region. Study of this region in detail is difficult due to its thin and subsurface nature, meaning the development of *operando* techniques will no doubt prove valuable [53].

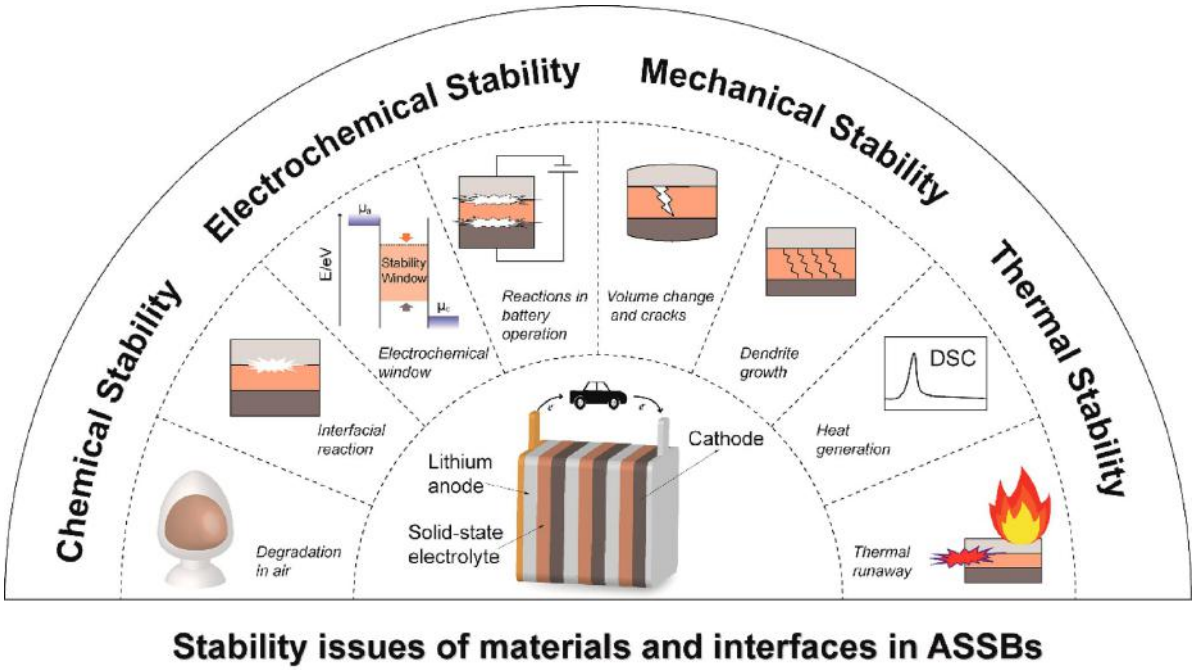

Figure 1.4: A diagram to illustrate some stability issues of solid-state batteries. Reprinted (adapted) with permission from [20]. Copyright 2020 American Chemical Society.

1.2.1 NASICON–structured solid electrolytes

NASICONs, an acronym for sodium super ionic conductor, are a class of solid electrolytes known for their high ionic conductivity and excellent chemical stability. While first inves-

tigated in the form $Na_{1+x}Zr_2P_{3-x}Si_xO_{12}$ by Goodenough *et al.* [54], the class has since been extended to explore Li^+ as the mobile cation. NASICONs have the general formula $AM_2(PO_4)_3$, where A is the mobile cation and M is a metal ion. The most common Li-based NASICON conductors are $LiTi_2(PO_4)_3$, $LiZr_2(PO_4)_3$, and $LiGe_2(PO_4)_3$, and dopants such as Al have been routinely explored since they are known to improve the conductivity [55]. NASICON materials generally exist in the triclinic or rhombohedral phase.

In the fast-conducting rhombohedral phase (space group $R\bar{3}C$), Li^+ is split across two sites: M_1 and M_2 (this is explored in Chapter 4). The M_1 site has six-fold coordination, while the M_2 site has eight-fold coordination [56]. Li^+ motion through the crystal structure passes from M_1 to M_2, and this diffusion pathway must pass between two close O anions. This is known as the M_1M_2 bottleneck, and control over its width is influential for Li^+ ion mobility. The bottleneck can be optimised by judicious choice of dopant and M-site metal cation. As well as the high conductivity of composition controlled NASICON phases, another strength lies in their air stability. Such stability vastly improves the ease of material handling and facilitates a scalability in manufacture. Although air stable, reports of the electrochemical stability of NASICON materials are conflicting, especially against a Li metal anode [57, 58], The properties of NASICON materials $LiTi_2(PO_4)_3$ and $LiZr_2(PO_4)_3$ are explored in Chapter 4.

1.2.2 Garnet-structured solid electrolytes

Garnet-structured ceramic electrolytes of the form $Li_7La_3Zr_2O_{12}$ (LLZO) are one of the most promising for SSBs. The strength of this material is demonstrated by its high ionic conductivity of up to $\sim$1 mS cm^{-1} and excellent chemical stability [59]. LLZO exists in both tetragonal (space group $I4_1/acd$) and cubic (space group $Ia\bar{3}d$) phases. It is well established that only the cubic symmetry is suitable for usage as a solid electrolyte, displaying ionic conductivities around two orders of magnitude higher than the tetragonal phase [60, 61]. The high ionic conductivity in the cubic phase arises from isotropic three-dimensional Li^+ ion diffusion facilitated by a degree of disorder amongst the partially occupied lithium sites [62]. In contrast, the tetragonal form exists with only an empty/full occupancy of lithium sites, increasing the difficulty of ionic transport [63]. Aliovalent cation doping (i.e., Al^{3+}) is regularly used to disrupt the local lithium occupancy, stabilising disordered and partially occupied Li sites characteristic of the cubic phase. As such, dopants allow the cubic phase to exist at room temperature. The choice of dopant has a significant effect. For example, Allen *et al.* have shown that dopants which sit outside the Li sublattice benefit ionic conductivity [64], whilst Zhu *et al.* have demonstrated the importance of the dopant upon the interfacial impedance [65].

The air stability of LLZO phases is a notable challenge [66], as the spontaneous sur-

face formation of Li_2CO_3 is rapid and debilitating for the interfacial resistance. Although early reports detail electrochemical stability over a wide voltage window, it is now believed that the theoretical window is extended towards the practical 0–5 V range not due to an intrinsic thermodynamic stability between components, but rather by kinetic stabilisation processes [26, 52]. As a result, redox decomposition does not occur without significant overpotential. Interfacial stability is crucial for the successful application of LLZO garnets; such properties hugely depend on the dopant used to stabilise the cubic phase. The interfacial characteristics of W-doped LLZO are investigated in Chapter 5.

1.3 Ionic Diffusion

Underpinning the functionality described for both lithium-ion and solid-state batteries is how fast Li^+ ions can be reversibly intercalated into the electrodes. This process forms the basis for a cell's power/rate capability, which is especially relevant for electric vehicles as fast charging becomes increasingly desirable. An ideal solid electrolyte should work as an inert medium for ionic transfer between electrodes; a material which minimises electronic conductivity and maximises ionic conductivity. For electrode materials, the goal is rapid and efficient extraction/insertion of both charge carriers. This involves the transport of ions to the electrolyte and of electrons to a current collector. In both types of material, the underlying process of conduction through a solid is the same, where the total conductivity (σ) can be described as:

$$\sigma = \sum n q \mu. \tag{1.2}$$

Every term in Equation 1.2 refers to the charge carriers, where n is their total number, q is their charge, and μ is their mobility. The charge carriers may be electrons or holes for electronic conductivity, and cations or anions for ionic conductivity. If a material is a mixed conductor, σ is the sum of both electronic and ionic components.

In general, a fast ionic conductor must possess two structural properties: the partial occupancy of the mobile ion sites, and a continuous pathway between these sites. Since in Equation 1.2, q is a fixed value, to increase the conductivity, either n or μ must be increased. However, it is often not as straightforward as simply increasing the Li content, as an increase in n means a higher occupancy on the mobile ion site which leads to a reduction in the overall ionic mobility, μ. As such, a balance of site vacancy to charge carrier concentration must be found by material design. These properties depend on the structure of the conductive material, with the dimensionality and pathway(s) for diffusion important to consider. It is well known that the macroscopic conductivity properties of a material are a consequence of the diffusional properties at microscopic level [26, 35].

In a crystalline solid the constituent atoms are arranged in a close-packed periodic style with fixed positions. For diffusion, an ion must pass through an energetically unfavourable

transition state to the next available stable site. This process is illustrated in Figure 1.5. The diffusion of an ion from one site to another is often termed a "hop". To complete a site-site hop, an ion must overcome an energy barrier to move through the transition state: this is called the activation energy (E_a). Three mechanisms are generally available for such diffusion processes: vacancy, direct interstitial, or correlated interstitial diffusion. The activation energy is generally highest for a vacancy hopping pathway as the ion must pass through the bottleneck between two stationary atoms. An interstitial site can be used as an energy saving intermediate state between stable positions, and these interstitial sites tend to be more energetically unstable. Correlated interstitial diffusion occurs when the diffusing ion pushes out the host ion to an adjacent site. The rate of ionic diffusion then depends on the activation energy, the number of available pathways, the site vacancy fraction in such pathways, and the site-site hopping distance. Conduction through defects is common for ionically conductive materials, however for solid electrolytes the vacancies are primarily provided by empty sites [67]. In general, body-centred cubic lattice structures make for ideal ionic conductors due to the low activation energy for diffusion between adjacent tetrahedral sites [68]. One technique to facilitate fast-ion diffusion is thus to synthesise materials with the mobile carriers placed on high energy sites in order to lower the activation barrier [69].

To overcome the energy barrier an ion must be sufficiently stimulated. For spontaneous diffusion, this can occur *via* the application of temperature, whereby ions can absorb enough thermal energy to overcome the activation energy, or the application of an electric field gradient to motivate directionally dependent diffusion. Conductivity can be related to the activation energy for ionic motion by an Arrhenius expression:

$$\sigma = A \exp(-\frac{E_a}{k_B T}), \tag{1.3}$$

where k_B is Boltzmann's constant and T is absolute temperature. Equation 1.3 can be derived from Fick's second law of diffusion. A is a pre-exponential factor which summarises several parameters, including structural properties and the hopping attempt frequency. To yield the activation energy of a material, one may complete a temperature dependent analysis of conductivity. Equation 1.3 relates a macroscopic quality (σ) to one which has just been defined at the atomic level (E_a). As a result, the determined activation energy corresponds to the energy required to motivate ionic motion across an entire sample. Such a diffusion pathway encompasses regions such as the bulk, the grain boundary, and the interface.

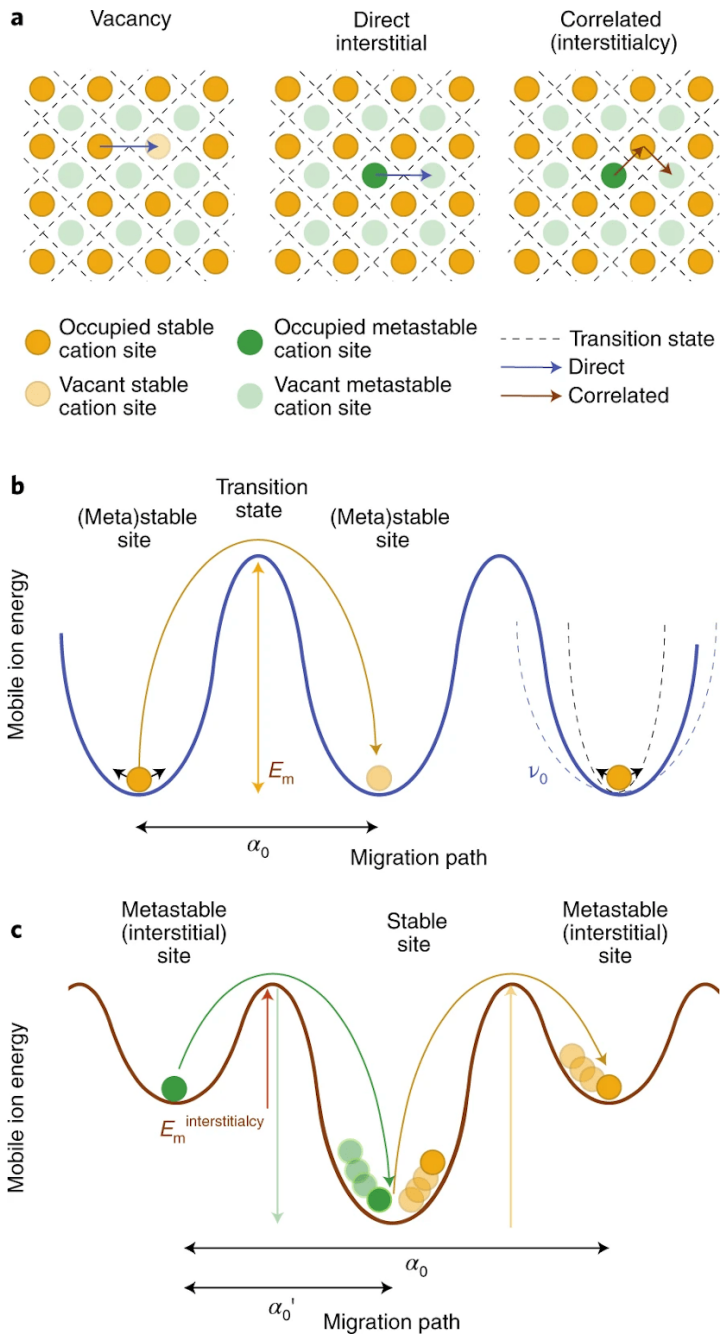

Figure 1.5: Schematic which presents the three most common processes for ionic diffusion in crystalline solids. (a) Vacancy (direct site-site hopping), direct interstitial (metastable transition site), and correlated interstitial (knock-on mechanism through interstitial sites) diffusion pathways are shown. (b), (c) The energy profiles for vacancy and correlated interstitial ionic diffusion, respectively, which are associated with the pathways shown in (a). α_0 is the hopping distance, E_m the activation energy for motion, and ν_0 is the hopping frequency. Reproduced and adapted from [26] with permission from Springer Nature Limited, Copyright 2019.

It is therefore important to also define a microscopic diffusion parameter, D, which corresponds to the intrinsic ionic hopping rate of a material. The chemical diffusion coefficient (D_σ) can be related to conductivity by the Nernst-Einstein relationship, described

as:

$$D_\sigma = \frac{\mu}{q}\, k_B\, T = \frac{k_B\, T}{n\, q^2}\, \sigma. \tag{1.4}$$

Equation 1.4 also relates two parameters which operate over different length scales, D and σ. This, in combination with the difficulty in precisely characterising n, has led recent works to question the validity of the Nernst-Einstein equation for fast-ion conductors [70]. Equation 1.4 is an approximation, as the diffusion coefficient also depends on the Haven ratio (H_R), which is defined as:

$$H_R = \frac{D}{D_\sigma}, \tag{1.4}$$

where D is the self-diffusion coefficient and D_σ is the chemical diffusion coefficient [71]. Self-diffusion is spontaneous, while chemical diffusion occurs under a potential gradient (i.e., it is directional). Although these two properties of diffusivity are related, crucially, they represent different physical properties [70]. It can be deduced that if hopping is directionally random, then $D = D_\sigma$. Which coefficient is evaluated depends on the nature of the measurement technique used (Figure 1.6).

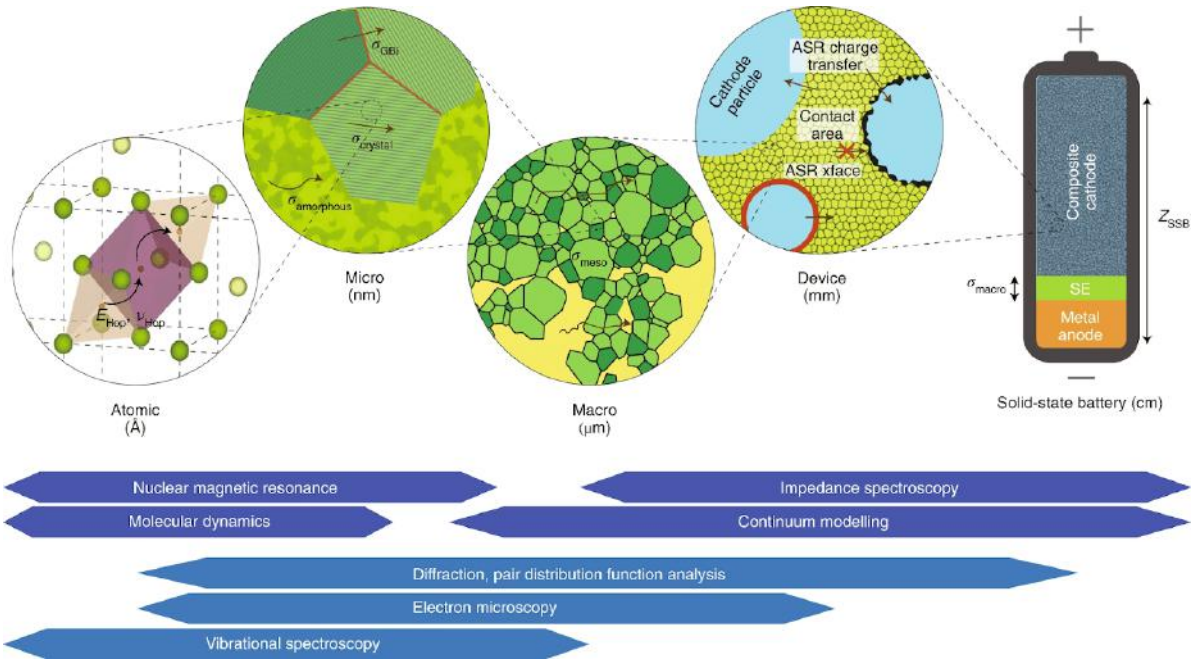

Figure 1.6: The length scale at which ionic transport processes occur in battery materials, and some example techniques to measure them. Reproduced and adapted from [26] with permission from Springer Nature Limited, Copyright 2019.

While the mechanism of ionic diffusion occurs at a site-site level (∼Å length scale), the macroscopic property of conductivity is a consequence of diffusion phenomena through a range of the length scales. To measure the conductivity of a cell, the diffusion properties across all these length scales must be considered. The transport of Li^+ ions across physical boundaries, such as surface layers or in between grains, generally has a much higher ionic resistance and will dominate the overall impedance of a cell [72]. For example, in

common solid electrolyte material lithium lanthanum titanate ($Li_{3x}La_{(2/3)-x}TiO_3$), the grain boundary has been found to possess an ionic conductivity around two orders of magnitude lower than the bulk [73]. Since no single technique can be used to understand this process at every length scale, a combination of complementary techniques is desirable.

1.3.1 Techniques to measure ionic diffusion

The choice of technique with which to measure ionic motion is often motivated by the time and length-scale of the dynamics under investigation. In solids the typical self-diffusion rates are between around 10^{-14} – 10^{-7} cm^2 s^{-1}. Very generally, these techniques can be grouped into microscopic and macroscopic methods. In essence, the former probes individual site hopping (often D) and the latter long-range transport (often D_σ). This is shown in Figure 1.7; NMR, μSR, and QENS probe on the microscopic level, and tracer diffusion, DC conductivity, and pulsed field-gradient (PFG) NMR probe on the macroscopic level. Electrochemical impedance spectroscopy (EIS) is another common technique to probe charge transport, although this is not included in Figure 1.7 as the length scale it operates over is dependent on the frequency applied, meaning it covers a wide range (∼10 MHz – 1 mHz). However, the parameters obtained from EIS are generally macroscopic resistances and capacitances. Microscopic techniques can inform on fundamental material properties, and macroscopic techniques on more realistic operating characteristics. In general, macroscopic techniques will yield higher values for the activation energy than microscopic ones since structural impurities and highly resistive regions play a larger role [74]. Meanwhile, the close connection between crystal structure and ionic dynamics motivates the usage of complementary techniques.

NMR is typically one of the most powerful methods to quantify microscopic diffusion rates. In NMR, the line-width arising from a particular ion is narrowed as the ion's mobility increases. The strength of NMR lies in its exceptional elemental selectivity, allowing direct isolation of the dynamic ion, as well as its ability to probe a wide time scale. Data analysis for NMR can become complicated for battery materials due to the additional effect of the electron spins from magnetic ions on the spin-lattice relaxation rate. Another microscopic technique is quasi-elastic neutron scattering (QENS), which is a powerful method of directly following the motion of ions and can resolve diffusion both spatially and temporally. QENS operates on a relatively fast time-scale, allowing the determination of dynamics in electrolytes but precluding the study of slower dynamics through certain solid materials. Furthermore, molecular dynamics (MD) simulations and *ab initio* modelling are valuable tools with which to validate experimental results and investigate new materials.

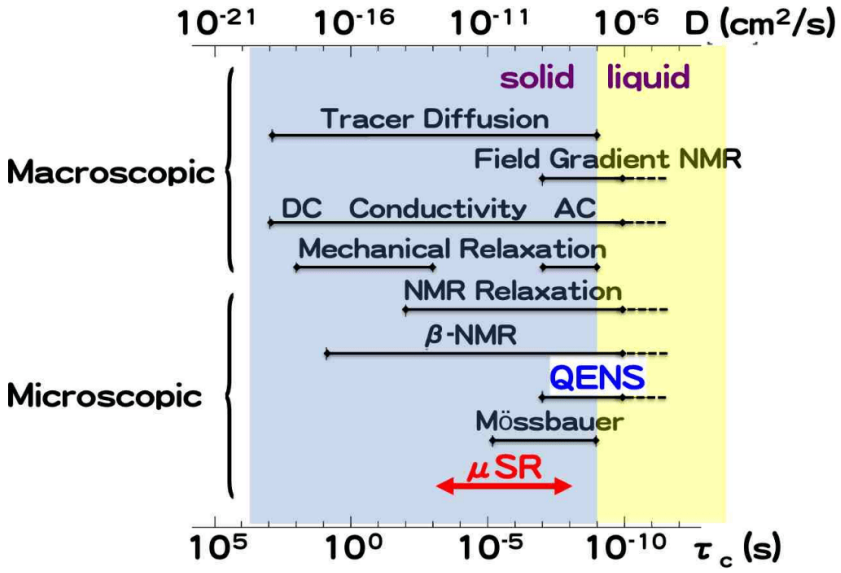

Figure 1.7: The time range of μSR is added to the typical ranges of a diffusion coefficient (D) and motional correlation time (τ_c) of some macroscopic and microscopic methods. Figure and caption reproduced with permission from [75]. Copyright 2014 Physical Society of Japan.

Electrochemical methods, such as DC/AC conductivity, impedance spectroscopy, and cyclic voltammetry, are a fast and ubiquitous way of characterising diffusion on a wide length scale. The availability and versatility of such methods allows for a range of applications across energy materials. For example, these can provide the transference number of ions and electrons. In general, these techniques probe D_σ rather than D. To effectively quantify the self-diffusion rate using electrochemical methods, a reactive surface area is required. This can be straightforward for solid electrolyte materials but is non-trivial for cathode materials which are immersed in a liquid electrolyte [76]. The quantification of diffusion by electrochemical methods is also highly dependent on the sample preparation method, as properties such as density and particle size are influential to the grain boundary properties [67]. As such, it is often difficult to compare microscopic and macroscopic techniques directly, although the combination of both affords a deeper understanding.

Muon spin relaxation spectroscopy, known as μSR, has an appropriate time-scale of measurement for ionic hopping in solids, and the separation of electronic and ionic effects is routine during data analysis. While the accessibility of μSR is perhaps limited due to its necessity for a particle accelerator, there is potential to develop the technique towards detailed *operando* measurements for specialist experiments. The application of the μSR technique will be further explored throughout this thesis, with an emphasis placed on the collaboration of complementary structural and diffusional techniques.

1.3.2 *Operando* methods for interrogating diffusion properties

To fully understand the behaviour of energy materials, it is necessary to investigate how the fundamental properties change during operation in a device. As such, *in situ* and

operando techniques have become increasing popular in battery research [53, 77]. The meaning of these terms is defined in Figure 1.8. For measurements regarding battery cells, "*ex situ*" is defined as a material which has been extracted from a battery for a measurement. This provides fundamental material properties where the material may or may not be cycled to a specific potential state. "*In situ*" is defined as an external measurement completed while the material is still inside the battery cell, but is not subject to an applied current simultaneously. This avoids any potential exposure or damage from removing a material from a cell and can inform on trends during cycling. "*Operando*" is defined as the simultaneous application of a measurement technique while a cell is cycling. This can follow the properties of an active material as it operates in real time, avoiding any relaxation effects. The level of detail and accuracy increases through these options although, generally, so does experimental complexity. Note that these terms are widely applied across the literature and are defined here for this work only.

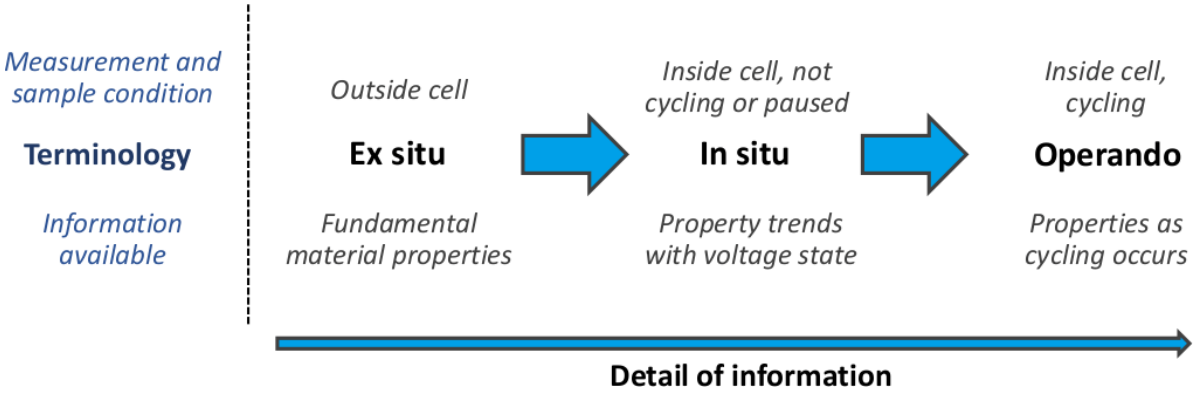

Figure 1.8: A schematic outlining how the terms "*ex situ*", "*in situ*", and "*operando*" are used in the work. This is classed by the measurement and sample condition, as well as the information available. The precision and detail gained from the measurement increases from *ex situ* to *operando*.

The application of *operando* measurements has expanded rapidly towards both synchrotron and lab-based techniques [16]. These offer significant advantages over an *ex situ* approach, namely: the avoidance of material relaxation effects, the opportunity of studying time-dependent phenomena, the avoidance of contamination, and the avoidance of user error. As such, the level of precision and reliability in measurement is improved. Recent studies using *in situ*/*operando* lab-based techniques such as NMR [8], electron microscopy [78], optical microscopy [79], Raman spectroscopy [80], and impedance spectroscopy [81] have all been used to excellent effect, while the opportunity to progress these towards an established methodology offers an accessible route to advanced material characterisation. Furthermore, developments to *in situ*/*operando* synchrotron techniques such as neutron diffraction [82], X-ray absorption spectroscopy [83], and X-ray photoelectron spectroscopy [84] have permitted the application of specialist techniques to a level of detail previously unachievable. Such advanced methodologies are crucial to under-

standing how material properties change during operation; knowledge which facilitates the design of next-generation high performance technology. To satisfy the experimental requirements for *operando* measurements, a custom cell is often required, such as the Battery Analysis by Muon cell which has been developed in this thesis.

1.4 Summary and Main Objectives

The pressing need for high performance energy materials has facilitated a global research effort towards the optimisation of lithium-ion batteries and to the rapid development of solid-state batteries. At the forefront of this push to solid-state is the desire for new, fast-conducting, and stable materials. Concurrently for cathodes, the development of a fundamental understanding of the underpinning charge transfer processes, alongside the highly correlated structural properties, is crucial to optimise the design and synthesis of next-generation materials. For this, advanced characterisation techniques are essential, and the development of *operando* methodologies offers the opportunity to gain highly detailed information in a realistic environment.

The μSR technique is applicable towards a range of energy storage technologies, such as lithium-ion and solid-state batteries, and provides complementary insight to existing methods such as NMR. Until now, μSR measurements have been reported on powder samples only: no *in situ* capability existed. The aim of this research is then to extend the capacity of muon spectroscopy towards a working methodology for *in situ* and *operando* measurements of ionic diffusion. For this, a working electrochemical cell is developed, and facilitates the μSR study of previously inaccessible battery phenomena. This includes the crucial role of the interfacial region in solid-state batteries, the influence of the dopant in fast conducting garnet phases, and the effect of phase changes during cycling in high Ni-content cathodes.

References

[1] J. Xie and Y. C. Lu. A retrospective on lithium-ion batteries. *Nature Commun.*, 11:2499, 2020.

[2] K. Mizushima, P. C. Jones, P. J. Wiseman, and J. B. Goodenough. Li_xCoO_2 ($0 < x \leq 1$): A New Cathode Material For Batteries Of High Energy Density. *Solid State Ion.*, 3:171–174, 1981.

[3] Y. Lyu, X. Wu, Z. Feng, T. Cheng, Y. Liu, M. Wang, R. Chen, L. Xu, J. Zhou, Y. Lu, and B. Guo. An Overview on the Advances of $LiCoO_2$ Cathodes for Lithium-Ion Batteries. *Adv. Energy Mater.*, 11:2000982, 2021.

[4] P. Miller. Automotive Lithium-Ion Batteries. *Johnson Matthey Technol. Rev.*, 59:4–13, 2015.

[5] J. P. Pender, G. Jha, D. H. Youn, J. M. Ziegler, I. Andoni, E. J. Choi, A. Heller, B. S. Dunn, P. S. Weiss, R. M. Penner, and C. B. Mullins. Electrode Degradation in Lithium-Ion Batteries. *ACS Nano*, 14:1243–1295, 2020.

[6] E. Trevisanello, R. Ruess, G. Conforto, F. H. Richter, and J. Janek. Polycrystalline and Single Crystalline NCM Cathode Materials—Quantifying Particle Cracking, Active Surface Area, and Lithium Diffusion. *Adv. Energy Mater.*, 11:2003400, 2021.

[7] T. Li, X. Z. Yuan, L. Zhang, D. Song, K. Shi, and C. Bock. Degradation Mechanisms and Mitigation Strategies of Nickel-Rich NMC-Based Lithium-Ion Batteries. *Electrochem. Energy Rev.*, 3:43–80, 2020.

[8] K. Märker, C. Xu, and C. P. Grey. Operando NMR of NMC811/Graphite Lithium-Ion Batteries: Structure, Dynamics, and Lithium Metal Deposition. *J. Am. Chem. Soc*, 142:17447–17456, 2020.

[9] P. He, H. Yu, D. Li, and H. Zhou. Layered lithium transition metal oxide cathodes towards high energy lithium-ion batteries. *J. Mater. Chem.*, 22:3680, 2012.

[10] R. Jung, M. Metzger, F. Maglia, C. Stinner, and H. A. Gasteiger. Oxygen Release and Its Effect on the Cycling Stability of $LiNi_xMn_yCo_zO_2$ (NMC) Cathode Materials for Li-Ion Batteries. *J. Electrochem. Soc.*, 164:A1261–A1377, 2017.

[11] J. T. Williams, A. M. Vangu, H. B. Mabiala, H. B. Mangungulu, and E. K. Tissingh. Toxicity in the supply chain: cobalt, orthopaedics, and the Democratic Republic of the Congo. *Lancet Glob. Health*, 5:E327–E328, 2021.

[12] Y. Lv, S. Huang, Y. Zhao, S. Roy, X. Lu, Y. Hou, and J. Zhang. A review of nickel-rich layered oxide cathodes: synthetic strategies, structural characteristics, failure mechanism, improvement approaches and prospects. *Appl. Energy*, 305:117849, 2022.

[13] J. B. Goodenough and Y. Kim. Challenges for Rechargeable Li Batteries. *Chem. Mater.*, 22:587–603, 2010.

[14] L. Ole Valøen and J. N. Reimers. Transport Properties of $LiPF_6$-Based Li-Ion Battery Electrolytes. *J. Elecrochem. Soc.*, 152:A882–A891, 2005.

[15] J. Zheng, M. H. Englehard, D. Mei, S. Jiao, and B. J. Polzin. Electrolyte additive enabled fast charging and stable cycling lithium metal batteries. *Nature Energy*, 2:17012, 2017.

[16] B. Liu, J. G. Zhang, and W. Xu. Advancing Lithium Metal Batteries. *Joule*, 2:833–845, 2018.

[17] D. Lu, Y. Shao, T. Lozano, W. D. Bennett, G. L. Graff, B. Polzin, J. Zhang, M. H. Engelhard, N. T. Saenz, W. A. Henderson, P. Bhattacharya, J. Liu, and J. Xiao. Failure mechanism for fast-charged lithium metal batteries with liquid electrolytes. *Adv. Energy Mater.*, 5:1400993, 2015.

[18] A. Guéguen, D. Streich, M. He, M. Mendez, F. F. Chesneau, P. Novák, and E. J. Berg. Decomposition of $LiPF_6$ in High Energy Lithium-Ion Batteries Studied with Online Electrochemical Mass Spectrometry. *J. Electrochem. Soc*, 163:A1095–A1100, 2016.

[19] G. Han, B. Kinzer, R. Garcia-Mendez, H. Choe, J. Wolfenstine, and J. Sakamoto. Correlating the effect of dopant type (Al, Ga, Ta) on the mechanical and electrical properties of hot-pressed Li-garnet electrolyte. *J. Eur. Ceram. Soc.*, 40:1999–2006, 2020.

[20] R. Chen, Q. Li, X. Yu, L. Chen, and H. Li. Approaching Practically Accessible Solid-State Batteries: Stability Issues Related to Solid Electrolytes and Interfaces. *Chem. Rev.*, 120:6820–6877, 2020.

[21] Y. Song, L. Yang, L. Tao, Q. Zhao, Z. Wang, Y. Cui, H. Liu, Y. Lin, and F. Pan. Probing into the origin of an electronic conductivity surge in a garnet solid-state electrolyte. *J. Mater. Chem. A.*, 7:22898—-22902, 2019.

[22] E. J. Cheng, A. Sharafi, and J. Sakamoto. Intergranular Li metal propagation through polycrystalline $Li_{6.25}Al_{0.25}La_3Zr_2O_{12}$ ceramic electrolyte. *Electrochim. Acta*, 223:85–91, 2017.

[23] J. van den Broek, S. Afyon, and J. L. M. Rupp. Interface-Engineered All-Solid-State Li-Ion Batteries Based on Garnet-Type Fast Li^+ Conductors. *Adv. Energy Mater.*, 6:1600736, 2016.

[24] R. Sudo, Y. Nakata, K. Ishiguro, M. Matsui, A. Hirano, Y. Takeda, O. Yamamoto, and N. Imanishi. Interface behavior between garnet-type lithium-conducting solid electrolyte and lithium metal. *Solid State Ion.*, 262:151–154, 2014.

[25] F. Han, A. S. Westover, J. Yue, x. Fan, F. Wang, M. Chi, D. N. Leonard, N. J. Dudney, H. Wang, and C. Wang. High electronic conductivity as the origin of lithium dendrite formation within solid electrolytes. *Nature Energy*, 4:187–196, 2019.

[26] T. Famprikis, P. Canepa, J. A. Dawson, M. S. Islam, and C. Masquelier. Fundamentals of inorganic solid-state electrolytes for batteries. *Nature Materials*, 18:1278–1291, 2019.

[27] F. M. Pesci, A. Bertei, R. H. Brugge, S. P. Emge, A. K. O. Hekselman, L. E. Marbella, C. P. Grey, and A. Aguadero. Establishing Ultralow Activation Energies for Lithium Transport in Garnet Electrolytes. *ACS Appl. Mater. Interfaces*, 12:32806–32816, 2020.

[28] R. Murugan, S. Ramakumar, and N. Janani. High conductive yttrium doped $Li_7La_3Zr_2O_{12}$ cubic lithium garnet. *Electrochem. Commun.*, 13:1373–1375, 2011.

[29] A. Yoshino. The birth of the lithium-ion battery. *Angew. Chem. Int. Ed.*, 51:5798–5800, 2012.

[30] S. Kumazaki, Y. Iriyama, K. H. Kim, R. Murugan, K. Tanabe, K. Yamamoto, T. Hirayama, and Z. Ogumi. High lithium ion conductive $Li_7La_3Zr_2O_{12}$ by inclusion of both Al and Si. *Electrochem. Commun.*, 13:509–512, 2011.

[31] Y. Li, Z. Wang, Y. Cao, F. Du, C. Chen, Z. Cui, and X. Guo. W-Doped $Li_7La_3Zr_2O_{12}$ Ceramic Electrolytes for Solid State Li-ion Batteries. *Electrochimica Acta*, 180:37–42, 2015.

[32] P. Tsai, B. Wen, M. Wolfman, M. Choe, M. S. Pan, L. Su, K. Thornton, J. Cabana, and Y. Chiang. Single-particle measurements of electrochemical kinetics in NMC and NCA cathodes for Li-ion batteries. *Energy Environ. Sci.*, 11:860–871, 2018.

[33] C. Brissot, M. Rosso, J-N Chazaviel, and S. Lascaud. Dendritic growth mechanisms in lithiumrpolymer cells. *J. Power Sources*, 81-82:925–929, 1999.

[34] A. R. Septiana, W. Honggowiranto, Sudaryanto, E. Kartini, and R. Hidayat. Comparative study on the ionic conductivities and redox properties of $LiPF_6$ and LiTFSI electrolytes and the characteristics of their rechargeable lithium ion batteries. *IOP Conf. Sereies: Mat. Sci. Engineer.*, 432:012061, 2018.

[35] V. Balos, S. Imoto, R. R. Netz, M. Bonn, D. J. Bouthuis, Y. Nagata, and J. Hunger. Macroscopic conductivity of aqueous electrolyte solutions scales with ultrafast microscopic ion motions. *Nature Commun.*, 11:1611, 2020.

[36] K. Fu, Y. Gong, B. Liu, Y. Zhu, S. Xu, Y. Yao, W. Luo, C. Wang, S. D. Lacey, J. Dai, Y. Chen, Y. Mo, E. Wachsman, and L. Hu. Toward garnet electrolyte–based Li metal batteries: An ultrathin, highly effective, artificial solid-state electrolyte/metallic Li interface. *Sci. Adv.*, 3:1–12, 2017.

[37] L. Cheng, W. Chen, M. Kunz, K. Persson, N. Tamura, G. Chen, and M. Doeff. Effect of surface microstructure on electrochemical performance of garnet solid electrolytes. *ACS Appl. Mater. Interfaces*, 7:2073–2081, 2015.

[38] S. J. Harris and P. Lu. Effects of Inhomogeneities - Nanoscale to Mesoscale - on the Durability of Li-Ion Batteries. *J. Phys. Chem. C*, 117:6481–6492, 2013.

[39] W. Luo, Y. Gong, Y. Zhu, Y. Li, Y. Yao, Y. Zhang, K. Fu, G. Pastel, C. Lin, Y. Mo, E. D. Wachsman, and L. Hu. Reducing Interfacial Resistance between Garnet-Structured Solid-State Electrolyte and Li-Metal Anode by a Germanium Layer. *Adv. Mater.*, 29:1606042, 2017.

[40] C. L. Tsai, V. Roddatis, C. V. Chandran, Q. Ma, S. Uhlenbruck, M. Bram, P. Heitjans, and O. Guillon. $Li_7La_3Zr_2O_{12}$ Interface Modification for Li Dendrite Prevention. *ACS Appl. Mater. Interfaces*, 8:10617–10626, 2016.

[41] Y. Shao, H. Wang, Z. Gong, D. Wang, B. Zheng, J. Zhu, Y. Lu, Y. S. Hu, H. Li, X. Huang, Y. Yang, C. W. Nan, and L. Chen. Drawing a Soft Interface: An Effective Interfacial

Modification Strategy for Garnet- Type Solid-State Li Batteries. *ACS Energy Lett.*, 3:1212–1218, 2018.

[42] W. Feng, X. Dong, X. Zhang, Z. Lai, P. Li, C. Wang, Y. Wand, and Y. Xia. Li/Garnet Interface Stabilization by Thermal-Decomposition Vapor Deposition of an Amorphous Carbon Layer. *Angew. Chem. Int. Ed.*, 59:5346–5349, 2020.

[43] K. Ishiguro, H. Nemori, S. Sunahiro, Y. Nakata, R. Sudo, M. Matsui, Y. Takeda, O. Yamamoto, and N. Imanishi. Ta-Doped $Li_7La_3Zr_2O_{12}$ for Water-Stable Lithium Electrode of Lithium-Air Batteries. *J. Electrochem. Soc.*, 161:A668–A674, 2014.

[44] B. Xu, W. Li, H. Duan, H. Wang, Y. Guo, H. Li, and H. Liu. Li_3PO_4-added garnet-type $Li_{6.5}La_3Zr_{1.5}Ta_{0.5}O_{12}$ for Li-dendrite suppression. *J. Power Sources*, 354:68–73, 2017.

[45] Y. Lu, X. Huang, Z. Song, K. Rui, Q. Wang, S. Gu, J. Yang, T. Xiu, M. E. Badding, and Z. Wen. Highly stable garnet solid electrolyte based Li-S battery with modified anodic and cathodic interfaces. *Energy Storage Mater.*, 15:282–290, 2018.

[46] Y. Li, B. Xu, H. Xu, H. Duan, X. Lü, S. Xin, W. Zhou, L. Xue, G. Fu, A. Manthiram, and J. B. Goodenough. Hybrid Polymer/Garnet Electrolyte with a Small Interfacial Resistance for Lithium-Ion Batteries. *Angew. Chem. Int. Ed.*, 56:753–756, 2017.

[47] X. Han, Y. Gong, K. Fu, X. He, G. T. Hitz, J. Dai, A. Pearse, B. Liu, H. Wang, G. Rubloff, Y. Mo, V. Thangadurai, E. D. Wachsman, and L. Hu. Negating interfacial impedance in garnet-based solid-state Li metal batteries. *Nat. Mater.*, 16:572–579, 2017.

[48] H. Huo, J. Luo, V. Thangadurai, X. Guo, C. W. Nan, and X. Sun. Li_2CO_3: A Critical Issue for Developing Solid Garnet Batteries. *ACS Energy Lett.*, 5:252–262, 2020.

[49] A. Banerjee, X. Wang, C. Fang, E. A. Wu, and Y. S. Meng. Interfaces and Interphases in All-Solid-State Batteries with Inorganic Solid Electrolytes. *Chem. Rev.*, 120:6878–6933, 2020.

[50] G. Bucci, B. Talamini, A. R. Balakrishna, Y. M. Chiang, and W. C. Carter. Mechanical instability of electrode-electrolyte interfaces in solid-state batteries. *Phys. Rev. Materials*, 2:105407, 2018.

[51] S. Wenzel, S. J. Sedlmaeier, C. Dietrich, W. G. Zeier, and J. Janek. Interfacial reactivity and interphase growth of argyrodite solid electrolytes at lithium metal electrodes. *Solid State Ion.*, 318:102–112, 2018.

[52] Y. Zhu, X. He, and Y. Mo. Origin of Outstanding Stability in the Lithium Solid Electrolyte Materials: Insights from Thermodynamic Analyses Based on First-Principles Calculations. *ACS Appl. Mater. Interfaces*, 7:23685–23693, 2015.

[53] P. P. R. M. L. Harks, F. M. Mulder, and P. H. L. Notten. *In situ* methods for Li-ion battery research: A review of recent developments. *J. Power Sources*, 288:92–105, 2015.

[54] J. B. Goodenough, H. Y-P. Hong, and J. A. Kafalas. Fast Na^+-Ion Transport in Skeleton Structures. *Mat. Res. Bull.*, 11:203–220, 1976.

[55] Z. Jian, Y-S. Hu, X. Ji, and W. Chen. NASICON-Structured Materials For Energy Storage. *Adv. Mater.*, 29:1601925, 2017.

[56] M. Hou, F. Liang, K. Chen, Y. Dai, and D. Xue. Challenges and perspectives of NASICON-type solid electrolytes for all-solid-state lithium batteries. *Nanotechnology*, 31:132003, 2020.

[57] P. Hartmann, T. Leichtweiss, M. Busche, M. Schneider, M. Reich, J. Sann, P. Adelhelm, and J. Janek. Degradation of NASICON-Type Materials in Contact with Lithium Metal: Formation of Mixed Conducting Interphases (MCI) on Solid Electrolytes. *J. Phys. Chem. C*, 117:21064–21074, 2013.

[58] X. Xu, Z. Wen, X. Wu, X. Yang, and Z. Gu. Lithium Ion-Conducting Glass-–Ceramics of $Li_{1.5}Al_{0.5}Ge_{1.5}(PO_4)_{3-x}Li_2O$ (x = 0.0–0.20) with Good Electrical and Electrochemical Properties. *J. Am. Ceram. Soc.*, 90:2802–2806, 2007.

[59] V. Thangadurai, S. Narayanan, and D. Pinzaru. Garnet-type solid-state fast Li ion conductors for Li batteries: Critical review. *Chem. Soc. Rev.*, 43:4714–4727, 2014.

[60] M. Klenk and W. Lai. Local structure and dynamics of lithium garnet ionic conductors: tetragonal and cubic $Li_7La_3Zr_2O_{12}$. *Phys. Chem. Chem. Phys.*, 17:8758–8768, 2015.

[61] J. Awaka, N. Kijima, H. Hayakawa, and J. Akimoto. Synthesis and structure analysis of tetragonal $Li_7La_3Zr_2O_{12}$ with the garnet-related type structure. *J. Solid State Chem.*, 182:2046–2052, 2009.

[62] C. A. Geiger, E. Alekseev, B. Lazic, M. Fisch, T. Armbruster, R. Langner, M. Fechtelkord, N. Kim, T. Pettke, and W. Weppner. Crystal Chemistry and Stability of "$Li_7La_3Zr_2O_{12}$" Garnet: A Fast Lithium-Ion Conductor. *Inorg. Chem*, 50:1089–1097, 2011.

[63] S. Afyon, F. Krumeich, and J. L. M. Rupp. A shortcut to garnet-type fast Li-ion conductors for all-solid state batteries. *J. Mater. Chem. A*, 3:18636–18648, 2015.

[64] J. L. Allen, J. Wolfenstine, E. Rangasamy, and J. Sakamoto. Effect of substitution (Ta, Al, Ga) on the conductivity of $Li_7La_3Zr_2O_{12}$. *J. Power Sources*, 206:315–319, 2012.

[65] Y. Zhu, J. G. Connell, S. Tepavcevic, P. Zapol, R. Garcia-Mendez, N. J. Taylor, J. Sakamoto, B. J. Ingram, L. A. Curtiss, J. W. Freeland, D. D. Fong, and N. M. Markovic. Dopant-Dependent Stability of Garnet Solid Electrolyte Interfaces with Lithium Metal. *Adv. Energy Mater.*, 9:1803440, 2019.

[66] W. Xia, B. Xu, H. Duan, X. Tang, Y. Guo, H. Kang, H. Li, and H. Liu. Reaction mechanisms of lithium garnet pellets in ambient air: The effect of humidity and CO_2. *J. Am. Ceram. Soc*, 100:1278–1291, 2017.

[67] P. P. Kumar and S. Yashonath. Ionic conduction in the solid state. *J. Chem. Sci*, 118:135–154, 2006.

[68] Y. Wang, W. D. Richards, S. P. Ong, L. J. Miara, J. C. Kim, Y. Mo, and G. Ceder. Design principles for solid-state lithium superionic conductors. *Nat. Mater.*, 14:1026–1031, 2015.

[69] X. He, Y. Zhu, and Y. Mo. Origin of fast ion diffusion in super-ionic conductors. *Nat. Comm.*, 8:15893, 2016.

[70] A. Marcolongo and N. Marzari. Ionic correlations and failure of Nernst-Einstein relation in solid-state electrolytes. *Phy. Rev. Mater.*, 1:025402, 2017.

[71] G. E. Murch. The Haven Ration In Fast Ionic Conductors. *Solid State Ion.*, 7:177–198, 1982.

[72] M. Park, X. Zhang, M. Chung, G. B. Less, and A. M. Sastry. A review of conduction phenomena in Li-ion batteries. *J. Power Sources*, 195:7904–7929, 2010.

[73] A. R. Symington, M. Molinari, J. A. Dawson, J. M. Statham, J. Purton, P. Canepa, and S. C. Parker. Elucidating the nature of grain boundary resistance in lithium lanthanum titanate. *J. Mater. Chem. A*, 9:6487–6498, 2021.

[74] P. Heitjans and S. Indris. Diffusion and ionic conduction in nanocrystalline ceramics. *J. Phys.: Condens. Matter*, 15:R1257–R1289, 2003.

[75] J. Sugiyama. Macroscopic Electrochemical Properties Clarified by Microscopic Measurements; Present and Future. *JPS Conf. Proc.*, 2:010304, 2014.

[76] J. Sugiyama, K. Mukai, M. Harada, H. Nozaki, K. Miwa, T. Shiotsuki, Y. Shindo, S. R. Giblin, and J. S. Lord. Reactive surface area of the $Li_x(Co_{1/3}Ni_{1/3}Mn_{1/3})O_2$ electrode determined by μ^+SR and electrochemical measurements. *Phys. Chem. Chem. Phys.*, 15:10402, 2013.

[77] X. Li, H-Y. Wang, H. Yang, W. Cai, S. Liu, and B. Liu. In situ/operando characterization techniques to probe the electrochemical reactions for energy conversion. *Small Methods*, 2:1700395, 2018.

[78] K. He, X. Bi, Y. Yuan, T. Foroozan, B. Song, K. Amine, J. Lu, and R. Shahbazian-Yassar. *Operando* liquid cell electron microscopy of discharge and charge kinetics in lithium-oxygen batteries. *Nano Energy*, 49:338–345, 2018.

[79] A. J. Merryweather, C. Schnedermann, Q. Jacquet, C. P. Grey, and A. Rao. Operando optical tracking of single-particle ion dynamics in batteries Imaging lithium-ion transport in LCO. *Nature*, 594:522–528, 2021.

[80] X. Li, J-P. Lee, K. S. Blinn, D. Chen, S. Yoo, B. Kang, L. A. Bottomley, M. A. El-Sayed, S. Park, and M. Liu. High-temperature surface enhanced Raman spectroscopy for in situ study of solid oxide fuel cell materials. *Energy Environ. Sci.*, 7:306–310, 2014.

[81] G. M. Rupp, A. K. Opitz, A. Nenning, A. Limbeck, and J. Fleig. Real-time impedance monitoring of oxygen reduction during surface modification of thin film cathodes. *Nat. Mater.*, 16:640–645, 2017.

[82] S. Taminato, M. Yonemura, S. Shiotani, T. Kamiyama, S. Torii, M. Nagao, Y. Ishikawa, K. Mori, T. Fukunaga, Y. Onodera, T. Naka, M. Morishima, Y. Ukyo, D. Sulistyanintyas Adipranoto, H. Arai, Y. Uchimoto, Z. Ogumi, K. Suzuki, M. Hirayama, and R. Kanno. Real-time observations of lithium battery reactions—operando neutron diffraction analysis during practical operation. *Sci. Rep.*, 6:28843, 2016.

[83] P. Ghigna and E. Quartarone. Operando x-ray absorption spectroscopy on battery materials: a review of recent developments. *J. Phys. Energy*, 3:032006, 2021.

[84] D. Chen, Z. Guan, D. Zhang, L. Trotochaud, E. Crumlin, S. Nemsak, H. Bluhm, H. L. Tuller, and W. C. Chueh. Constructing a pathway for mixed ion and electron transfer reactions for O_2 incorporation in $Pr_{0.1}Ce_{0.9}O_{2-x}$. *Nat. Catal.*, 3:116–124, 2020.

Review Article

Muon Spectroscopy for Investigating Ionic Diffusion in Energy Storage Materials

Innes McClelland, Beth I. J. Johnston, Peter J. Baker, Marco Amores, Edmund J. Cussen, Serena A. Corr

[I. McClelland, B. Johnston, P. J. Baker, M. Amores, E. J. Cussen, and S. A. Corr. Muon Spectroscopy for Investigating Diffusion in Energy Storage Materials. *Annu. Rev. Mater. Res.*, 50:15.1-15.23, 2020.]

Abstract

We review recent applications of positive muon spin relaxation (μSR) spectroscopy as an active probe of ion diffusion in energy storage materials. μSR spectroscopy allows the study of ionic diffusion in solid-state materials on a time scale between 10^{-5} and 10^{-8} s where most long-range and consecutive short-range jumps of ions between interstitial sites occur. μSR also allows one to probe and model ionic diffusion in materials that contain magnetic ions, since both electronic and nuclear contributions to the muon depolarization can be separated, making μSR an excellent technique for the microscopic study of the ionic motions in crystalline materials. We highlight a series of battery materials for which μSR has provided insight into intrinsic ionic conduction and magnetic properties without interference of external factors, such as the presence of magnetic ions, macroscopic particle morphologies, or elaborate measurement setups.

Introduction

The process of translational movement, or diffusion, of ions in solids underpins the functionality of next-generation energy materials. Examples include oxide conduction in solid oxide fuel cells and Li- or Na-ion diffusion in electrodes (and electrolytes) in (solid-state) batteries. Ionic conductivity in solids requires that an ion moves from the site it occupies to a vacant energetically equivalent adjacent site or that an ion at an interstitial site hops to an adjacent interstitial site [1, 2]. For both cases, these are thermally activated processes wherein the ion requires sufficient energy and momentum to move from its initial state through a transition state to its final state, with a probability per unit time given by:

$$P_0(T) = \nu \exp(-\frac{\Delta E_a}{k_B T}), \tag{2.1}$$

where E_a is the activation barrier associated with this hopping motion and ν is a vibrational frequency [3]. There exist multiple experimental and theoretical tools by which the ionic diffusion properties of solid materials, such as the activation energy and the diffusion coefficient, may be examined. Examples include spectroscopic techniques, such as nuclear magnetic resonance (NMR) [4–7], ^{8}Li β–NMR [8], secondary ion mass [9], Raman [10], and electrochemical impedance (EIS) spectroscopies [5, 11–13]; titration methods, including galvanostatic [14–16], potentiostatic [15, 17], and capacity intermittent titration techniques [18]; simulation methods, including molecular dynamics [19, 20] and *ab initio* calculations [21]; electrochemical means, such as cyclic voltammetry [22, 23]; and the application of neutrons, including radiography [24] and quasi-elastic neutron scattering [20, 25]. Such an array of techniques presents the opportunity for a holistic insight into diffusion properties and their underpinning mechanisms, where more than one examination method is employed. It has been observed that, for example, Li^+ ion diffusion rates for the same electrode material do not always yield the same value across multiple techniques [26]. This can be appreciated when one considers the potential complexities and variables involved, such as sufficient contact between electrodes/particles, which is highly variable depending on how the sample is prepared for measurement, sample texture and surface effects, and the scale of time and distance over which the measurement technique in question is performed. Galvanostatic intermittent titration techniques (GITT) and EIS, for example, are macroscopic techniques which can probe long-range diffusion kinetics and provide a bulk value of conductivity; this includes contributions from grain boundaries and interfacial layers, each of which can have a profound effect on the result. Conversely, NMR and quasi-elastic neutron scattering are microscopic techniques of measurement, probing ion transport at the atomic scale, and thus can overcome some of the sensitivities to surface effects or grain boundaries [27, 28]. However, in some instances, the time scale for the study of motional correlation events may be outside the diffusion rate range of some ionic species (e.g., quasi-elastic neutron scattering is typically on the order of 10^{-9} to 10^{-12} s). In other cases (e.g., NMR), the presence of magnetic ions in the material can interfere with the spin-lattice relaxation rate ($1/T_1$), which may complicate the diffusion analysis. An important consideration is that ionic motion has to result in translation of the ion through the material. Rotational motion or oscillatory hopping that

can govern NMR peak broadening may have a smaller impact on an implanted muon. Careful experimental design allows these highly complementary techniques the scope to build a subtle model of motion involving variable length and time scales.

To fully exploit the potential of fast-ionic conduction in energy storage materials, it is important to probe transport mechanisms in detail so as to deepen our understanding of the underpinning ion kinetics. This review focuses on the application of muon spin relaxation (μSR) spectroscopy, a powerful tool gaining use in the study of ion migration in solids, to probe diffusion mechanisms in solid-state materials for energy storage applications. In the case of materials where ion transport governs performance, spin-polarized muons provide an atom-level probe for studying the ion diffusion dynamics at the heart of functionality in many energy storage materials as they are implanted within the sample under investigation. The time scale measurable by μSR, between 10^{-5} and 10^{-8} s, provides a window through which most long-range and consecutive short-range jumps of ions between interstitial sites may be studied. An additional advantage of μSR is that it allows one to probe and model ionic diffusion in those materials which contain magnetic ions, since both electronic and nuclear contributions to the muon depolarization can be separated, making μSR an excellent technique for the microscopic study of the ionic motions in crystalline materials [29].

Properties of the Muon

The positive muon (μ^+) is a naturally occurring unstable antiparticle (spin $-1/2$) that has a mean lifetime of 2.2 μs and mass of 105.7 MeV/c^2, akin to a heavy positron. Negative muons (μ^-) also occur in nature, with the same mass but a lifetime that depends on the material into which they are implanted since they can undergo nuclear capture. They are part of the family of leptons, intermediate in mass between the electron (0.511 MeV/c^2) and the tau (1777 MeV/c^2). Since the positive muon is far more commonly used in materials science studies, we will hereafter refer to it as the muon [30]. Muons are produced in nature when cosmic rays collide with the upper atmosphere, and they reach the Earth's surface with a flux of about one muon per square centimeter per minute, despite their short lifetime. Indeed, this process has become one of the most commonly used examples of time dilation due to special relativity [31]. Cosmic ray muons can be used for radiography studies of very large objects, such as tomb discovery in ancient Egyptian pyramids [32], but their flux is too low for atomic-scale measurements, and so muons are made using particle accelerators for such studies. Muons provide a volume-averaged probe of the local magnetic fields. This uniquely weighted perspective on a material's magnetic properties allows muons to give insights into a range of magnetic phenomena. Muons have been particularly effective in describing magnetic states within a material, with striking examples in the areas of distinguishing dynamic and static antiferromagnetic ordering [33], identifying the coexistence of superconductivity and magnetism [34, 35], and mapping the volumetric destruction of antiferromagnetic order to form a metallic state [36].

The μSR Technique

μSR spectroscopy can be used to study various dynamic and static properties of materials using the interaction between the muon spin and their internal magnetic fields, including molecular dynamics, superconductivity, semiconductivity, and magnetism [37]. The muon's gyromagnetic ratio of $2\pi \times 135.5$ MHz T^{-1} is smaller than the electron's but larger than that of any nucleus, making it exceptionally sensitive to small magnetic fields inside materials. An important distinction ratio between μSR and neutron diffraction, a technique often employed at similar facilities, is that muons are not scattered from the sample. Instead, the muons are implanted inside the sample to probe internally, akin to nuclei probing their environment in NMR. With the muons implanted within the sample, i.e., the bulk of the particle, they are not as susceptible to surface effects (though they contribute, they will not dominate). Therefore, the μSR measurement can give insights on the intrinsic diffusion properties, regardless of the synthetic approach taken. Diffusion measurements are generally used to study the microscopic properties of bulk powder materials. However, recent pursuit of *in situ* experiments opens up potential avenues for the investigation of a full battery cell and interfacial layer changes during cycling.

While Li ionic motion has been the principal area of interest, μSR has also been used to investigate the dynamics of other ions such as Na^+ and the iodide ion [29, 38, 39]. Muons also have the potential to be used to study the diffusion of other types of ions (such as Al and V), so long as the ionic species under investigation has a nuclear magnetic moment. Examples of such possibilities are given in Table 2.1, which illustrates the chance of success for the study of various ions using μSR.

Table 2.1: Nuclei of interest in energy materials, their nuclear magnetic moments [40], natural abundance [41], and the chance of success in studying their motion using muons.

Nucleus	**Moment** (μ/μ_N)	**Abundance (%)**	**Chance of success**
^{1}H	+4.84	99.9885	Have to separate μ^+ and H^+ motion
^{7}Li	+4.20	92.41	Excellent and well-studied
^{19}F	+2.63	100	Difficulties due to F-μ bond formation
^{23}Na	+2.86	100	Excellent; some work has been done
^{25}Mg	−0.86	10.13	Works but with a small signal
^{27}Al	+3.64	100	Promising
^{43}Ca	−1.49	0.135	Poor unless enriched
^{51}V	+5.15	99.76	Promising
^{67}Zn	+0.875	4.1	Poor unless enriched
^{127}I	+2.81	100	Excellent

Muon Production and Implantation

Muons are artificially produced by first using a synchrotron or cyclotron to produce a high-energy beam of protons (approximately 800 MeV). This beam is accelerated toward a static target (often graphite), where the protons collide and interact with other protons to produce

positive pions and neutrons:

$$p + p \rightarrow \pi^+ + p + n. \tag{2.2}$$

Pions will be produced only if the proton beam is of sufficient energy. The pion will subsequently decay (mean pion lifetime ≈26 ns) *via* the weak interaction into a muon and a muon–neutrino (Figure 2.1):

$$\pi^+ \rightarrow \mu^+ + \nu_\mu. \tag{2.3}$$

μSR has two established modes of operation, which measure complementary information: pulsed beams (e.g., at ISIS in the United Kingdom and J-PARC in Japan) and continuous beams (e.g., at the Paul Scherrer Institute in Switzerland and TRIUMF in Canada). Each mode requires very different instrumental set-up and thus they exist at separate facilities. Pulsed muon beams are well suited to studying weakly magnetic materials because the detector background is low, allowing good data to be collected for ≥10 τ_μ (where τ_μ is the mean lifetime of 2.2 μs), and the counting rate is high. In this mode of operation, the muons arrive rapidly in an intense burst, meaning that many detectors are needed but time resolution is limited by the width of the pulse. Continuous muon beams measure the implantation and decay times of individual muons, allowing a much higher time resolution but lower count rate and flux, with a higher background contribution due to events where a second muon entered the sample before the previous muon decayed. Continuous muon facilities are ideal for studying strongly magnetic materials [37, 42, 43]. It is the pulsed beam mode that is discussed further here since it is better suited to ionic motion studies (Figure 2.1a).

It is experimentally vital that all the muons produced share a common spin polarization. This can be achieved if the beamline transporting muons from the production target to the sample is tuned to transport muons produced from pions decaying at rest on or near the surface of the target with energies of approximately 4.1 MeV. These surface muons are forced to have their spins polarized opposite to their direction of travel by the particle physics processes involved with the pion decay. Since the beamline accepts muons over a small angular range and preserves the spin polarization of the muons, it can be ≥95% polarized when reaching the sample [37, 44, 45].

Surface muons with energy 4.1 MeV penetrate between 0.1 and 1.0 mm into materials, the depth depending on incoming muon energy and the sample density [30]. This is commonly expressed in terms of an areal sample density with muons stopping in a range of approximately 100 to 200 mg cm^{-2} below the sample surface. After entering the sample, the muons rapidly lose energy to a few keV *via* atom ionization and inelastic scattering with electrons in the sample. Their kinetic energy is further reduced to a few hundred eV by a series of electron capture and loss reactions, temporarily forming muonium ($\mu^+ e^-$). This happens when the muon velocity matches the orbital velocity of an orbiting electron, resulting in the muon capturing an electron. The muonium will generally be stripped of the electron, and this process is repeated a few hundred times. The final stage of thermalization consists of inelastic collisions between host atoms and muonium, bringing the muons to a halt more than 1 μm away from any vacancies they may have produced near the surface [37].

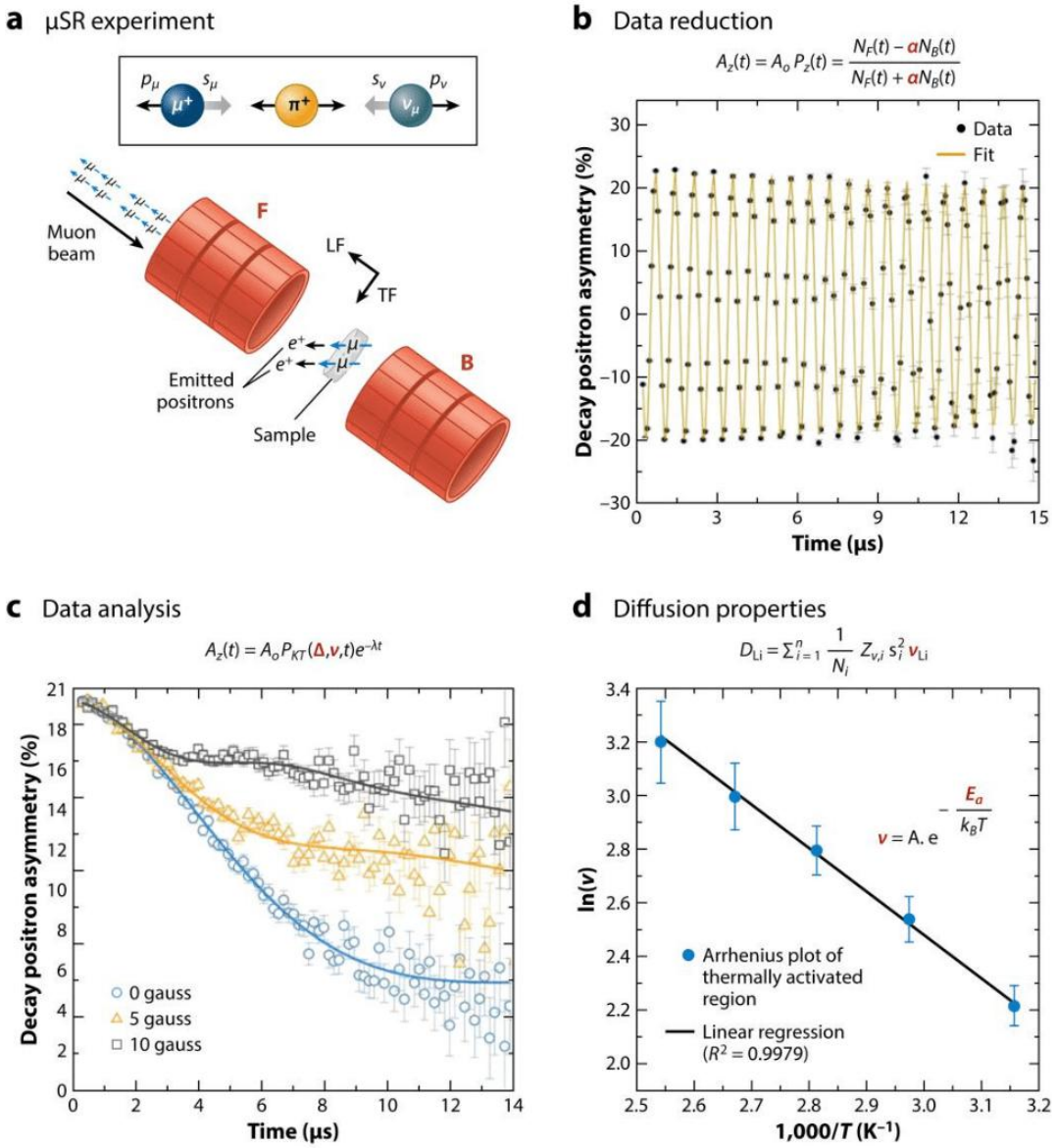

Figure 2.1: (a) Schematic displaying pion (π) decay and a typical spin relaxation experimental set-up for a pulsed muon source. Pion decay is a two-body process, producing a muon (μ) and a muon neutrino (ν_μ) which both possess spin (s) in the opposite direction to their momentum (p). Polarized muons are implanted within a sample and subsequently decay, emitting positrons that are detected using forward (F) and backward (B) detector banks, with the z axis defined between these detectors along the direction of the initial muon spin polarization. A longitudinal magnetic field (LF) or a transverse magnetic field (TF) can be applied. (b) Data collected are reduced to ascertain the evolution of the asymmetry (A_z) of emitted positrons with time by determining the difference in counts between the forward (N_F) and backward (N_B) detectors and using an α factor to compensate for efficiency discrepancies between the two detectors. (c) Ionic diffusion data are commonly analyzed by constraining the dynamic Kubo-Toyabe function to three separate measurements at different applied magnetic field strengths simultaneously, allowing reliable determination of key parameters such as the static field distribution width (Δ) and field fluctuation rate (ν). (d) Intrinsic diffusion properties such as the diffusion rate coefficient (D_{Li}) and activation energy (E_a) can be extracted from the parameters determined from data analysis [46].

This thermalization process takes about 1 ns, a time far shorter than the average muon

lifetime, and importantly preserves spin polarization because the majority of interactions are electrostatic. Therefore, the spin direction is changed by less than 15 mrad, essentially maintaining spin polarization [30]. The implanted muons tend to occupy interstitial sites of high electron density. For cathode materials, and indeed many solid electrolyte materials, these tend to be in the vicinity of O^{2-}, which generally trap the muon in a fixed position in the lattice over the temperature range of interest (see Figure 2.2 for an example).

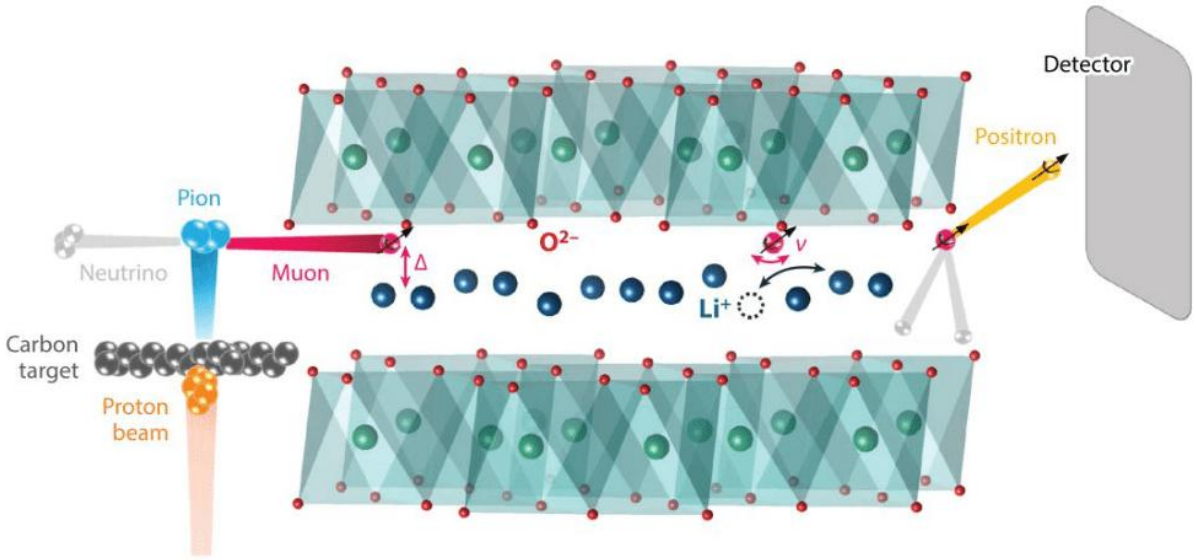

Figure 2.2: Simplified version of the muon implantation and interaction with the crystalline material under study. Light blue spheres represent the pions, grey spheres represent the expelled neutrinos, and pink spheres represent the positive muons. Here, the muons are located close to the oxide ions. Δ and ν are the static width of the local field distribution and the field fluctuation rate, respectively.

Muon Decay and Detection

Decay occurs with probability directly proportional to e^{-t/τ_μ}, where the mean muon lifetime is $\tau_\mu \approx 2.2$ μs. Decay proceeds by a three-body process governed by the weak interaction:

$$\mu^+ \rightarrow e^+ + \nu_{e^+} + \bar{\nu}_\mu. \tag{2.4}$$

This decay violates parity conservation as it is *via* the weak interaction, meaning that the positron (e^+) is emitted preferentially along the direction of the muon spin at the time of decay [37, 47]. This is a crucial property of the technique, as it provides information about a muon's spin direction at the time of its decay, and recording the directions and times of positrons emitted from muons in the sample allows the polarization of the muon ensemble over time, $P(t)$, to be deduced. To illustrate this, consider a simplified muon spectrometer with two detectors, forward (F) and backward (B) with respect to the initial muon spin direction (along z), and with relative counting efficiency α (Figure 2.1a). The asymmetry in their count rate, as a function of time

after muon implantation in the sample, is:

$$A(t) = A_0 P_z(t) = \frac{N_F(t) - \alpha N_B(t)}{N_F(t) + \alpha N_B(t)}, \tag{2.5}$$

where A_0 is the initial asymmetry, while N_{F}(t)and $N_{\mathrm{B}}(t)$ are the number of detected positrons at the forward and backward detectors, respectively (illustrated in Figure 2.1b) [37]. In general, measured asymmetry $A(t) = A_{\mathrm{s}} \times P(t) + A_{\mathrm{bg}}$, where A_{s} is the signal from the sample and A_{bg} is the the background signal. Typically around 10–50 million events (positron counts) are detected during each measurement.

Experiments and Data Analysis

In studies of energy materials, the normal physical situation is that the muons stop in the material with some nuclei around them that possess magnetic moments. The muons experience a static distribution of magnetic fields from these nuclei, causing an incoherent spin precession, and fluctuating fields from any paramagnetic ions present, causing spin relaxation. When an ion with a nuclear magnetic moment moves near the muon, the muon spin will flip, due to the change in the field it experiences. The resulting asymmetry signal depends on the size of the nuclear magnetic field distribution, the paramagnetic spin dynamics, and how often an ion passed the muon. Experiments can be carried out in the presence of zero magnetic field (ZF), longitudinal (parallel to initial spin polarization) fields (LF), or transverse (perpendicular to initial spin polarization) fields (TF). In a TF experiment, the muon spin precesses at the Larmor frequency, ω, in the applied and internal fields. In an LF experiment, the LF field acts to decouple the muon spin from the static fields in the sample. It also alters the frequency at which the muon probes the dynamic fields arising from movement of diffusing species [37]. While the rate of muon spin flips can be measured at a particular temperature and the rate of ion motion inferred, studies are generally made as a function of temperature (∼100–400 K) to gain information on energy barriers affecting the motion. Magnetic fields up to ∼10 mT are used since the nuclear field distribution is normally far smaller than this. The muon spin polarization in ZF and LF is usefully described by the dynamic Gaussian Kubo-Toyabe function [48], which in the static, zero-field limit takes the form:

$$P(t) = \frac{1}{3} + \frac{2}{3}(1 - \Delta^2 t^2)\exp(-\frac{\Delta^2 t^2}{2}), \tag{2.6}$$

where Δ is the static width of the local field distribution (with the dynamic form of this function shown in Figure 2.1c). The dynamics take a Markovian form with rate ν and mean that the function must be evaluated numerically. The long-time trend of this function is particularly sensitive to ν, and this favours measurements at pulsed muon sources where the long-time behaviour can be probed in detail. In paramagnetic systems, this function is multiplied by an exponential relaxation exp(-λt) to account for the spin dynamics, where λ is the relaxation rate constant.

For the TF case, an analogy with NMR was drawn by Abragam [49], and the muon polar-

ization is described by:

$$P(t) = \cos(\omega t + \varphi) \times \exp(-\sigma^2\tau^2 t^2 \times [\exp(\frac{t}{\tau}) - 1 + \frac{t}{\tau}]) \tag{2.7}$$

where ω is the angular precession frequency, φ is the phase of oscillation, σ is the field distribution width, and τ is the correlation time, the inverse of ν above. TF measurements are rarely used for studying ionic motion but have the advantage in wide bandgap systems that the signal from muonium (which has a far higher gyromagnetic ratio) is removed from the data to be analyzed. This model has subsequently been applied to LF-μSR [50], where it has the advantage over the Kubo-Toyabe function that the dynamics are treated analytically.

The field fluctuation rate, ν, measured by the muon, can be assumed to be a direct measure of the hop rate of Li^+ ions in the material and therefore can be used to calculate the Li^+ ion diffusion rate coefficient [51]:

$$D_{Li} = \sum_{i=1}^{n} (\frac{1}{N_i})\ Z_{\nu,i}\ s_i^2\ \nu_{Li}, \tag{2.8}$$

where Ni is the number of Li sites in the i^{th} path, $Z_{\nu,i}$ is the vacancy fraction, and s_i is the hopping distance for Li^+ ions. These parameters can be deduced from structural data for the sample in question. D_Li illustrates how quickly ionic species move, a key parameter for energy materials.

Activation energies (E_a) of diffusion can be determined by completing an Arrhenius analysis of the field fluctuation rate, ν. This must be done over the thermally activated region of the sample, which generally occurs at temperatures over 150 K and is found by analysis of the temperature dependency of the field fluctuation rate, ν_Li (51). In general, ν will remain level as the temperature of the sample is increased until the thermally activated region is reached, where ν will increase sharply. This is illustrated in Figure 2.1d.

Properties of Battery Materials Probed By μSR

Determination of ion diffusion parameters for battery materials is important, as these are key determinants in the power and rate capability of a battery. In the case of Li-ion batteries, Li^+ mobility can be influenced by the Li concentration, the temperature, and the crystal structure of the host material. For example, the ability of Li^+ ions to migrate or hop is limited by their surrounding vacancies, which provide accessible pathways for diffusion to occur. Conversely, a high Li concentration can act as a barrier for fast ionic movement. As a result, diffusion rates can be influenced by a material's crystal structure, to which small changes such as dopant atoms can make a large difference that affects the ionic dynamics [52]. Diffusion properties obtained through μSR measurements, such as D_Li and E_a, have been reported for a myriad of battery materials, and Table 2.2 gives three examples [47, 53]. The μSR technique has been demonstrated as a reliable and reproducible measure of self-diffusion rates, with reported values consistently agreeing with first-principles calculations [26, 29, 39, 51, 53, 54]. In a typical μSR measurement,

approximately 1 g of the powdered material to be investigated is transferred into a Ti sample holder with a Ti foil window. Ti is employed because it depolarizes muons very weakly and allows for simple background subtraction. In the following sections, we discuss how μSR studies have been applied across a range of battery materials to interrogate their properties, including cathodes, anodes, and solid-state electrolytes. This is not intended to be an exhaustive review, but rather a highlighting of insights garnered from μSR studies of energy storage materials.

Table 2.2: Examples of reported values of E_a and D_{Li} for three materials using μSR.

Material	E_a **(meV)**	D_{Li} $(\times 10^{-11})(cm^2\ s^{-1})$	**References**
Li_xFePO_4	130	46	[26]
	99	36	[55]
$Li_{6.5}Al_{0.25}La_{2.92}Zr_2O_{12}$	190	4.6	[46]
$LiNi_{1/3}Mn_{1/3}Co_{1/3}O_2$	≈100	0.35	[56]
	74	≈1	[51]

Cathodes for Li-Ion Batteries

The diffusion pathway dimensionality in battery electrodes can have a significant impact on electrochemical performance. As an illustration of this, Figure 2.3 shows the diffusion pathways for three common cathode crystal structures. Spinels (Figure 2.3a) possess a cubic structure (space group *Fd3m*) which exhibits three-dimensional Li^+ ion diffusion due to the extra pathways provided by the vacant tetrahedral and octahedral interstitial sites. In the case of layered metal oxides, which adopt an α-$NaFeO_2$ trigonal structure (space group $R\bar{3}m$), two-dimensional Li^+ ion diffusion occurs in planes (Figure 2.3b) [57]. The olivine $LiFePO_4$ has an orthorhombic structure (space group Pnma) within which Li^+ ions can be inserted and extracted along the b-axis only *via* one- dimensional diffusion, in the [010] direction (Figure 2.3c) [58, 59]. Strategies exist to improve rate capability, for example, shortening the path length of diffusing ions *via* nanostructuring [60], improving electron transport along the surface or within the bulk of materials [61], carbon coating [62], and the use of dopants [63]. In the following sections, we review some examples where μSR has been applied to examine Li-ion diffusion behaviour in cathodes. We also discuss cases where magnetic ordering in cathode materials can be assessed by muons.

Layered materials

Intercalation into the layered material $LiCoO_2$ was first reported by Goodenough and co-workers in 1980, and it remains the cathode of choice in today's portable electronics [64]. Sugiyama and co-workers applied μSR techniques to reliably determine D_{Li} values for Li_xCoO_2, where the muons are located close to the O^{2-} ions in the crystal structure, for the first time in 2009 [51]. The value determined by experiment for $Li_{0.73}CoO_2$ (13.3×10^{-11} $cm^2\ s^{-1}$) is in close agreement with those predicted by first-principles and demonstrated the use of μSR as a reliable probe of the diffusion coefficient. The temperature dependence of ν and Δ was clearly observed, with a thermally activated region noted between 160 and 250 K indicative of Li^+ ion diffusion. With concerns surrounding materials cost, supply chain risks, and a desire to increase the specific

capacity of cathodes, much research has focused on increasing the Ni content and reducing the Co content in these layered materials, for example, moving to mixed transition metal oxides, such as the $LiNi_xMn_yCo_zO_2$ (NMC-xyz) family, which can deliver high capacities and rate capability [65, 66]. These materials adopt a layered structure and display interesting properties due to magnetic interactions between transition metal ions [67]. Månsson *et al.* [56] have used μSR as a probe to investigate the Li diffusion properties in NMC-111, as well as the low-temperature magnetic properties. ZF and LF spectra, fit using an exponentially relaxing dynamic Kubo-Toyabe function, revealed an activation barrier of ≈100 meV and a D_{Li} of 3.5×10^{-12} cm^2 s^{-1}, in line with previous μSR values obtained on the same stoichiometric samples from different suppliers. The reported paramagnetic to spin-glass transition is observed at ≈12 K. Studies on $LiNi_{0.8}Mn_{0.1}Co_{0.1}O_2$ followed, where interestingly this transition is more gradual, occurring over a 50 K temperature range [68].

Moving further toward $LiNiO_2$ could be a transformative step in realizing high-capacity cathodes, where the theoretical capacity is 275 mAh g^{-1}. However, challenges remain in determining reliable synthetic routes to stoichiometric $LiNiO_2$. Previous μSR measurements have been performed on Ni-excess samples, specifically $Li_{1-x}Ni_{1+x}O_2$ phases (where $x \geq 0$), to gain insights into the magnetic behaviour and high-temperature Li diffusion properties [53]. Not only is the magnetic nature strongly dependent on x but there also exists a relationship between D_{Li} and x, since excess Ni may reside in the Li^+ ion diffusion plane. Evidence for this is found in the observation of ν values between 300 K and 400 K, which reveals smaller ν values for $Li_{0.85}Ni_{1.15}O_2$ compared to $Li_{0.98}Ni_{1.02}O_2$. With the recent advent of synthetic approaches that minimize cation mixing, it will be interesting to evaluate stoichiometric $LiNiO_2$ not only for its Li diffusion properties but also for its magnetic ground state, which has been previously described as spin-glass, frustrated antiferromagnet, or disordered quantum state [69–71].

Spinels

LiMn oxides present great promise as environmentally sustainable, low-cost cathodes with three-dimensional Li^+ ion diffusion pathways available. $LiMn_2O_4$ adopts a normal spinel structure in the *Fd3m* space group, where Mn ions are located on 16*d* octahedral sites, while Li ions sit in the 8*a* tetrahedral sites. This arrangement gives rise to mixed Mn oxidation states (Mn^{4+} with a t_{2g}^3 eg^0 configuration and Mn^{3+} with a $t_{2g}^3 eg^1$ configuration). Mn^{3+} ions can become Jahn-Teller active and the resulting distortion, which occurs at ≈285 K, can induce poor cycling behaviour [72, 73]. Capacity can also be deleteriously affected by Mn dissolution [74]. The synthesis conditions employed can have implications for the local structure and Mn oxidation state, with detailed information on the Li environment previously interrogated by NMR [73]. Li substitution on the 16*d* Mn sites increases the population of Mn^{4+}, thereby limiting the Jahn-Teller effect, and a stoichiometry given by $Li_x[Mn_{2-y}Li_y]O_4$ is helpful in visualizing this site occupation. Ariza and co-workers have investigated $Li[Mn_{1.67}Li_{0.33}]O_4$ and the delithiated H^+–MnO_2 phase by μSR to assess the dynamic properties of Li^+ and/or H^+ in these materials [75, 76]. The observations are consistent with the 8*a* and 16*d* Li and Mn defect sites and interstitial 16*c* sites as likely muon sites in these phases. However, the results indicate that the

nature of proton and Li diffusion is different in these frameworks. Below 150 K, the occupancy of the 16*c* interstitial site is higher for the protonated phase and increases with temperature, while the occupancy remains constant for the lithiated phase. Kaiser and co-workers have employed μSR to investigate the Li mobility in $Li_x[Mn_{1.96}Li_{0.04}]O_4$ for $x = 1$, $x = 0.2$, and $y = 0.04$ [77]. They report an interesting temperature dependence of the Li^+ ion diffusion dynamics, where the onset of Li^+ ion diffusion occurs at 230 K for the $Li[Mn_{1.96}Li_{0.04}]O_4$ phase, while for the $x = 0.2$ phase the onset temperature is higher at 300 K.

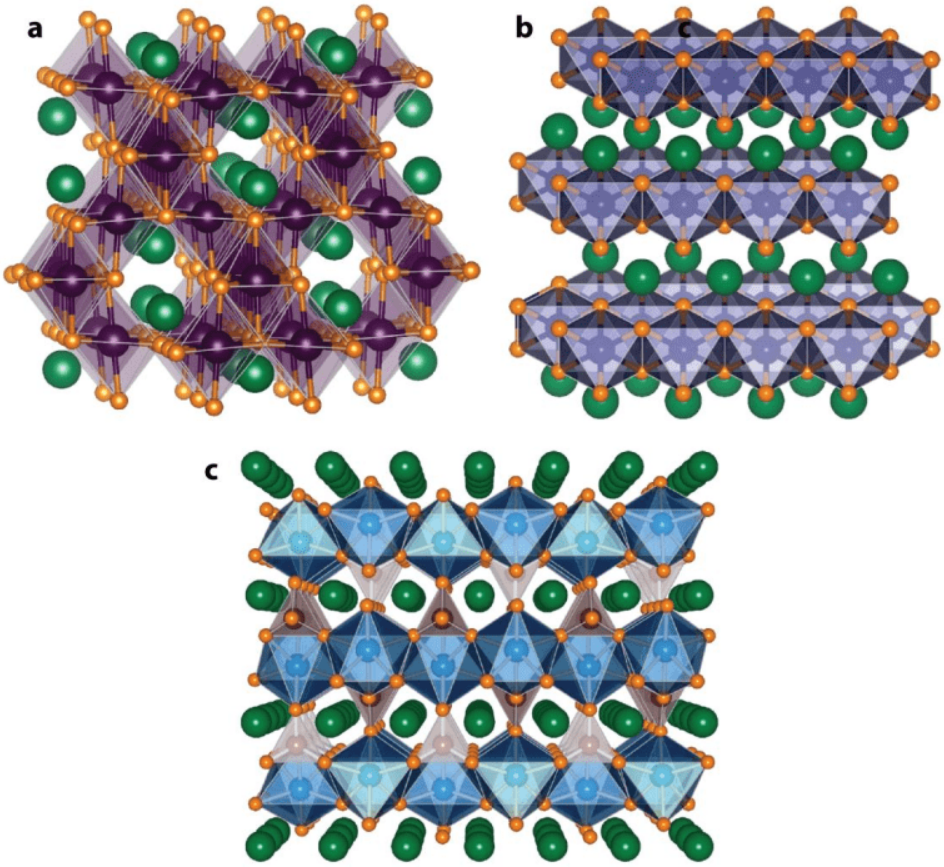

Figure 2.3: Structures of common cathode materials illustrating the diffusion pathways for Li^+ ions (green spheres): (a) spinel framework $LiMn_2O_4$ with three dimensional diffusivity channels, where Mn and O are purple and orange spheres, respectively; (b) layered metal oxide $LiCoO_2$ with two dimensional diffusivity channels, where Co and O are blue and orange, respectively; (c) olivine structured $LiFePO_4$ with one dimensional diffusivity channels, where PO_4 and FeO_6 are brown tetrahedra and blue octahedra, respectively.

Olivines

The *Pnma* structure of $LiFePO_4$ is characterized by chains of edge-sharing LiO_6 octahedra along the *b*-axis, FeO_6 octahedra occupying corner-sharing positions, and P in PO_4 tetrahedra, an arrangement which gives rise to one-dimensional Li^+ ion transport along the [010] direction. This one-dimensional nature of Li^+ diffusion in $LiFePO_4$ was elegantly verified experimentally by Yamada and co-workers [78], who used a combination of maximum entropy methods and neutron diffraction experiments and were the first to visualize Li distribution along the [010] direction.

The nature of Li^+ ion diffusion in olivines had attracted considerable attention. Depending on the experimental technique applied, the reported values for D_{Li} span several orders of magnitude [55, 79]. Interestingly, the diffusion behaviour of bulk $LiFePO_4$ was investigated using μSR previously, with reported agreement in E_a values of ≈0.10 eV and diffusion constants of 10^{-9} to 10^{-10} cm^2 s^{-1} [27, 80, 81]. To investigate this behaviour, it is necessary to apply a LF to decouple the interaction between the muon and the Fe^{2+} magnetic moment. A high-pressure polymorph of $LiFePO_4$, the *Cmcm*-β phase, also exists, where the Li hopping mechanism is disturbed by large Li–Li distances, making this phase electrochemically inactive [82]. Our group has investigated the Li^+ diffusion properties of nanostructured *Pnma* and *Cmcm* $LiFePO_4$ phases and has shown that D_{Li} rates and activation energies for *Pnma* $LiFePO_4$ are in excellent agreement with measurements carried out previously on bulk materials of the same phase [83]. These similarities demonstrate the robustness of the μSR method for interrogating ion diffusion properties. In the case of the electrochemically inactive *Cmcm* species, measurements on mixed phase samples (80:20 *Pnma:Cmcm*) reveal expected lower D_{Li} and E_a values.

Substitution of Mn^{2+} for Fe^{2+} in the olivines allows access to higher redox potentials (3.45 V vs. Li^+/Li^0 for $LiFePO_4$ and 4.10 V vs. Li^+/Li^0 for $LiMnPO_4$). The large magnetic moment of Mn^{2+} ions has previously precluded measurement of ion diffusion properties in $LiMnPO_4$ by μSR methods, since the interaction between the muon and the magnetic moment makes detection of ion diffusivity difficult [81]. However, it is possible to examine Mn-containing olivines by investigating across the $LiF_{1-x}Mn_xPO_4$ solid solution, where we have found that a LF field of 20 G is sufficient to decouple these interactions, and experiments reveal a decrease in D_{Li} and E_a with increasing Mn content [47]. This opens up the use of the μSR technique to probe other Mn^{2+}-containing systems which may prove insightful.

Table 2.3 compares the activation energies reported for pristine $LiFePO_4$, partially delithiated $LiFePO_4$, and Mn-doped $LiFePO_4$ from μSR measurements. The reported values are in close agreement for pristine $LiFePO_4$, with values for E_a between 58 meV and 99 meV. The values of E_a reported from experiments using μSR are slightly smaller than those reported from other experimental techniques [26]. For $LiFePO_4$, there are multiple modes of motion which can contribute to the measure of E_a [84]. These include site-to-site motion, antisite defects, and vacancies. μSR generally probes the lowest energy barrier, which may account for the observed smaller E_a values.

Table 2.3: Comparison of reported values of E_a using μSR for pristine $LiFePO_4$, partially delithiated $LiFePO_4$, and Mn-substituted $LiFePO_4$.

Material	**E_a (meV)**	**Reference**
$LiFePO_4$ (*Pnma*)	58	[83]
$LiFePO_4$ (*Cmcm*)	46	[83]
$LiFePO_4$	99 ± 20	[81]
$Li_{1.0}FePO_4$	130 ± 10	[26]
$Li_{0.9}FePO_4$	80 ± 10	[26]
$Li_{0.8}FePO_4$	60 ± 10	[26]
$LiFe_{0.75}Mn_{0.25}PO_4$	122 ± 18	[47]

Anodes for Li-Ion Batteries

While anode materials have not been as extensively studied as cathodes using μSR techniques, there have been recent reports on the use of μSR to investigate the diffusion properties in intercalated graphites, the current anode material of choice for Li-ion batteries. Sugiyama and co-workers have studied $C_{12}Li_x$ and $C_{18}Li_x$ samples prepared on Cu foils in half pouch cells [85]. DFT calculations reveal that implanted muons form stable bonds with C in the graphene layer, akin to an sp^3-hybridized C–H bond, shown in red in Figure 2.4. The muon site within the structure of the anode is found to change depending on the state of lithiation (Figure 2.4). Room-temperature D_{Li} values on the order of those observed for cathodes are found ($\approx 10^{-10}$ cm^2 s^{-1}) in both cases, with E_a values of 270 (5) meV and 170 (20) meV for C_6Li and $C_{12}Li$ respectively, in keeping with previous experimental and theoretical observations.

Doped transition metal nitrides have demonstrated promising electrochemical properties as anodes for Li-ion batteries, though examining Li^+ ion diffusion dynamics *via* traditional routes has proven challenging due to interference from the metal paramagnetic moments [86, 87]. μSR studies have presented an attractive means to examine the Li^+ ion diffusion properties of these materials, for example $Li_{3-x-y}Co_xN$ [88]. For a family of $Li_{3-x-y}Ni_xN$, an increase in E_a with x is observed, which is attributed to a reduction in the layer spacing [89].

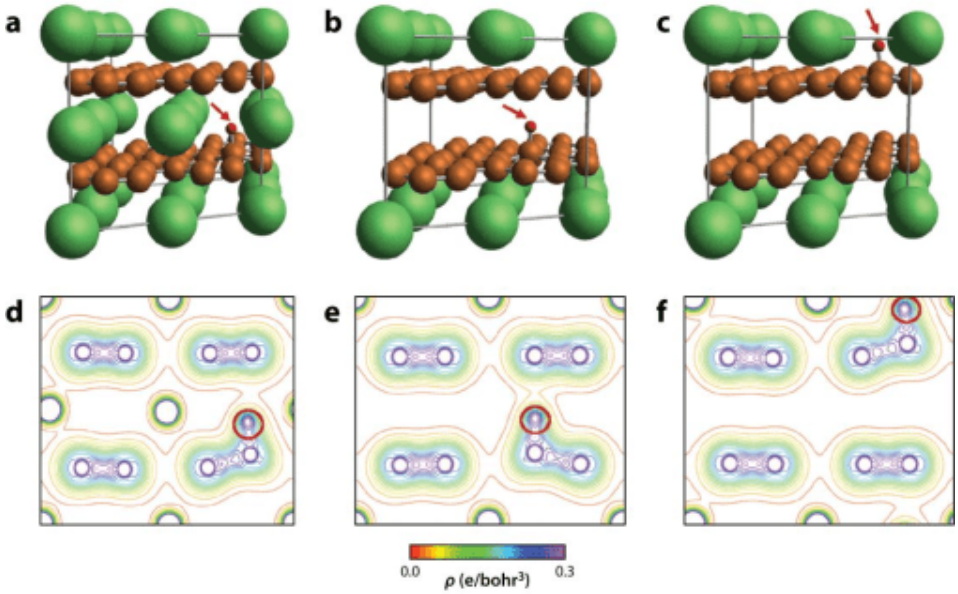

Figure 2.4: Structural optimization of the muon site in (a) C_6Li, (b) graphene, and (c) $C_{12}Li$ from first-principles calculations. Panels d–f represent charge contour plots in the (110) plane corresponding to panels a–c. Figure adapted from Reference [85] by permission of the PCCP Owner Societies.

Ceramic Electrolytes for All-Solid-State Batteries

To overcome safety issues associated with liquid electrolytes in Li-ion batteries, a number of alternatives have been explored, such as the use of polymer electrolytes, composite materials, or solid-state electrolytes. Replacing currently applied liquid electrolytes with a solid electrolyte

could allow the long-desired application of Li metal as an anode material. The Li-rich garnet materials have received considerable attention over the past decade due to their high Li-ion conductivities, excellent stability at high voltages, and stability against Li metal. The garnet structure may be described by the general formula $A_3B_3C_2O_{12}$, where A cations are located in tetrahedral positions, B cations are surrounded by eight O anions, and C cations are accommodated in O-octahedral sites. The versatility of the garnet structure means a wide variety of cations may be accommodated in this framework. Judicious choice of the B and C cation can lead to extra Li^+ ions within interstitial distorted octahedral positions, in addition to the three fully occupied tetragonal A-site occupancy, where A=Li^+. In Li-stuffed garnets, additional Li^+ ions can be accommodated within interstitial distorted octahedral positions, in addition to the three full occupied tetragonal sites in the conventional garnet. Aliovalent doping with Al^{3+} ions can stabilize the $Li_7La_3Zr_2O_{12}$ (LLZO) high-ionic-conducting cubic phase [90].

Our group has investigated the diffusion properties of the Al–doped LLZO phase ($Li_{6.5}Al_{0.25}La_{2.92}Zr_2O_{12}$) using μSR. The muon decay asymmetry data were fit using Keren's analytic generalization of the Abragam function to obtain the fluctuation rate of the muons due to Li^+ ion diffusion [46]. A thermally activated region is observed above 290 K. The main hopping pathways for Li^+ ion diffusion in Al–doped LLZO involve jumps from (a) the tetrahedral $24d$ site to the four neighbouring $96h$ octahedral sites and from (b) the octahedral $96h$ sites to the two surrounding $24d$ tetrahedral sites. From these pathways, the calculated D_{Li} at room temperature is 4.62×10^{-11} cm^2 s^{-1}. The activation energy is found to be 0.19(1) eV, which is lower than that obtained from EIS measurements [0.55(4) eV]. In EIS, resistance to Li-ion diffusion through grain boundaries contributes to the total resistance of the sample, increasing the activation energy required for Li-ion conduction, while μSR acts as a local probe, sensing mostly intragrain diffusion for Li ions. This may account for the higher activation barrier to Li diffusion for EIS.

D_{Li} Comparison by Technique

Figure 2.5a provides a visual representation of reported D_{Li} values for three common battery materials: olivine-structured $LiFePO_4$, $LiNi_xMn_yCo_zO_2$ (NMC), and solid garnet electrolyte materials. Within these individual material types, there are differences in stoichiometry, states of charge, and dopants. This figure is not intended to be quantitative but rather to demonstrate the variability in D_{Li} values reported in the literature. What is clear from the plot is that, even for a given experimental technique, the reported D_{Li} values span several orders of magnitude. In particular, for techniques which probe macroscopic Li diffusion, the results obtained are dependent on sample preparation [91]. The D_{Li} values obtained from μSR for material type are clustered, while for techniques where sample preparation plays a vital role, the D_{Li} values span several orders of magnitude. Microscopic techniques generally provide values which are fundamental to the material, meaning they are not so dependent on factors such as sample morphology, particle size, and density.

Figure 2.5b shows that, despite a small sample size, D_{Li} values measured by μSR for anode materials are consistent. The materials measured are lithiated graphite [85], lithium titanate

[92], and nitrides [89].

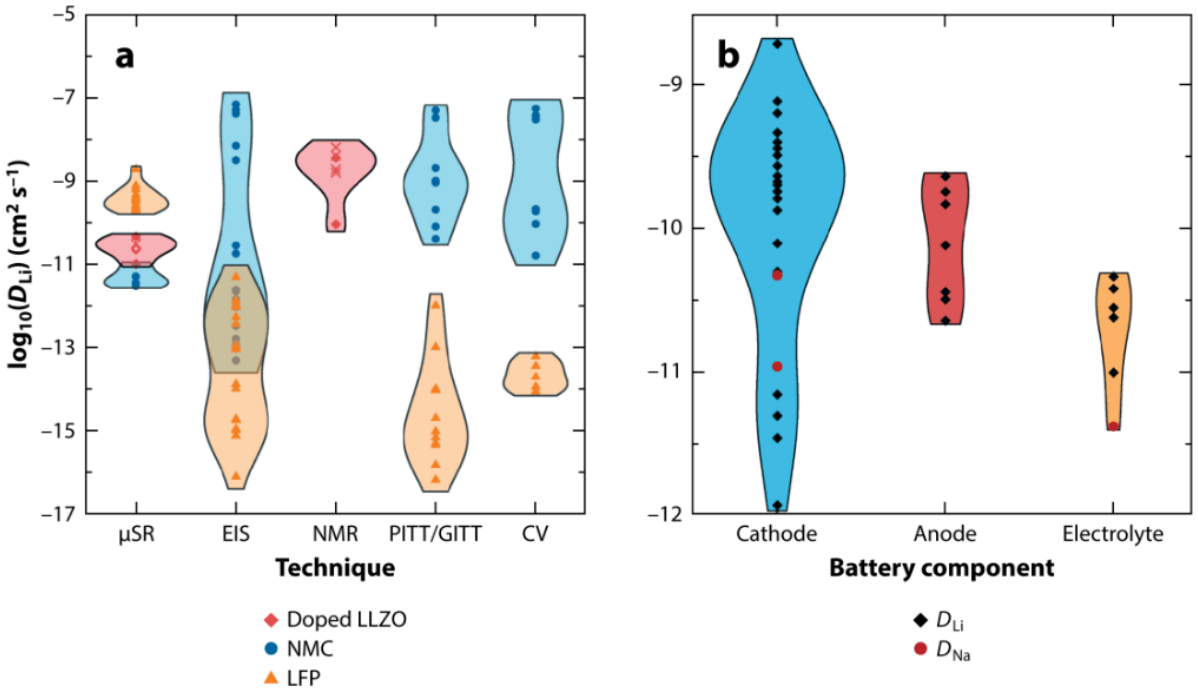

Figure 2.5: (a) D_{Li} values reported for olivine $Li_{1-x}FePO_4$ (orange triangles), layered NMC structures (blue circles), and doped garnet materials (red filled diamonds for Al-doped LLZO; hollow red diamonds for Nb-doped LLZO; and red crosses for Ta-doped LLZO) across multiple techniques, including μSR, EIS, NMR, titration, and cyclic voltammetry. Each individual point represents a literature-reported value. The shape taken by each grouping is intended to give a qualitative idea of the clustering of points [7, 11, 12, 14, 21, 23, 26, 46, 47, 54–56, 81, 83, 93–113]. (b) D_{Li} and D_{Na} values for cathodes, anodes, and solid electrolytes from μSR measurements [26, 29, 39, 46, 47, 54, 56, 81, 83, 85, 88, 89, 92, 93, 108, 114–120]. Abbreviations: CV, cyclic voltammetry; EIS, electrochemical impedance; GITT, galvanic intermittant titration technique; LFP, $Li_{1-x}FePO_4$; LLZO, $Li_7La_3Zr_2O_{12}$; μSR, muon spin relaxation; NMC, $LiNi_xMn_yCo_zO_2$; NMR, nuclear magnetic resonance; PITT, potentiostatic intermittant titration technique.

Muons for Na-Ion Diffusion

Na batteries represent a cheap alternative to Li batteries, due to the lower price of Na, while offering a similar redox couple potential (≈0.3 V lower for Na/Na^+ compared to Li/Li^+). The larger size and weight of Na^+ promotes the application of Na batteries primarily for medium- to large-scale stationary energy storage. A number of electrode materials currently used in Li-ion batteries can be adapted for application in Na-ion batteries, for example, olivine $NaFePO_4$ [121]. The Na analogue of $LiCoO_2$ is the layered oxide $NaCoO_2$ [122, 123]. Slight changes in the stacking sequence of CoO_6 layers in $Na_{1-x}CoO_2$ materials result in O3-, P3-, and P2-type structures. All three layered phases have shown the ability to intercalate Na ions [124, 125]. The charge and discharge profiles for the different phases of $NaCoO_2$ show evidence of complicated phase transitions. Månsson *et al.* [29] have studied the local Na^+ diffusion in Na_xCoO_2 for x= 0.5, 0.6, and 0.7. When the data were fit using an exponentially relaxing Kubo-Toyabe function, the field fluctuation rate profiles for all samples showed behaviour typical of thermally activated

ionic diffusion, although the onset temperature of this diffusion decreased as the Na content in the sample increased. The activation energies were found to be inversely proportional to the Na content, with calculated values of 478, 528, and 571 meV for $x = 0.7$, 0.6, and 0.5, respectively. Room-temperature Na^+ ion diffusion coefficients were also calculated, yielding values of $D_{Na} = 3.99 \times 10^{-11}$ cm^2 s^{-1} ($x = 0.7$) and $D_{Na} = 5.0 \times 10^{-12}$ cm^2 s^{-1} ($x = 0.5$).

The spinel-type compound $NaMn_2O_4$ has been reported as a Na-ion cathode, possessing a one-step voltage profile, limited polarization, and excellent capacity retention [126]. Data from μSR investigations by Umegaki and co-workers were fit using a dynamic Gaussian Kubo-Toyabe function and a time-independent background [117]. Above 300 K, the field fluctuation rate rapidly increases, indicating the onset of Na^+ ion diffusion. The activation energy was estimated as 180(9) meV, and a diffusion coefficient at 300 K was calculated to be (1.1 ± 0.1) $\times 10^{-11}$ cm^2 s^{-1}. The ionic diffusion of Na in the Na analogue of olivine type $LiFePO_4$ has also been studied [116]. A Na^+ ion diffusion onset temperature of 200 K was observed for $Na_{0.7}FePO_4$. Na-ion diffusion in NaV_2O_4 has also been studied by μSR [127]. It was observed in the field fluctuation rate data that the onset of Na-ion diffusion occurred at a temperature of approximately 250 K. Arrhenius analysis of these data yielded an activation energy of ≈225 meV.

The use of solid-state electrolytes in Na batteries could increase the safety and energy density of the battery, provide longer cyclability, and enable the use of versatile geometries. Recently, Amores *et al.* [39] performed μSR measurements on a new Na-rich double perovskite material, $Na_{1.5}La_{1.5}TeO_6$, a candidate solid-state electrolyte for all solid-state Na batteries. By measuring the time evolution of the positron asymmetry a function of temperature, Arrhenius analysis revealed an activation energy for Na-ion diffusion of 169(9) meV and a room-temperature diffusion coefficient of 4.2×10^{-12} cm^2 s^{-1}. To compare microscopic and macroscopic diffusion properties, EIS using Na-blocking Au electrodes was also used to characterize the bulk Na-ion diffusion in $Na_{1.5}La_{1.5}TeO_6$ [39]. An activation energy of 270 meV was obtained, again higher than that found from μSR.

Outlook

Broadening the Range if Ions Studied

As the study of H^+, Li^+, and Na^+ ionic motion using muons has become routine, other ions which could be studied in the same way have been considered. The principal questions to consider are:

1. How fast do ions move through the material?
2. Is the material magnetic?
3. Are NMR studies feasible?

It is often possible to estimate an answer to the first question by using bulk measurements, computational theory, or experience with related materials. Since muons are typically sensitive to ionic motion on roughly microsecond time scales for a hop between sites, this rate must be

expected to occur at some experimentally accessible temperature (0.1 to 1500 K), and muons must stop at some electronegative sites in the material's structure that will act to trap them as the ions move past.

Muons measure ionic motion using the magnetic fields from the nuclei moving past them. These are relatively small (≈1 mT) in comparison to fields from ordered electronic moments in (anti-)ferromagnets (≈100 mT), but comparable to fields from paramagnetic moments (≈1mT). This has two consequences. First, it is not possible to study ionic motion in the ordered phase of (anti-)ferromagnets, but this is rarely a problem since few energy materials of interest are magnetic at the temperatures where ionic motion is significant. Second, paramagnetic ions complicate the data analysis for the same reason as in NMR, but their contribution to muon spectra is quite distinct and therefore proves far easier to separate in the data analysis [128].

Whether study by NMR spectroscopy is feasible in the system is a good indicator of the applicability muon measurements. The nuclei of the ion of interest must have a magnetic moment with some significant abundance (≥10%) to produce changing magnetic fields that the muons can measure (Table 2.1 gives examples). An example of an element with highly abundant magnetic moments that are too small to easily study with muons is Ag. NMR measurements are also affected by the presence of quadrupolar (or higher-order) moments on the nuclei. These are generally a second-order effect in muon measurements of ionic motion but can be exploited to obtain more information about the muon stopping position and state.

As shown in Table 2.1, four nuclei that are important in energy materials are amenable to muon study but have barely been explored to date: Mg, Al, V, and I. As multivalent battery chemistries become more widely studied and research on hybrid perovskite solar cell materials continues apace, these are likely to enter the realm of muon spectroscopy.

Looking at Surface and Interfaces

Many of the processes key to improving battery function occur at the interface between materials, a topic which has not yet been studied with muons. This is because, for conventional muon measurements, the small volume fraction of the cell occupied by interfaces and the variable depth from the surface prevent implantation of muons in the volume of interest. However, at least for systems where the interface can be replicated in thin-film form, the use of low-energy muons with kinetic energy in the 1—20 keV range allows depths from 5 to 200 nm from the upper surface to be probed with a narrow depth range (instead of ≈100 (50) μm in conventional muon beams). A low-energy muon beam is available at the Paul Scherrer Institute [129] with a muon flux sufficient for ionic motion studies. A similar beam is under development at J-PARC with the intention of carrying out user experiments in the near future [130]. Such beamlines will permit the study of buried interfaces and surfaces in detail as before unobtainable from surface muon beams, affording vital information on these regions which are essential to battery operation.

New Technical Capabilities

Other major developments in muon experimental equipment are working toward far higher data rates to shorten counting times and increase the statistical quality of data. Muon experiments at continuous sources historically recorded ∼10 million muon decays per hour. The latest instruments at pulsed muon sources have increased this to ∼100 million per hour, and instruments now being planned aim to increase this to ∼1,000 million per hour [131]. The increased rate has allowed more detailed studies of the motion of ions like Li, raised the possibility of studying more challenging ions like Mn, and enabled the beginning of *operando* studies. Future instruments will increase the throughput for samples, make studies of more challenging ions routine, and allow *operando* charging and discharging studies at rates that are of practical interest.

Another area for development is the simultaneous combination of muon spectroscopy with other techniques on the same cell in the beamline. This is a particular challenge for reproducibility in electrochemical cells, as it is natural to optimize cell designs for each technique, but effective cell designs for combining muon spectroscopy with perturbations such as laser light, impedance spectroscopy, microwave, RF, and pressure, as well as *in situ* chemical reactions, have been developed in other contexts. Much that has been learned from developing *operando* cells for NMR [132] and neutron scattering [133] will be transferable to muon spectroscopy. While applying these developments to electrochemistry will involve considerable technical effort, the prize of gaining consistent information from multiple probes as the cell is operated provides considerable justification.

Acknowledgements

The authors gratefully acknowledge the support of the ISIS Neutron and Muon Facility, through the award of beamtime and a Facility Development Studentship for I.M.C. B.J. acknowledges the award of a Carnegie PhD Scholarship. This work was supported by the EPSRC (Engineering and Physical Sciences Research Council, EP/N001982/2), the ISCF (Industry Strategy Challenge Fund) Faraday Challenge projects FutureCat (grant number FIRG017), SOLBAT (grant number FIRG007), and the University of Sheffield.

References

[1] A. R. West. Basic Solid State Chemistry. *Wiley and Sons*, Vol. 2, 1999.

[2] A. V. Chadwick. *Ionic conduction and diffusion in solids.* Digital Encyclopedia of Applied Physics. Wiley-VCH, 2003.

[3] A. R. Allnatt and A. V. Chadwick. Thermal diffusion in crystalline solids. *Chem. Rev.*, 67:681–705, 1967.

[4] A. Kuhn, S. Narayanan, L. Spencer, G. Goward, V. Thangadurai, and M. Wilkening.

Li self-diffusion in garnet-type $Li_7La_3Zr_2O_{12}$ as probed directly by diffusion-induced ^7Li spin-lattice relaxation NMR spectroscopy. *Phys. Rev. B*, 83:94302, 2011.

[5] S. Narayanan, V. Epp, M. Wilkening, and V. Thangadurai. Macroscopic and microscopic Li^+ transport parameters in cubic garnet-type "$Li_{6.5}La_{2.5}Ba_{0.5}ZrTaO_{12}$" as probed by impedance spectroscopy and NMR. *RSC Adv.*, 2:2553–2561, 2012.

[6] K. J. Griffith, K. M. Wiaderek, G. Cibin, L. E. Marbella, and C. P. Grey. Niobium tungsten oxides for high-rate lithium-ion energy storage. *Nature*, 559:556–563, 2018.

[7] K. Hayamizu, Y. Matsuda, M. Matsui, and N. Imanishi. Lithium ion diffusion measurements on a garnet-type solid conductor $Li_{6.6}La_3Zr_{1.6}Ta_{0.4}O_{12}$ by using a pulsed-gradient spin-echo NMR method. *Solid State Nucl. Magn. Reson.*, 70:21–27, 2015.

[8] J. Sugiyama, I. Umegaki, T. Uyama, R. M. L. McFadden, and S. Shiraki *et al.*. Lithium diffusion in spinel $Li_4Ti_5O_{12}$. *Phys. Rev. B*, 96:094402, 2017.

[9] N. Kuwata, M. Nakane, T. Miyazaki, K. Mitsuishi, and J. Kawamura. Lithium diffusion coefficient in $LiMn_2O_4$ thin films measured by secondary ion mass spectrometry with ion-exchange method. *Solid State Ion.*, 320:266–271, 2018.

[10] T. Yamanaka, T. Minato, K. Okazaki, T. Abe, K. Nishio, and Z. Ogumi. Evolution and Migration of Lithium-Deficient Phases during Electrochemical Delithiation of Large Single Crystals of $LiFePO_4$. *ACS Appl. Energy Mater.*, 1:1140–1145, 2018.

[11] S. Chen, T. He, Y. Su, Y. Lu, L. Bao, L. Chen, Q. Zhang, J. Wang, R. Chen, and F. Wu. Ni-Rich $LiNi_{0.8}Co_{0.1}Mn_{0.1}O_2$ Oxide Coated by Dual-Conductive Layers as High Performance Cathode Material for Lithium-Ion Batteries. *ACS Appl. Mater. Interfaces*, 9:29732–29743, 2017.

[12] J. Zhang, Z. Li, R. Gao, Z. Hu, and X. Liu. High Rate Capability and Excellent Thermal Stability of Li^+-Conductive Li_2ZrO_3-Coated $LiNi_{1/3}Co_{1/3}Mn_{1/3}O_2$ via a Synchronous Lithiation Strategy. *J. Phys. Chem. C*, 119:20350–20356, 2015.

[13] G. T. Hitz, E. D. Wachsman, and V. Thangadurai. Highly Li-Stuffed Garnet-Type $Li_{7+x}La_3Zr_{2-x}Y_xO_{12}$. *J. Electrochem. Soc.*, 160:1248–1255, 2013.

[14] Z. Huang, Z. Wang, H. Guo, and X. Li. Influence of Mg^{2+} doping on the structure and electrochemical performances of layered $LiNi_{0.6}Co_{0.2-x}Mn_{0.2}Mg_xO_2$ cathode materials. *J. Alloys Compd.*, 671:479–485, 2016.

[15] A. V. Churikov, A. V. Ivanishchev, I. A. Ivanishcheva, V. O. Sycheva, N. R. Khasanova, and E. V. Antipov. Determination of lithium diffusion coefficient in $LiFePO_4$ electrode by galvanostatic and potentiostatic intermittent titration techniques. *Electrochim. Acta*, 55:2939–2950, 2010.

[16] P.D. Weidman, D. Ahn, and R. Raj. Diffusive relaxation of Li in particles of silicon oxycarbide measured by galvanostatic titrations. *J. Power Sources*, 249:219–230, 2014.

[17] E. Markevich, M. D. Levi, and D. Aurbach. Comparison between potentiostatic and galvanostatic intermittent titration techniques for determination of chemical diffusion coefficients in ion-insertion electrodes. *J. Electroanal. Chem.*, 580:231–237, 2005.

[18] X. Tang, X. Song, P. Shen, and D. Jia. Capacity intermittent titration technique (CITT): A novel technique for determination of Li^+ solid diffusion coefficient of $LiMn_2O_4$. *Electrochim. Acta*, 50:5581–5587, 2005.

[19] K. Miwa and R. Asahi. Molecular dynamics simulations with machine learning potential for Nb-doped lithium garnet-type oxide $Li_{7-x}La_3(Zr_{2-x}Nb_x)O_{12}$. *Phys. Rev. Mater.*, 2:105404, 2018.

[20] M. J. Klenk, S. E. Boeberitz, J. Dai, N. H. Jalarvo, V. K. Peterson, and W. Lai. Lithium self-diffusion in a model lithium garnet oxide $Li_5La_3Ta_2O_{12}$: A combined quasi-elastic neutron scattering and molecular dynamics study. *Solid State Ion.*, 312:1–7, 2017.

[21] S. Cui, Y. Wei, T. Liu, W. Deng, Z. Hu, Y. Su, H. Li, M. Li, H. Guo, Y. Duan, W. Wang, M. Rao, J. Zheng, X. Wang, and F. Pan. Optimized Temperature Effect of Li-Ion Diffusion with Layer Distance in $Li(Ni_xMn_yCo_z)O_2$ Cathode Materials for High Performance Li-Ion Battery. *Adv. Energy Mater.*, 6:1501309, 2016.

[22] X. H. Rui, N. Ding, J. Liu, C. Li, and C. H. Chen. Analysis of the chemical diffusion coefficient of lithium ions in $Li_3V_2(PO_4)_3$ cathode material. *Electrochim. Acta*, 55:2384–2390, 2010.

[23] Y. Zhu, Y. Xu, Y. Liu, C. Luo, and C. Wang. Comparison of electrochemical performances of olivine $NaFePO_4$ in sodium-ion batteries and olivine $LiFePO_4$ in lithium-ion batteries. *Nanoscale*, 5:780–787, 2013.

[24] S. Takai, K. Yoshioka, H. Iikura, M. Matsubayashi, T. Yao, and T. Esaka. Tracer diffusion coefficients of lithium ion in $LiMn_2O_4$ measured by neutron radiography. *Solid State Ion.*, pages 93–96, 2014.

[25] R. L. Sacci, M. L. Lehmann, S. O. Diallo, Y. Q. Cheng, L. L. Daemen, J. F. Browning, M. Doucet, N. J. Dudney, and G. M. Veith. Lithium Transport in an Amorphous Li_xSi Anode Investigated by Quasi-elastic Neutron Scattering. *J. Phys. Chem. C*, 121:11083–11088, 2017.

[26] P. J. Baker, I. Franke, F. L. Pratt, T. Lancaster, D. Prabhakaran, W. Hayes, and S. J. Blundell. Probing magnetic order in $LiMPO_4$ (M= Ni, Co, Fe) and lithium diffusion in Li_xFePO_4. *Phys. Rev. B*, 84:1–8, 2011.

[27] S. F. J. Cox. Implanted muon studies in condensed matter science. *J. Phys. Condens. Matter*, 20:3187–3319, 1987.

[28] M. Wilkening and P. Heitjans. From Micro to Macro: Access to Long-Range Li^+ Diffusion Parameters in Solids via Microscopic ^{6,7}Li Spin-Alignment Echo NMR Spectroscopy. *Chem. Phys. Chem*, 13:53–65, 2012.

[29] M. Månsson and J. Sugiyama. Muon-spin relaxation study on Li- and Na-diffusion in solids. *Physica Scripta*, 88:1402–4896, 2013.

[30] L. Nuccio, L. L. Schulz, and A. J. Drew. Muon spin spectroscopy: Magnetism, soft matter and the bridge between the two. *J. Phys. D: Appl. Phys*, 47:473001, 2014.

[31] B. Rossi and D. B. Hall. Variation in the rate of decay of mesotrons with momentum. *Phys. Rev.*, 59:223–228, 1941.

[32] K. Morishima, M. Kuno, A. Nishio, N. Kitagawa, Y. Manabe, *et al.* S. Procureur, D. Attié, S. Bouteille, D. Calvet, C. Filosa, P. Magnier, I. Mandjavidze, M. Riallot, B. Marini, P. Gable, Y. Date, M. Sugiura, Y. Elshayeb, M. Ezzy, E. Guerriero, V. Steiger, N. Serikoff, J. B. Mouret, B. Charlès, H. Helal, and M. Tayoubi. Discovery of a big void in Khufu's Pyramid by observation of cosmic-ray muons. *Nature*, 552:386–390, 2017.

[33] B. H. Yan, A. K. Paul, S. Kanungo, M. Reehuis, and A. Hoser *et al.*. Lattice-site-specific spin dynamics in double perovskit Sr_2CoOsO_6. *Phys. Rev. Lett.*, 112:147202, 2014.

[34] B. Fak, E. Kermarrec, L. Messio, B. Bernu, and C. Lhuillier *et al.*. Kapellasite: a kagome quantum spin liquid with competing interactions. *Phys. Rev. Lett.*, 109:037208, 2012.

[35] R. Khasanov, Z. Guguchia, A. Amato, E. Morenzoni, and X. L. Dong *et al.*. Pressure-induced magnetic order in FeSe: a muon spin rotation study. *Phys. Rev. B*, 95:180504, 2017.

[36] B. A. Fransden, L. Liu, S. C. Cheung, Z. Guguchia, and R. Khasanov *et al.*. Volume-wise destruction of the antiferromagnetic Mott insulating state through quantum tuning. *Nat. Commun.*, 7:12519, 2016.

[37] S. J. Blundell. Spin-polarized muons in condensed matter physics. *Contemporary Physics*, 40:175–192, 1999.

[38] D. W. Ferdani, S. R. Pering, D. Ghosh, P. Kubiak, A. B. Walker, S. E. Lewis, A. L. Johnson, P. J. Baker, S. M. Islam, and P. J. Cameron. Partial cation substitution reduces iodide ion transport in lead iodide perovskite solar cells. *Energy Environ. Sci.*, 12:2264–2272, 2019.

[39] M. Amores, P. J. Baker, E. J. Cussen, and S. A. Corr. $Na_{1.5}La_{1.5}TeO_6$: Na^+ conduction in a novel Na-rich double perovskite. *Chem. Commun.*, 54:10040–10043, 2018.

[40] N. J. Stone. Table of nuclear magnetic dipole and electric quadrupole moments. *At. Data Nucl. Data Tables*, 90:75—176, 2005.

[41] D. Strominger, J. M. Hollander, and G. T. Seaborg. Table of isotopes. *At. Data Nucl. Data Tables*, 30:585–904, 1958.

[42] P. Dalmas De Réotier and A. Yaouanc. Muon spin rotation and relaxation in magnetic materials. *J. Phys. Condens. Matter*, 9:9113–9166, 1997.

[43] K. Mukai, J. Sugiyama, Y. Ikedo, H. Nozaki, K. Shimomura, K. Nishiyama, K. Ariyoshi, and T. Ohzuku. Magnetism and lithium diffusion in Li_xCoO_2 by a muon-spin rotation and relaxation (μ^+SR) technique. *J. Power Sources*, 174:711–715, 2007.

[44] S. J. Blundell. Muon-spin rotation studies of electronic properties of molecular conductors and superconductors. *Chem. Rev.*, 104:5717–5735, 2004.

[45] T. Prokscha, E. Morenzoni, K. Deiters, F. Foroughi, D. George, R. Kobler, A. Suter, and V. Vrankovic. The new μE4 beam at PSI: A hybrid-type large acceptance channel for the generation of a high intensity surface-muon beam. *Nucl. Instrum. Methods Phys. Res. A*, 595:317–331, 2008.

[46] M. Amores, T. E. Ashton, P. J. Baker, E. J. Cussen, and S. A. Corr. Fast microwave-assisted synthesis of Li-stuffed garnets and insights into Li diffusion from muon spin spectroscopy. *J. Mater. Chem. A*, 4:1729–1736, 2016.

[47] J. V. Laveda, B. Johnston, G. W. Paterson, P. J. Baker, and M. G. Tucker *et al.*. Structure-property insights into nanostructured electrodes for Li-ion batteries from local structural and diffusional probes. *J. Mater. Chem. A*, 6:127–137, 2017.

[48] R. S. Hayano, Y. J. Uemura, J. Imazato, N. Nishida, T. Yamazaki, and R. Kubo. Zero-and low-field spin relaxation studied by positive muons. *Phys. Rev. B*, 20:850–859, 1979.

[49] A. Abragam. *The Principles of Nuclear Magnetism.* Oxford, UK. Clarendon, 1961.

[50] A. Keren. Generalization of the Abragam relaxation function to a longitudinal field. *Phys. Rev. B*, 50:10039–10042, 1964.

[51] J. Sugiyama, K. Mukai, Y. Ikedo, H. Nozaki, M. Månsson, and I. Watanabe. Li diffusion in Li_xCoO_2 probed by Muon-Spin spectroscopy. *Phys. Rev. Lett.*, 103, 2009.

[52] C. P. Grey and N. Dupre. NMR Studies of Cathode Materials for Lithium-Ion Rechargeable Batteries. *Chem. Rev.*, 104:4493–4512, 2004.

[53] J. Sugiyama, Y. Ikedo, K. Mukai, H. Nozaki, M. Månsson, O. Ofer, M. Harada, K. Kamazawa, Y. Miyake, J. H. Brewer, E. J. Ansaldo, K. H. Chow, I. Watanabe, and T. Ohzuku. Low-temperature magnetic properties and high-temperature diffusive behavior of $LiNiO_2$ investigated by muon-spin spectroscopy. *Phys. Rev. B*, 82:1–11, 2010.

[54] J. Sugiyama, K. Mukai, M. Harada, H. Nozaki, and K. Miwa *et al.*. Reactive surface area of the $Li_x(Co_{1/3}Ni_{1/3}Mn_{1/3})O_2$ electrode determined by μ^+SR and electrochemical measurements. *Phys. Chem. Chem. Phys.*, 15:10402, 2013.

[55] P. P. Prosini, M. Lisi, D. Zane, and M. Pasquali. Determination of the chemical diffusion coefficient of lithium in LiFePO4. *Solid State Ion.*, 148:45–51, 2002.

[56] M. Månsson, H. Nozaki, J. M. Wikberg, K. Pra, Y. Sassa, M. Dahbi, K. Kamazawa, K. Sedlak, I. Watanabe, and J. Sugiyama. Lithium diffusion & magnetism in battery cathode material $Li_xNi_{1/3}Co_{1/3}Mn_{1/3}O_2$. *J. Phys. Conf. Ser.*, 551, 2014.

[57] Y. Shao-Horn, L. Croguennec, C. Delmas, E. C. Nelson, and M. A. O'Keefe. Atomic resolution of lithium ions in $LiCoO_2$. *Nat. Mater.*, 2:464–467, 2003.

[58] Y. Fernández Pulido, C. Blanco, D. Anseán, V. M. García, F. Ferrero, and M. Valledor. Determination of suitable parameters for battery analysis by Electrochemical Impedance Spectroscopy. *Measurement*, 106:1–11, 2017.

[59] J. W. Fergus. Recent developments in cathode materials for lithium ion batteries. *J. Power Sources*, 195:939–954, 2010.

[60] N. Spinner and W. E. Mustain. Nanostructural effects on the cycle life and Li^+ diffusion coefficient of nickel oxide anodes. *J. Electroanal. Chem.*, 711:8–16, 2013.

[61] B. Kang and G. Ceder. Battery materials for ultrafast charging and discharging. *Nature*, 458:190–193, 2009.

[62] Q. Cao, H. P. Zhang, G. J. Wang, Q. Xia, Y. P. Wu, and H. Q. Wu. A novel carbon-coated $LiCoO_2$ as cathode material for lithium ion battery. *Electrochem. Commun.*, 9:1228–1232, 2007.

[63] Y. Chen, E. Rangasamy, C. Liang, and K. An. Origin of High Li^+ Conduction in Doped $Li_7La_3Zr_2O_{12}$ Garnets. *Chem. Mater.*, 27:5491–5494, 2015.

[64] K. Mizushima, P. C. Jones, P. J. Wiseman, and J. B. Goodenough. Li_xCoO_2 ($0 < x \leq 1$): a new cathode material for batteries of high energy density. *Mat. Res. Bull.*, 15:783–389, 1980.

[65] S. H. Park, H. S. Shin, S. T. Myung, C. S. Yoon, K. Amine, and Y. K. Sun. Synthesis of nanostructured $Li[Ni_{1/3}Co_{1/3}Mn_{1/3}]O_2$ via a modified carbonate process. *Chem. Mater.*, 17:6–8, 2005.

[66] U. H. Kim, D. W. Jun, K. J. Park, Q. Zhang, and P. Kaghazchi *et al...* Pushing the limit of layered transition metal oxide cathodes for high-energy density rechargeable Li ion batteries. *Energy Environ. Sci.*, 11:1271–1279, 2018.

[67] N. A. Chernova, M. Ma, J. Xiao, M. S. Whittingham, J. Breger, and C. P. Grey. Layered $Li_xNi_yMn_yCo_{1-2y}O_2$ cathodes for lithium ion batteries: understanding local structure via magnetic properties. *Chem. Mater.*, 19:4682–4693, 2007.

[68] J. M. Wikberg, M. Månsson, M. Dabhi, K. Kamazawa, and J. Sugiyama. Magnetic order and frustrated dynamics in $Li(Ni_{0.8}Co_{0.1}Mn_{0.1})O_2$: a study by μ^+SR and SQUID magnetometry. *Phys. Proc.*, 30:202–205, 2012.

[69] U. H. Kim, D. W. Jun, K. J. Park, Q. Zhang, and P. Kaghazchi *et al.*. Pushing the limit of layered transition metal oxide cathodes for high-energy density rechargeable Li ion batteries. *Energy Environ. Sci.*, 11:1271–1279, 2018.

[70] T. Chatterji, W. Henggeler, and C. Delmas. Muon spin rotation investigation of the S = 1/2 triangular lattice $LiNiO_2$. *J. Phys. Condens. Matter*, 17:1341–1350, 2005.

[71] M. Bonda, M. Holzapfel, S. de Brion, C. Darie, and T. Feher *et al.*. Effect of magnesium doping on the orbital and magnetic order in $LiNiO_2$. *Phys. Rev. B*, 78:104409, 2008.

[72] A. S. Wills, N. P. Raju, and J. E. Greedan. Low-temperature structure and magnetic properties of the spinel $LiMn_2O_4$: a frustrated antiferromagnet and cathode material. *Chem. Mater.*, 11:1510–1518, 1999.

[73] Y. J. Lee, F. Wang, and C. P. Grey. ^{6}Li and ^{7}Li MAS NMR studies of lithium manganate cathode materials. *J. Am. Chem. Soc.*, 120:12601–12613, 1998.

[74] C. Jiang, Z. Tang, S. Deng, Y. Hong, S. Wang, and Z. Zhang. High-performance carbon-coated mesoporous $LiMn_2O_4$ cathode materials synthesized from a novel hydrated layered-spinel lithium manganate composite. *RSC Adv.*, 70:3746–3751, 2017.

[75] M. J. Ariza, D. J. Jones, J. Roziére, J. S. Lord, and D. Ravot. Muon spin relaxation study of spinel lithium manganese oxides. *J. Phys. Chem. B*, 107:6003–6011, 2003.

[76] M. J. Ariza, D. J. Jones, J. Roziére, and J. S. Lord. Muon spectroscopy for studying magnetism and protons and lithium dynamics in spinel manganese oxides. *J. Phys. Chem. Solids*, 65:597–602, 2004.

[77] C. T. Kaiser, V. W. J. Verhoeven, P. C. M. Gubbens, F. M. Mulder, and I. de Schepper *et al.*. Li mobility in the battery cathode material $Li_x[Mn_{1.96}Li_{0.04}]O_4$ studied by muon-spin relaxation. *Phys. Rev. B*, 62:9236–9239, 2000.

[78] S. Nishimura, G. Kobayashi, K. Ohoyama, R. Kanno, M. Yashima, and A. Yamada. Experimental visualization of lithium diffusion in Li_xFePO_4. *Nat. Mater.*, 7:707–711, 2008.

[79] B. Ellis, L. K. Perry, D. H. Ryan, and L. F. Nazar. Small polaron hopping in Li_xFePO_4 solid solutions: coupled lithium-ion and electron mobility. *J. Am. Chem. Soc.*, 128:11416–11422, 2006.

[80] J. Sugiyama, H. Nozaki, M. Harada, K. Kamazawa, and O. Ofer *et al.*. Magnetic and diffusive nature of $LiFePO_4$ investigated by muon spin rotation and relaxation. *Phys. Rev. B*, 84:54111, 2011.

[81] J. Sugiyama, H. Nozaki, M. Harada, K. Kamazawa, Y. Ikedo, Y. Miyake, O. Ofer, M. Månsson, E. J. Ansaldo, K. H. Chow, G. Kobayashi, and R. Kanno. Diffusive behavior in $LiMPO_4$ with M = Fe, Co, Ni probed by muon-spin relaxation. *Phys. Rev. B*, 85:54111, 2012.

[82] G. Zeng, R. Caputo, D. Carriazo, L. Luo, and M. Niederberger. Tailoring two polymorphs of $LiFePO_4$ by efficient microwave-assisted synthesis: a combined experimental and theoretical study. *Chem. Mater.*, 25:3399–3407, 2013.

[83] T. E. Ashton, J. V. Laveda, D. A. Maclaren, P. J. Baker, A. Porch, M. O. Jones, and S. A. Corr. Muon studies of Li^+ diffusion in $LiFePO_4$ nanoparticles of different polymorphs. *J. Mater. Chem. A*, 2:6238–6245, 2014.

[84] D. J. Adams. Quantum mechanical theory diffusion in solids. An application to H in silicon and Li in $LiFePO_4$. *Solid State Ion.*, 290:116–120, 2016.

[85] I. Umegaki, S. Kawauchi, H. Sawada, H. Nozaki, Y. Higuchi, K. Miwa, Y. Kondo, M. Månsson, M. Telling, F. C. Coomer, S. P. Cottrell, T. Sasaki, T. Kobayashi, and J. Sugiyama. Li-ion diffusion in Li intercalated graphite C_6Li and $C_{12}Li$ probed by μ^+SR. *Phys. Chem. Chem. Phys.*, 19:19058–19066, 2017.

[86] N. Tapia-Ruiz, J. V. Laveda, R. I. Smith, S. A. Corr, and D. H. Gregory. Ultra-rapid microwave synthesis of $Li_{3-x-y}M_xN$ (M= Co, Ni and Cu) nitridometallates. *Inorg. Chem. Front.*, 2:1045–1050, 2015.

[87] T. Shodai, S. Okada, S. Tobishima, and J. Yamaki. Study of $Li_{(3-x)}M_{(x)}N$ (M:Co,Ni or Cu) system for use as anode material in lithium rechargeable cells. *Solid State Ion.*, 86-88:785–789, 1996.

[88] A. S. Powell, J. S. Lord, D. H. Gregory, and J. J. Titman. Insight into lithium transport in lithium nitridometallate battery materials from muon spin relaxation. *J. Phys. Chem. C*, 15:20758–20763, 2013.

[89] A. S. Powell, J. S. Lord, D. H. Gregory, and J. J. Titman. Muon spin relaxation studies of lithium nitridometallate battery materials: Muon trapping and lithium ion diffusion. *J. Phys. Chem. C*, 113:20758–20763, 2009.

[90] H. El-Shinawi, G. W. Paterson, D. A. MacLaren, E. J. Cussen, and S. A. Corr. Low-temperature densification of Al-doped $Li_7La_3Zr_2O_{12}$ a reliable and controllable synthesis of fast-ion conducting garnets. *J. Mater. Chem. A*, 5:319–329, 2017.

[91] J. Xie, N. Imanishi, T. Matsumura, A. Hirano, Y. Takeda, and O. Yamamoto. Orientation dependence of Li–ion diffusion kinetics in $LiCoO_2$ thin films prepared by RF magnetron sputtering. *Solid State Ion.*, 179:362–370, 2008.

[92] J. Sugiyama, H. Nozaki, I. Umegaki, K. Mukai, K. Miwa, S. Shiraki, T. Hitosugi, A. Suter, T. Prokscha, Z. Salman, J. S. Lord, and M. Månsson. Li-ion diffusion in $Li_4Ti_5O_{12}$ and $LiTi_2O_4$ battery materials detected by muon spin spectroscopy. *Phys. Rev. B*, 92:1–9, 2015.

[93] H. Nozaki, M. Harada, S. Ohta, I. Watanabe, Y. Miyake, Y. Ikedo, N. H. Jalarvo, E. Mamontov, and J. Sugiyama. Li diffusive behavior of garnet-type oxides studied by muon-spin relaxation and QENS. *Solid State Ion.*, 262:585–588, 2014.

[94] H. Buschmann, J. Dölle, S. Berendts, A. Kuhn, P. Bottke, M. Wilkening, P. Heitjans, A. Senyshyn, H. Ehrenberg, A. Lotnyk, V. Duppel, L. Kienle, and J. Janek. Structure and dynamics of the fast lithium ion conductor $Li_7La_3Zr_2O_{12}$. *Phys. Chem. Chem. Phys*, 13:19378–19392, 2011.

[95] A. Dorai, N. Kuwata, R. Takekawa, J. Kawamura, K. Kataoka, and J. Akimoto. Diffusion coefficient of lithium ions in garnet-type $Li_{6.5}La_3Zr_{1.5}Ta_{0.5}O_{12}$ single crystal probed by ^{7}Li pulsed field gradient- NMR spectroscopy. *Solid State Ion.*, 327:18–26, 2018.

[96] Y. Matsuda, Y. Itami, K. Hayamizu, T. Ishigaki, M. Matsui, Y. Takeda, O. Yamamoto, and N. Imanishi. Phase relation, structure and ionic conductivity of $Li_{7-x-3y}Al_yLa_3Zr_{2-x}Ta_xO_{12}$. *RSC Adv.*, 6:78210–78218, 2016.

[97] K. Kataoka and J. Akimoto. High ionic conductor member ofgarnet-type oxide $Li_{6.5}La_3Zr_{1.5}Ta_{0.5}O_{12}$. *ChemElectroChem*, 5:2551–2557, 2018.

[98] K. Hayamizu, S. Seki, and T. Haishi. Lithium ion micrometer diffusion in a garnet-type cubic $Li_7La_3Zr_2O_{12}$ (LLZO) studied using ^{7}Li NMR spectroscopy. *J. Chem. Phys.*, 146:024701, 2017.

[99] J. W. Kim, J. J. Travis, E. Hu, K. Nam, and S. C. Kim *et al...* Unexpected high power performance of atomic layer deposition coated $Li[Ni_{1/3}Mn_{1/3}Co_{1/3}]O_2$ cathodes. *J. Power Sources*, 254:190–197, 2014.

[100] W. Meng, C. Yunbo, W. Feng, C. Lin, and S. Yuefeng. The electrochemical performance of yttrium oxide coated $LiNi_{1/3}Mn_{1/3}Co_{1/3}O_2$ as cathode material for lithium-ion batteries. *Int. Conf. Adv. Technol. Des. Manufacture*, pages 450–453, 2010.

[101] H. Wu, G. Chan, J. W. Choi, I. Ryu, Y. Yao, M. T. Mcdowell, S. W. Lee, A. Jackson, Y. Yang, L. Hu, and Y. Cui. High rate capability of $LiNi_{1/3}Mn_{1/3}Co_{1/3}O_2$ electrode for Li-ion batteries. *Nat. Nanotechnol.*, 7:310–315, 2012.

[102] X. Zhan, S. Gao, and Y. T. Cheng. Influence of annealing atmosphere on Li_2ZrO_3-coated $LiNi_{0.6}Co_{0.2}Mn_{0.2}O_2$ and its high-voltage cycling performance. *Electrochim. Acta.*, 300:36–44, 2019.

[103] X. Li, J. Liu, M. N. Banis, A. Lushington, R. Li, M. Cai, and X. Sun. Atomic layer deposition of solid-state electrolyte coated cathode materials with superior high-voltage cycling behavior for lithium ion battery application. *Energy Environ. Sci.*, 7:768–778, 2014.

[104] J. Tian, Y. Su, F. Wu, S. Xu, F. Chen, R. Chen, Q. Li, J. Li, F. Sun, and S. Chen. High-rate and cycling-stable nickel-rich cathode materials with enhanced Li^+ diffusion pathway. *ACS Appl. Mater. Interfaces*, 8:582–587, 2016.

[105] R. Amin and Y. Chiang. Characterization of Electronic and Ionic Transport in $Li_{1-x}Ni_{0.33}Mn_{0.33}Co_{0.33}O_2$ (NMC 333) and $Li_{1-x}Ni_{0.50}Mn_{0.20}Co_{0.30}O_2$ (NMC 523) as a Function of Li Content. *J. Electrochem. Soc.*, 163:1512–1517, 2016.

[106] Y. J. Gu, Q. G. Zhang, Y. B. Chen, H. Q. Liu, J. X. Ding, Y. M. Wang, H. F. Wang, L. Chen, M. Wang, S. W. Fan, Q. F. Zang, and X. L. Yang. Reduction of the lithium and nickel site substitution in $Li_{1+x}Ni_{0.5}Co_{0.2}Mn_{0.3}O_2$ with Li excess as a cathode electrode material for Li-ion batteries. *J. Alloys Compd.*, 630:316–322, 2015.

[107] S. Sun, C. Du, D. Qu, X. Zhang, and Z. Tang. Li_2ZrO_3-coated $LiNi_{0.6}Co_{0.2}Mn_{0.2}O_2$ for high-performance cathode material in lithium-ion battery. *Ionics*, 21:2091–2100, 2015.

[108] I. D. Johnson, T. E. Ashton, E. Blagovidova, G. J. Smales, M. Lübke, P. J. Baker, S. A. Corr, and J. A. Darr. Mechanistic insights of Li^+ diffusion within doped $LiFePO_4$ from Muon Spectroscopy. *Sci. Rep.*, 8:4114, 2018.

[109] F. Gao and Z. Tang. Kinetic behavior of $LiFePO_4$/C cathode material for lithium-ion batteries. *Electrochim. Acta*, 53:5071–5075, 2008.

[110] H. Liu, C. Li, H. P. Zhang, L. J. Fu, Y. P. Wu, and H. Q. Wu. Kinetic study on $LiFePO_4$/C nanocomposites synthesized by solid state technique. *J. Power Sources*, 159:717–720, 2006.

[111] J. Xie, N. Imanishi, T. Zhang, A. Hirano, Y. Takeda, and O. Yamamoto. Li-ion diffusion kinetics in $LiFePO_4$ thin film prepared by radio frequency magnetron sputtering. *Electrochim. Acta*, 54:2329–2334, 2009.

[112] X. Tang, L. Li, Q. Lai, X. Song, and J. Jiang. Investigation on diffusion behavior of Li^+ in $LiFePO_4$ by capacity intermittent titration technique (CITT). *Electrochim. Acta*, 54:2329–2334, 2009.

[113] J. Li, B. L. Armstrong, J. Kiggans, C. Daniel, and D. L. Wood. Lithium ion cell performance enhancement using aqueous $LiFePO_4$ cathode dispersions and polyethyleneimine dispersant. *J. Electrochem. Soc.*, 160:201–206, 2013.

[114] J. Sugiyama, K. Mukai, H. Nozaki, M. Harada, K. Kamazawa, Y. Ikedo, M. Månsson, O. Ofer, E. J. Ansaldo, J. H. Brewer, K. H. Chow, I. Watanabe, Y. Miyake, and T. Ohzuku. Lithium Diffusion in Lithium-Transition-Metal Oxides Detected by μ+SR. *Phys. Procedia*, 30:105–108, 2012.

[115] J. Sugiyama, K. Mukai, Y. Ikedo, H. Nozaki, M. Månsson, and I. Watanabe. A novel tool for detecting Li diffusion in solids containing magnetic ions; μ^+SR study on Li_xCoO_2. *J. Phys. Conf. Ser.*, 225:012052, 2010.

[116] J. Sugiyama, H. Nozaki, I. Umegaki, M. Harada, Y. Higuchi, E. J. Ansaldo, J. H. Brewer, Y. Miyake, G. Kobayashi, and R. Kanno. Structural, magnetic, and diffusive nature of olivine-type Na_xFePO_4. *J. Phys. Conf. Ser.*, 551(1):012012, 2014.

[117] I. Umegaki, H. Nozaki, M. Harada, M. Månsson, H. Sakurai, I. Kawasaki, I. Watanabe, and J. Sugiyama. Na Diffusion in Quasi One-Dimensional Ion Conductor $NaMn_2O_4$ Observed by μ^+SR. *JPS Conf. Proc.*, 21:011018, 2018.

[118] Y. Ikedo, J. Sugiyama, O. Ofer, M. Månsson, and H. Sakurai *et al...* Comparative μ^+SR study of the zigzag chain compounds $NaMn_2O_4$ and $LiMn_2O_4$. *J. Phy. Conf. Ser.*, 225:012017, 2010.

[119] J. S. Lord, S. P. Cottrell, and W. G. Williams. Muon sites and diffusion in doped lithium oxide. *Physica B*, 289:491–494, 2000.

[120] J. Sugiyama, H. Nozaki, I. Umegaki, K. Mukai, and S. P. Cottrell *et al...* μ^+SR study on Li ionic conductors. *JPS Conf. Proc.*, 21:14–17, 2018.

[121] P. Moreau, D. Guyomard, J. Gaubicher, and F. Boucher. Structure and Stability of Sodium Intercalated Phases in Olivine $FePO_4$. *Chem. Mater*, 22:4126–4128, 2010.

[122] C. Delmas, J. Braconnier, C. Fouassier, and P. Hagenmuller. Electrochemical intercalation of sodium in Na_xCoO_2 bronzes. *Solid State Ion.*, 3-4:165–169, 1981.

[123] K. Mizushima, P. C. Jones, P. J. Wiseman, and J. B. Goodenough. Li_xCoO_2 ($0 < x \leq 1$): A NEW CATHODE MATERIAL FOR BATTERIES OF HIGH ENERGY DENSITY. *Solid State Ion.*, 3:171–174, 1981.

[124] L. W. Shacklette, T. R. Jew, and L. Townsend. Rechargeable Electrodes from Sodium Cobalt Bronzes. *J. Electrochem. Soc.*, 135:2669–2674, 1980.

[125] R. Berthelot, D. Carlier, and C. Delmas. Electrochemical investigation of the P2-Na_xCoO_2 phase diagram. *Nat. Mater.*, 10:74–80, 2010.

[126] X. Liu, X. Wang, A. Iyo, H. Yu, D. Li, and H. Zhou. High stable post-spinel $NaMn_2O_4$ cathode of sodium ion battery. *J. Mater. Chem. A*, 2:14822–14826, 2014.

[127] M. Månsson, K. Prša, and Y. Sassa. Na-ion dynamics in Quasi-1D compound NaV_2O_4. *J. Phys.: Conf. Ser*, 551:12035, 2014.

[128] J. Sugiyama. Ion Diffusion in Solids Probed by Muon-Spin Spectroscopy. *J. Phys. Soc. Jpn.*, 82:SA023, 2013.

[129] E. Morenzoni, H. Glückler, T. Prokscha, H. P. Weber, E. M. Forgan, T. J. Jackson, H. Luetkens, C. Niedermayer, M. Plienes, M. Birke, A. Hofer, J. Litterst, T. Riseman, and G. Schatz. Low energy μSR at PSI: present and future. *Physica B*, 289-290:653–657, 2000.

[130] J. Nakamura, T. Nagatomo, Y. Oishi, Y. Ikedo, P. Strasser, N. Saito, K. Miyazaki, K. Yokoyama, K. Okamura, Y. Miyake, S. Makimura, K. Nishiyama, K. Shimomura, N. Kawamura, A. Koda, W. Higemoto, S. Wada, M. Iwasaki, and E. Torikai. Ultra Slow Muon Microscope at MUSE / J-PARC. *J. Phys.: Conf. Ser.*, 502:012042, 2014.

[131] A. D. Hillier, M. Aramini, P. J. Baker, A. Berlie, P. K. Biswas, S. P. Cottrell, K. Ishida, T. Loe, J. S. Lord, D. E. Pooley, F. L. Pratt, N. J. Rhodes, R. J. da Silva Afonso, M. T. F. Telling, and K. Yokoyama. Developing the Muon Facilities at ISIS. *JPS Conf. Proc.*, 21:011055, 2018.

[132] O. Pecher, J. Carretero-González, K. J. Griffith, and C. P. Grey. Materials' Methods: NMR in Battery Research. *Chem. Mater.*, 29:213–242, 2017.

[133] B. Dong, J . J. Biendicho, S. Hull, R. I. Smith, and A. R. West. In-Situ Neutron Studies of Electrodes for Li-Ion Batteries Using a Deuterated Electrolyte: LiCoO2 as a Case Study. *J. Electrochem. Soc.*, 165:A793, 2018.

3 Experimental Methods

3.1 Materials

The materials used for synthesis and the specific parameters for characterisation techniques are given in each results chapter individually.

3.2 Sol-gel Synthesis

A sol-gel is wet chemical method which can be used to synthesise a range of ceramic materials from solid powder precursors [1]. Reactants are weighed in stoichiometric quantities and mixed in suitable solvents to form a colloidal suspension, which is subject to constant stirring. This colloidal solution, termed a "sol", is heated to gradually evaporate solvent and form a network structure of viscous precursor "gel". The gel is further heated to first remove any remaining solvent, and then burn off any organic material. This generally occurs between 300 – 400 °C, depending on which metal ions and additives are present. A burnt residue can then be collected and heated in a muffle furnace to further remove organics and obtain a powdered ceramic product. Whilst used exclusively to produce ceramics in this work, the sol-gel method is applicable for a diverse range of inorganic chemical reactions.

The sol-gel method has several advantages over more traditional solid-state synthesis routes, namely the avoidance of mass transport limitations. During a solid-state reaction, complete conversion to a product can be limited by the inhomogeneity of starting materials due to the large diffusion distances involved. This is particularly pertinent when a mixture of many starting materials is used [2]. As such, subsequent ball-milling steps are often used to increase the reactant surface area, or extended annealing times can be required to allow sufficient time for diffusion throughout the mixture. Conversely, the liquid-based approach of sol-gel ensures the precursor is trapped in a solution state before heating, resulting in a random mixture of reactants at the atomic level. This can result in a more homogeneous single-phase crystal structure and allows for a greater degree of morphological control. Importantly, the crystallite homogeneity after synthesis allows the powder to be processed to high densities during sintering, which is crucial for ceramic solid electrolyte materials.

In this work, citric acid was incorporated into the sol to act as a chelating agent, a common technique during the synthesis of metal oxides. The addition of citric acid is beneficial due to its ability to maintain the stability and homogeneity of reactant metal ions in a water-soluble complex. The formation of an organic matrix of precursor molecules ensures an even distribution of nucleation sites for crystallisation. Therefore, this method can permit the synthesis of smaller crystallite sizes over traditional solid-state reaction routes. pH additives are also regularly used in the sol-gel method to enhance cation

binding or improve the solubility of reactants, particularly important during syntheses involving many metal reactants. For example, in Chapter 5, ammonium hydroxide is employed to successfully incorporate the tungsten metal precursor (ammonium tungsten pentoxide hydrate). Due to a difficulty in dissolving this precursor, it is conducted in a separate sol to the other reactants. Under vigorous mixing and a high heat, ammonium hydroxide is added slowly, before the reactant is visibly dissolved around pH 8 with a clear colour change. Citric acid is then added to lower the pH and avoid precipitation. This separate solution can then be added to the main solution to form a single, well mixed, precursor network.

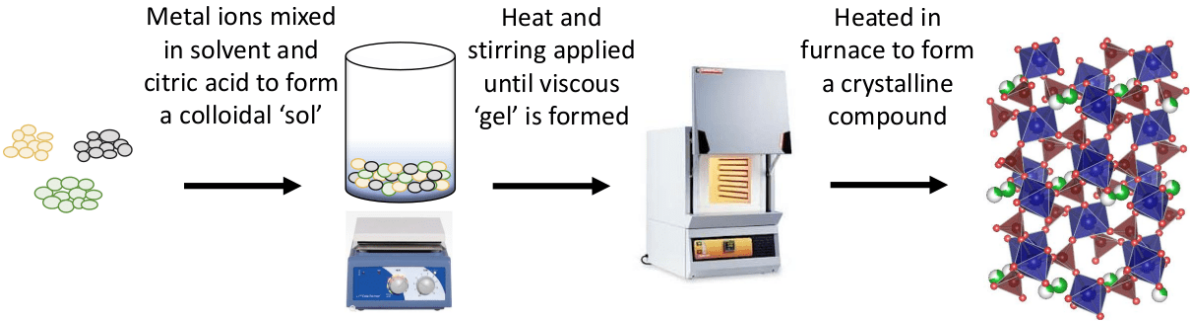

Figure 3.1: Schematic showing the sol-gel synthesis methodology. Reactant metal ions are mixed thoroughly in solvent to form a "sol", which is gradually evaporated to form a homogeneous network of viscous precursor "gel". This is heated further in a furnace to remove any organics and form the desired crystalline powder.

3.3 Field Assisted Sintering Technology

Sintering is a process to convert loose powder particles into a dense, contiguous mass *via* the application of heat and/or pressure without melting the material to liquefaction. For ceramics, this is conventionally completed within a furnace at high temperatures and for a long duration. Field assisted sintering technology (FAST) is an alternative densification method which allows the rapid sintering of ceramics *via* Joule heating (resistive heating) under a high current. This is often referred to as spark plasma sintering (SPS), generally considered a misnomer due to the lack of observable spark or plasma during application. This technique has been employed previously for a range of ceramic processing capabilities; namely for battery research, the densification of solid electrolyte materials [3, 4]. In FAST, DC current pulses are applied through a graphite mould set-up where a powdered sample is housed (Figure 3.2). The high current (∼kA) produces rapid heating through the graphite mould. The low resistance of the mould material means that generally only low voltages (∼5 V) are required to produce fast heating. If the powdered sample is electronically conductive, the applied current directly heats the powdered sample housed in the mould, otherwise it is heated indirectly by thermal conduction [5].

As can be seen in Figure 3.2, the mould set up creates an electrical circuit where

a uniaxial pressure is applied through rams at either side. The powdered sample is sandwiched between six graphite foil discs and assembled inside the graphite mould, which is similarly lined with graphite foil. The foil acts to protect the sample from the mould, and *vice versa*. The entire set-up is held within a vacuumed chamber for the duration of the experiment. In this work, a thermocouple hole was incorporated inside the graphite mould as close to the sample as possible, in order to monitor and control the sample temperature accurately. Although the pressure applied during sintering was low (50 MPa), the constant pressure on the sample greatly improves densification over traditional sintering methods; the improved contact between particles allows heat transfer through the sample to progress rapidly [6].

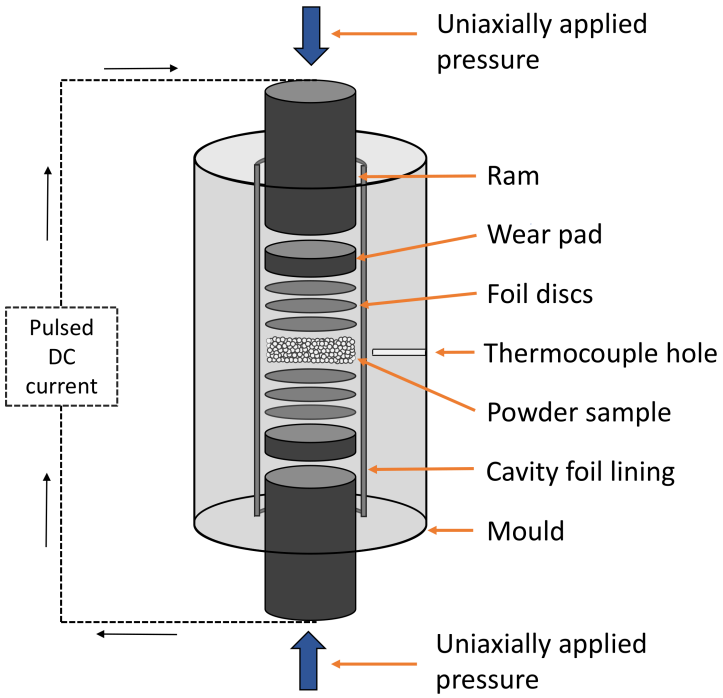

Figure 3.2: Diagram which shows the experimental set-up to densify a powdered sample using FAST. A powder is loaded inside a graphite mould which is lined with graphite foil. The full mould is placed inside a vacuumed chamber and subjected to a uniaxial pressure during sintering. DC current pulses rapidly heat the entire set-up *via* Joule heating.

Utilising FAST, heating rates of up to 500 °C min^{-1} are possible, reducing sintering times towards zero minutes [5]. This greatly improves the sintering time over conventional methods, which can take multiple days. Samples may be processed to extremely high densities using FAST ($\geq$99% relative density), which leads to exceptionally high strength and high hardness. In the case of solid electrolyte ceramics, this also results in fast ionic conductivities [3]. However, the experimental equipment required for FAST is often bulky and expensive. Other sintering techniques such as flash sintering [7] and cold sintering [8] are under development to improve efficiency, sintering temperature, and scalability.

3.4 Powder X-ray Diffraction

Powder X-ray Diffraction (XRD) is a non-destructive, analytical technique which has become one of the most ubiquitously used for the structural characterisation of crystalline materials. It is employed extensively in material science for phase identification and the elucidation of important structural parameters, such as unit cell dimensions and lattice spacings. Since its inception, the improvements in the equipment required for crystallographic studies are impressive; scans are now regularly completed to produce good quality data using a bench-top diffractometer in minutes.

X-rays are a form of electromagnetic radiation with a wavelength similar to the lattice plane spacing of most crystal structures (1 – 100 Å), and an energy ranging between ∼0.1 – 100 keV. X-rays can be produced through the interaction of an electron beam with a material. First, electrons are produced by applying a current through a filament, which heats up and thermionically emits electrons. The electrons are then accelerated by an electric field to collide with a metal target, often Cu, Fe, or W, although many metals can be used. The interaction between the electrons and metal target releases X-rays with two different energy profiles: polychromatic bremsstrahlung radiation caused by the deceleration of electrons within the target material, and monochromatic X-rays at the characteristic wavelength(s) of the target material. Bremsstrahlung radiation covers a wide energy profile which is of little use to the experimenter. Characteristic radiation occurs when electrons possessing a specific energy collide with an atom in the target material to eject a core shell electron. A higher energy level electron in the target material subsequently drops down to fill the created vacancy, emitting a photon with a particular energy in the process. This produces X-rays with a set of characteristic energies which are dependent on the target material; each has a unique energy spectrum. For example, a Cu target will produce K_α and K_β radiation with wavelength 1.541 and 1.544 Å, respectively. K_α refers to the radiation emitted when an electron transitions between the $2p$ and $1s$ orbital, while K_β is from the $3p$ to the $1s$. A monochromator is used to dispose of the bremsstrahlung radiation and select a single wavelength for experimental use, generally K_α for a Cu source because it has the strongest intensity. During an XRD experiment, often the X-ray source will remain fixed while the sample and the detector are allowed to rotate through ϑ and 2ϑ, respectively, to cover a wide-angle range. This is called Bragg-Brentano geometry, which was used in this work.

The similarity between the wavelength of X-rays and most crystal lattice spacings means that when monochromatic X-rays are used to irradiate crystal structures, they will be diffracted to an extent depending on Bragg's Law:

$$n\lambda = 2d\sin(\vartheta). \tag{3.1}$$

In Equation 3.1, n is an integer, d is the crystalline layer spacing, and ϑ and λ are

the incidence angle and wavelength of incoming radiation, respectively. Bragg's law is satisfied when two waves are diffracted from the structure at an angle which produces constructive interference between the waves. The intensity of radiation at these angles is then detected as peaks in the generated diffraction pattern, where each peak corresponds to a different lattice plane. The lattice planes within a disordered powdered sample are randomly orientated in every direction, meaning all possible diffraction directions from the sample can be collected. Sample homogeneity is therefore important for good quality data acquisition. As every crystalline material has a unique set of lattice planes, it will produce a characteristic X-ray diffraction pattern. This can be used to determine its crystal phase by correlation with reference patterns. As such, the diffraction pattern of well-known crystal structures can be used as a pre-defined fingerprint to identify new compounds.

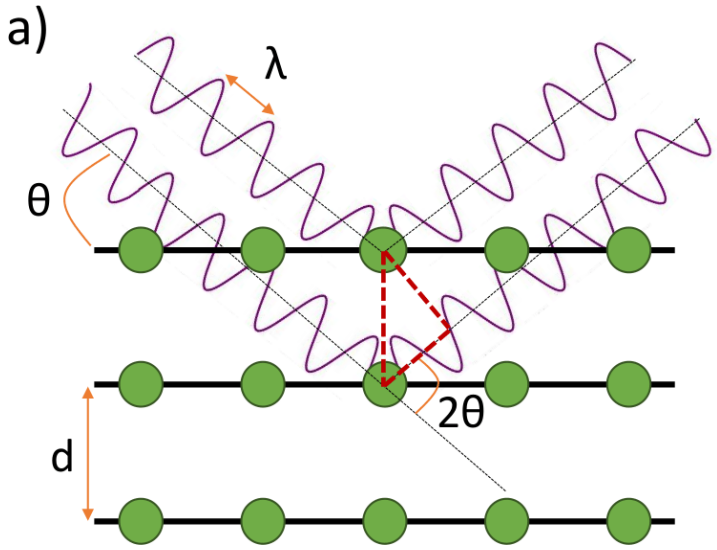

Figure 3.3: (a) Diagram showing how Bragg's law, $n\lambda = 2d\sin(\vartheta)$, is employed during an X-ray diffraction experiment. The equation is satisfied when two waves are diffracted from different crystallographic planes and interfere constructively.

In this work, diffraction patterns were collected using a Rigaku Miniflex with a Cu K_α source with a wavelength of 1.541 Å. The diffractometer was operated at a voltage of 40 kV and a current of 15 mA, using a step size of 0.02 ° (2ϑ).

3.4.1 The Rietveld method

A Rietveld refinement is a computational analysis method performed using diffraction data to obtain the structural parameters of a sample, such as the unit cell dimensions [9]. The method uses an algorithm to derive a theoretical diffraction pattern and sequentially iterates it until it resembles an inputted pattern as closely as possible. Various parameters are considered, such as peak width, intensity, shape, and position. The calculated pattern can be refined until extremely similar to the inputted data, which allows the estimation

of important structural parameters from an unknown sample.

To do this, a least squares approach is employed to iterate the theoretical model towards the collected data. The difference function M between the data and theoretical can be described as:

$$M = \sum_i W_i[y_i(\text{obs}) - \frac{1}{c}\, y_i(\text{calc})]^2, \tag{3.2}$$

where i is the i^{th} atom, W_i is a statistical weighting factor, c is an overall scale factor, and y(obs) and y(calc) are the observed and calculated patterns, respectively. Thus, it is desirable to minimise the value of the function M whilst maintaining a physically reasonable model.

To ensure the accuracy of any model, there are a few statistical parameters which can be used: a weighted profile factor (R_{wp}), an expected factor (R_{exp}), and a goodness of fit value (χ^2). These parameters are determined computationally during each refinement, where R_{wp} is described as:

$$R_{\text{wp}} = \sqrt{\frac{M}{\sum_i W_i y_i(\text{obs})^2}}\,, \tag{3.3}$$

and R_{exp} can be expressed as:

$$R_{\text{exp}} = \sqrt{\frac{N - P}{\sum_i W_i y_i(\text{obs})^2}}\,. \tag{3.4}$$

In Equation 3.4, N is defined as the number of data points and P as the number of parameters. Generally, $N \gg P$, meaning N dominates the numerator. This illustrates the desire for high quality diffraction data before a Rietveld refinement is attempted. R_{exp} is a theoretical minimum error for the calculated model. Therefore, R_{wp} should be as close to R_{exp} as possible after a structural refinement. These values are often displayed simply as a goodness of fit parameter, χ^2, which can be defined as:

$$\chi^2 = (\frac{R_{\text{wp}}}{R_{\text{exp}}})^2. \tag{3.5}$$

It is therefore desirable for χ^2 to be as close to unity as possible.

In this work, Rietveld refinements were performed using the GSAS II program (Generalised Structure Analysis System) by using a least squares approach [10]. Care was taken when applying the Rietveld method to perform analysis in a similar manner for similar materials to ensure the accuracy of the derived structural model. For example, fit parameters were refined in the same sequence each time.

3.5 Scanning Electron Microscopy

Scanning Electron Microscopy (SEM) is an imaging technique used to understand the topography, morphology, and composition of a sample. It is widely employed to determine particle size and distribution, pore shape, and surface features. Optical microscopes have been used since the 18^{th} century, however, they are fundamentally limited by the wavelength of visible light (400 – 700 nm), meaning that resolution on the length scale required for material characterisation is difficult. This has motivated the development of high-energy electron microscopy, enabling the imaging of surfaces with a spatial resolution on the nm scale.

For SEM, an electron beam is generated using an electron gun which operates *via* a heated tungsten filament. The beam is then accelerated by a potential through a vacuum towards the sample. The potential can be controlled to suit the application and is generally between 0.2 – 30 kV. The wavelength of the electron beam is given by the De Broglie equation:

$$\lambda = \frac{h}{p} = \frac{h}{\sqrt{2mE}}. \tag{3.6}$$

In Equation 3.6, h is Planck's constant, while λ, p, and E are the electron's wavelength, momentum, and energy, respectively. Low energy electrons (high wavelength) may be preferable to image beam sensitive or non-conductive specimens. The lower energy reduces the chance of beam damage to the sample but inevitably decreases the imaging resolution due to the longer wavelength of incident radiation. As such, depending on the specimen of interest, a balance must be struck when choosing the accelerating voltage.

The beam is scanned across the sample so that the sample-electron response is collected from the full surface. The electrons interact within the sample in many ways (Figure 3.4), and each interaction can be used to probe different regions of the sample [11]. Lower energy electrons from the beam will produce secondary electrons *via* inelastic collisions during deceleration near the sample surface. As such, the detection of secondary electrons will yield topographical and morphological information of the sample's surface or near-surface regions. These are generally detected using an Everhart-Thornley detector, which uses a scintillator to convert detected electrons to photons, which are then converted to electrical signals using a photomultiplier. The intensity of the detected electrons can therefore be used to generate an image of the sample. Arising from slightly deeper inside the specimen are back-scattered electrons, which occur when an elastic collision between an electron and a host atom scatters the electron. This interaction occurs over a broad depth range in the sample. By nature, an atom's scattering strength is proportional to its atomic number; back scattered electrons are thus used to differentiate between different phases within a sample. Even deeper in the sample, X-rays are produced in the manner outlined in Section 3.4 (powder X-ray diffraction). These can be used for alternative applications, such as the energy dispersive X-ray spectroscopy

technique, which is discussed below.

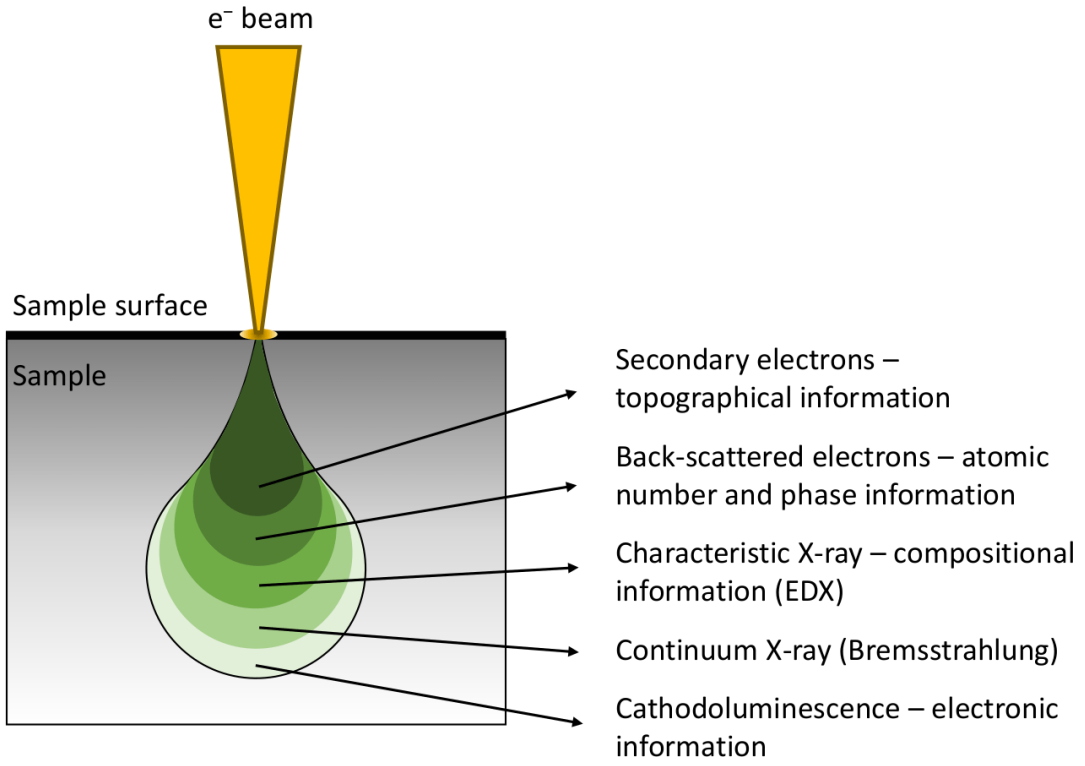

Figure 3.4: Diagram outlining the interaction of an electron beam with a sample. The various sample-electron interactions can be used to provide different types of information in SEM and EDX.

In this thesis, SEM measurements were completed using an FEI Inspect F50 microscope. Samples were mounted on conductive carbon adhesive tape on an aluminium stub and sometimes gold-coated for between 10 – 30 seconds, depending on the specimen of interest. The accelerating voltage used was between 2 – 10 kV and both secondary and back-scattered electron detectors were used depending on the circumstance. A beam spot size of between 3 – 4 mm was used.

3.6 Energy Dispersive X-ray Spectroscopy

Energy dispersive X-ray (EDX or EDS) spectroscopy, as discussed for SEM, uses the interaction between a scanning electron beam and a sample to gain valuable compositional information. EDX is commonly incorporated into the equipment for electron microscopes so that both techniques are possible using the same electron beam. The X-rays which are produced (shown in Figure 3.4) from deeper in the sample than either secondary or back-scattered electrons can yield information on both the relative quantity and distribution of atoms within the sample. Since the energy of an incoming electron required to displace a core shell electron from an atom depends on the atomic number, the energy of X-rays produced by such an interaction can be matched to the characteristic X-ray energy profile

of any element.

Once the emitted X-rays are detected, the distribution of energies can be matched to a database of characteristic X-ray energies. As such, the energy spectrum will indicate the abundance and position of atomic species within a sample. This can be used to locate elements across a sample to build an elemental distribution image (called elemental mapping), which can determine whether a homogeneous distribution of elements is present or identify any impurity phases. This may be particularly useful to relate morphology to phase in unknown, multi-phase samples. Furthermore, spots can be chosen to analyse the spectrum emitted from specific features displayed on the electron micrograph. Unfortunately for battery materials, the light atomic composition of lithium results in a very low energy of characteristic radiation. Therefore, the detection of lithium with non-specialist EDX equipment is difficult and poses a current research challenge [12]. EDX data in this thesis was collected using X-ray detection equipment inside an FEI Inspect F50 SEM. Oxford Instruments ©AZtec program was used for data collection and analysis.

3.7 Galvanostatic Cycling with Potential Limitation

Galvanostatic cycling with potential limitation (GCPL), more casually referred to as charge/discharge cycling, is an electrochemical technique which is crucial to understanding the performance of energy materials. The technique reflects how batteries are used commercially; thorough characterisation using GCPL under different current rates and different potential limitations represents the real operating conditions of a cell. Galvanostatic means constant current, while potential limitation means the cell is operated within two pre-defined voltage limits. For example, to cycle a cathode material, a positive current is applied through the cell which will act to increase the working voltage to an upper limit at a rate defined by the current amplitude. At the upper voltage limit, the current polarity is flipped to negative, meaning electrons are being extracted from the anode to provide power through the external circuit, and the voltage will decrease towards to lower limit. This corresponds to one full charge/discharge, or cycle, of the battery. For a cathode material, the structure is delithiated during the charging process, and reversibly lithiated during discharge.

The capacity of a battery is a measure of the total amount of charge (energy) which can be stored within it. The specific capacity (units of mAh g^{-1}) is a measure of the capacity per unit mass, which is often used to easily compare electrode materials. A material has a theoretical capacity because it possesses a finite number of mobile ions. As such, if a cathode material can display a practical capacity which is the same as its theoretical capacity, 100% of the ionic species can be reversibly intercalated. The

theoretical capacity can be calculated using the relationship:

$$Q = \frac{nF}{M_w}. \tag{3.7}$$

The capacity (Q) is calculated in C kg^{-1} from the number of Li^+ (n) stored within the active material (in the case of a Li-ion battery), the Faraday constant (F), and the molecular weight of the active material (M_w). The practical capacity of an active material can be found simply by using the current passed during a time duration and the mass of active material.

To define the rate of cycling in battery research, the term "C-rate" is generally used. 1C describes a full addition/removal of the battery capacity in one hour. For example, a rate of C/20 would denote a charge or discharge process to occur over 20 hours, or, conversely, a rate of 20C would describe the same process occurring in 3 minutes. Thus, GCPL experiments are used to find a cell's rate capability, which means how it will perform under the application of high applied current.

Constant current constant voltage (CCCV) is a charging method used to improve the electrochemical performance of batteries (Figure 3.5). As in normal charging, a constant current is used to shuttle ions across a cell to increase the working voltage. In CCCV, however, once the cell reaches its voltage limit it is held at that potential while the current is allowed to decay exponentially to a defined value (often around 5% of the constant current value). This allows an increase in capacity without the need to increase the voltage and potentially induce harmful degradation processes. However, the time used to complete this step can somewhat negate the advantage gained when fast charging a cell. This technique is commonly used commercially and can be particularly useful at higher C-rates where large over-potentials are common.

A separate dataset which can be extracted from a typical GCPL experiment is a differential capacity (dQ/dV) plot. This provides the rate of change of capacity with respect to voltage during cycling. Through such a plot the voltage regions where large changes in ionic (re)intercalation occur can be identified. Such changes in dQ/dV are intrinsically linked to the redox activity of the cathode. This can prove a useful tool in understanding material behaviour, and particularly, in quantifying degradation processes. dQ/dV plots often bear similarities to cyclic voltammetry (CV) experiments, although it is important to remember that no current is applied during CV, meaning a firm comparison requires an understanding of the nature of each technique [13]. In this work, GCPL was completed using several cell styles: Swagelok, coin, and a custom muon cell. The specifics of cell assembly are given in the materials and methods section of each chapter individually.

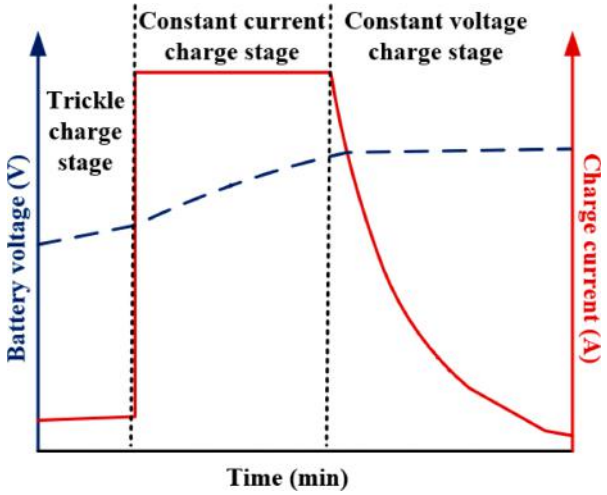

Figure 3.5: Example of Constant Current Constant Voltage (CCCV) charging. The current (in red) is held at a constant value until the voltage (in blue) reaches a set value, where the voltage is then held and the current decays exponentially. Adapted and reused with permission from MDPI [14].

3.8 Electrochemical Impedance Spectroscopy

Electrochemical impedance spectroscopy (EIS) is used to study the electrochemical reactions which occur across a range of materials, including electroceramics, solid-state conductors, ferroelectrics, fuel cells, and batteries [15]. EIS scans across a frequency range, which allows the electrical and ionic properties of different regions within a specimen to be distinguished. As the properties of ionic conductivity and resistivity within the bulk, grain boundary, and electrode interface may be readily separated, EIS is particularly useful for batteries and battery materials. For example, it can find the dominant resistive component in a cell or determine the total conductivity of a solid electrolyte. The speed (generally minutes) and versatility of EIS highlights why it has become a ubiquitous technique for battery characterisation.

Alternating current (AC) EIS measurements involve the application of a small voltage perturbation through a circuit over a range of frequencies. The voltage (E), which is applied sinusoidally, excites the electrochemical system and its corresponding response can be measured as an oscillating current (I). Impedance (Z) is defined at the complex representation of resistance (R), and can be defined *via* Ohm's law as:

$$E = IZ. \tag{3.8}$$

Since the applied voltage is sinusoidal it can be defined by a wave equation expressed as:

$$E(t) = E_0 \sin(\omega t), \tag{3.9}$$

where E_0 is the amplitude of the applied voltage signal, ω is the angular frequency (defined

as $\omega = 2\pi f$, where f is frequency in Hz), and t is time. As the measured current is also a sinusoidal response, it can be written as:

$$I(t) = I_0 \sin(\omega t + \vartheta), \tag{3.10}$$

where I_0 is the current amplitude of the response and ϑ is the phase shift from the applied voltage to the measured current. Given Equations 3.8 – 3.10, the impedance can be defined as:

$$Z = \frac{E(t)}{I(t)} = \frac{E_0 \sin(\omega t)}{I_0 \sin(\omega t + \vartheta)} = Z_0 \frac{\sin(\omega t)}{\sin(\omega t + \vartheta)}, \tag{3.11}$$

where Z_0 is the initial impedance magnitude. By the application of Euler's relationship, Equation 3.11 can be rewritten as:

$$Z = Z_0(\cos\vartheta + j\sin\vartheta). \tag{3.12}$$

In this instance j is used as an imaginary unit to avoid confusion of i with current. j is defined as:

$$j = \sqrt{-1}. \tag{3.13}$$

The impedance can then be rewritten as:

$$Z = Z' + jZ'', \tag{3.14}$$

where *Z'* and *Z"* are the real and complex, or resistive and reactive, parts of the impedance, respectively. Both parts are frequency dependent [16].

EIS spectra are often displayed using a Nyquist representation, which plots -*Z"* against *Z'*, and Bode plots, which display frequency information. The common convention of using the negative of *Z"* allows the plot to be displayed on the first quadrant of a graph to ease readability. An example of this for a perfect electrically resistive material, as may be approximated for some solid electrolyte materials, is shown in Figure 3.6. The resistance, R, is equal to the magnitude of the real impedance *Z'* when ϑ is zero. The frequency of measurement is not shown on Nyquist plots; the plot can be read from left to right with the frequency range from high to low. Figure 3.7 displays various aspects of a typical EIS experiment, showing the (a) system set-up, (b) the applied sinusoidal voltage, (c) the received response, and (d, e) example representations of the data with an equivalent circuit model. In (c), it is clear that the selected domain for analysis can be approximated as linear. This is a consequence of the small perturbation signal applied and is necessary to simplify the analysis. If a system is non-linear, the harmonics of the excitation frequency will be shown in the current response, complicating analysis.

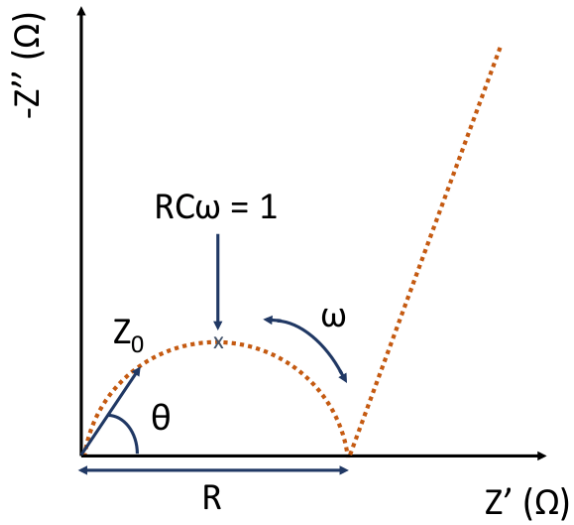

Figure 3.6: Schematic representation of a typical Nyquist plot for a perfectly electron resisting material using ion-blocking electrodes.

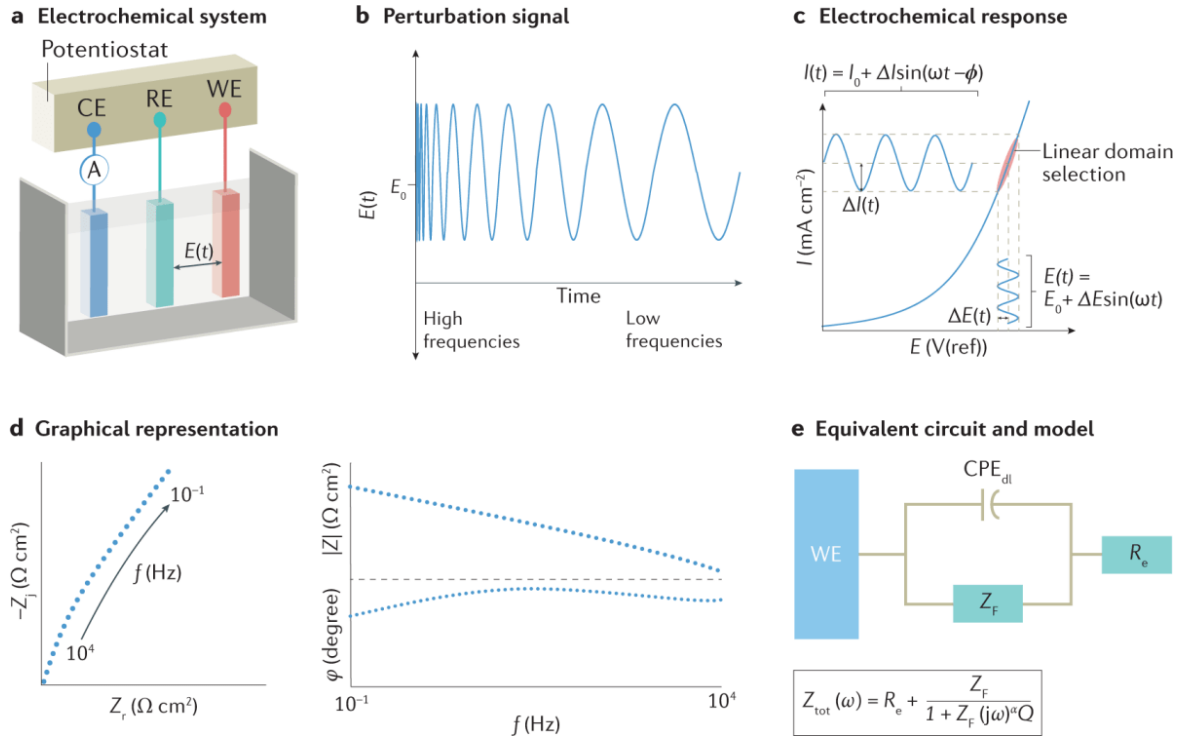

Figure 3.7: An example of various aspects of an EIS experiment. (a) A model electrochemical system with a counter, reference, and working electrode (CE, RE, WE, respectively). A potential *E(t)* is applied across the electrodes and measured as current at location (A). (b) A sinusoidal potential with voltage amplitude *E* applied from high to low frequency. (c) The measured electrochemical response to the applied perturbation in (b), showing the linear domain of *I* vs. *E*. (d) Example Nyquist and Bode plots to display measured data in alternative formats. (e) An example of an equivalent circuit used to extract meaningful parameters. A CPE is a constant phase element. Reused with permission from Springer Nature [16].

EIS experiments can be used to study a variety of materials; typical Nyquist plots for two such scenarios are shown in Figure 3.8. In the typical Nyquist plot of a LIB (Figure

3.8a), various resistive components are seen to produce different features which can be roughly characterised by the frequency at which the charge transfer processes occur. Semi-circular components are generally produced by ionic diffusion through particle surfaces or interfacial layers, while a tail in the plot arises from capacitive effects for ionic diffusion in either the electrode or electrolyte phase. Li^+ blocking electrodes (such as Au) will produce this sharp tail at low frequency due to the build-up of charge at the interface. Any features in a Nyquist plot may be overlapping due to similarity in the characteristic frequency of the underlying process, or not seen at all due to a negligible resistance.

In Figure 3.8b, ionic motion in each region of a solid electrolyte appears as different semi-circles on the Nyquist plot. The diffusion of an ion through the bulk of a grain, across a grain boundary between grains, or through the sample-electrode interface, all contain a specific impedance response dependent on the characteristic frequency of the underlying charge transfer process. Each response may vary in resistance and/or capacitance, which will define its location and magnitude on the Nyquist plot. In both instances of Figure 3.8, equivalent circuit fitting is necessary to elucidate the properties of any features and assign them to specific effects.

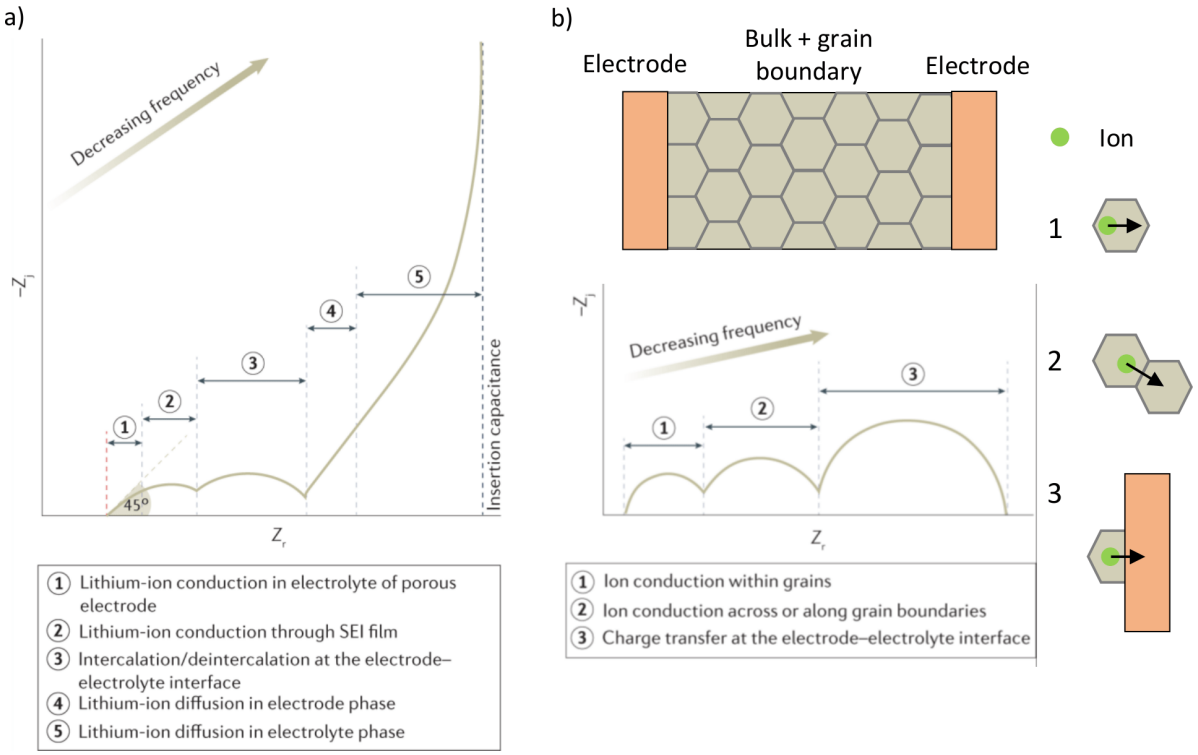

Figure 3.8: Typical Nyquist plots produced from EIS experiments of two different configurations: (a) a lithium-ion battery and (b) a solid electrolyte with symmetrical electrodes. In both cases the different features in the Nyquist plot can be referenced to different charge transfer phenomena. Adapted and reused with permission from Springer Nature [16].

The process of equivalent circuit fitting involves constructing a theoretical electrical circuit to reflect the real conditions of the experiment. The model system can then be

used to estimate parameter values for the real system. Such a circuit generally consists of a combination of resistors and capacitors in parallel (an RC circuit). To describe the impedance profile, the real (Z_{R}) and complex (Z_{C}) parts can be used individually to show that:

$$Z = Z_R + Z_C = R + \frac{1}{j\omega C}, \tag{3.15}$$

where R is resistance and C is capacitance. If the characteristic time constant of each RC element is denoted as τ, such that:

$$\tau = RC = \frac{1}{\omega} = \frac{1}{2\pi f}, \tag{3.16}$$

then $RC\omega$ is found to be equal to 1 at the top of a semi-circle in a Nyquist plot (see Figure 3.6). Therefore, each different element, or feature in a Nyquist plot, will possess a different τ *via* which it can be categorised. In this way, different regions can be modelled by a combination of RC elements in series. For example, elements with a higher τ will appear at a lower frequency in the Nyquist plot.

Other elements may be used in the equivalent circuit, such as a constant-phase element (CPE) or a Warburg element. A CPE may be used in place of a capacitor to model a distribution of τ over a region, through which a capacitance can be extracted indirectly. A CPE then models a non-ideal scenario where the electrical properties of a region are inhomogeneous. The capacitance can be found using the relationship:

$$C = \frac{(RQ)^{1/n}}{R}, \tag{3.17}$$

where Q is the CPE value (in units of S s^n) and n is a number between 0 and 1. A Warburg element is used to model semi-infinite diffusion, which is generally represented by a straight tail at low frequency in a Nyquist plot.

Any obtained capacitance can be used to describe features of interest in the specimen. Table 3.1 outlines this; in general, low capacitances represent bulk effects, while interfacial effects hold a much higher capacitance. Furthermore, the conductivity of these features can be determined *via* the relationship:

$$\sigma = \frac{1}{\rho} = \frac{L}{RA}. \tag{3.18}$$

Conductivity (σ) is described as the reciprocal of resistivity (ρ), which is determined using the resistance (R), and sample geometry parameters the thickness (L) and area (A). The total ionic conductivity of a sample may be obtained from the sum of resistivity obtained from each feature in the Nyquist plot. This highlights the importance of high densities for ionic conductivity in solids; the resistive contribution from the grain boundary should

be minimised.

Moreover, the energy barrier for ionic motion can be found by measuring the temperature dependence of the impedance profile. More precisely, the Arrhenius relationship for ionic conductivity can be used:

$$\sigma = B \exp(-\frac{E_a}{kT}), \tag{3.19}$$

where B is a constant, k is the Boltzman constant, T is temperature, and E_a is the activation energy for ionic motion [17]. As such, a plot of $\log(\sigma)$ against $1/T$ can yield a straight line with a gradient equal to the negative of E_a/k. In an insulator or a semiconductor, the shape of the relationship between conductivity and reciprocal temperature is altered. The conductivity is proportional to the charge (q), concentration (c), and mobility of the charge carriers (μ)[18]:

$$\sigma \approx \sum \mathrm{qc}\mu. \tag{3.20}$$

As a consequence, the temperature dependence of conductivity can also inform of the nature of conductivity within a sample.

Table 3.1: Capacitance values and their possible interpretation. Adapted and reused with permission from John Wiley and Sons [15].

Capacitance (F)	**Phenomenon**
10^{-12}	Bulk
10^{-11}	Minor, second phase
10^{-11} – 10^{-8}	Grain boundary
10^{-9} – 10^{-7}	Surface layer
10^{-7} – 10^{-5}	Sample-electrode interface
10^{-4}	Electrochemical reactions

In this thesis, AC EIS measurements are applied to a range of different materials and cells, including both solid- and liquid-based chemistries. For solid electrolytes, often Au was sputter coated onto either side of a solid pellet to act as thin Li^+ blocking electrodes. Li electrodes were also used to test the interfacial stability of the material against a Li anode. EIS measurements on battery cells were completed on assembled Swagelok, coin, or BAM cells, all containing a Li counter electrode. Generally, a Biologic VMP-300 potentiostat was used, although an MTZ-35 impedance analyser was used in Chapter 5, and VSP potentiostat was also used. A potential amplitude of between 10 – 40 mV was used given the high conductivity of most samples measured. In all instances the reference electrode was defined as the counter electrode in a 3-electrode set-up.

3.9 Cyclic Voltammetry

Cyclic voltammetry (CV) is a popular technique with which to probe electron transfer reactions within battery materials. For battery analysis, a linear potential is applied across the cell as a sweep back and forth between two defined voltages. The current response is recorded, which reflects which voltage thermodynamically favourable redox processes occur at in both the oxidation and reduction process, as shown in Figure 3.9a. Since the potential is swept across a range, CV allows the determination of reversibility in the redox process. This is shown in Figure 3.9b, where the oxidation peak is shifted to higher voltages and the peak current depressed for quasi-reversible processes. CV is therefore used to analyse the redox stability and the electron-transfer kinetics of materials [19]. The rate information about electron-transfer kinetics which can be gained from CV distinguishes it from the capacity analysis (Section 3.7) [13]. Furthermore, the degradation of such electron-transfer effects can be followed by employing a set number of voltage sweeps. The speed and versatility of CV has established it as a valuable tool for battery characterisation.

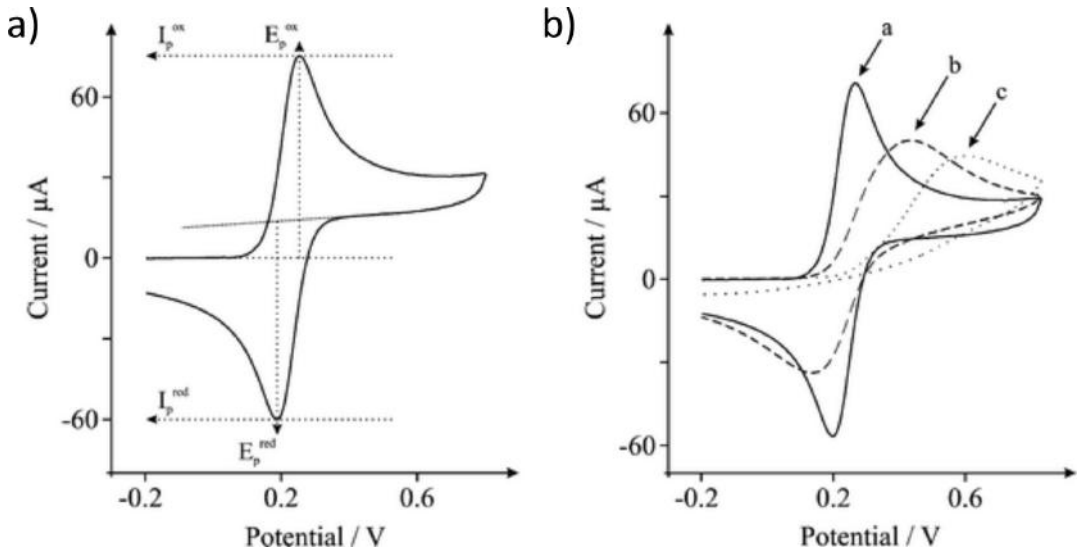

Figure 3.9: Typical cyclic voltammograms of the traditional "duck-billed" shape, showing (a) the peak positions E_p for the oxidation and reduction processes, and (b) how the reversibility of the electron transfer process affects the current response. *a* outlines a reversible process, *b* quasi-reversible, and *c* irreversible. Adapted and reused with permission from the Royal Society of Chemistry [20].

In the case of Li^+ half cells, as in this research, CV permits the analysis of the redox activity within the working electrode when reacting with Li^+. This allows the determination of a stable potential window where no decomposition occurs; such a window provides the voltage limits between which the material can be charged/discharged in a battery. This is particularly useful for new solid electrolyte materials. Furthermore, by altering the scan rate (in mV s^{-1}) of the applied voltage during a CV scan, the chemical diffusion coefficient of Li^+ (D_σ) can be obtained. The position of the oxidation

and reduction potential varies with the square root of the scan rate, according to the Randles-Secvik equation. A plot of I_p vs. scan rate will then yield a linear correlation. However, D_σ obtained by CV requires an estimation of the electrode surface area, which is notoriously difficult to obtain [21]. CV measurements in this work were completed using a 3-electrode set-up where Li was used as both the counter and reference electrode.

3.10 DC Polarisation

Direct current (DC) polarisation is an important tool to characterise both the ionic and electronic conductivity of solid materials [22]. While AC EIS is generally used to investigate the ionic conductivity through a sample, DC polarisation can be used to inform on the extent of the contribution from both ions and electrons. This is done by determining the fraction of mobile charge carriers and is particularly useful in materials which are primarily ionic conductors but show a degree of electronic conductivity, such as solid electrolytes.

When a DC potential is applied across a cell with a solid electrolyte between two electrodes, the charge carriers will migrate towards the electrode of their opposite charge. Generally, one ion-blocking and one non-blocking material are used as electrodes, although two blocking electrodes may also be used. This is called Wagner's method of DC polarisation [23]. When the potential is applied, there is a rapid spike in measured current as the charge carriers are polarised towards the electrodes. The current then decays rapidly towards zero as ionic movement through the blocking electrode is impeded. The residual current will generally level off at a non-zero value due to the movement of the electrons/holes in the system. As such, a material is not a perfect ionic conductor if the residual current is non-zero.

Since total conductivity is the sum of its ionic and electronic conductivity (Equation 3.20), the ionic transference number (t_{ion}) can be described as:

$$t_{\text{ion}} = \frac{\sigma_{ion}}{\sigma_e} = \frac{(I_i - I_f)}{I_i}, \tag{3.21}$$

where σ represents the conductivity, I_{i} is the initial current from the spike upon polarisation, and I_{f} is the residual current [22, 24]. This relationship is a consequence of the vastly different speed of conductivity for electrons and ions through a solid. Similarly, the electronic transference number (t_{e}), can be described as:

$$t_e = \frac{\sigma_e}{\sigma_{ion}} = \frac{I_f}{I_i}. \tag{3.22}$$

Thus, the smaller I_{f} is, the lower t_{e} is.

Generally, DC polarisation experiments employ multiple applied voltages on the same

cell, with a relaxation time in between steps. Equation 3.22 can then be employed to find the transference value at each potential; these can be averaged to improve precision. Importantly, any applied potential must be below the decomposition potential of the material under study. To estimate a material's electronic conductivity, Ohm's law can be used to find the resistance as the gradient of a straight line fitted to V vs. I_{f}. The geometrical properties of the specimen of interest can then be used in Equation 3.18 to determine the electronic conductivity. It is important to remember that ion-blocking electrodes do not show ideal behaviour, with interfacial transport effects and Li-Au alloying possible [25]. A residual current analysis therefore provides only an upper limit for electronic conductivity. In this thesis, DC polarisation measurements were completed in Swagelok cells under applied potentials between 0.3 – 1.2 V for 24 h each.

3.11 X-ray Photoelectron Spectroscopy

X-ray photoelectron spectroscopy (XPS) is a surface sensitive technique used to analyse chemical state and electronic structure. It can be used to identify the presence and chemical binding state of any element. The analysis depth of XPS is roughly 10 nm, yielding very surface sensitive information. However, ion sputtering can be used to gently drill into a sample to collect information from beneath the surface, meaning depth resolved XPS is possible if care is taken not to damage the sample.

The working principle of XPS is based on the photoelectric effect which was discovered by Heinrich Hertz in 1887. The photoelectric effect is a phenomenon whereby, when a material is illuminated by electromagnetic radiation, charged particles are released by the absorption of radiation of a particular energy (Figure 3.10). In the case of XPS, X-rays are used to illuminate a sample which will emit electrons of a measurable energy. Although X-ray penetration is much deeper than the analysis depth (given as ∼10 nm), the photoelectron escape energy limits the depth that information can be collected from. The Fermi level is defined as the surface level at a temperature of absolute zero through which no electrons will have enough energy to leave.

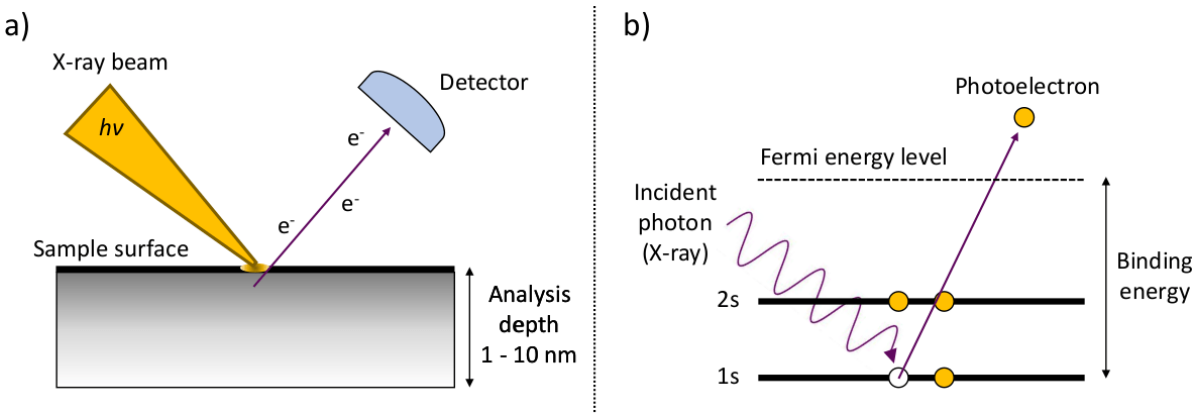

Figure 3.10: X-ray photoelectron spectroscopy (XPS) experiment showing (a) the analysis depth of an X-ray beam in XPS, and (b) the photoelectron effect, whereby a core level electron is emitted by the absorption of an incident photon.

According to the Planck-Einstein equation, the incident photon will possess energy $E = h\nu$, where h is Planck's constant and ν is frequency. By conservation of energy, the binding energy of a detected electron can be expressed as:

$$E_{binding} = h\nu - (\frac{1}{2}mv^2 + \varphi). \tag{3.23}$$

In this case, $\frac{1}{2}mv^2$ represents the kinetic energy of an emitted electrons and φ is the work function of the spectrometer [26]. The kinetic energy can be easily determined, and the work function is known, meaning the binding energy of a detected electron may be readily determined. An electron's binding energy is elementally dependent; the atomic orbital, oxidation state, and local environment all have an influence. A plot of photoelectron count against binding energy will display a spectrum of emission peaks. As each element has a specific set of binding energies, XPS may be used for compositional analysis and the determination of chemical states. Since an atom's electron arrangement will act to sightly alter the binding energy of core electrons, oxidation state can also be determined. Furthermore, the photoelectron count rate can also be used to directly quantify an element's concentration in the sample, or the abundance of a particular oxidation state. Thus, XPS can yield highly detailed composition and chemical state information from a sample surface. In this thesis, XPS measurements were collected using a monochromatic Al K_α X-ray source.

3.12 X-ray Absorption Spectroscopy

X-ray absorption spectroscopy (XAS) is a broadly applied technique through which local electronic structure and coordination environment can be analysed. When an X-ray is shone at a specimen it can be absorbed by a core energy level to either excite an electron to an unoccupied higher energy level or into the continuum (Figure 3.11c). This occurs if the

incoming radiation is equal to or above the binding energy of the core shell electron. The continuum is an unbound electron state outside the initial absorbent atom. Typically, the electrons excited are from the $1s$ or $2p$ orbitals, meaning that high energy X-ray radiation must be used (0.1 – 100 keV, known as hard X-rays). Therefore, while it was developed in a laboratory, XAS has been traditionally a synchrotron-based technique, although recent progress has been made towards lab-based XAS measurements [27]. Given the local region of study (∼Å level), a consequence of the short X-ray wavelength, the sample does not need to be crystalline or even solid phase, making XAS highly versatile. The hard X-rays used have a much higher penetration depth than for XPS, meaning the technique is mostly bulk sensitive. The elemental selectivity of X-rays allows the investigation of individual elements within a sample. The applications of XAS are vast and, as such, it has been applied across a multitude of research areas. Of further interest is the development of *operando* XAS measurements, which offer a valuable addition to the growing arsenal of *operando* methodologies available for battery research [28].

Unlike other X-ray techniques such as diffraction, XAS uses a spectrum of incident energy. Each element has specific energy limits at and above which the incident X-ray will be absorbed and core shell electrons will be excited. When the incident energy matches the absorption energy for a particular orbital there is a spike in absorption which is called the "edge jump". Different orbitals have different edge energies: the K edge for the $1s$ orbital, L edge for the $2s$ and $2p$ orbital, and M edge for the $3s$, $3p$, and $3d$ orbitals. A subscript is used to denote the difference between electrons within orbitals of the same principal quantum number. For example, L_1, L_2, and L_3 refer to the transitions from the $2s$, $2p_{1/2}$, and $2p_{3/2}$, respectively. During an XAS experiment, the incident X-ray energy is increased from below to above the edge energy of the particular element and edge of interest. Any edge may be used depending on the experimental goals.

There are three types of experimental configuration to collect a signal from XAS: transmission, fluorescence, and electron yield. Transmission is the most common sample geometry, where any attenuation in X-ray intensity must be due to absorption in the sample. This geometry is best for homogeneous and concentrated samples which can yield high quality data. Fluorescence occurs from the detection of photons which are emitted when an excited electron relaxes back to a lower energy level. Therefore, this mode is better suited to the study of samples which are more inhomogeneous, or the element of interest is dilute. The third mode, called the electron yield mode, measures the emitted photoelectrons produced from the sample. This mode is surface sensitive as the escape depth of photoelectrons is very low, such as described for XPS, while transmission and fluorescence are both bulk sensitive.

The attenuation of X-rays through a material is given by Beer's law:

$$I_t = I_0 \exp(-\mu(E)\, t), \tag{3.24}$$

where I_t and I_0 are the transmitted and initial X-ray intensities, respectively, t is the sample thickness, and $\mu(E)$ is the absorption coefficient. $\mu(E)$, which depends on the incident X-ray energy, is generally the most important parameter to extract from a typical XAS experiment. In transmission mode this can be simplified to:

$$\mu(E) = \ln(\frac{I_0}{I_t}). \tag{3.25}$$

This scenario is depicted in Figure 3.11a, which shows a simple example of the attenuation of an X-ray beam through a sample. Below the edge, when the incident energy is not high enough to be absorbed by a sample, μ(E) will remain unchanged: this is shown at low energy in Figure 3.11b. Near the absorption energy of the edge under investigation there is often a pre-edge peak which is caused by an unfavourable electron transition. Just above this energy the large edge jump occurs, this energy region is referred to as the X-ray Absorption Near Edge Structure (XANES) region. Above this energy is referred to as Extended X-ray Absorption Fine Structure (EXAFS). These regions are discussed in further detail below.

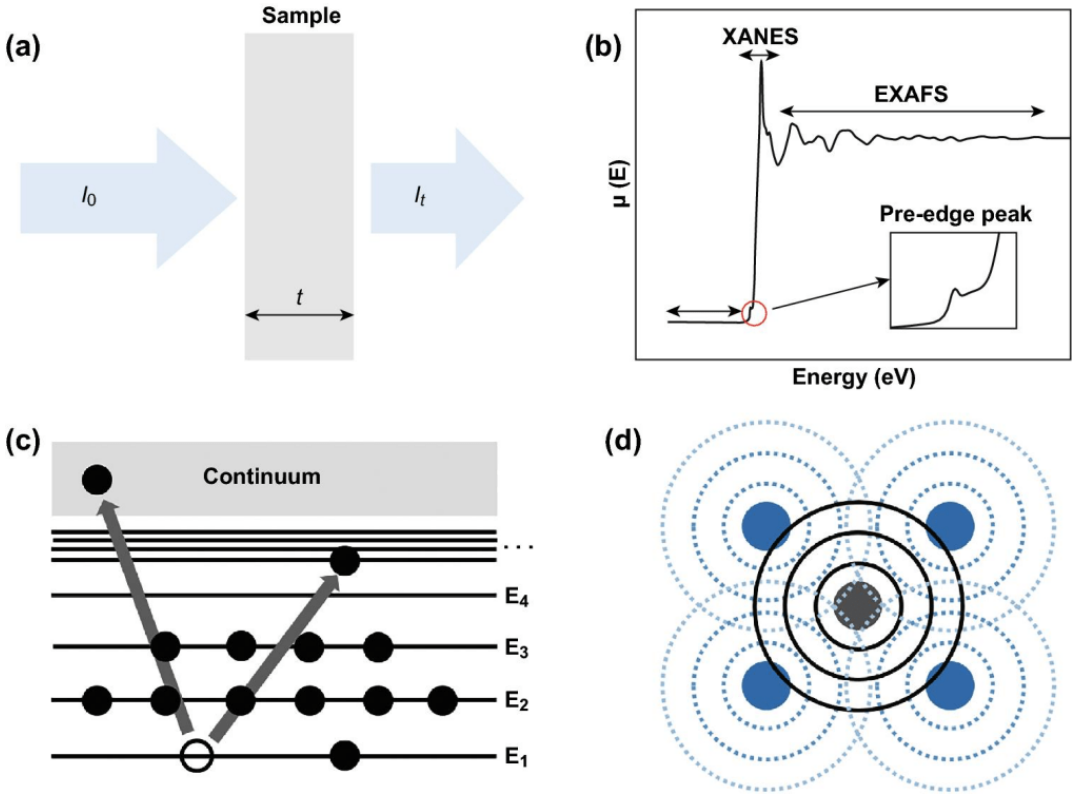

Figure 3.11: An XAS experiment. (a) Schematic of a transmission mode geometry showing the incident and transmitted X-ray beam. (b) A typical absorption spectrum against incident X-ray energy, including the pre-edge, XANES, and EXAFS regions. (c) Schematic of the X-ray absorption process and electron excited process. The black circles represent electrons. (d) Schematic of an interference pattern created by the outgoing (solid black lines) and reflected (dashed blue lines) photoelectron waves between absorbing atom (grey) and its nearest atoms (blue). Figure reproduced from Springer [29]. This work is licensed under CC BY 4.0.

3.12.1 XANES

The XANES region is generally defined as between 50 – 100 eV either side of the absorption edge, which includes the pre-edge. Since the edge is at a specific energy and an element's electron arrangement is affected by its valence, the XANES part of the spectrum affords information about the elemental oxidation states and electronic structure. For example, a high oxidation state results in more tightly bound core shell electrons, and thus the absorption energy of X-rays required to excite these electrons is shifted to slightly higher energies. This is reflected in the position of the absorption edge. By appropriate use of standard materials, the oxidation state of a specimen may be deduced through a visual, "fingerprinting", analysis of the XANES data only. This can be particularly useful in the case of samples with mixed elemental valence states, which will present as an absorption edge shape somewhere in between two standards with known oxidation state. A more quantitative analysis can be gained from linear combination fitting, which can provide the relative concentration of different species.

Further valuable information from the XANES region is held in the pre- and post-edge features. As the name pre-edge would suggest, this effect can arise from the excitation of core electrons to less energetic orbitals, such as from s to d in transition metals. This transition is generally forbidden by the dipole selection rule, although can become partially allowed by effects such as $3d/4p$ orbital mixing or a deviation from centrosymmetry. As such, non-centrosymmetric coordination geometries often show more defined pre-edge features. The XANES region can also include multi-scattering features from above the edge energy due to the detection of low-energy photoelectrons from near the surface. This can be used to detect subtle changes in molecular geometry which may not be apparent in the EXAFS region.

3.12.2 EXAFS

The EXAFS region is the fluctuations in the absorption coefficient at energies roughly between 100 – 1000 eV above the XANES region. Generally, an oscillating signal is received as a result of the interactions of backscattered photoelectrons emitted from the target atom into the continuum (Figure 3.11d). The EXAFS region provides information about the surrounding atoms in a specimen and not just the absorbent atom. Atomic bond lengths and the concentration/type of neighbouring species can be obtained. The scattering effect will unavoidably create an interference pattern; data fitting, rather than a visual analysis, is thus necessary to obtain structural information. When emitted and backscattered electrons interfere constructively, the wavefunction can increase to produce a peak in the EXAFS profile, and *vice versa* for destructive interference. This produces the oscillatory pattern typical of an EXAFS region.

To analyse the EXAFS profile, a fine-structure parameter ($\chi(E)$) can be used, defined

as:

$$\chi(E) = \frac{\mu(E) - \mu_0(E)}{\Delta\mu_0(E)}, \tag{3.26}$$

where μ_0(E) is a smooth background function. This background is evaluated as the edge position for a generated photoelectron from a singular atom which is not modulated. The X-ray energy data is commonly transformed to k-space, where k represents the wavefunction of the photoelectron, which can be expressed as:

$$k = \sqrt{\frac{2m(E - E_0)}{\hbar}^2}, \tag{3.27}$$

where m is the electron mass, E is energy, E_0 is the absorption edge energy, and ħ is the reduced Planck constant ($h/2\pi$). To describe the oscillations, $\chi(k)$ can then be defined by what is sometimes known as the EXAFS equation, as:

$$\chi(k) = \sum_j \frac{N_j f_j(k) \exp(-2k^2\sigma_j^2) \exp(\frac{2R_j}{\lambda(k)})}{kR_j^2} \sin[2kR_j + \delta_j(k)]. \tag{3.28}$$

In Equation 3.28, N is the number of atoms surrounding atom j, $f_j(k)$ and $\delta(k)$ relate to the scattering properties of surrounding atoms, R is the distance from the surrounding atom to atom j, σ is the Debye-Waller factor and λ is the mean free path of photoelectrons. During data processing, k may be weighted by an integer power (usually between 1 and 3) to amplify features at a high wavenumber. Once a good fit to the data is obtained, $\chi(k)$ can be Fourier transformed to separate the frequency-dependent oscillations. As $\chi(k)$ is a combination of multiple unique photoelectron scattering paths from the surrounding atoms of the absorbent atom, the radial distance between the absorbing atom and its surrounding coordination shells can be resolved. This allows a high resolution of local atomic structure which decreases in quality with a rate proportional to $1/R^2$. As a result, the coordination environment below ~5 Å from the absorbent atom can generally be well defined, whereas most features at higher length scales cannot be resolved as accurately.

The XAS data in this thesis were collected from both the Rock beamline at SOLEIL, France, and the quick B18 beamline at Diamond, UK. Transmission and fluorescence modes were both employed. Samples were mixed in appropriate quantities with cellulose to avoid saturating the detectors, while both the XANES and EXAFS data was analysed across both experiments. The Demeter software package was used for data analysis [30].

3.13 Muon Spin Relaxation

To avoid repetition with the review article in Chapter 2, pieces of information about the μSR technique, such as the technique background, muon production and decay, experi-

mental basics, and material properties are omitted here. Instead, this section will focus on polarisation functions, the fast Fourier transform, and *operando* methodologies.

3.13.1 Polarisation functions

Detecting ionic motion using μSR by necessity corresponds to a dynamical field at the muon site. In this thesis, the dynamic contribution is assumed to be a result of ionic motion, although care must be taken to ensure it is not actually a consequence of magnetic fluctuations or muon diffusion. Therefore, an understanding of the magnetic properties of the system are important during data analysis, and electrochemical measurements can be used to corroborate the ionic diffusion properties to aid in identifying any contribution from muon diffusion. To evaluate a function which models dynamical behaviour at the muon site, the static Kubo-Toyabe function can be modified to a dynamicized version. The Kubo-Toyabe function in the static, zero-field limit, given in Chapter 2 (Equation 2.6), is redefined here as:

$$P_z^s(t) = \frac{1}{3} + \frac{2}{3}(1 - \Delta^2 t^2)\exp(-\frac{\Delta^2 t^2}{2}), \tag{3.29}$$

for clarity. In Equation 3.29, $P_z{}^s(t)$ is the static polarisation function, Δ is the static field distribution width, and t is time. For a dynamic situation it can be adapted by modelling a stationary Gaussian-Markovian process [31]. This assumes that the dynamic process acts to change the local static field at the muon site to a new value; this change can be evaluated either as a series of rapid changes or a continuous variation. Both follow similar derivations. The scenario which assumes a series of rapid changes will be evaluated here using a strong collision model where the local field of a muon is suddenly changed upon Li^+ ion diffusion [32]. This event causes an effective resetting of the muon precession process, for which the probability can be described as ν, the field fluctuation rate. This is shown in Figure 3.12e, where $\nu = 0$ corresponds to the static Kubo-Toyabe (KT) relaxation function in zero-field.

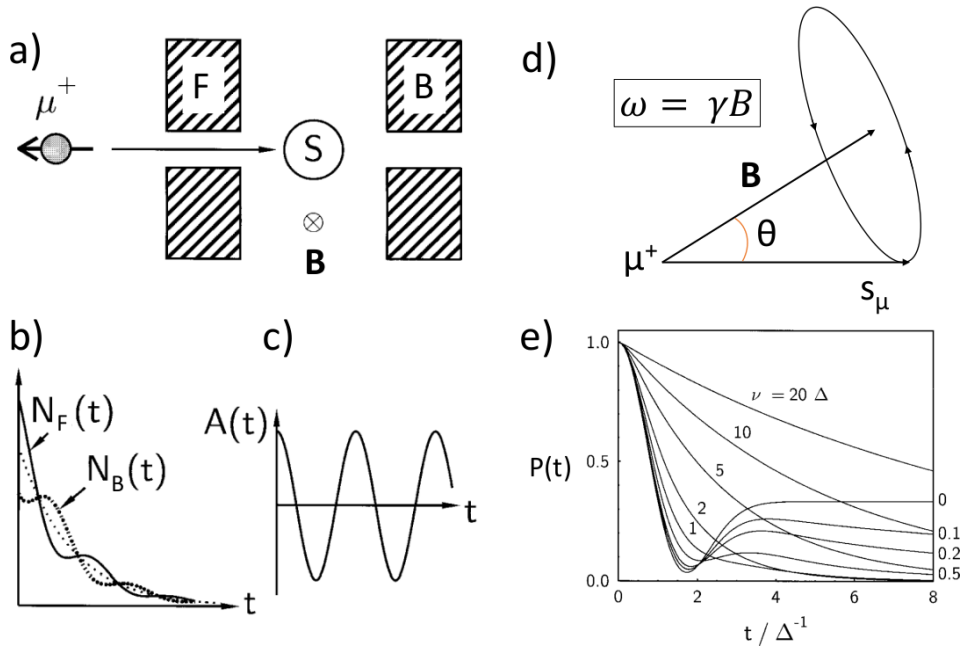

Figure 3.12: Various aspects of a μSR experiment. (a) Experimental schematic showing a spin polarised muon (μ^+) being implanted into a sample (S), in between forward and backward detectors (F, B) in a magnetic field B. (b) The number of detected positrons in each detector. (c) The asymmetry function in a transverse applied field. (d) Larmor precession of a muon spin around an applied field at an angle ϑ. (e) The transition from the static to the dynamic Gaussian Kubo-Toyabe function for *P(t)* vs. *t*. The shape of the dynamic function is largely dependent on the field fluctuation rate, ν. Figure adapted and reproduced with permission from Taylor and Francis [33].

In the slow dynamic limit, it is the relaxation at higher timescales (≥3 μs) which is influenced, while the initial relaxation is unaffected. In the fast limit the full relaxation in asymmetry is affected, which generally leads to an exponential relaxation in polarisation. This is often the case for energy materials. Such limits set the boundaries on the rate of ionic motion which can be resolved using μSR, whereby diffusion rates above $\sim 10^{-8}$ cm^2 s^{-1} act to flip the muon spin too regularly to be precisely resolved, and diffusion rates below $\sim 10^{-13}$ cm^2 s^{-1} do not flip the spin often enough to reflect a change in the asymmetry function inside the muon lifetime.

To modify the static KT function shown in Equation 3.29 for dynamic fluctuations, the polarisation function ($P_z(t)$) can first be described as a sum of contributions ($R_{z,\,l}(t)$). Each contribution refers to a muon which has experienced l field changes in the time interval between 0 and t. The polarisation function can then be given as:

$$P_z(t) = \sum_{l=0}^{\infty} R_{z,l}(t). \tag{3.30}$$

If the probability that the local field has not changed between time 0 and t is $\exp(-\nu t)$, then the first contribution ($l = 0$) can be written in terms of the static polarisation

function as:

$$R_{z,0}(t) = P_z^s(t)\exp(-\nu t). \tag{3.31}$$

Thus, it is possible to describe subsequent contributions as:

$$R_{z,l+1}(t) = \nu \int_0^t R_{z,l}(t-t')R_{z,0}(t')\,dt'. \tag{3.32}$$

By a combination of these Equations 3.30 – 3.32, it follows that the dynamic polarisation function is:

$$P_z(t) = P_z^s(t)\exp(-\nu t) + \nu \int_0^t P_z(t-t')R_z^s(t')\exp(-\nu t')\,dt'. \tag{3.33}$$

Equation 3.33 relates the static to the dynamic polarisation function. Although some progress can be made by solving Equation 3.33 analytically, it is more common to solve this numerically, especially when toward the fast limits in dynamics, as is expected in energy materials. The transition of the static to the dynamic Kubo-Toyabe relaxation is shown graphically to depend on ν in Figure 3.12e. In the static function, when $\nu = 0$, there is a fast relaxation before a recovery to around 1/3 of the initial polarisation value. This can be understood by considering the initial direction of magnetic fields within a sample which, if randomly orientated, will point in the same direction as the initial muon spin in roughly 1/3 of the cases. Initially, all directions will dephase from one another as the muon spin begins to precess, before the polarisation will recover to a value of 1/3 if in the presence of static fields. This can be understood by considering the muon spin as dephased in only two axis directions, rather than all three. For slow diffusion events ($\nu \approx 0.2\Delta$), the effect appears to be a relaxation of the 1/3 tail of the polarisation (Figure 3.12e). This principle is regularly used to describe experimental data in this thesis.

While Equation 3.33 represents the polarisation function in zero-field, this can be easily adapted to the longitudinal field scenario. Longitudinal fields are generally applied to weakly dephase the muon from its local environment in one direction. This acts to decrease the relaxation in the asymmetry profile. By fitting a polarisation function across three fields, generally zero field and two weakly applied longitudinal fields of different strengths, the parameters of interest can be accurately constrained to reflect the dynamic contribution to the spin relaxation. In the longitudinal field scenario, the polarisation function now also depends on the magnetic field, B_0. In the fast fluctuation limit the polarisation thus becomes an exponential relationship described as:

$$P_z(t) = \exp(-\lambda t), \tag{3.34}$$

where λ is the relaxation rate. λ can then be given as:

$$\lambda = \frac{2\Delta^2\nu}{\nu^2 + \gamma_\mu^2 B_0^2}, \tag{3.35}$$

where γ_μ is the gyromagnetic ratio of the muon. Equation 3.35 illustrates the dependence of the relaxation rate on the rate of dynamical events near the muon site. This scenario corresponds to a Lorentzian decay of the polarisation function in an applied field.

To evaluate dynamics as a continuously changing magnetic field near the muon site, the polarisation function in a transverse field ($P_x(t)$) can be analysed. This scenario is different from the relaxation in zero field as only one component perpendicular to the magnetic field direction contributes to the muon spin relaxation, rather than two in zero field. The precession frequency depends on the local field and not on the angle between the field and the muon spin. This can be described as the Abragam function which is given in Chapter 2 (Equation 2.7). In this instance, the correlation time is evaluated, given as the average time between fluctuations such that $\nu^{-1} = \tau$. In the slow limit, where ν approaches zero ($\nu \rightarrow 0$), an exponential term can be removed such that the polarisation function is described by:

$$P_x(t) = \exp(-\frac{\Delta^2 t^2}{2}) \cos(\gamma_\mu B_0 t), \tag{3.36}$$

This corresponds to a scenario where the muon spin would be expected to precess multiple times around the local field (defined as Δ/γ_μ) before a fluctuation occurs due to ionic diffusion. In the opposite scenario, the fast diffusion limit ($\nu t \gg 1$), the polarisation function is seen to be very similar to the longitudinal field case but with a cosine oscillation, described as:

$$P_x(t) = \exp(-\lambda t)\cos(\gamma_\mu B_0 t). \tag{3.37}$$

In this case, the relaxation rate can be given as:

$$\lambda = \frac{\Delta^2}{\nu} = \Delta^2 \, \tau, \tag{3.38}$$

where λ clearly depends heavily on the local field distribution. In the asymmetry profile of a transverse field experiment, a fast dynamic process acts to rapidly dampen the envelope of the oscillating signal. One advantage of the transverse field environment is that the muonium signal can be removed from the data because of its much larger gyromagnetic ratio, which acts to increase the amplitude of the local field near the muon site.

3.13.2 Fast Fourier transform

A fast Fourier transform (FFT) is an algorithm which uses discrete Fourier transforms to express complex time domain data in frequency space. The algorithm allows the simplification of a Fourier transform range so that the number of computations is reduced by several orders of magnitude [34]. This is done by factorising a matrix of discrete transforms into a separate matrix where most of the components are zero. As such, the speed of computation is vastly improved.

A Fourier transform of a complex function can be described as:

$$F(\xi) = \int_{-\infty}^{\infty} f(x) \exp(-2\pi j x \xi)\, dx, \tag{3.39}$$

where *f(x)* represents a complex function depending on time x and $F(\xi)$ represents the function depending on frequency ξ. Programs such as Mantid can perform these transforms during data analysis to convert experimental data in seconds. This can be particularly useful to distinguish separate features when there are multiple contributing factors to the muon spin relaxation. For example, a FFT can be used to distinguish different muon precession contributions in a two-phase or inhomogeneous material, as is shown in Chapter 5.

3.13.3 *Operando* methodologies

The primary goal of this research is to develop working methodologies for the *operando* investigation of ionic diffusion in functioning batteries. To successfully complete such experiments there are several factors which must be considered that are not relevant for traditional powdered sample measurements. *Operando* experiments are non-trivial; the dynamical contribution to the muon spin must be extracted from a battery containing many different materials. While most of the features can be distinguished during data analysis, the crucial aspect is in the cell/experimental design. The optimisation of cell design will result in a configuration which maximises the dynamic signal of interest and ensures any other signal may be treated as background.

To complete such *operando* μSR experiments, a custom cell holder is required to suit the properties of the technique. In this thesis, the cell is referred to as the Battery Analysis by Muon (BAM) cell, which is described in Chapter 6. For *operando* μSR experiments, one must consider the full length scale of operation: this is outlined in Figure 3.13. Fundamentally, the muon is sensitive to magnetic field effects at the atomic level inside the unit cell of material. This means that the muon spin contains information about only locally residing magnetic moments, both static and dynamic. An understanding of the muon site within the unit cell therefore helps to characterise the diffusion processes.

At the μm scale, the experimenter must consider the region of muon implantation

within the cell. Muon implantation can be understood as volume-averaged over all materials in the cell; for a working battery cathode this will likely include binder, carbon, active material, and electrolyte. To obtain the best possible signal it is then desirable to maximise the ratio of muons implanted in the active material over the muons implanted in other parts of the cell. This can be done by increasing the fraction of active material, decreasing the fraction of other components, or attempting to remove some components entirely (such as the binder). The cell additives, electrolyte, and cell body should be selected as materials which do not allow ionic motion in the timescale probed by the muon, and ideally do not contain magnetic elements.

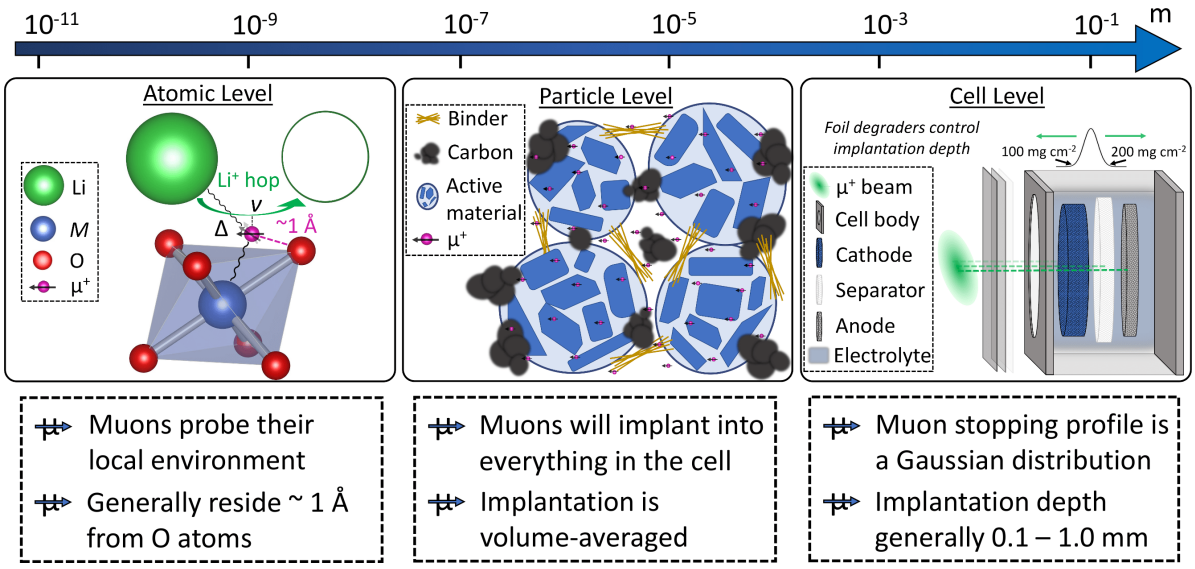

Figure 3.13: Depiction across length scales of how muons would be used to study a typical Li-ion battery. Produced to reflect the conditions on the EMU spectrometer at the ISIS Neutron and Muon Source.

Finally, at the macroscopic level, the penetration depth of the muon ensemble should be carefully managed. On EMU, this is given as a range curve for a Gaussian distribution of penetration depth from 100 – 200 mg cm^{-2}. This can be controlled using foil degraders in front of the cell or different current collector thicknesses. The muon ensemble is dilute; around 2000 muons are implanted every pulse across a range between 0.1 – 1.0 mm in thickness. This depth range predicates the desirability of a thick electrode to ensure adequate muon implantation in the active material. The cell design should consider all these areas without compromising on electrochemical performance.

This is specific to pulsed sources, since continuous muons sources implant muons individually, affording a greater depth penetration control. While this has applications for certain battery materials, the specialist timing control means far fewer muons are implanted. On the contrary, at a pulsed source, the detection of positrons is timed from the arrival of the pulse as time zero. As pulsed sources implant far more muons they afford far higher statistics data, which is preferable for ionic diffusion experiments.

3.13.4 Cell assembly

Specific cell assembly methods are required to ensure the reliable operation of the BAM cell. The cell is designed for glovebox assembly using air sensitive battery components. Figure 3.14 displays photos of the BAM cell components and how they are assembled. Further detail on the cell and its assembly procedures are given in Chapters 6 and 7. In this thesis, μSR measurements were all performed on the EMU spectrometer at ISIS Neutron and Muon Source, UK.

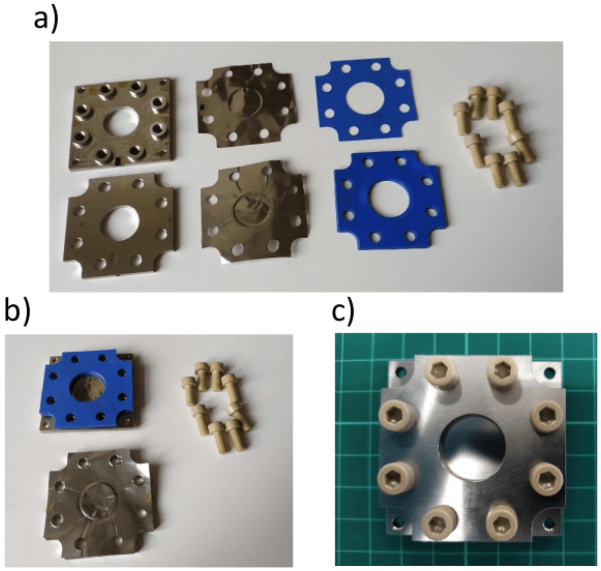

Figure 3.14: Photos of the Battery Analysis by Muon (BAM) cell. (a) Deconstructed cell showing the holder top and bottom, current collectors, fluorosilicone gaskets, and PEEK screws. (b) Half-assembled cell. (c) A fully assembled BAM cell as viewed from above.

References

[1] A. R. West. *Basic Solid State Chemistry*, volume 2. Wiley and Sons, 1999.

[2] A. E. Danks, S. R. Hall, and Z. Schnepp. The evolution of 'sol-gel' chemistry as a technique for materials synthesis. *Mater. Horiz.*, 3:91–112, 2016.

[3] H. Yamada, T. Ito, and R. Hongahally Basappa. Sintering Mechanisms of High-Performance Garnet-type Solid Electrolyte Densified by Spark Plasma Sintering. *Electrochimica Acta*, 222:648–656, 2016.

[4] S. Baek, J. Lee, T. Y. Kim, M. Song, and Y. Park. Garnet related lithium ion conductor processed by spark plasma sintering for all solid state batteries. *J. Power Sources*, 249:197–206, 2014.

[5] O. Guillon, J. Gonzalez-Julian, B. Dargatz, T. Kessel, G. Schierning, J. Räthel, and M. Herrmann. Field-Assisted Sintering Technology/ Spark Plasma Sintering: Mechanisms, Materials, And Technology Developments. *Adv. Eng. Mater.*, 16:830–849, 2014.

[6] C. Magnus and W. M. Rainforth. Influence of sintering environment on the spark plasma sintering of Maxthal 312 (nominally-Ti_3SiC_2) and the role of powder particle size on densification. *J. Alloys Compd.*, 801:208–219, 2019.

[7] C E J Dancer. Flash sintering of ceramic materials. *Mater. Res. Express*, 3:102001, 2016.

[8] Y. Liu, Q. Sun, , D. Wang, K. Adair, J. Liang, and X. Sun. Development of the cold sintering process and its application in solid-state lithium batteries. *J. Power Sources*, 393:193–203, 2018.

[9] H. Rietveld. A profile refinement method for nuclear and magnetic structures. *Acta Crystallogr.*, 20:508–513, 1966.

[10] B. H. Toby and R. B. Dreele. GSAS-II: the genesis of a modern open-source all purpose crystallography software package. *J. Appl. Cryst.*, 46:544–549, 2013.

[11] B. Inkson. 2- Scanning electron microscopy (SEM) and transmission electron microscopy (TEM) for materials characterization. *Mater. Charact. Using Nondestruct. Eval. Methods*, pages 17–43, 2016.

[12] P. Hovington, V. Timoshevskii, S. Burgess, H. Demers, P. Statham, R. Gauvin, and K. Zaghib. Can We Detect Li K X-ray in Lithium Compounds Using Energy Dispersive Spectroscopy. *Scanning*, 38:571–578, 2016.

[13] T. Kim, W. Choi, H. C. Shin, J. Y. Choi, J. M. Kim, M. S. Park, and W. S. Yoon. Application of Voltammetry in Lithium Ion Battery Research. *J. Electrochem. Sci. Technol.*, 11:14–25, 2020.

[14] J. M. Amanor-Boadu and A. Guiseppi-Elie. Improved Performance of Li-ion Polymer Batteries Through Improved Pulse Charging Algorithm. *Appl. Sci.*, 10:895, 2020.

[15] J. T. S. Irvine, D. C. Sinclair, and A. R. West. Electroceramics: Characterization by Impedance Spectroscopy. *Adv. Mater.*, 2:132–138, 1990.

[16] S. Wanga, J. Zhang, O. Gharbi, V. Vivier, M. Goo, and M. E. Orazem. Electrochemical impedance spectroscopy. *Nat. Rev. Methods Primers*, 41:1–21, 2021.

[17] R. J. D. Tilley. Defect Crystal Chemistry. *Blackie and Son Ltd., London*, 1987.

[18] J. Popovic. Chemistry of Soft Matter Battery Electrolytes. *EIBC*, 2019.

[19] N. Elgrishi, K. J. Rountree, B. D. McCarthy, E. R. Rountree, T. T. Eisenhart, and J. L. Dempsey. A Practical Beginner's Guide to Cyclic Voltammetry. *J. Chem. Educ.*, 95:197–206, 2018.

[20] D. A. C. Brownson, D. K. Kampouris, and C. E. Banks. Graphene electrochemistry: fundamental concepts through to prominent applications. *Chem. Soc. Rev.*, 41:6944–6976, 2012.

[21] J. Sugiyama, K. Mukai, M. Harada, H. Nozaki, K. Miwa, T. Shiotsuki, Y. Shindo, S. R. Giblin, and J. S. Lord. Reactive surface area of the $li_x(co_{1/3}ni_{1/3}mn_{1/3})o_2$ electrode determined by μ^+sr and electrochemical measurements. *Phys. Chem. Chem. Phys.*, 15:10402, 2013.

[22] R. C. Agrawal. DC Polarisation: An experimental tool in the study of ionic conductors. *Indian J. Pure Appl. Phys.*, 37:294–301, 1999.

[23] J. B. Wagner and C. Wagner. Electrical Conductivity Measurements on Cuprous Halides. *J. Chem. Phys.*, 26:1597, 1957.

[24] M. Hema, S. Selvasekarapandian, D. Arunkumar, A. Sakunthala, and H. Nithya. FTIR, XRD and ac impedance spectroscopic study on PVA based polymer electrolyte doped with $NH4_X$ (X = Cl, Br, I). *J. Non-Cryst. Solids*, 355:84–90, 2009.

[25] F. Aguesse, W. Manalastas, L. Buannic, J. M. Lopez del Amo, G. Singh, A. Llordés, and J. Kilner. Investigating the Dendritic Growth during Full Cell Cycling of Garnet Electrolyte in Direct Contact with Li Metal. *ACS Appl. Mater. Interfaces*, 9:3808–3816, 2017.

[26] M. H. Engelhard, T. C. Droubay, and Y. Du. X-Ray Photoelectron Spectroscopy Applications. *Encyclopedia of Spectroscopy and Spectrometry*, pages 716–724, 2013.

[27] P. Zimmermann, S. Peredkov, P. M. Abdala, S. DeBeer, M. Tromp, C. Müller, and J. A. can Bokhoven. Modern X-ray spectroscopy: XAS and XES in the laboratory. *Coord. Chem. Rev.*, 423:5213466, 2020.

[28] P. Ghiga and E. Quartarone. Operando x-ray absorption spectroscopy on battery materials: a review of recent developments. *J. Phys. Energy*, 3:032006, 2021.

[29] M. Wang, L. Árnadóttir, Z. J. Xu, and Z. Feng. In Situ X-ray Absorption Spectroscopy Studies of Nanoscale Electrocatalysts. *Nano-Micro Lett.*, 11:47, 2019.

[30] B. Ravel and M. Newville. ATHENA, ARTEMIS, HEPHAESTUS: data analysis for X-ray absorption spectroscopy using IFEFFIT. *J. Synchrotron Rad.*, 12:537–541, 2005.

[31] R. S. Hayano, Y. J. Uemura, J. Imazato, N. Nishida, T. Yamazaki, and R. Kubo. Zero- and low-field spin relaxation studied by positive muons. *Phys. Rev. B*, 20:850–859, 1979.

[32] S. J. Blundell, R. De Renzi, T. Lancaster, and F. L. Pratt. *Muon Spectroscopy: An Introduction.* Oxford University Press, 2021.

[33] S. J. Blundell. Spin-polarized muons in condensed matter physics. *Contemporary Physics*, 40:175–192, 1999.

[34] H. J. Nussbaumer. *The Fast Fourier Transform*, volume 2. Springer, Berling, Heidelberg, 1981.

Research Article

In Situ Diffusion Measurements of a NASICON-Structured All-Solid-State Battery Using Muon Spin Relaxation

Innes McClelland, Samuel G. Booth, Hany El-Shinawi, Beth I. J. Johnston, Jasmin Clough, Weimin Guo, Peter J. Baker, Edmund J. Cussen, Serena A. Corr

[I. McClelland, S. G. Booth, H. El-Shinawi, B. I. J. Johnston, W. Guo, E. J. Cussen, P. J. Baker, and S. A. Corr. *In Situ* Diffusion Measurements of a NASICON-Structured All-Solid-State Battery Using Muon Spin Relaxation. *ACS Appl. Energy Mater.*, 2021, 4:1527-1536.]

Abstract

In situ muon spin relaxation is demonstrated as an emerging technique that can provide a volume-averaged local probe of the ionic diffusion processes occurring within electrochemical energy storage devices as a function of state of charge. Herein, we present work on the conceptually interesting NASICON-type all-solid-state battery $LiM_2(PO_4)_3$, using M = Ti in the cathode, M = Zr in the electrolyte, and a Li metal anode. The pristine materials are studied individually and found to possess low ionic hopping activation energies of ∼50 – 60 meV and competitive Li^+ self-diffusion coefficients of $\sim 10^{-10} - 10^{-9}$ cm^2 s^{-1} at 336 K. Lattice matching of the cathode and electrolyte crystal structures is employed for the all-solid-state battery to enhance Li^+ ion diffusion between the components in an attempt to minimise interfacial resistance. The cell is examined by *in situ* muon spin relaxation, providing the first example of such ionic diffusion measurements. This technique presents an opportunity to the materials community to observe intrinsic ionic dynamics and electrochemical behaviour simultaneously in a non-destructive manner.

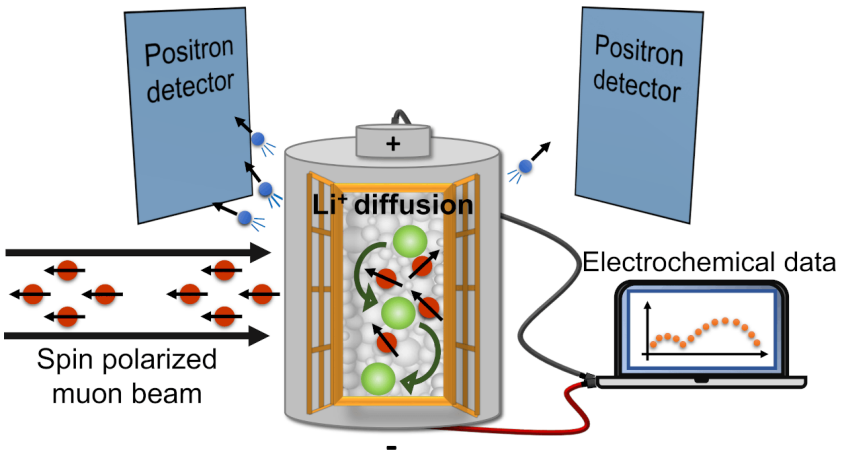

Graphical abstract. How μSR can be used to probe batteries *in situ*.

Introduction

As the electric vehicle market expands rapidly, the social and economic importance of improved energy storage devices grows concurrently, thus proving vital the utilisation of next-generation technologies such as solid-state-batteries (SSBs) [1]. The benefits of SSBs are well-established: increased safety (removal of flammable organic solvent), an enhanced potential window, extended cycle life and stability against a Li metal anode [2–5]. However, serious challenges, such as large interfacial resistances, scalability, chemical stability, low ionic conductivity, and dendritic growth remain prevalent [6–9]. Material development remains crucial and commercial uptake demands SSBs possessing excellent ionic diffusivity through the bulk and across chemically stable interfaces between the components to function efficiently.

Problematic tendencies of SSBs include abrupt short-circuits during cycling, regularly manifested through electrolyte cracking or inadequate electrode wetting which can lead to the deterioration of electrical contact. These mechanisms are linked to electrode volume change on charge/discharge which can induce significant internal strain, especially at interfaces [10, 11]. Deleterious interfacial strain has previously been linked to increased resistances and capacity fade and has also been known to increase with variable current densities and at certain discharge states within SSBs [12, 13]. Indeed, poor electrical contact caused by interfacial strain often accentuates an uneven current distribution which can expedite a short-circuit [2, 14]. On the cathode/electrolyte boundary, methods such as lattice matching [15], which involve pairing structurally similar electrolytes/electrodes, have been employed in an attempt to harmonise ionic diffusion pathways across interfacial regions and minimise resistance [16], whilst thin buffer layers have been used for the anode/electrolyte boundary [17]. Control over both the anode and cathode interfacial areas is crucial for battery performance; especially for long-term cyclability [15, 17]. A further challenge for solid electrolytes is that of ionic conductivity, a process generally governed by defect/vacancy concentration and distribution. Diffusion is often hindered by rigid crystalline electrolytes and consequently slower ionic conductivities are commonplace in comparison to liquid electrolytes [2, 4, 18].

Ceramic NASICON-structured $LiZr_2(PO_4)_3$ (LZP) has been investigated previously as a

potential solid-state electrolyte due to its fast ionic conductivity, high upper working voltage limit (up to 5.5 V vs. Li^+/Li), and air stability [17, 19]. The phosphate structure provides an open three-dimensional diffusion framework with large cavity sizes which can enhance Li^+ mobility [20–22]. However, difficulties using conventional sintering methods to obtain dense forms of the fast ionically-conducting α-type phase at room temperature have limited progression [15]. LZP possesses complex polymorphism: only the stabilised rhombohedral α-type phase (space group $R\bar{3}c$) and not the β-type polymorph is suitable for use as a solid electrolyte, displaying ionic conductivities of $\geq 1\times10^{-4}$ S cm^{-1} [15, 17, 23]. The triclinic α-type phase (space group $C\bar{1}$) which is generally present at room temperature displays low ionic conductivities ($\approx 10^{-8}$ S cm^{-1}), only transitioning to the rhombohedral phase at around 50 °C [24]. Within the rhombohedral phase Li^+ occupies disordered tetrahedral 36*f* sites located near 6*b* (M1) sites, with Li^+ ion conduction occurring *via* hops between these sites [21]. It was previously believed that only a single 36*f* site around a 6*b* site was occupied by a Li atom; however Noda *et al.* have recently shown that double occupancy is possible when both Li^+ ions locate further from the centre of the 6*b* site, and that diffusion occurs *via* a pushing-out and repulsion mechanism [19].

Dopant atoms such as Ti, Ge, and Al have previously been used to stabilise the rhombohedral phase at room temperature and enhance ionic conductivity, yet often do so at the expense of enlarged interfacial impedances due to the reducible oxidation state of some of the doped cations against Li metal [25–29]. Dopants have also been reported to increase interfacial resistances between the cathode and electrolyte and, therefore, their avoidance is preferable for lattice matching [16]. When LZP is placed in contact with Li metal a passivating interphase consisting of Li_3P and Li_8ZrO_6 forms, and the stable oxidation state of the Zr^{4+} cation against this layer provides chemical stability [5, 15, 30]. $LiTi_2(PO_4)_3$ (LTP) offers an improved Li^+ ion conductivity over LZP as a consequence of the suitability of the diffusion channels provided by Ti's apt ionic radius (the ionic radii of Ti^{4+} and Zr^{4+} are 60.5 and 72.0 pm, respectively) which permits facile Li^+ movement between the two possible Li^+ ion sites. The diffusion pathway is referred to as the M1-M2-M1 channel, where the bottleneck size between metal ions is crucial for rapid diffusivity. [22, 25, 31, 32]. However, the reactivity of LTP against Li metal combined with the variable Ti^{3+}/Ti^{4+} redox couple suggests suitability as an electrode material [15, 19].

Muon spin relaxation spectroscopy (μSR) implants spin polarized, positively charged muons within a target material to act as a local probe [33]. Once embedded, the evolution of the muon spin direction is affected by any magnetic fields it experiences, before decaying with an average lifetime of 2.2 μs into two neutrinos and a positron. Importantly, the positron is emitted preferentially along the direction of the muon spin at the time of decay. The magnetic environment which influences the muon spin includes any externally applied magnetic field, the fluctuating electronic fields from paramagnetic ions present, and any nuclear dipole fields present within the sample, both static and dynamic. Thus, muons probe ionic fluctuations on a length-scale of only a few unit cells and at a time-scale dependent on the frequency of Larmor precession due to the magnetic field they experience. By following the time-dependant progression of the count rate asymmetry of daughter positrons, $A(t)$, between detectors on opposite sides of the sample, the muon's local magnetic environment can be inferred. The externally applied

magnetic field can be used to isolate the contribution to the received signal from any moving nuclear dipole fields of diffusing species, and consequently key ionic diffusion parameters can be elucidated [33, 34]. μSR has been proven as a reliable and reproducible probe of the mobility of various ions (such as Li^+, Na^+ and I^-) on a time scale of 10^{-5} – 10^{-8} s [35–47]. Given recent successes on the study of isolated materials, the possibility of *in situ* diffusion measurements using μSR represents an enticing opportunity to directly track ionic dynamics within batteries as a function of state of charge. Furthermore, the non-destructive nature of the technique means that intrinsic material properties and electrochemical behaviour can be followed simultaneously without interference. This microscopic insight can be coupled with complementary macroscopic information from various electrochemical techniques to link phenomena observed from multiple viewpoints to the performance of functioning cells.

Herein, we report on the diffusion characteristics of pristine LZP and LTP using non-destructive temperature dependant muon spin relaxation (μSR). We also report, for the first time, the use of *in situ* μSR to follow the diffusivity behaviour within the solid electrolyte of an all-solid-state Li | LZP | LTP cell as a function of discharge voltage, reaching low potentials to follow the point of cell failure.

Experimental

Synthesis and Characterisation

LZP, LTP and an Li | LZP | LTP solid-state battery cell were synthesised and prepared using the procedures described previously by our group and El-Shinawi *et al.* [15, 48]. High calcination temperatures of 1100 °C for 50 minutes and rapid quenching to room temperature were used to obtain pure α-type phase LZP. LTP was synthesised using a similar sol-gel procedure to LZP, but instead lower calcination temperatures of 550 °C and an increased dwell time of 24 hours was employed. Powder X-ray diffraction (PXRD) characterisation of the samples was performed using a Rigaku Miniflex diffractometer in reflection mode using Cu-K_α radiation. Electrochemical measurements were performed using a BioLogic VSP potentiostat. Electrochemical impedance spectroscopy measurements were carried out within a frequency range of 1 MHz to 1 Hz. The Li | LZP | LTP cell was assembled and sealed at 1.5 bar within a CR2016 MTI coin cell with a 10 mm diameter Kapton inspection window. The co-sintered electrolyte/cathode pellet with a diameter of 13 mm was modified by polishing by papers with grit numbers from 400 to 2500 to a final thickness of 1.0 mm. VESTA was used to create unit cell depictions [49].

Muon Spectroscopy

μSR measurements were completed on the EMU beamline at the ISIS Pulsed Neutron and Muon Source. Powdered samples (∼1 g) of LZP and LTP were transferred into Ti sample holders with a thin Ti foil window to allow muon implantation. Spin polarised positive muons of initial energy 4.12 MeV were implanted into the samples to act as a probe of Li^+ ion diffusion. Muons were implanted with a controllable penetration range of between 0.1 – 1.0 mm, and after rapid

thermalization preferentially stop at electronegative interstitial sites in the crystal structure, commonly near oxygen. Thin Ag foil was used in front of the cell as a beam degrader when necessary to control the penetration depth. Applied longitudinal magnetic fields were used to decouple the muon spin from its surrounding local nuclear moments. Measurements were performed in 0, 5, and 10 G longitudinal fields, as well as 100 G transverse field calibration runs. A temperature range of 100 – 400 K was measured, encapsulating a low temperature baseline and the thermally activated region where Li^+ ions overcome the energetic barriers opposing ionic transport. The beam spot has a roughly Gaussian profile and its size was collimated to optimise the rate of data collection and minimise background noise. Data fitting was completed using Mantid software package [50].

In Situ Cell Holder

A custom-built holder to house the coin cell was designed in collaboration with the ISIS Neutron and Muon Source. A cell was placed inside the adapted holder design and the inspection windows aligned to allow muon implantation. Teflon screws were used to tighten the holder and secure the cell whilst ensuring electrical isolation between terminals. An Ag mask was included on the front of the holder to stop any wayward muons that were not incident on the inspection window. Ag (similar to Ti, which is used for the powdered sample holders) has a very small nuclear magnetic moment, meaning the signal from any muons implanted within the mask itself could be subtracted as background. Wires were fed through the closed cycle refrigerator of the EMU beamline to attach a connector on each side of the cell holder.

Results and discussion

$LiTi_2(PO_4)_3$ and $LiZr_2(PO_4)_3$

$LiTi_2(PO_4)_3$ (LTP) and $LiZr_2(PO_4)_3$ (LZP) were synthesised by an unmodified sol-gel method [15, 48]. Prepared LZP contained only the α-type polymorph, with primarily the triclinic phase present at room temperature, as expected (Figure S4.1). For LZP, the triclinic phase is known to go through a phase transition to the conductive rhombohedral phase around 50 °C [15]. LTP does not undergo a phase change in this temperature range and exists in a rhombohedral structure of space group $R\bar{3}c$, as shown in Figure 4.1a.

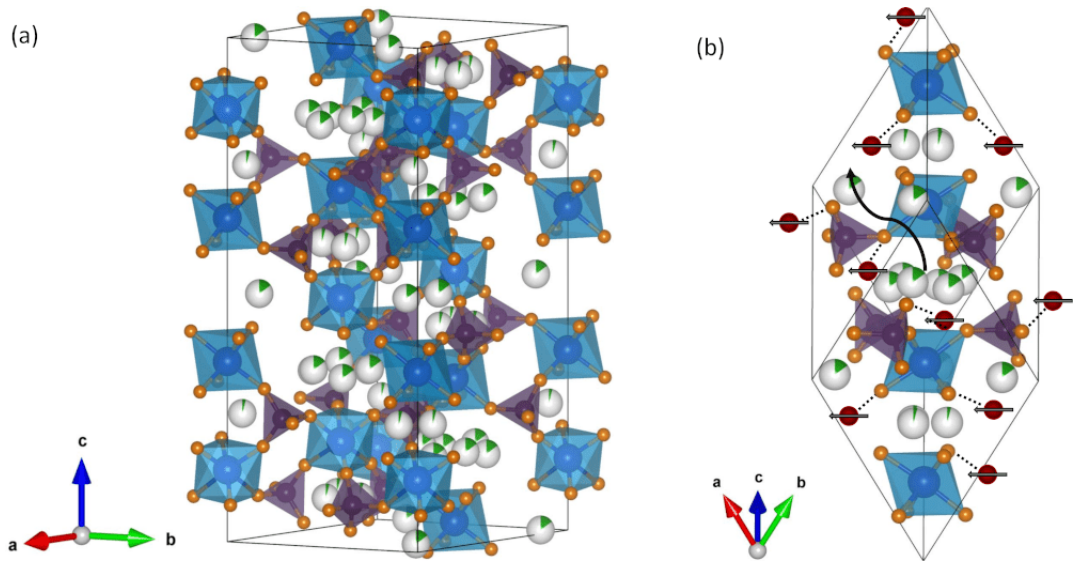

Figure 4.1: (a) The unit cell of rhombohedral ($R\bar{3}c$) LZP [51]. Li is displayed as green spheres in tetrahedral sites with a high vacancy fraction, Zr as blue, P as purple and O as orange. ZrO_6 and PO_4 are shown as blue octahedra and purple tetrahedra, respectively. (b) A view of LZP with rhombohedral axes. The curved black arrow indicates the Li^+ diffusion pathway from the $6b$ site surrounded by six split $36f$ Wyckoff positions to the neighbouring $6b$ site. The maroon spheres indicate implanted muons, which are known to chemically bond to oxygen atoms at a distance of around 1 Å [33, 52]. The muon spins are all facing the same direction, as is the case upon initial implantation. The potential muon stopping sites shown here are displayed for qualitative purposes only, while further information on potential muon stopping sites can be found in Tables S4.1 – S4.6.

A fitted 100 G transverse field μSR measurement for LZP is displayed in Figure 4.2a, showing the rapid change in the asymmetry of positron detection as the muon spin precesses around the applied field, which is much stronger than any internal field of nuclear or electronic origin. Fitting multiple oscillation functions reveals that all muons precess at the Larmor frequency of a free muon in an applied field 135.5 MHz T^{-1}. The low ionic dynamics at 150 K and the lack of unpaired electron spins mean that the asymmetry envelope takes a relatively flat form with little relaxation. Similar data were observed for the cathode LTP (Figure S4.2). Consequently, no relaxation component was used in the longitudinal field data analysis. To confirm this quantitatively, transverse field data were modelled using a background component and an oscillating exponential relaxation with rate λ, shown in Figure 4.2. Both materials exhibit low λ values; the flat regions at low temperatures indicate a static environment whilst the subsequent decrease is a consequence of dynamical field fluctuations above 300 K, indicating the onset of Li^+ diffusion. This occurs at a lower temperature of between 250 – 300 K for cathode LTP. The larger drop in λ for LZP is likely due to the phase change from triclinic to rhombohedral around 320 K, which will alter the spatial distribution of muon stopping sites.

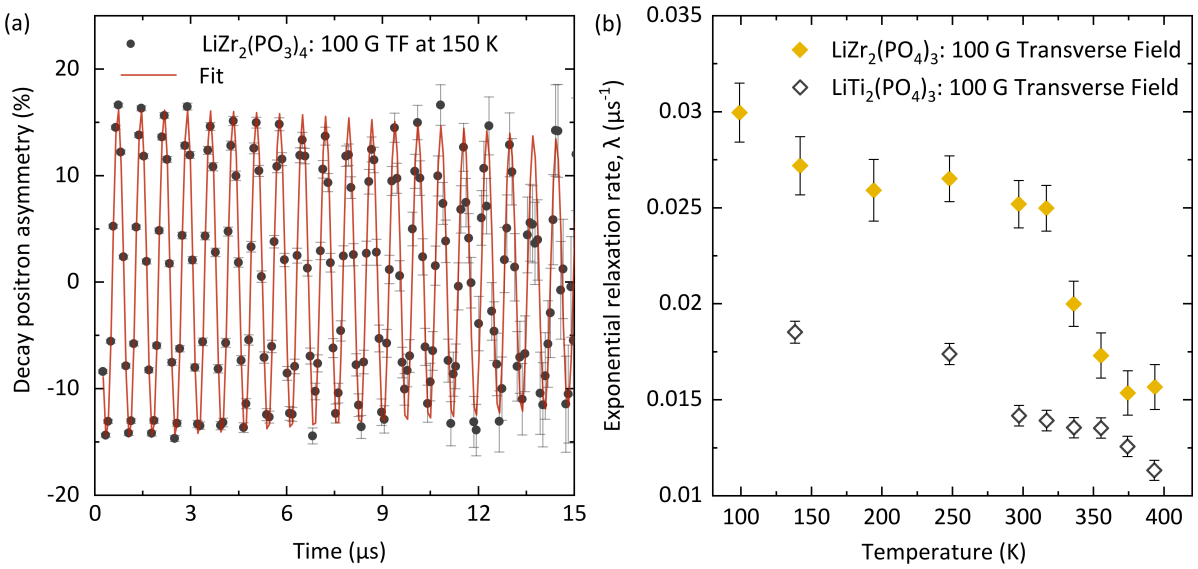

Figure 4.2: (a) μSR measurement of solid electrolyte LZP in a 100 G applied transverse field at 150 K. (b) The temperature dependent relaxation rate λ obtained *via* fitting of an oscillating exponential decay function to transverse field data.

Longitudinal field (0, 5, and 10 G) experiments were also applied for which the dynamical field fluctuations created by the nuclear dipole of Li^+ hopping between crystal sites causes a spin flip *via* the absorption of energy by the muon spin Zeeman levels [53]. Longitudinal field data were fit using a flat background component and the dynamical form of the Kubo-Toyabe function described as:

$$A_0 P(t) = A_{bg} + A_{KT} P_{KT}(\Delta, \nu, t), \tag{4.1}$$

where A_{bg} and A_{KT} are the respective amplitudes of the two components. P_{KT} represents the dynamic Kubo-Toyabe function, which is sensitive to the trend of the static field distribution width (Δ) and the field fluctuation rate (ν) with time [54]. The field fluctuation rate offers information on any dynamical fields felt by the muons, which most likely arise from diffusing Li^+. Hence, ν is analogous to the ionic hopping rate [34].

A longitudinal field strength of 10 G was found sufficient to retain muon spin polarization by quenching the relaxation contribution from nearby nuclear magnetic moments and broadly align the spin along the direction of the applied field (Figures S4.3 and S4.4). Constraining the Kubo-Toyabe function to three applied field strengths provided an accurate model by isolating the contribution to the asymmetry signal from Li^+ hopping. Given that LZP is an excellent insulator and that relatively small initial asymmetry values were observed (Figure S4.3), an appreciable fraction of implanted muons may pick up an electron to form a muonium state (μ^+e^-) [55]. This manifests in the data as an exponential decay in an early time domain from a rapidly relaxing muonium signal. To combat this effect, early time domain points were discarded, and the data were fit in a time range of 1 – 25 μs for LZP. The onset of Li^+ diffusion is seen to occur at around 300 K for the electrolyte LZP and 250 K for the cathode LTP, in agreement with the transverse field data in both instances. Above these temperatures ν increases rapidly with temperature as Li^+ becomes increasingly mobile. The high temperature drop in ν for LTP can be explained by the Li^+ dynamics becoming too fast to be probed effectively: an effect

commonly seen in μSR [36, 46].

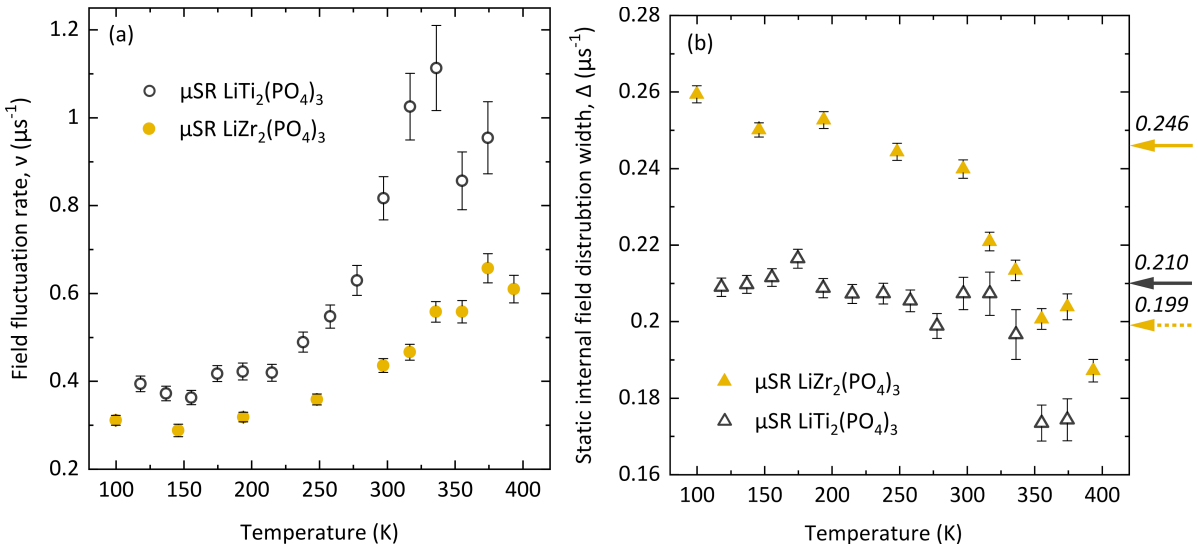

Figure 4.3: A μSR measurement of (a) the field fluctuation rate ν, which is directly analogous to the ionic jump frequency and (b) the static field distribution width Δ of the implanted muons within LZP and LTP. Computationally predicted Δ values are shown on the opposite y-axis as a yellow arrow for triclinic LZP, a black arrow for LTP, and a dotted yellow arrow for rhombohedral LZP.

Figure 4.3b displays the temperature dependence of Δ, defined as the width of the static distribution of magnetic fields experienced by the muons, primarily decided by the proximity and strength of nearby nuclear dipole fields. The increased value of Δ for LZP can be attributed to the larger nuclear magnetic moment of the Zr^{4+} cation in comparison to Ti^{4+} [56]. Both samples exhibit a relatively constant value or a slight decrease, before a sharper drop is seen at high temperatures. This is a consequence of a motional narrowing effect: as Li^{+} ions begin to diffuse rapidly, their nuclear fields increasingly differ throughout the structure and thus their contribution to Δ is lowered [46]. The larger decrease observed for LZP may be explained by the phase change from triclinic to rhombohedral at around 320 K as the spatial arrangement of muon stopping sites is altered. To distinguish between the effects on Δ of the structural transition in LZP and potential motional narrowing, Δ was calculated and averaged over a selection of potential muon stopping sites in each material, for which details can be found in Tables S4.1 – S4.6. Very good agreement with the data was found for potential muon sites approximately 1 Å from an oxygen site, similar to the length of an O-H bond (∼0.97 Å) [52]. From the calculations, Δ is predicted to decrease from 0.246 to 0.199 μs^{-1} with the phase change in LZP. These results show that the different Δ values observed experimentally all relate to common muon stopping sites and that the structural transition dominates the change seen in LZP, rather than the motional narrowing which is also evident. Δ was also predicted as around 0.210 μs^{-1} at potential muon stopping sites in LTP, matching well with experimental values.

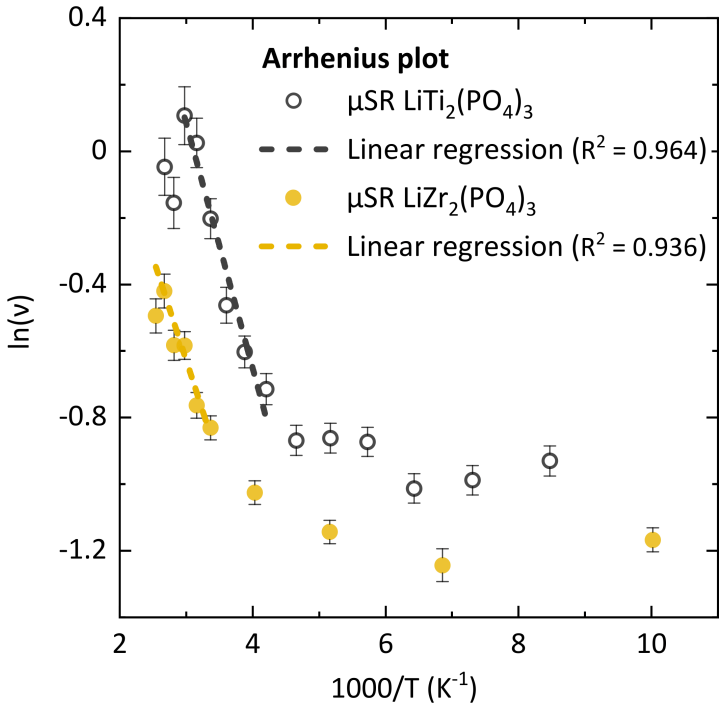

Figure 4.4: An Arrhenius plot of the logarithm of the field fluctuation rate ν against reciprocal temperature for both LZP and LTP. Only the thermally activated region of both materials (300 – 380 K for LZP and 240 – 340 K for LTP) was fitted by a linear regression which is shown as a dotted line.

An Arrhenius analysis of the temperature dependence of ν was completed to yield an activation energy barrier E_A for Li^+ diffusion (Figure 4.4). This was extracted for LZP (electrolyte) and LTP (cathode) as around 51 ± 8 and 63 ± 6 meV, respectively. In comparison to other solid electrolyte materials investigated using μSR, these values are lower than for garnet structured materials (≈200 meV), comparable to sulfide electrolyte material $Li_{10}GeP_2S_{12}$ (≈90 meV), and very similar to many cathode materials [35–37, 39, 40, 55, 57–59]. It is worth noting that μSR is a volume-averaged probe, meaning intra-grain diffusion mechanisms will dominate the signal. As such, there is a reduced contribution from grain boundaries and other extrinsic factors which often hinder ionic transport. Consequently, reported activation energies tend to be lower for μSR in comparison to other techniques, as μSR probes the fundamental energy required to motivate singular ionic hops at a unit cell length-scale [37, 47].

Within rhombohedral LZP, Li^+ is distributed over six disordered 36*f* tetrahedral sites surrounding the 6*b* site (Figure 4.1) [21]. The chemical configuration of the Li sites is relatively unstable due to a distortion of their tetrahedral environment through a lengthening of the Li-O bond: an increase to 2.27 Å from 2.09 Å in comparison with the triclinic ($C\bar{1}$) phase. The distorted tetrahedral environment of Li^+ benefits mobility due to its inherent instability, and affords structural reasoning for ease of hopping between vacant 36*f* sites. The length of the Li-O bond depends on the cation used [60]. Structurally, the replacement of Ti for Zr reduces the bottleneck in the Li^+ conduction channel between the M1 and M2 sites (6*b* and 18*e*, respectively). This corresponds to the observed reduction in temperature required to motivate spontaneous diffusion [25, 61].

To deduce the diffusion coefficient of Li^+ ions, D_{Li}, the following equation was applied:

$$D_{Li} = \sum_{i=1}^{n} (1/N_i)\ Z_{\nu,i}\ {s_i}^2\ \nu_{Li}. \tag{4.1}$$

N_i is the number of Li^+ sites in the i^{th} path, $Z_{\nu,i}$ is the vacancy fraction, s_i is the Li^+ hopping distance and ν is the field fluctuation rate obtained *via* μSR [34, 40, 57]. There are two established mechanisms of Li^+ hopping: vacancy assisted and interstitial. Lu *et al.* have shown the importance of interstitial sites at elevated temperatures for LTP, and that close to room temperature Li^+ opts to remain at the thermodynamically stable $6b$ sites [32]. The pathway considered for D_{Li} is thus from the $6b$ sites to the $6b$ sites *via* vacancy assisted hopping. For both materials there are six potential pathways if we consider three-dimensional diffusivity. The hopping distances were taken from $6b$ to $6b$ sites at the centre of the $36f$ Wyckoff positions from the recent studies by Noda *et al.* [19] and Lu *et al.* [32], for LZP and LTP, respectively. Noda *et al.* have shown that Li^+ migration proceeds *via* a pushing-out and repulsion mechanism, whereby a diffusing Li^+ pushes out another Li^+ occupying a $6b$ site, encouraging it to also diffuse. It is therefore assumed that every $6b$ site is available for diffusion and that Z is 1.

The diffusion coefficient, D_{Li}, of the electrolyte LZP and cathode LTP were estimated as $3.7(2)\times10^{-10}$ cm^2 s^{-1} and $6.9(6)\times10^{-10}$ at 336 K [$5.1(3)\times10^{-10}$ cm^2 s^{-1} at 297 K for LTP], respectively. Data at 336 K was used for LZP to ensure that the material had fully transitioned to the rhombohedral phase. LTP is seen to display slightly faster dynamics than LZP, as expected. This can be rationalised by the increased width of the M1-M2 bottleneck which is known to hinder diffusion. Subramanian *et al.* showed that the substitution of Ti^{4+} for Zr^{4+} decreased both the a and c cell parameters significantly, shortening the diffusion pathway and increasing cavity size to afford greater Li^+ mobility [31].

All-solid-state Li | LZP | LTP cell

As was recently reported, LTP and LZP can be co-sintered together and a Li anode attached to form an all-solid-state cell [15]. A typical discharge/charge profile for this configuration displays an electrochemical window between 1.0 – 3.5 V. The beam penetration depth is a Gaussian distribution roughly between 100 – 200 mg cm^{-2} as an areal density. Accounting for a small amount of beam attenuation by the Kapton window, and assuming a negligible affect from the thin (∼20 μm) cathode layer [15], muons were predicted to stop with a range between 0.09 – 0.47 mm deep inside the 1.0 mm thick pellet (Figure 4.5). The μSR signal received was thus from the solid electrolyte itself. Zero and longitudinal field muon measurements were taken at six distinct discharge voltages, at which points the discharge was paused and the cell was allowed to relax for around 2 hours and 40 minutes to open circuit voltage (OCV). Data were again fit using Equation 4.1 in the time range 1 – 25 μs. The entire set-up was held at 345 K to ensure that the solid electrolyte LZP existed in purely the fast-conducting rhombohedral phase. A low current density of 8 μA cm^{-2} was applied for the discharge, which is shown in Figure 4.6a.

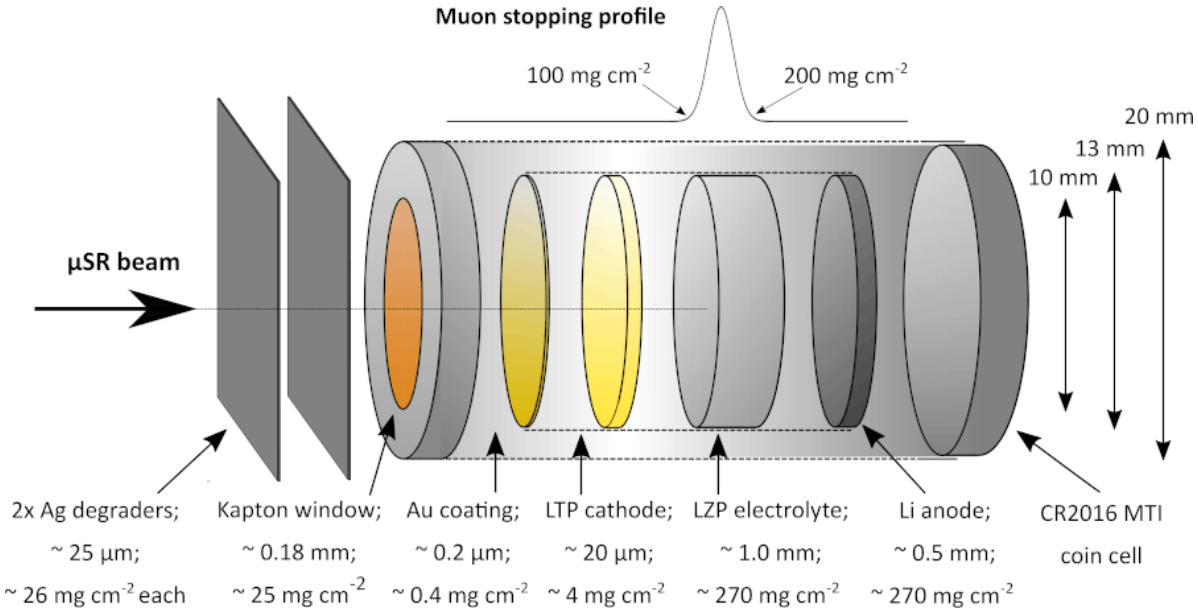

Figure 4.5: A labelled schematic of the Li | LZP | LTP cell as measured on the beamline. The battery constituents were assembled within a CR2016 MTI coin cell. The thickness of each component is given, along with an areal density which is used to determine the amount of beam attenuation. The muon stopping profile is shown as a Gaussian distribution between around 100 – 200 mg cm^{-2}; muons which enter through the 10 mm diameter Kapton inspection window are predicted to come to rest within the LZP solid electrolyte.

Figure 4.7a reflects how the Li^+ dynamics within the solid LZP electrolyte change depending on cell potential. The values obtained for ν and Δ in comparison to the powdered LZP sample are similar and rationalise that the signal was collected from the electrolyte LZP within the cell. The field fluctuation rate ν is expected to stay constant within the inert solid electrolyte as the battery discharges, as it acts as a medium for ionic transfer. The following is observed: ν remains relatively constant as the cell is discharged until around 1.2 V below which there is a sharp drop in magnitude. The reduction in the rate of Li^+ diffusion in the electrolyte evidences a degree of instability at deep discharge of the battery ($\leq$1.2 V). The low current density applied here is not expected to damage the electrolyte significantly over one discharge and thus the reduction in intrinsic self-diffusion at low temperatures is attributed to electrolyte instability at low electrochemical potential [15, 17]. Using the same calculation method as in the previous section, D_{Li} is observed to decrease from an average of $2.2(2)\times10^{-10}$ above 1.2 V to an average value of $1.6(1)\times10^{-10}$ cm^2 s^{-1} below. These results demonstrate the sensitivity of this *in situ* muon technique in assessing ion transport properties under working conditions and at extreme conditions where instabilities become apparent.

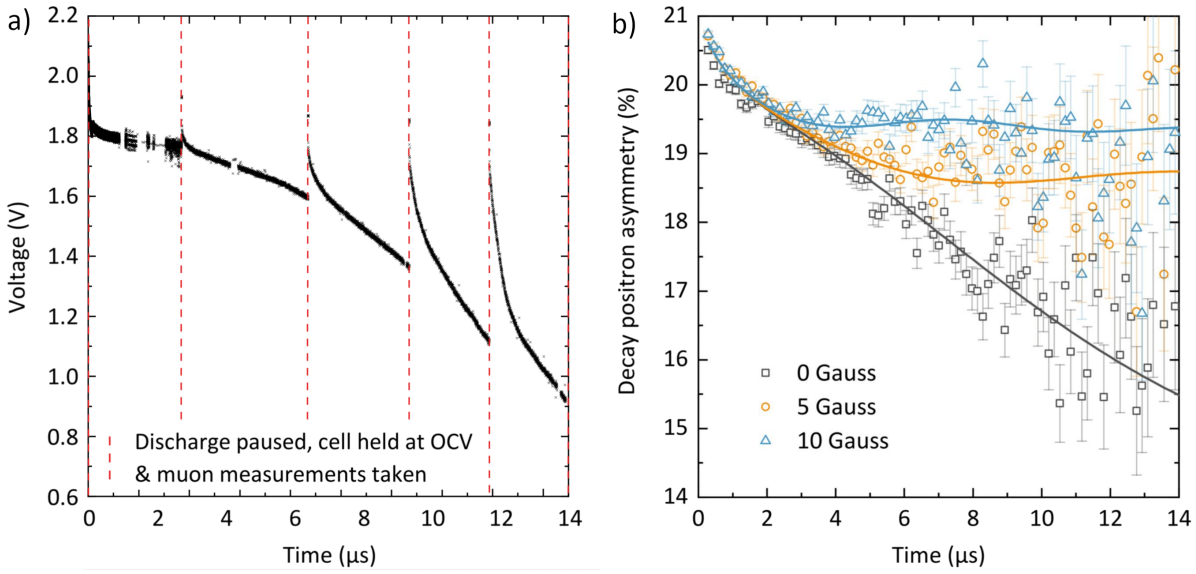

Figure 4.6: (a) Discharge profile of the Li | LZP | LTP cell at 8 μA cm^{-2}; the dotted lines show points at which the cell relaxed for 2 hours 40 minutes to OCV and μSR and EIS measurements were performed. The discharge corresponds to a capacity of around 30 mAh g^{-1}. Further characterisation of the solid-state cell configuration can be found in reference [15]. (b) Raw μSR data from the electrolyte LZP within the all-solid-state cell at 345 K, showing the reduced depolarization as the applied field increases.

Δ is observed to fluctuate slightly with a general decreasing trend which becomes more pronounced below 1.2 V. This suggests a changing spatial distribution of nuclear dipole fields near the muon site as the muon site itself is unlikely to change with voltage state. Since the Li content within the electrolyte is independent of the state of charge of the cell, it follows that Δ would be predicted to remain constant during cycling. The change in Δ may be caused by a narrowing of the bottleneck along the 6*b*-6*b* diffusion pathway between the 18*e* (M2) sites through a structural distortion of the Zr-O octahedra and P-O tetrahedra. The mechanism of attempting to extract excess Li^+ into lithiated LTP at a low potential may drive ions into the vacant 18*e* (M2) sites, hampering potential diffusion pathways between 6*b* sites and lowering the width of the field distribution felt by the implanted muons. The reduction in Δ may also be due to the decomposition of LZP at low potential. The magnitude of the reduction is comparable to a structural change, however the structural evolution of LZP at deep discharge has not yet been determined.

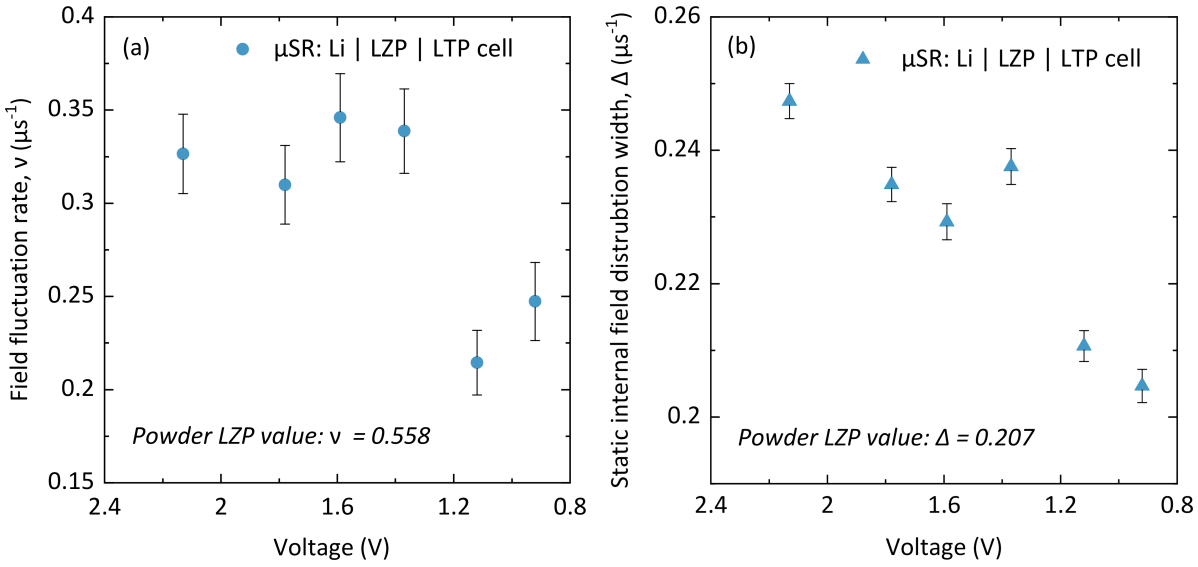

Figure 4.7: μSR measurements displaying (a) the field fluctuation rate ν, and (b) the static field distribution width Δ as a function of discharge state of the Li | LZP | LTP cell. The values for the pristine LZP powder at 345 K are given in μs^{-1}.

Along with muon measurements at each stopping point in the discharge cycle, electrochemical impedance spectroscopy (EIS) measurements were also taken in order to provide complementary information to the local diffusion probed by μSR. The overall cell resistance is seen to increase steadily from around 51 kΩ cm^2 before discharge to around 74 kΩ cm^2 at deep discharge (0.92 V) (Figure 4.8). The spectra shown are dominated by one large resistive effect in the battery which is likely to be the Li/LZP interfacial layer [15]. LZP reacts with metallic Li to form a black, amorphous, passivating layer, which has been reported to consist of Li_3P and Li_8ZrO_6 (the interphase is pictured in the inset of Figure 4.8) [15, 17]. X-ray absorption spectroscopy experiments reveal that the interphase can be propagated using either applied heat or current, and that there is a clear change during interphase growth as the pristine material is converted to an amorphous material. XANES measurements find a shift in edge position which indicates a small change in the local structure (Figures S4.7 – S4.11), whilst the EXAFS data displays a significant reduction in the Zr-O oxidation number from the pristine material to the interphase.

The shift of the EIS peak of the semi-circle to higher time constants as the cell discharges is thus attributed to an interphase growth which acts as an increasingly resistive boundary. The resistive component from the LZP/LTP interface is indistinguishable from the total resistance in the EIS spectra, suggesting the resistance across the all-NASICON boundary is substantially less. Whilst the interface is essential to wet both LZP and Li and maintain stability across both components, the resistive increase observed over the first discharge will impede charge transfer across the boundary and consume active material. Interfacial resistance growth is not expected to contribute towards the reduced self-diffusion observed within the bulk at low potential; however, over extended cycling it will lead to an inhomogenous current distribution and ultimately a short-circuit.

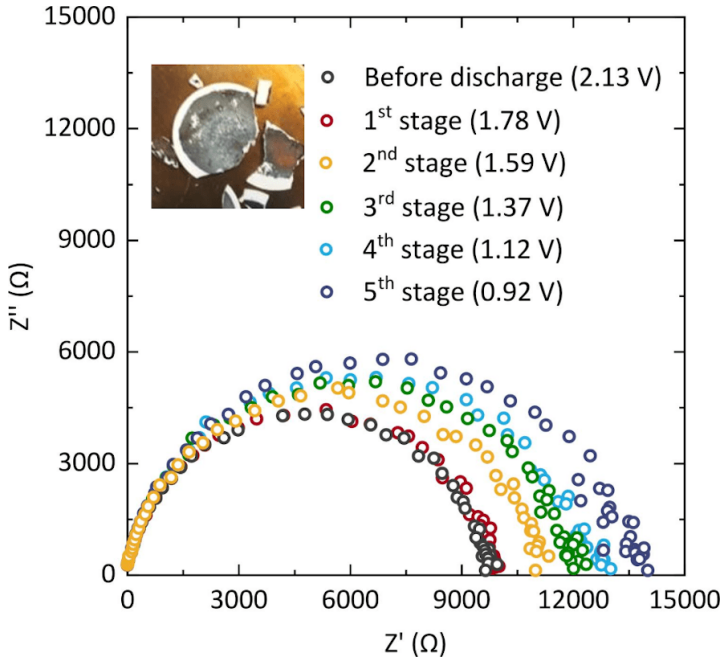

Figure 4.8: An EIS measurement at each OCV voltage in the first discharge of the Li | LZP | LTP cell. The inset shows the Li/LZP black interfacial layer on a broken LZP pellet.

Conclusions

Activation energies of LZP and LTP have been estimated as 51 ± 8 and 63 ± 6 meV, respectively. From this, the diffusion rate coefficient was estimated as $3.7(2)\times10^{-10}$ and $6.9(6)\times10^{-10}$ cm^2 s^{-1} at 336 K for LZP and LTP, respectively, and as $5.1(3)\times10^{-10}$ cm^2 s^{-1} at room temperature for LTP. Both NASICON materials exhibit low energetic barriers for Li^+ hopping and fast ion mobility, while LTP displays faster transport due to the smaller effective ionic radius of Ti^{4+} easing the bottleneck restriction on the M1-M2-M1 diffusion pathway. XAS results indicate decomposition at the Li-LZP interface, with the resultant phase possessing high amorphicity and a reduction in Zr-O coordination number. μSR results for a NASICON-structured Li | LZP | LTP SSB displayed a drop in the Li^+ diffusion rate below low potential (≤1.2 V), indicating ionic conductivity is significantly hindered at deep discharge. A reduction in the static field distribution width with discharge reveals potential structural distortion which may be the cause of the reduced hopping rate by a narrowing of the diffusion pathway between M1 sites. The correlated reduction in both ν and Δ indicates that LZP may undergo structural decomposition at low voltage. Electrochemical impedance spectroscopy indicates the Li/LZP interfacial layer is the dominant resistive barrier within the cell and becomes increasingly resistive throughout the first discharge. This work offers an initial insight into the applicability of *in situ* μSR and electrochemical techniques as a combined tool to investigate energy storage devices by elucidating the relationship between diffusional properties and electrochemistry. The technique can be applied to study of the behaviour of a singular battery component or a whole device, and can be extended towards the study of interfacial regions and degradation mechanisms [47]. *In situ* cell design improvements to further develop this technique are underway to optimise data

quality, electrochemistry, and cell assembly.

Acknowledgements

The authors thank the ISIS Neutron and Muon facility, through the award of beamtime (DOI:10.5286/ISIS.E.RB1820558), a Facility Development Studentship for IMC, and Josef Lewis and Jamie Nutter for enabling the in-situ muon experiment. BIJ acknowledges the award of a Carnegie PhD scholarship. This work was supported by the EPSRC [EP/N001982/2], the ISCF Faraday Challenge projects SOLBAT [grant number FIRG007] and FutureCat [FIRG017]. We acknowledge SOLEIL for provision of synchrotron radiation facilities, and we would like to thank Stéphanie Belin for assistance in using the ROCK beamline, proposal number 20181039.

References

[1] Y. Ding, Z. P. Cano, A. Yu, J. Yu, and Z. Chen. Automotive Li-Ion Batteries: Current Status and Future Perspectives. *Electrochem. Energy Rev.*, 2:1–28, 2019.

[2] K. Fu, Y. Gong, B. Liu, Y. Zhu, S. Xu, Y. Yao, W. Luo, C. Wang, S. D. Lacey, J. Dai, Y. Chen, Y. Mo, E. Wachsman, and L. Hu. Toward garnet electrolyte–based Li metal batteries: An ultrathin, highly effective, artificial solid-state electrolyte/metallic Li interface. *Sci. Adv*, 3:e1601659, 2017.

[3] F. Zheng, M. Kotobuki, S. Song, M. O. Lai, and L. Lu. Review on solid electrolytes for all-solid-state lithium-ion batteries. *J. Power Sources*, 389:198–213, 2018.

[4] A. Manthiram, X. Yu, and S. Wang. Lithium battery chemistries enabled by solid-state electrolytes. *Nat. Rev. Mater.*, 2:16103, 2017.

[5] B. Liu, J. G. Zhang, and W. Xu. Advancing Lithium Metal Batteries. *Joule*, 2:833–845, 2018.

[6] S. Wang, H. Xu, W. Li, A. Dolocan, and A. Manthiram. Interfacial Chemistry in Solid-State Batteries: Formation of Interphase and Its Consequences. *J. Am. Chem. Soc*, 140:250–257, 2018.

[7] Z. Gao, H. Sun, L. Fu, F. Ye, Y. Zhang, W. Luo, and Y. Huang. Promises, Challenges, and Recent Progress of Inorganic Solid-State Electrolytes for All-Solid-State Lithium Batteries. *Adv. Mater.*, 30:1705702, 2018.

[8] C. Sun, J. Liu, Y. Gong, D. Wilkinson, and J. Zhang. Recent advances in all-solid-state rechargeable lithium batteries. *Nano Energy*, 33:362–386, 2017.

[9] T. Famprikis, P. Canepa, J. A. Dawson, M. S. Islam, and C. Masquelier. Fundamentals of inorganic solid-state electrolytes for batteries. *Nat. Mater.*, 18:1278–1291, 2019.

[10] H. Chung and B. Kang. Mechanical and Thermal Failure Induced by Contact between a $Li_{1.5}Al_{0.5}Ge_{1.5}(PO_4)_3$ Solid Electrolyte and Li Metal in an All Solid-State Li Cell. *Chem. Mater.*, 29:8611–8619, 2017.

[11] H. Huo, J. Liang, N. Zhao, X. Li, X. Lin, Y. Zhao, K. Adair, R. Li, X. Guo, and X. Sun. Dynamics of the Garnet/Li Interface for Dendrite-Free Solid-State Batteries. *ACS Energy Lett.*, 5:2156–2164, 2020.

[12] G. Li and C. Monroe. Dendrite nucleation in lithium-conductive ceramics. *Phys. Chem. Chem. Phys.*, 21:20354–20359, 2019.

[13] H. Yamada, T. Ito, R. H. Basappa, and R. Bekarevich. Influence of strain on local structure and lithium ionic conduction in garnet-type solid electrolyte. *J. Power Sources*, 368:97–106, 2017.

[14] F. Flatscher, M. Philipp, S. Ganschow, H. Martin R. Wilkening, and D. Rettenwander. The natural critical current density limit for $Li_7La_3Zr_2O_{12}$ garnets. *J. Mater. Chem. A*, 8:15782–15788, 2020.

[15] H. El-Shinawi, A. Regoutz, D. J. Payne, E. J. Cussen, and S. A. Corr. NASICON $LiM_2(PO_4)_3$ electrolyte (M = Zr) and electrode (M = Ti) materials for all solid-state Li-ion batteries with high total conductivity and low interfacial resistance. *J. Mater. Chem. A*, 6:5296–5303, 2018.

[16] C. O'Rourke and B. Morgan. Interfacial strain effects on lithium diffusion pathways in the spinel solid electrolyte Li-doped $MgAl_2O_4$. *Phys. Rev Mater.*, 2:045043, 2018.

[17] Y. Li, W. Zhou, X. Chen, X. Lü, Z. Cui, S. Xin, L. Xue, Q. Jia, and J. B. Goodenough. Mastering the interface for advanced all-solid-state lithium rechargeable batteries. *PNAS*, 113:13313–13317, 2016.

[18] A. A. Andriiko, P. V. Rudenok, and L. I. Nyrkova. Diffusion coefficient of Li^+ in solid-state rechargeable battery materials. *J. Power Sources*, 72:146–149, 1998.

[19] Y. Noda, K. Nakano, H. Takeda, M. Kotobuki, L. Lu, and M. Nakayama. Computational and Experimental Investigation of the Electrochemical Stability and Li-Ion Conduction Mechanism of $LiZr_2(PO_4)_3$. *Chem. Mater.*, 29(21):8983–8991, 2017.

[20] J. Zhang, J. Zhang, X. Ou, C. Wang, C. Peng, and B. Zhang. Enhancing High-Voltage Performance of Ni-Rich Cathode by Surface Modification of Self-Assembled NASICON Fast Ionic Conductor $LiZr_2(PO_4)_3$. *ACS Appl. Mater. Interfaces*, 11:15507–15516, 2019.

[21] M. Catti, S. Stramare, and R. Ibberson. Lithium location in NASICON-type Li^+ conductors by neutron diffraction. I. Triclinic α'-$LiZr_2(PO_4)_3$. *Solid State Ion.*, 123:173–180, 1999.

[22] A. Rossbach, F. Tietz, and S. Grieshammer. Structural and transport properties of lithium-conducting NASICON materials. *J. Power Sources*, 391:1–9, 2018.

[23] Y. Meesala, A. Jena, H. Chang, and R. S. Liu. Recent Advancements in Li-Ion Conductors for All-Solid-State Li-Ion Batteries. *ACS Energy Lett.*, 2:2734–2751, 2017.

[24] V. Ramar, S. Kumar, S. R. Sivakkumar, and P. Balaya. NASICON-type La^{3+} substituted $LiZr_2(PO_4)_3$ with improved ionic conductivity as solid electrolyte. *Electrochim. Acta*, 271:120–126, 2018.

[25] M. Hou, F. Liang, K. Chen, Y. Dai, and D. Xue. Challenges and perspectives of NASICON-type solid electrolytes for all-solid-state lithium batteries. *Nanotechnology*, 31:132003, 2020.

[26] T. Pareek, S. Dwivedi, B. Singh, D. Kumar, P. Kumar, and S. Kumar. $LiSnZr(PO_4)_3$: NASICON-type solid electrolyte with excellent room temperature Li^+ conductivity. *J. Alloys Compd.*, 777:602–611, 2019.

[27] H. Xie, J. B. Goodenough, and Y. Li. $Li_{1.2}Zr_{1.9}Ca_{0.1}(PO_4)_3$, a room-temperature Li-ion solid electrolyte. *J. Power Sources*, 196:7760–7762, 2011.

[28] Y. Zhang, K. Chen, Y. Shen, Y. Lin, and C. W. Nan. Enhanced lithium-ion conductivity in a $LiZr_2(PO_4)_3$ solid electrolyte by Al doping. *Ceram. Int.*, 43:S598–S602, 2017.

[29] P. Hartmann, T. Leichtweiss, M. Busche, M. Schneider, M. Reich, J. Sann, P. Adelhelm, and J. Janek. Degradation of NASICON-Type Materials in Contact with Lithium Metal: Formation of Mixed Conducting Interphases (MCI) on Solid Electrolytes. *J. Phys. Chem. C*, 117:21064–21074, 2013.

[30] A. Cassel, B. Fleutot, M. Courty, V. Viallet, and M. Morcrette. Sol-gel synthesis and electrochemical properties extracted by phase inflection detection method of NASICON-type solid electrolytes $LiZr_2(PO_4)_3$ and $Li_{1.2}Zr_{1.9}Ca_{0.1}(PO_4)_3$. *Solid State Ion.*, 309:63–70, 2017.

[31] M. A. Subramanian, R. Subramanian, and A. Clearfield. Lithium ion conductors in the system $AB(IV)_2(PO_4)_3$ (B = Ti, Zr and Hf). *Solid State Ion.*, 18-19:562–569, 1986.

[32] X. Lu, S. Wang, R. Xiao, S. Shi, H. Li, and L. Chen. First-principles insight into the structural fundamental of super ionic conducting in NASICON $MTi_2(PO_4)_3$ (M = Li, Na) materials for rechargeable batteries. *Nano Energy*, 41:626–633, 2017.

[33] S. J. Blundell. Spin-polarized muons in condensed matter physics. *Contemporary Physics*, 40:175–192, 1999.

[34] J. Sugiyama, K. Mukai, Y. Ikedo, H. Nozaki, M. Månsson, and I. Watanabe. Li Diffusion in Li_xCoO_2 Probed by Muon-Spin Spectroscopy. *Phys. Rev. Lett.*, 103:147601, 2009.

[35] T. E. Ashton, J. V. Laveda, D. A. Maclaren, P. J. Baker, A. Porch, M. O. Jones, and S. A. Corr. Muon studies of Li^+ diffusion in $LiFePO_4$ nanoparticles of different polymorphs. *J. Mater. Chem. A*, 2:6238–6245, 2014.

[36] J. V. Laveda, B. Johnston, G. W. Paterson, P. J. Baker, M. G. Tucker, H. Y. Playford, K. M. Ø. Jensen, S. J. L. Billinge, and S. A. Corr. Structure-property insights into nanostructured electrodes for Li-ion batteries from local structural and diffusional probes. *J. Mater. Chem. A*, 6:127–137, 2018.

[37] P. J. Baker, I. Franke, F. L. Pratt, T. Lancaster, D. Prabhakaran, W. Hayes, and S. J. Blundell. Probing magnetic order in LiMPO$_4$ (M = Ni, Co, Fe) and lithium diffusion in Li$_x$FePO$_4$. *Phys. Rev. B*, 84:174403, 2011.

[38] I. D. Johnson, T. E. Ashton, E. Blagovidova, G. J. Smales, M. Lübke, P. J. Baker, S. A. Corr, and J. A. Darr. Mechanistic insights of Li_+ diffusion within doped LiFePO$_4$ from Muon Spectroscopy. *Sci. Rep.*, 8:4114, 2018.

[39] M. Månsson, H. Nozaki, J. M. Wikberg, K. Prša, Y. Sassa, M. Dahbi, K. Kamazawa, K. Sedlak, I. Watanabe, and J. Sugiyama. Lithium diffusion & magnetism in battery cathode material Li$_x$Ni$_{1/3}$Co$_{1/3}$Mn$_{1/3}$O$_2$. *J. Phys. Conf. Ser.*, 551:012037, 2014.

[40] M. Månsson and J. Sugiyama. Muon-spin relaxation study on Li- and Na-diffusion in solids. *Phys. Scr.*, 88:068509, 2013.

[41] I. Umegaki, S. Kawauchi, H. Sawada, H. Nozaki, Y. Higuchi, K. Miwa, Y. Kondo, M. Månsson, M. Telling, F. C. Coomer, S. P. Cottrell, T. Sasaki, T. Kobayashi, and J. Sugiyama. Li-ion diffusion in Li intercalated graphite C$_6$Li and C$_{12}$Li probed by μ^+SR. *Phys. Chem. Chem. Phys.*, 19:19058–19066, 2017.

[42] J. Sugiyama, H. Nozaki, I. Umegaki, K. Mukai, K. Miwa, S. Shiraki, T. Hitosugi, A. Suter, T. Prokscha, Z. Salman, J. S. Lord, and M. Månsson. Li-ion diffusion in Li$_4$Ti$_5$O$_{12}$ and LiTi$_2$O$_4$ battery materials detected by muon spin spectroscopy. *Phys. Rev. B*, 92:014417, 2015.

[43] A. S. Powell, J. S. Lord, D. H. Gregory, and J. J. Titman. Muon Spin Relaxation Studies of Lithium Nitridometallate Battery Materials: Muon Trapping and Lithium Ion Diffusion. *J. Phys. Chem. C*, 113:20758–20763, 2009.

[44] D. W. Ferdani, S. R. Pering, D. Ghosh, P. Kubiak, A. B. Walker, S. E. Lewis, A. L. Johnson, P. J. Baker, M. S. Islam, and P. J. Cameron. Partial cation substitution reduces iodide ion transport in lead iodide perovskite solar cells. *Energy Environ. Sci.*, 12:2264–2272, 2019.

[45] M. Amores, P. J. Baker, E. J. Cussen, and S. A. Corr. Na$_{1.5}$La$_{1.5}$TeO$_6$: Na^+ conduction in a novel Na-rich double perovskite. *Chem. Commun.*, 54:10040–10043, 2018.

[46] D. Z. C. Martin, A. R. Haworth, W. L. Schmidt, P. J. Baker, R. Boston, K. E. Johnston, and N. Reeves-McLaren. Evaluating lithium diffusion mechanisms in the complex spinel Li$_2$NiGe$_3$O$_8$. *Phys. Chem. Chem. Phys.*, 21:23111–23118, 2019.

[47] I. McClelland, B. Johnston, P. J. Baker, M. Amores, E. J. Cussen, and S. A. Corr. Muon Spectroscopy for Investigating Diffusion in Energy Storage Materials. *Annu. Rev. Mater. Res.*, 50:1–15, 2020.

[48] H. El-Shinawi and J. Janek. Low-temperature synthesis of macroporous $LiTi_2(PO_4)_3$/C with superior lithium storage properties. *RSC Advances*, 5:14887–14891, 2015.

[49] K. Momma and F. Izumi. VESTA 3 for three-dimensional visualization of crystal, volumetric and morphology data. *J. Appl. Cryst.*, 44:1272–1276, 2010.

[50] O. Arnold, J. C. Bilheux, J. M. Borreguero, A. Buts, S. I. Campbell, L. Chapon, M. Doucet, N. Draper, R. Ferraz Leal, M. A. Gigg, V. E. Lynch, A. Markvardsen, D.J. Mikkelson, R. L. Mikkelson, R. Miller, K. Palmen, P. Parker, G. Passos, T. G. Perring, P. F. Peterson, S. Ren, M. A. Reuter, A. T. Savici, J. W. Taylor, R. J. Taylor, R. Tolchenov, W. Zhou, and J. Zikovsky. Mantid - Data analysis and visualization package for neutron scattering and μSR experiments. *Nucl. Instrum. Meth. A*, 764:156–166, 2014.

[51] M. Catti, A. Comotti, and S. Di Blas. High-Temperature Lithium Mobility in α-$LiZr_2(PO_4)_3$ NASICON by Neutron Diffraction. *Chem. Mater.*, 15:1628–1632, 2003.

[52] (E. Holzschuh, A. B. Denison, W. Kündig, P. F. Meier, and B. D. Patterson. Muon-spin-rotation experiments in orthoferrites. *Phys. Rev. B*, 27:5294–5307, 1983.

[53] A. Keren. Generalization of the Abragam relaxation function to a longitudinal field. *Phys. Rev. B: Condens. Matter Mater. Phys.*, 50:10039–10042, 1994.

[54] R. S. Hayano, Y. J. Uemura, J. Imazato, N. Nishida, T. Yamazaki, and R. Kubo. Zero-and low-field spin relaxation studied by positive muons. *Phys. Rev. B*, 20:850–859, 1979.

[55] J. Sugiyama, H. Nozaki, I. Umegaki, K. Mukai, S. P. Cottrell, S. Shiraki, T. Hitosugi, Y. Sassa, A. Suter, Z. Salman, T. Prokscha, and M. Månsson. μ^+SR Study on Li Ionic Conductors. *JPS Conf. Proc.*, 21:14–17, 2018.

[56] N. J. Stone. Table of nuclear magnetic dipole and electric quadrupole moments. *At. Data Nucl. Data Tables*, 90:75—176, 2005.

[57] M. Amores, T. E. Ashton, P. J. Baker, E. J. Cussen, and S. A. Corr. Fast microwave-assisted synthesis of Li-stuffed garnets and insights into Li diffusion from muon spin spectroscopy. *J. Mater. Chem. A*, 4:1729–1736, 2016.

[58] H. Nozaki, M. Harada, S. Ohta, I. Watanabe, Y. Miyake, Y. Ikedo, N. H. Jalarvo, E. Mamontov, and J. Sugiyama. Li diffusive behavior of garnet-type oxides studied by muon-spin relaxation and QENS. *Solid State Ion.*, 262:585–588, 2014.

[59] J. Sugiyama, K. Mukai, H. Nozaki, M. Harada, K. Kamazawa, Y. Ikedo, M. Månsson, O. Ofer, E. J. Ansaldo, J. H. Brewer, K. H. Chow, I. Watanabe, Y. Miyake, and T. Ohzuku.

Lithium Diffusion in Lithium-Transition-Metal Oxides Detected by μ^+SR. *Phys. Procedia*, 30:105–108, 2012.

[60] A. Aatiq, M. Ménétrier, L. Croguennec, E. Suard, and C. Delmas. On the structure of $Li_3Ti_2(PO_4)_3$. *J. Mater. Chem.*, 12:2971–2978, 2002.

[61] A. Martínez-Juárez, C. Pecharromán, J. E. Iglesias, and J. M. Rojo. Relationship between activation energy and bottleneck size for Li^+ ion conduction in NASICON materials of composition LiMM'$(PO_4)_3$; M, M' = Ge, Ti, Sn, Hf. *J. Phys. Chem. B*, 102:372–375, 1998.

Supporting Information

In Situ Diffusion Measurements of a NASICON-Structured All-Solid-State Battery Using Muon Spin Relaxation

Innes McClelland,[1,3,4] Samuel G. Booth,[1,4] Hany El-Shinawi,[1,4] Beth I. J. Johnston,[1,4] Jasmin Clough,[2,4] Weimin Guo,[1] Edmund J. Cussen,[2,4] Peter J. Baker,[3,4] and Serena A. Corr*[1,4]

[1] Department of Chemical and Biological Engineering, The University of Sheffield, Sheffield, S1 3JD, UK.

[2] Department of Materials Science and Engineering, The University of Sheffield, Sheffield, S1 3JD, UK.

[3] ISIS Neutron and Muon Source, Science and Technology Facilities Council, Rutherford Appleton Laboratory, Harwell Campus, Didcot, OX11

[4] The Faraday Institution, Quad One, Harwell Campus, OX11 0RA, UK

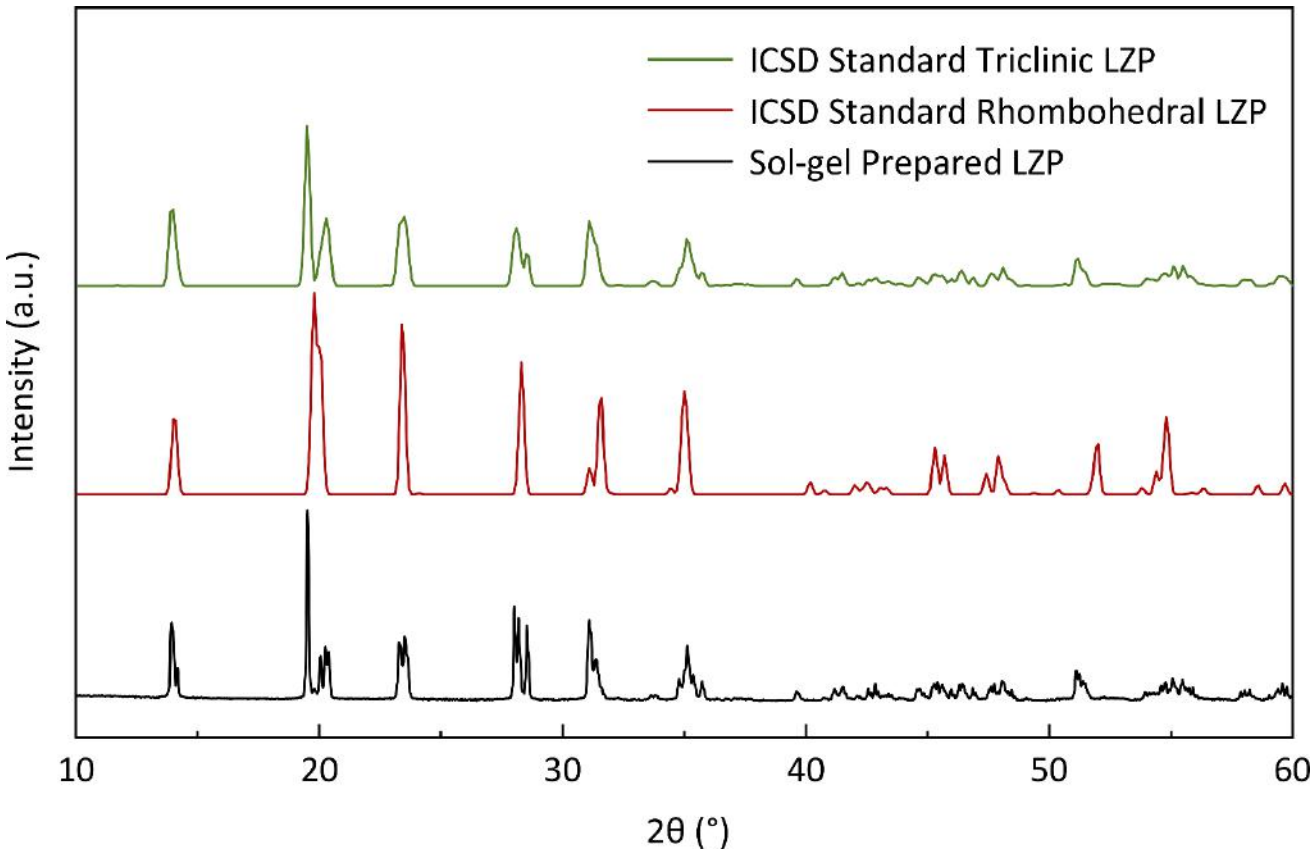

Figure S4.1. Powder X-ray diffraction pattern of $LiZr_2(PO_4)_3$ prepared *via* sol-gel synthesis involving a high calcination temperature. This is compared to an Inorganic Crystal Structure Database standard for both α-type phases [1, 2].

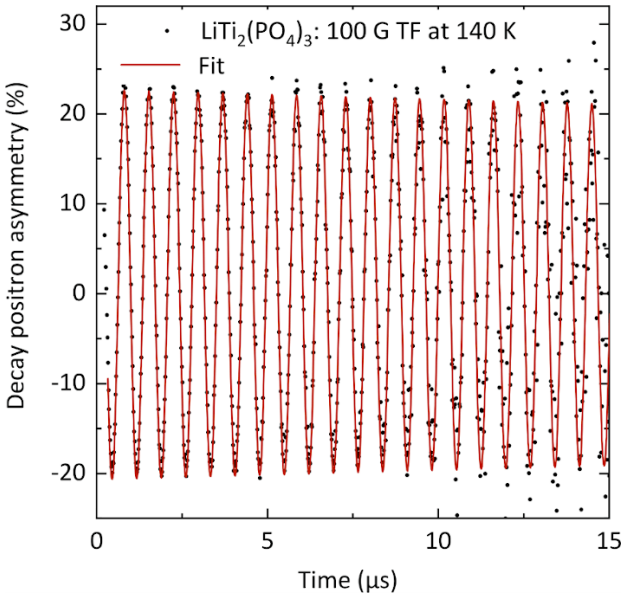

Figure S4.2. Muon spin relaxation measurement of NASICON-structured cathode material $LiTi_2(PO_4)_3$ in a 100 G applied transverse field at 140 K, fit by an oscillating exponentially relaxing function. Very little relaxation is seen in the envelope of the function due to the small internal magnetic fields of the sample and the lack of unpaired electrons. The data becomes noisier at longer time scales due to the exponential decay lifetime of muons; fewer positrons are detected at longer times.

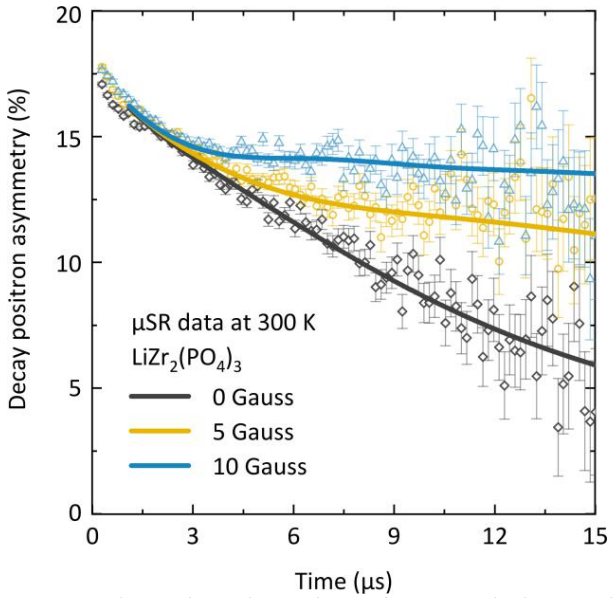

Figure S4.3. Fitted muon spin relaxation data for a pristine solid electrolyte sample $LiZr_2(PO_4)_3$ at 300 K. Fitting was completed within a time range of 1 - 25 μs. The sample was measured in externally applied longitudinal fields of 0, 5, and 10 G. The asymmetry is preserved at higher applied fields as the muon is gradually decoupled from its local magnetic environment and aligns with the external field, which is applied along the direction of initial muon spin polarization.

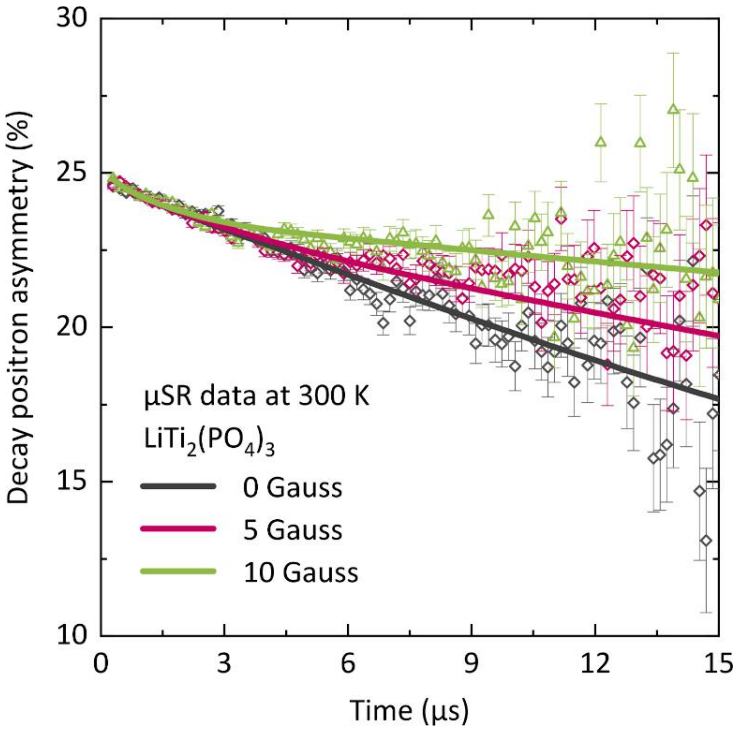

Figure S4.4. Fitted muon spin relaxation data for a pristine sample of cathode material $LiTi_2(PO_4)_3$ at 300 K. The sample was measured in externally applied longitudinal fields of 0, 5, and 10 G.

Calculating Δ at Potential Muon Stopping Sites

To understand the different strengths of the static field distribution width, Δ, found experimentally for the two different phases of LZP, Equation S4.1 was used to find Δ computationally on a (41×41×50) grid of points through the unit cell for z ≤ 0.5 [3].

$$\Delta^2 = \frac{2}{3}\mu_0^2\gamma_\mu^2\hbar^2\sum_i \frac{I_i(I_i+1)\gamma_i^2}{r_i^6} \quad \text{(S4.1)}$$

Equation S4.1 calculates Δ for a given site, where γ_μ is the muon's gyromagnetic ratio, I_i and γ_i are the spin and the nuclear gyromagnetic ratio of the i^{th} nucleus, respectively, and r_i is the distance between the i^{th} nucleus and the muon site.

The sum was evaluated for nuclei within a radius of ten-times the longest unit cell parameter from the point being calculated, in excess of the distance within which these fields contribute measurably to the observed signal. The positively charged muons generally stop in the vicinity of negative ions within a material, and so plausible oxide ions in the structure were considered as potential muon site hosts. Muon sites were thus searched for ~1 Å away from these oxide

ion hosts. The distance 1 Å is assumed based on the OH^- bond length, ~0.97 Å, and the results of detailed muon studies using multiple approaches to find muon stopping sites such as by Holzschuh *et al.* [4].

Triclinic $LiZr_2(PO_4)_3$

12 oxygen symmetric sites in the unit cell [1], 4 considered:

Table S4.1. Symmetric oxygen sites and their fractional coordinates within the unit cell of triclinic LZP [1].

Oxygen symmetric site	**Fractional coordinate, x**	**Fractional coordinate, y**	**Fractional coordinate, z**
O4	0.3724	0.4327	0.2769
O6	0.4393	0.1071	0.3099
O11	0.7550	0.1463	0.2470
O12	0.5721	0.1477	0.2257

Table S4.2. Details of potential muon stopping sites and their respective host oxygen symmetric site for triclinic LZP. The Δ values for each site plus an average over 12 potential sites is given.

Host oxygen site	**Fractional coordinate, x**	**Fractional coordinate, y**	**Fractional coordinate, z**	**Δ (μs^{-1})**
O4	0.325	0.500	0.270	0.255
O4	0.325	0.500	0.280	0.248
O6	0.450	0.075	0.300	0.268
O6	0.475	0.125	0.300	0.237
O6	0.450	0.075	0.300	0.249
O6	0.475	0.125	0.310	0.221
O6	0.475	0.075	0.320	0.228
O11	0.800	0.175	0.240	0.272
O11	0.800	0.175	0.250	0.274
O12	0.550	0.125	0.230	0.212
Average				**0.246**

Rhombohedral $LiZr_2(PO_4)_3$

2 oxygen symmetric sites in the unit cell [2], 2 considered:

Table S4.3. Symmetric oxygen sites and their fractional coordinates within the unit cell of rhombohedral LZP [2].

Oxygen symmetric site	**Fractional coordinate, x**	**Fractional coordinate, y**	**Fractional coordinate, z**
O1	0.1853	-0.0116	0.1937
O2	0.1968	0.1718	0.0848

Table S4.4. Details of potential muon stopping sites and their respective host oxygen symmetric site for rhombohedral LZP. The Δ values for each site plus an average over 7 potential sites is given.

Host oxygen site	**Fractional coordinate, x**	**Fractional coordinate, y**	**Fractional coordinate, z**	**Δ (μs^{-1})**
O1	0.225	0.000	0.200	0.225
O1	0.225	0.025	0.200	0.195
O1	0.225	0.100	0.200	0.225
O1	0.275	0.100	0.190	0.183
O1	0.275	0.000	0.190	0.183
O2	0.275	0.200	0.080	0.194
O2	0.475	0.075	0.320	0.189
Average				**0.199**

In conclusion, these calculations appear to find sites near host oxygen ions where muons may be likely to stop within each structure. Although not all oxygen sites have been considered, as there are few outliers for the sites in question, the sites studied correlate very well with experimental data and therefore can be considered representative of the structure and of potential muon stopping sites.

There is a clear difference between the phases of LZP of around 0.047 μs^{-1} which correlates well with the experimental data seen in Figure 4.2b.

Rhombohedral $LiTi_2(PO_4)_3$

2 oxygen sites identified in the unit cell [5]:

Table S4.5. Symmetric oxygen sites and their fractional coordinates within the unit cell of rhombohedral LTP [5].

Oxygen symmetric site	**Fractional coordinate, x**	**Fractional coordinate, y**	**Fractional coordinate, z**
O1	0.1848	0.9957	0.1901
O2	0.3094	0.8311	0.2475

Table S4.6. Details of potential muon stopping sites and their respective host oxygen symmetric site for rhombohedral LTP. The Δ values for each site plus an average over 12 potential sites is given.

Host oxygen site	**Fractional coordinate, x**	**Fractional coordinate, y**	**Fractional coordinate, z**	**Δ (μs^{-1})**
O1	0.250	0.950	0.190	0.189
O1	0.275	0.975	0.190	0.210
O1	0.275	1.000	0.190	0.213
O1	0.275	0.000	0.190	0.213
O2	0.225	0.825	0.240	0.187
O2	0.275	0.850	0.240	0.228
O2	0.325	0.875	0.240	0.212
O2	0.325	0.875	0.250	0.225
Average				**0.210**

***In situ* Li | LZP | LTP cell**

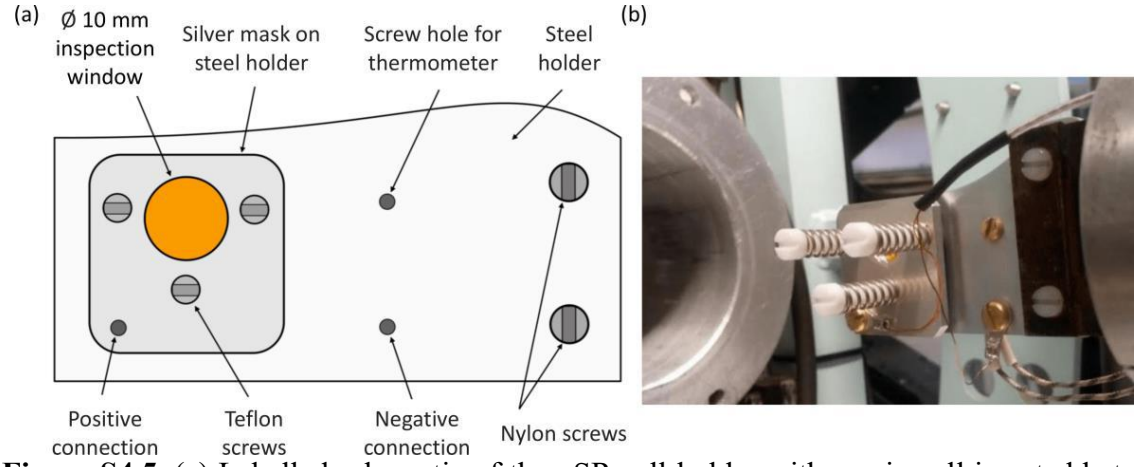

Figure S4.5. (a) Labelled schematic of the μSR cell holder with a coin cell inserted between the positive and negative terminals. Teflon screws were used to hold these terminals in contact with the cell whilst keeping them electrically isolated. Muons were implanted through the Kapton inspection window and into the active material inside the cell. In this experiment, the muons which were implanted inside the cell itself stopped almost all implanted in the solid LZP electrolyte. Nylon screws were used to attach the holder to the closed cycle refrigerator. (b) A picture of the cell holder on EMU, ISIS.

Due to the small inspection window used, data were collected to 50 million positron detection events for each applied field to ensure good quality. A relatively low sample signal was observed due to the experimental set-up. Equation 4.1 was again used for data fitting and was applied in the time range 1-25 s. The asymmetries were fixed to constant values for the fitting.

Table S4.7. Full fitting table for the Li | LZP | LTP *in situ* cell studied, including the temperature values of each measurement.

Voltage discharge stopped at (V)	**Sample Temp. (K)**	**Flat Background Amplitude**	**Dynamic Kubo-Toyabe Amplitude**	**Δ (μs^{-1})**	**ν (μs^{-1})**	**χ^2**
2.13	345.21	0.172 (1)	0.032 (1)	0.247 (3)	0.327 (21)	0.955
1.78	342.772	0.172 (1)	0.032 (1)	0.235 (3)	0.310 (21)	1.043
1.59	345.349	0.172 (1)	0.032 (1)	0.229 (3)	0.346 (24)	1.024
1.37	345.355	0.172 (1)	0.032 (1)	0.238 (3)	0.339 (23)	1.019
1.12	343.921	0.172 (1)	0.032 (1)	0.211 (2)	0.215 (17)	1.003
0.92	342.834	0.172 (1)	0.032 (1)	0.205 (2)	0.248 (21)	1.002

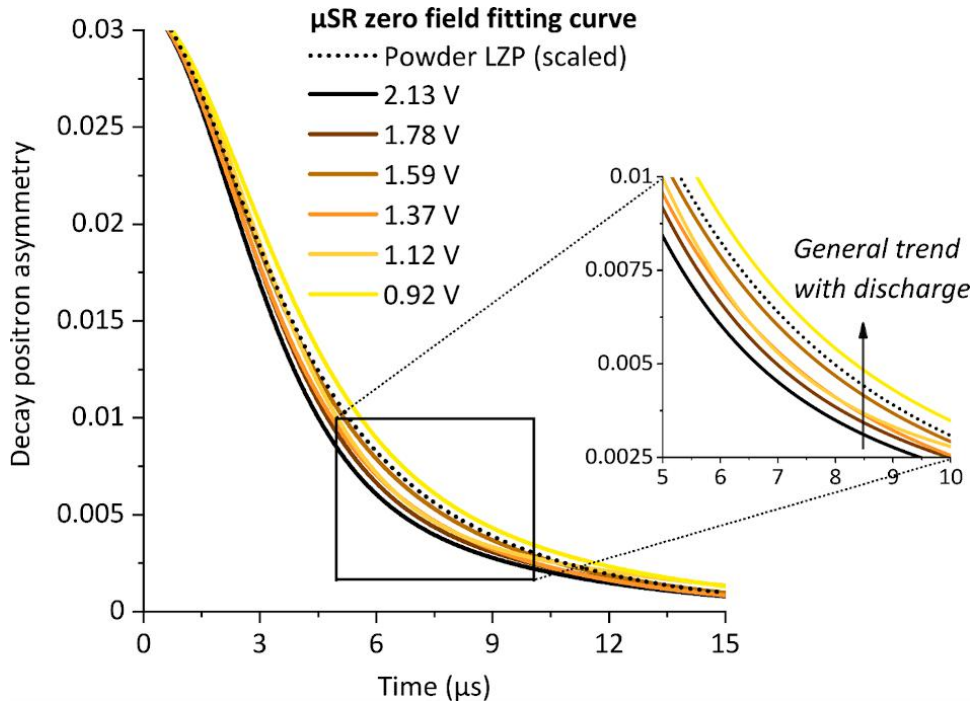

Figure S4.6. A comparison of the zero-field fitting curve of the raw μSR data at each voltage for the *in situ* Li | LZP | LTP cell. The decay positron asymmetry is given as a fraction rather than a decimal here, and low y axis values are observed as the flat background signal has been subtracted from the data. The powder LZP fitting curve at zero field is also shown, and this has been scaled to the same initial asymmetry to compare with the cell data. The general trend with the discharge of the cell is displayed as the muons retain a small amount more spin polarisation with time. This general change seen justifies the trend seen in Δ which gradually decreases with voltage state. The fitting parameters and χ^2 values for the fits are visible in Table S4.7.

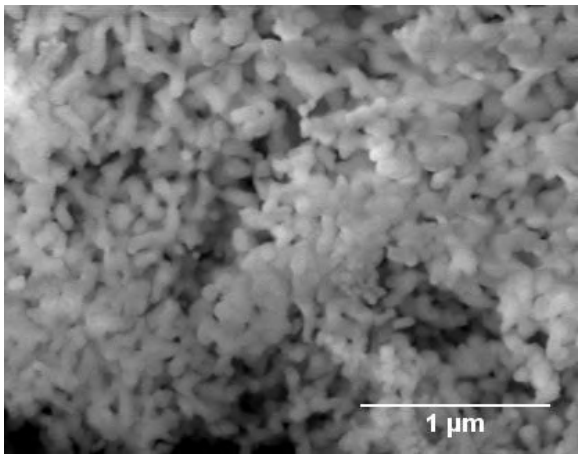

Figure S4.7. Scanning electron microscopy image of the powder cathode material $LiTi_2(PO_4)_3$. A uniform oval particle shape is observed.

Extended X-ray Absorption Fine Structure (EXAFS) Experimental Description:

XAFS measurements were conducted on the ROCK beamline at Synchrotron SOLEIL collecting measurements of the Zn K-edge in fluorescence yield detection mode [6]. The synchrotron at SOLEIL runs at 2.75 GeV. Zn K-edge data was provided by tuning the incoming X-rays with a double bounce single crystal monochromator (Si 220) producing a beam of 470×363 μm. Fluorescence measurements of the dense LZP pellets were collected using a passivated implanted planar silicon detector (PIPS, Canberra). The spectra were collected at a rate of 0.5 Hz, >1000 spectra were combined for each measurement to provide high signal to noise. The collected data was calibrated and normalised using the Demeter software package [7]. Initially, all sample spectra were merged and then calibrated to a Zn foil collected at the same time; the peak of the first derivative was adjusted to the known Zn K-edge energy of 17998 eV. A Hanning-type window was applied to Fourier Transform the *k*-data into *R*-space. The EXAFS data fitting was completed concurrently on the k^1, k^2 and k^3 data using scattering paths from the published α-type LZP crystal structure [1] over a *k* range of 3-14 Å.

Henceforth:

Pristine – A LZP pellet

Cycled interphase – A LZP pellet prepared in a symmetric Li | LZP | Li Swagelok cell and subjected to galvanostatic cycling. The interfacial layer formed on contact between Li and LZP was extended (visually) by cycling. Li was removed from the pellet to expose the surface of the interphase for XAFS measurements. To prevent possible air exposure of the interface, the sample was sealed under argon in a kapton tape package, and this package was placed directly onto the beamline.

Thermal interphase – A LZP pellet was attached to Li foil under Argon. This was sealed in a Swagelok cell and the whole cell was subjected to a heat treatment at 170 ˚C for 12 hours. This accelerated the spontaneous reaction between LZP and Li. The sample was then prepared in the same manner as the *cycled interphase*.

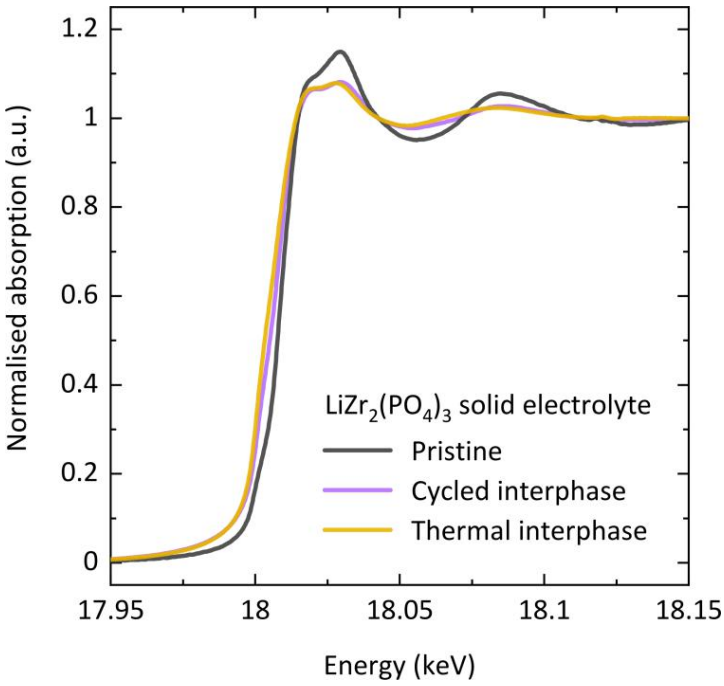

Figure S4.8. Normalised Zr K-edge X-ray absorption spectra collected in fluorescence yield detection mode of the solid electrolyte $LiZr_2(PO_4)_3$ in the pristine state, after electrochemical cycling in a symmetric cell, and after thermal treatment in contact with lithium metal. The features at the edge show the significant structural change that occurs on formation of the interphase between LZP and Li metal. The interfacial decomposition to Li_3P and Li_8ZrO_6 clearly alter the local coordination environment of Zr. The thermal and cycled samples showed a similar extent of conversion.

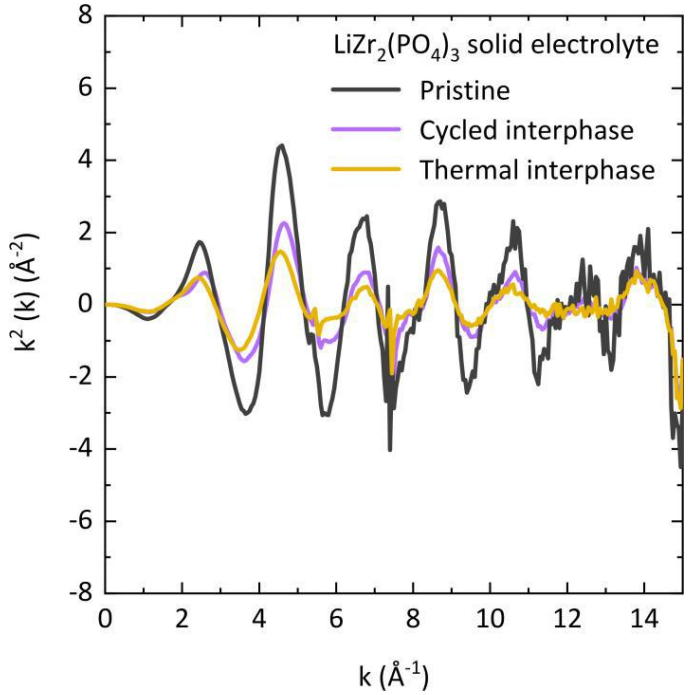

Figure S4.9. k^2 data for the pristine LZP material alongside the cycled and thermally treated samples.

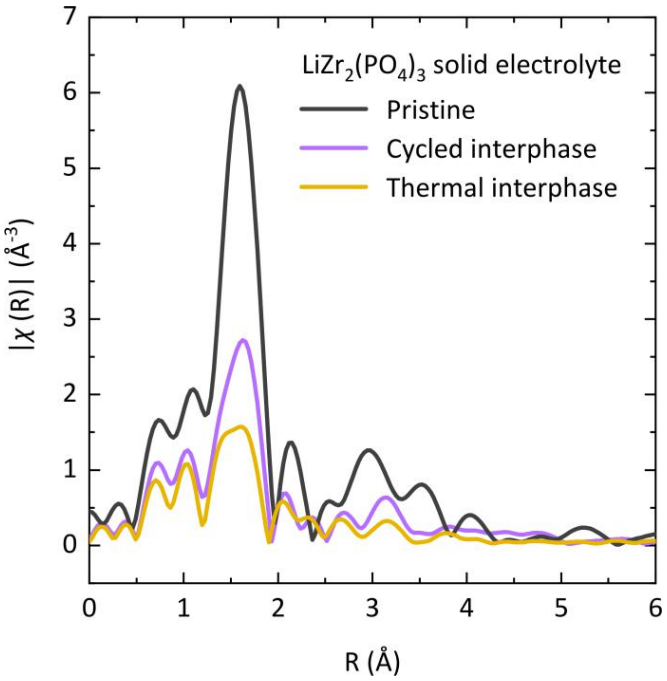

Figure S4.10. *R*-space data for the pristine LZP pellet alongside the cycled and thermally treated samples.

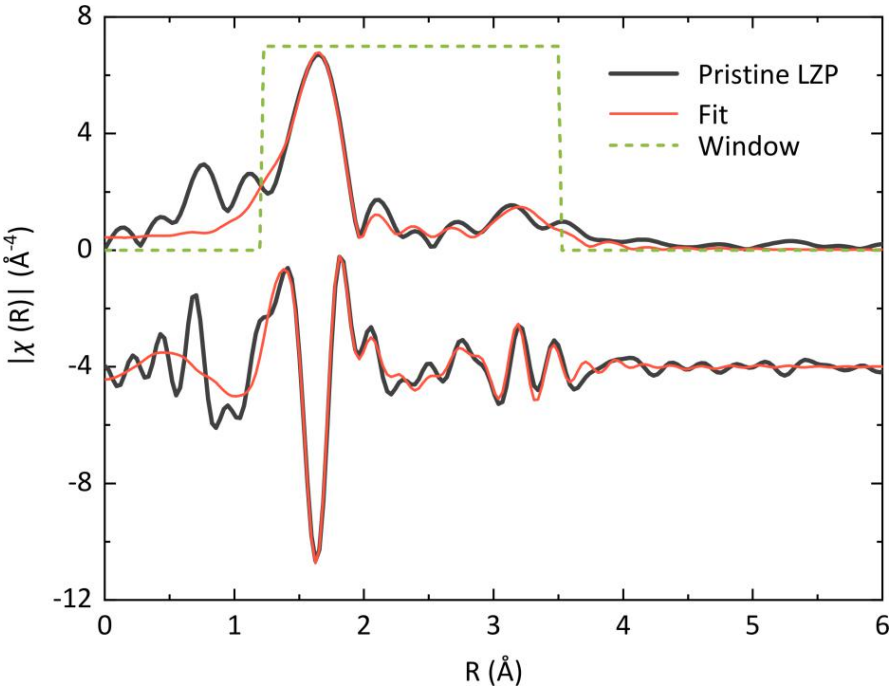

Figure S4.11. Fitted EXAFS data for the pristine LZP sample showing the magnitude and real data (real data has been slightly off set in the y-axis). The fitting range is marked out by the window (1.2 – 3.5 Å ΔR and 3 – 14 Å^{-1} Δk). The paths used to fit the data are included in Table S4.8.

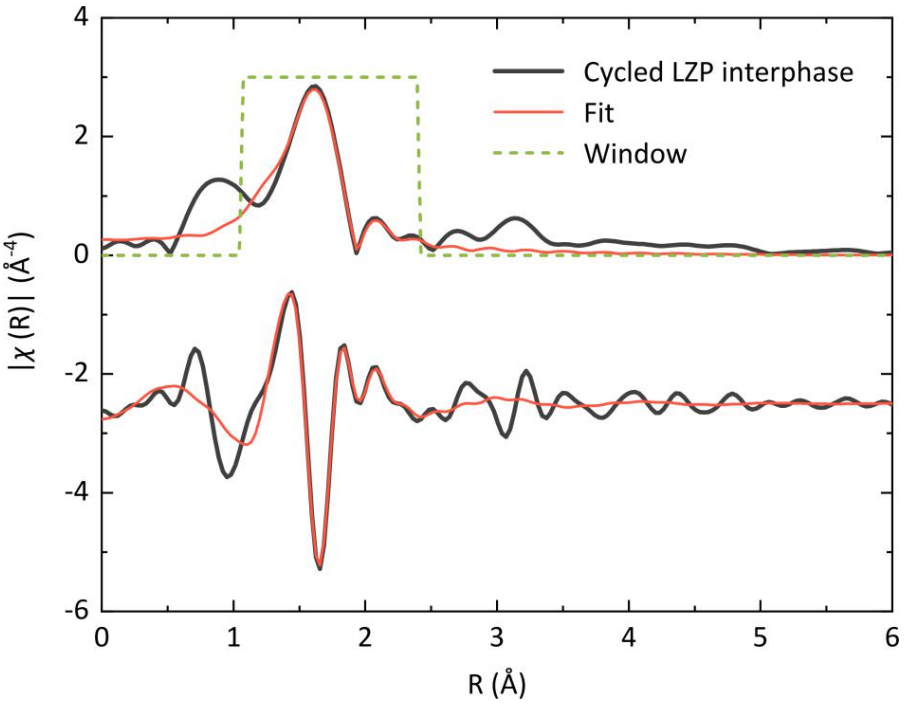

Figure S4.12. Fitted EXAFS data for the cycled LZP material showing the magnitude and real data (real data has been slightly off set in the y-axis). The fitting range is marked out by the window (1.1 – 2.4 Å ΔR and 3 – 14 Å^{-1} Δk). The paths used to fit the data are included in Table S4.9. The cycled material shows a clear reduction in the first shell coordination number suggesting a loss of oxygen. The precise species has not been resolved.

Table S4.8. EXAFS fitting result for pristine LZP between 1.2-3.5 Å, or 3-14 Å in the *k*-space data.

Path	**S_0^2**	**E_0 / eV**	**R / Å**	**Debye-Waller Factor**	**Coordination Number**
Zr-O_1	0.66 (± 0.057)	5.09 (± 1.139)	2.055 (± 0.0092)	0.00546 (± 0.001192)	3 (set)
Zr-O_2	Same as Zr-O_1	Same as Zr-O_1	2.080 (± 0.0092)	Same as Zr-O_1	3 (set)
Zr-P	Same as Zr-O_1	Same as Zr-O_1	3.430 (± 0.0213)	0.00281 (± 0.002108)	3 (set)
Zr-O-P	Same as Zr-O_1	Same as Zr-O_1	3.519 (± 0.0305)	0.00827 (± 0.003400)	6 (set)

Table S4.9. EXAFS fitting results for cycled LZP interphase between 1.055 - 2.4 Å, or 3 - 14 Å in the *k*-space data.

Path	S_0^2	E_0 / eV	R / Å	Debye-Waller Factor	Coordination Number
Zr-O_1	Set to 0.66	0.42 (± 2.465)	2.077 (± 0.0164)	0.00644 (± 0.001889)	2.82 (± 0.4997)
Zr-Li	Set to 0.66	Same as Zr-O_1	2.508 (± 0.1270)	0.0163 (± 0.01353)	3 (set)

XAS Discussion

Visually, the interphase is formed through contact between the two materials. The extent of conversion towards the interfacial layer can be increased through the application of either current or heat. To study surface oxidation and coordination number changes between LZP and the interphase, XAS data was collected on both a pristine LZP pellet and the LZP/Li interphase (Figures S4.8-S4.12). The propagated interphase was prepared *via* both galvanostatic cycling (using a symmetric Li | LZP | Li cell) and heat (thermal treatment of Li attached to an LZP pellet at 170 ˚C for 12 hours). The fluorescence detector mode used for all measurements depends on the X-ray penetration depth and therefore provides a greater contribution from the surface of the pellet. The XANES data displays clear changes in the features following interphase formation in both the cycled and heat-treated interphase samples. The slight shift in the edge position is likely due to the change in the local structure rather than a change in Zr oxidation state. Fitting of the EXAFS data from the pristine and cycled samples indicates a significant reduction in the Zr-O coordination number on formation of the interphase. X-ray absorption spectroscopy demonstrates a clear change as the pristine material is converted to an amorphous material.

Supporting Information References

[1] M. Catti, S. Stramare, R. Ibberson. Lithium location in NASICON-type Li^+ conductors by neutron diffraction. I. Triclinic α'-$LiZr_2(PO_4)_3$. *Solid State Ion.,* 123:173–180, 1999.

[2] M. Catti, A. Comotti, S. D. Blas. High-Temperature Lithium Mobility in α-$LiZr_2(PO_4)_3$ NASICON by Neutron Diffraction. *Chem. Mater.,* 15:1628–1632, 2003.

[3] R. S. Hayano, Y. J. Uemura, J. Imazato, N. Nishida, T. Yamazaki, R. Kubo. Zero and low-field spin relaxation studied by positive muons. *Phys. Rev. B*, 20:850– 859, 1979.

[4] E. Holzschuh, A. B. Denison W. Kündig, P. F. Meier, B. D. Patterson. Muon-spin-rotation experiments in orthoferrites. *Phys. Rev. B.* 27:5294-5307, 1983.

[5] G. J. Redhammer, D. Rettenwander, S. Pristat, E. Dashjav, C. M. N. Kumar, D. Topa, F. Tietz. A single crystal X-ray and powder neutron diffraction study on NASICON-type $Li_{1+x}Al_xTi_{2-x}(PO_4)_3$ ($0 \leq x \leq 0.5$) crystals: Implications on ionic conductivity. *Solid State Sci.*, 60:99-107, 2016.

[6] V. Briois, C. La Fontaine, S. Belin, L. Barthe, Th. Moreno, V. Pinty, A. Carcy, R. Girardot, E. Fonda. ROCK: the new Quick-EXAFS beamline at SOLEIL. *J. Phys.: Conf. Ser*. 712:012149, 2016.

[7] B. Ravel, M. Newville. *ATHENA, ARTEMIS, HEPHAESTUS*: data analysis for X-ray absorption spectroscopy using *IFEFFIT*. *J. Synchrotron Rad.*, 12:537-541, 2005.

Research Article

The Role of the Reducible Dopant in Solid Electrolyte-Lithium Metal Interfaces

Innes McClelland, Hany El-Shinawi, Samuel G. Booth, Jasmin Clough, Sebastian Altus, Anna Regoutz, Edmund J. Cussen, Peter J Baker, and Serena A. Corr

[Innes McClelland, Hany El-Shinawi, Samuel G. Booth, Anna Regoutz, Jasmin Clough, Sebastian Altus, Edmund J. Cussen, Peter J. Baker, and Serena A. Corr. The Role of the Reducible Dopant in Solid Electrolyte-Lithium Metal Interfaces. *Chem. Mater.*, 34:5054–5064, 2022.]

Abstract

Garnet solid electrolytes, of the form $Li_7La_3Zr_2O_{12}$ (LLZO), remain an enticing prospect for solid-state batteries owing to their chemical and electrochemical stability in contact with metallic lithium. Dopants, often employed to stabilize the fast ion conducting cubic garnet phase, typically have no effect on the chemical stability of LLZO in contact with Li metal, but have been found recently to impact the properties of the Li/garnet interface. For dopants more "reducible" than Zr (e.g., Nb and Ti), contradictory reports of either raised or reduced Li/garnet interfacial resistances have been attributed to the dopant. Here, we investigate the Li/LLZO interface in W-doped $Li_7La_3Zr_2O_{12}$ (LLZWO) to determine the influence of a "reducible" dopant on the electrochemical properties of the Li/garnet interface. Single-phase LLZWO is synthesized by a new sol-gel approach and densified by spark plasma sintering. Interrogating the resulting Li/LLZWO interface/interphase by impedance, *in situ* muon spin relaxation and X-ray absorption spectroscopies uncovers the significant impact of surface lithiation on electrochemical performance.

Upon initial contact, an interfacial reaction occurs between LLZWO and Li metal, leading to the reduction of surface W^{6+} centres and an initial reduction of the Li/garnet interfacial resistance. Propagation of this surface reaction, driven by the high mobility of Li^+ ions through the grain surfaces, thickens the resistive interphases throughout the material and impedes Li^+ ion transport between the grains. The resulting high resistance accumulating in the system impedes cycling at high current densities. These insights shed light on the nature of lithiated interfaces in garnet solid electrolytes containing a reducible dopant where high Li^+ ion mobility and the reducible nature of the dopant can significantly affect electrochemical performance.

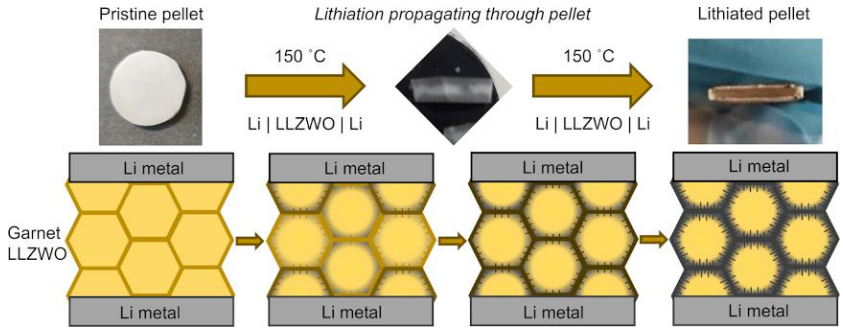

Graphical abstract. The propagation of the interfacial reaction between a garnet solid electrolyte and metallic lithium with applied heat.

Introduction

Doped garnet structured ceramics such as $Li_7La_3Zr_2O_{12}$ (LLZO) are amongst the most attractive commercial candidates for solid electrolyte materials. LLZO demonstrates high ionic conductivities (up to 1 mS cm^{-1} [1]), a large shear modulus (60 GPa [2]) and stability over a wide voltage window [3]. Doped garnet electrolytes may be accessed through traditional synthetic routes [4–8] and processed to high relative densities ($\geq$95%) *via* techniques such as hot-pressing [9] and spark plasma sintering [10–13].

Undoped LLZO has a tetragonal symmetry characterised by Li^+ ordering and limited ion mobility [14]. Conventionally, dopants are employed to disrupt the Li^+ ordering, generating isotropic three-dimensional diffusion pathways by inducing a stable cubic phase [15, 16]. Dopant elements employed thus far include, but are not limited to: Ca^{2+} [17], $Fe^{2+/3+}$ [18], Al^{3+} [19, 20], Ga^{3+} [5], Y^{3+} [21], Si^{4+} [22], Gd^{4+} [23], Ge^{4+} [24], Nb^{5+} [25–27], Ta^{5+} [28, 29], Sb^{5+} [30, 31], W^{6+} [7, 32], and Te^{6+} [33]. The choice of dopant has crucial influence over the resulting garnet properties: elements such as Zn^{2+}, Al^{3+}, and Ga^{3+} preferentially substitute for Li^+; Ti^{4+}, Ge^{4+}, and Ta^{5+} show a tendency to occupy the Zr^{4+} site; Ca^{2+}, Y^{3+}, and Nd^{3+} are most stable on the La^{3+} site [34].

Even when immersed in molten lithium at 300 °C over prolonged periods, doped-LLZO-based solid electrolytes retain their cubic garnet structure [35]. Recently, it has been suggested that doped-LLZO surfaces undergo structural modifications when in contact with Li. These include

the possible formation of an ultrathin oxygen-deficient interphase layer [36], or a tetragonal-like LLZO interphase [37] due to reduction of Zr (and/or the dopant element) which is charge balanced by additional incorporation of Li^+ ions [38]. LLZO phases doped with species more prone to reduction than Zr^{4+} (e.g., Nb^{5+}, Fe^{3+}, Ti^{4+}) undergo discolouration in contact with Li metal, often indicating the formation of a reduced interphase [35, 39–41]. The nature of the reducible dopant significantly influences the properties of any emergent interphase [42, 43]. For example, in the case of Nb-doped LLZO, experimental observations are consistent with the formation of an oxygen-deficient interphase region while DFT calculations suggest the segregation of reduced Nb species to the LLZO surface [36]. Such processes are often associated with significant interfacial impedances which increase over time [36, 40, 44]. Selective doping of LLZO also affords an opportunity to fine-tune the properties of the surface. In one such example, Zhu *et al.* [41] report increased wettability of a Ti-doped LLZO system by Li metal due to the emergence of a reduced interphase containing Ti^{4+}/Ti^{3+} resulting in lower interfacial impedances. They suggest the surface reaction between Ti-LLZO and Li metal enhances the wettability in a manner similar to alloy-formation or intercalation reactions in Li/LLZWO systems modified by metal [45–48] or graphite [49, 50] surface layers, respectively.

Detailed study of these phenomena is often challenging due to the thin and buried nature of the interphases. Here, we demonstrate the muon spin relaxation (μSR) method as a non-invasive, non-destructive, and bulk sensitive technique to directly study the Li/LLZO interphase where we apply W^{6+} as the reducible dopant (LLZWO). Guided by impedance spectroscopy (EIS), μSR affords a unique insight into ionic dynamics and structural properties in the Li/LLZWO interphase; an understanding which can be extrapolated to other Li/LLZMO systems, where M is a reducible dopant.

Experimental

Synthesis and SPS

A sol-gel approach was used to prepare $Li_{7-x}La_3Zr_{2-x}W_xO_{12}$ with $x = 0.4$. Lithium acetate (Sigma Aldrich, 99.95%), lanthanum oxide (Alfa Aesar, 99.99%, pre-dried), zirconium oxynitrate hydrate (Sigma Aldrich, 99.99%) and ammonium tungsten oxide hydrate (Alfa Aesar, 99.999%) were used as starting materials. 10% excess lithium acetate was included to compensate for losses during sintering. Stoichiometic quantities of reagents were dissolved in nitric acid and water under constant mixing. The solvents were evaporated to form a gel, which was burnt, collected, ground, and heated at 550 °C to remove organic carbon residues. The resultant powder was pressed at 1500 kg in a uniaxial hydraulic press and pre-sintered at 900 °C for 6 h. Spark plasma sintering (SPS) experiments were performed using an identical methodology as a previous study from our group [51] with the sintering conditions of 50 °C min^{-1} heating rate to 1090 °C, followed by a 10 minute dwell then cooling.

Characterisation and cell assembly

X-ray diffraction data were collected using a Rigaku Miniflex with a Cu K_α source. Density values were obtained *via* helium gas displacement pycnometry using a Micromeritics AccuPyc II 1340. SEM images and EDX experiments were conducted using an FEI Inspect F50 high resolution electron microscope. For EIS and DC polarization measurements, blocking gold electrodes were applied. For galvanostatic cycling, pellets were sandwiched between two Li foils (Sigma Aldrich, 0.38 mm), pressed at 100 kg, and assembled within a Swagelok cell in an Ar-filled glovebox. Lithium foil was scraped using a stainless-steel blade to ensure optimal contact and a clean surface. AC impedance and galvanostatic cycling measurements were performed using a Biologic VSP potentiostat. To produce "lithiated" pellets (fully reacted with metallic lithium, described in the results section), cells were prepared identically as for galvanostatic cycling measurements, followed by a heat treatment at 150 °C. Origin was used to create all graphs shown, whilst VESTA was used to design unit cell depictions [52].

Muon Spin Relaxation

Muon measurements were completed on the EMU spectrometer at the ISIS Neutron and Muon Source. Temperature-dependent measurements between 150 – 400 K, whereby spin polarized, positively charged muons were implanted into both pristine and lithiated LLZWO to act as a local probe of nearby fluctuating magnetic moments. Longitudinal field measurements of 0, 5, and 10 G were applied alongside 100 G transverse field runs at each temperature. A custom steel cell was used to contain sample pellets, which were polished to around 1.1 mm thick to ensure adequate muon implantation. Any muons not incident on the inspection window were stopped by the silver mask; any consequent signal was subtracted as background. All data analysis was completed using Mantid [53].

X-ray Absorption Spectroscopy and X-ray Photoelectron Spectroscopy

X-ray Absorption Spectroscopy (XAS) measurements were completed using BAG access at the quick XAS beamline B18, at the Diamond Light Source. Measurements were conducted on the W L_3 edge in transmission mode. Samples were mixed thoroughly with cellulose in appropriate quantities and pressed at 500 kg into 13 mm diameter pellets. Pellets were loaded into a rack using Kapton tape and heat-sealed in an Al bag under an Ar atmosphere. Data analysis was completed using the Demeter software package [54].

X-ray photoelectron spectroscopy (XPS) experiments were performed on a Thermo Scientific K-Alpha$^+$ X-ray Photoelectron Spectrometer, which incorporates a monochromated, microfocused Al K_α X-ray source ($h\nu$ = 1486.7 eV) and a 180° double focusing hemispherical analyzer with a 2D detector. Data were collected at 200 eV pass energy for survey and 20 eV pass energy for core level spectra using an X-ray spot size of 400 μm. All data were analyzed using the Avantage software package.

Results and Discussion

Dense ceramics of single-phase W-doped LLZO ($Li_{6.2}La_3Zr_{1.6}W_{0.4}O_{12}$, hereafter referred to as LLZWO) were successfully achieved *via* sol-gel synthesis followed by spark plasma sintering (SPS). A small impurity (∼1.5 wt.%) of Li_6WO_6 was observed in the as-synthesized material but subsequently not distinguishable by X-ray diffraction upon SPS treatment. Figure 5.1a shows X-ray diffraction patterns of an as-synthesized sample and sample post-SPS treatment. The material crystallizes in a cubic garnet structure (Figure 5.1b) with a refined unit cell parameter of a = 12.9294 (4) Å, determined by a Rietveld fit to the XRD data (shown in Figure S5.1). SPS-processed samples possessed relative densities of ≥94 % (see Figure 5.1c), found by He gas pycnometry. EDX mapping through a cross-section of a pellet (Figure 5.1d) revealed a homogeneous distribution of tungsten within the material, consistent with the incorporation of tungsten in the cubic garnet lattice as indicated by XRD [1].

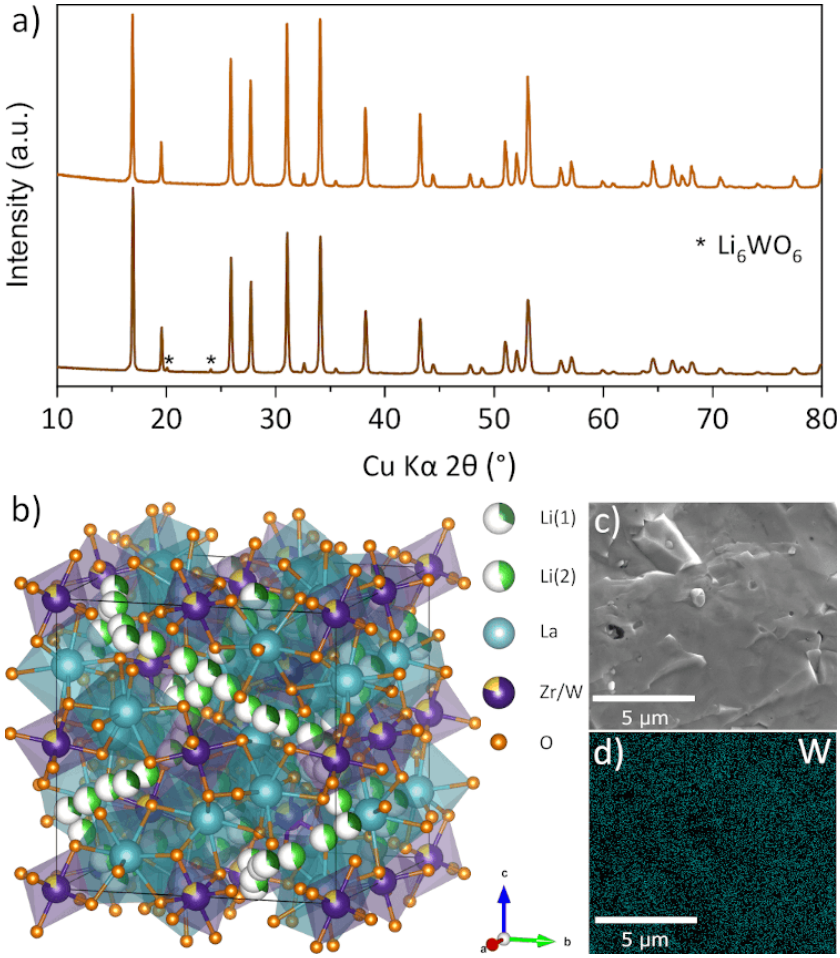

Figure 5.1: (a) X-ray diffraction patterns of sol-gel synthesized (bottom) and SPS-treated (top) $Li_{6.2}La_3Zr_{1.6}W_{0.4}O_{12}$ (LLZWO). A small 1.5 wt.% Li_6WO_6 impurity phase present in the as-synthesized pattern is removed after SPS processing. (b) Unit cell diagram of LLZWO. Li(1) ($24d$) is dark green and tetrahedrally coordinated, Li(2) ($96h$) is light green and octahedrally coordinated, with both sites displaying a vacancy fraction (white). La^{3+} is turquoise and arranges in LaO_8 dodecahedron, and Zr/W is purple/yellow and forms a $[Zr/W]O_6$ octahedra [27]. (c) Cross-sectional SEM image of an SPS pellet and (d) EDS image revealing uniform tungsten dispersion across the sample.

Impedance spectroscopy measurements on LLZWO using blocking gold electrodes revealed a room temperature conductivity of 3×10^{-4} S cm^{-1}, and an activation energy of Li^+ ion transport (E_a) of 0.403 eV in the temperature range 0 – 120 °C. The impedance plot collected at 0 °C is shown in Figure 5.2a. Fitting to these data were performed using the equivalent circuit $[R_1Q_1][R_2Q_2][R_3Q_3][Q_4]$, where $[RQ]$ is a resistor (R) in parallel with a constant phase element $[Q]$. The semi-circle observed at high frequencies ($[R_1Q_1]$) represents the total resistance of the material, with a capacitance, calculated from the fit parameter (Q), of $\sim5\times10^{-11}$ F. The features observed at intermediate/low frequencies ($[R_2Q_2][R_3Q_3]$) possess refined capacitances in the range of $\sim1\times10^{-6}$ F, and therefore likely represent surface/interfacial effects [55, 56]. These features lose definition at higher temperatures (Figure S5.4), complicating the fitting process. A detailed analysis of these features is omitted from this work.

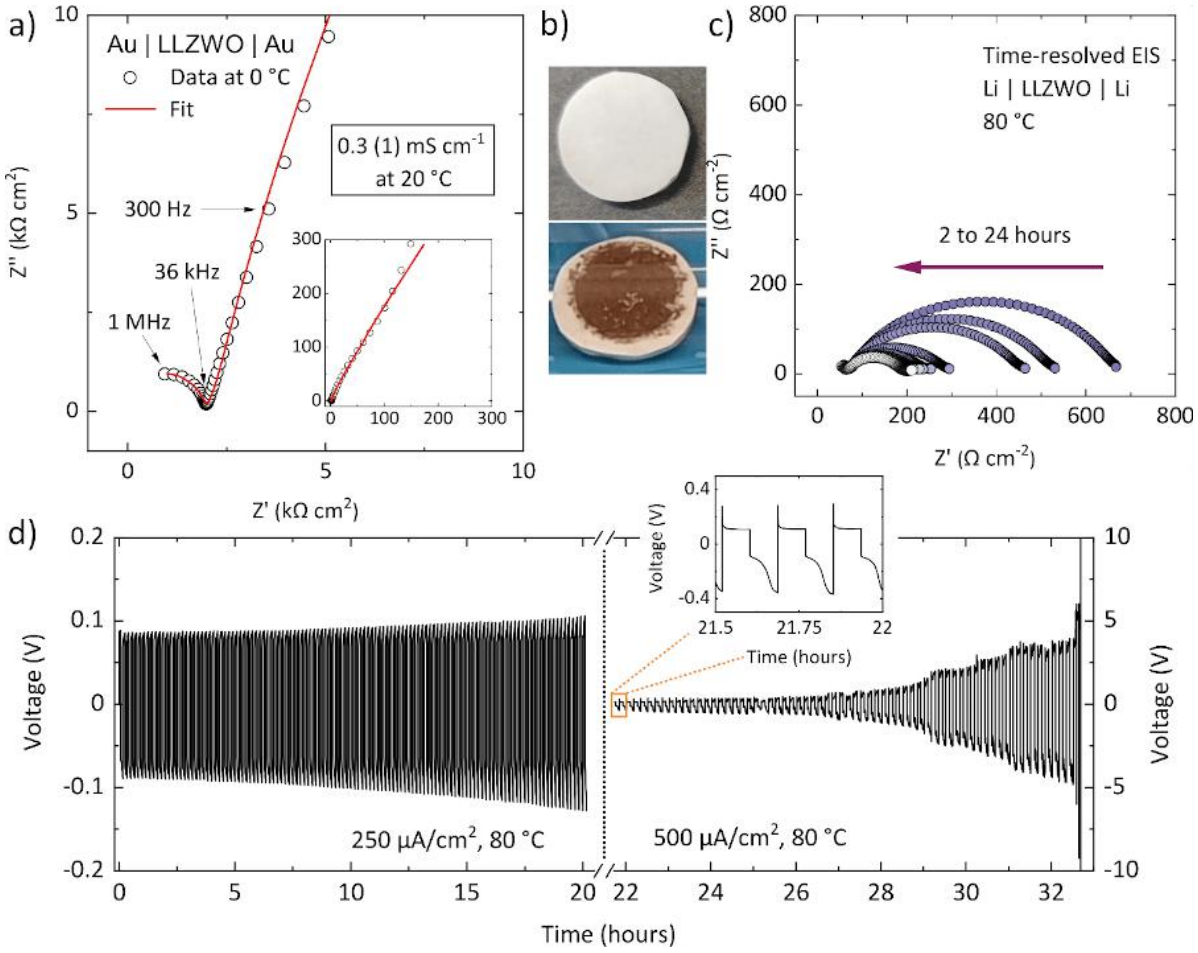

Figure 5.2: (a) Impedance spectroscopy measurement of LLZWO at 0 °C with blocking Au electrodes, fitted using an $[R_1Q_1][R_2Q_2][R_3Q_3][Q_4]$ equivalent circuit. (b) A pristine LLZWO pellet (upper), and the same pellet with brown colouration upon interfacial reaction with metallic Li (below). (c) Time resolved EIS experiment in a symmetric cell with Li electrodes at 80 °C. The interfacial resistance decreases over time before reaching a minimum. The bulk resistance (small semi-circle at high frequency) remains constant. (d) Galvanostatic cycling profile at 80 °C of a Li/LLZWO/Li cell at 250 and 500 μA cm^{-2}. The electrolyte is stable at 250 μA cm^{-2} but its resistance begins to grow upon application of 500 μA cm^{-2} before short-circuiting at 33 hours. Inhomogeneous Li stripping/plating is observed (inset).

To investigate the contribution of electronic conductivity to the total conductivity of LLZWO, a DC polarization measurement was performed between 0.6 and 1.2 V in 0.3 V steps (Figure S5.6) which estimated a partial electronic conductivity of $5(1)\times10^{-10}$ S cm^{-1}. This value, several orders of magnitude lower than the measured conductivity from EIS, suggests a very low contribution from electronic conductivity in the pure material. Furthermore, to examine the effect of W-doping on the "reducibility" of the garnet material, a 70:30 wt.% mixture of LLZWO and conductive carbon (LLZWO/C) was assembled in a half-cell using Li metal as the counter electrode and 1 M $LiPF_6$ (in 1:1 EC/DMC) as a liquid electrolyte. A similar cell containing Ta-doped LLZO (LLZTO/C) was assembled for comparison. The redox stability of Ta-doped garnets is well-documented [36, 39] and this comparison allows us to rule out the consumption of Li^+ in the build-up of the solid-electrolyte interface. Figure S5.7 shows identical discharge profiles of the two half-cells, indicating identical redox activities. Hence, unlike W-containing garnet compound $Li_3Nd_3W_2O_{12}$ [57–59], Li^+ is not simply intercalated into LLZWO/C in the presence of a Li^+ liquid electrolyte. This is attributed to the discontinuity of W centres in the material and is consistent with the low observed electronic conductivity.

In contact with Li metal, LLZWO surfaces undergo faint colouration to a yellowish-brown colour (Figure 5.2b). This turns to a deep brown/black colour upon mild heating to temperatures as low as 80 °C, indicating a surface reaction occurs between LLZWO and metallic lithium. This reaction likely involves the incorporation of Li^+ into the surface grains, associated with the reduction of W^{6+} centres on the surface (confirmed later by XAS, Figure 5.6a). Wolfstein *et al.* have reported chemical colouration of LLZO after heating with Li metal at elevated temperatures, assigning this to the formation of colour centres composed of electrons trapped at oxygen vacancy sites [35]. Colouration of garnets in contact with Li metal is also reported in garnets containing Fe and Nb and was attributed to the reduction of these elements to lower oxidation states [36, 39, 40, 43]. Colouration in these systems often disappears after a short heat treatment in an oxidizing atmosphere, which is also observed for our LLZWO (Figure S5.8).

To investigate the electrochemical properties of the Li/LLZWO interface, symmetric Li/LLZWO/Li cells were constructed and tested at 80 °C. A time-resolved impedance study is shown in Figure 5.2c. The spectra reveal a high-frequency semicircle which agrees well with the total resistance of the pellet measured using gold blocking electrodes (Figure S5.4), and a second semicircle at lower frequency characteristic of Li^+ transport at the Li/LLZWO interface. A significant drop in the interfacial resistance is observed with time, reaching a stable value after 24 h. Hence, under the employed cell preparation and testing conditions, the Li/LLZWO surface reaction supports low interfacial resistances, likely through enhancement of the garnet surface's wettability by Li with the aid of elevated temperature [60]. This is consistent with recent observations of garnet systems containing Ti as the reducible element [41], and also agrees well the improved wettability accessible through other surface reactions, such alloy-formation or Li^+-intercalation in Li/M/garnet or Li/C/garnet systems, respectively [46–49].

To further study the stability of the Li/LLZWO interface during Li-stripping and deposition, symmetric Li/LLZWO/Li cells were cycled at 250 μA cm^{-2} at 80 °C (Figure 5.2d). A small increase in cell resistance (voltage) is observed within 20 hours of cycling, which rose notably

as the current density was increased to 500 μA cm^{-2}. The pellet resistance then grows rapidly after cycling at 500 μA cm^{-2} for more than eight hours. Interestingly, after the galvanostatic cycling experiment, the brown/black colour characteristic of the Li/LLZWO interface was deeply propagated across the pellet and is coupled by a noticeable loss in mechanical properties. Despite the importance of the formation of the Li/LLZWO interface to ensure good contact between Li and LLZWO (as shown in Figure 5.2c), the propagation of the surface reaction through the pellet upon cycling adds a large resistance to the system. This propagation is clearly driven by the high mobility of Li^+ through the pellet under the experimental conditions applied.

We assumed that this highly dynamic state of Li^+ can also be achieved by heating a Li/LLZWO/Li cell at a relatively high temperature (≤melting point of Li) in the absence of electric potential. Interestingly, when a Li/LLZWO/Li cell was heated at 150 °C in the absence of an external electric field, we observed a propagation of the yellowish-brown colour through the LLZWO pellet to an extent dependent on the heating time. To correlate this process with the build-up of resistance during galvanostatic cycling, we heated a freshly prepared symmetric Li/LLZWO/Li cell at 150 °C for set time periods (2 h, 24 h, 48 h and 72 h) and measured the room temperature impedance of the cell afterwards. By the end of the experiment, we observed colouration across the whole pellet (Figure 5.3a). X-ray diffraction data collected of the reacted pellet after lithiation reveal that the material preserves the cubic garnet phase (Figure S5.10).

Figure 5.3b shows the impedance spectra collected from the cell after each heat treatment. The initial impedance of the cell (RT; no heating) is nicely fitted using two [RQ] equivalent circuit components ($[R_1 Q_1][R_2 Q_2]$), corresponding to the total resistance of the pellet and the interfacial resistance. The total resistance here refers to the resistance within the grains (bulk resistance) and in-between the grains (grain-boundary resistance) and agrees well with the total LLZWO pellet resistance measured using gold blocking electrodes. After 2 h heating at 150 °C, the cell displays an initial drop in interfacial resistance consistent with the formation of the Li/LLZWO interface. No change is observed in the high-frequency semicircle, indicating no effect from the interface formation (at this stage) on the bulk and grain-boundary resistances. Upon further heating at 150 °C (for 24 h, 48 h and 96 h), a reduction in size of the high-frequency semicircle and a gradual increase of the low-frequency semicircle were observed. The resistance associated with the high-frequency semicircle is approximately half of the initial (bulk + gain-boundary) resistance and is constant in the three spectra (at 24 h, 48 h and 96 h).

The three spectra were fitted using $[R_1 Q_1][R_2 Q_2][R_3 Q_3]$ equivalent circuits, where two $[RQ]$ terms were required to fit the low-frequency semicircle due to the growth of the interphase (see Figure S5.11 and Table S5.2 for the fitting results). For the three spectra, the capacitance associated with high-frequency semicircle is of the order of 10^{-11} – 10^{-12} F, while the capacitance associated with the low-frequency semicircle is $\sim 10^{-6}$ F. The former capacitance value clearly reflects a contribution from the bulk resistance [55]. These results indicate that the grain-boundary contribution to the resistance has been separated from the bulk resistance, suggesting that the diffusion processes within these areas now occur at different time-scales. The evolution of a new component from the interfacial resistance indicates that the Li^+ transport between the grains likely occurs through modified, more resistive, interfaces, which can be linked to the

propagation of the Li/LLZWO interphase through the pellet. This is schematically represented in Figure 5.3a.

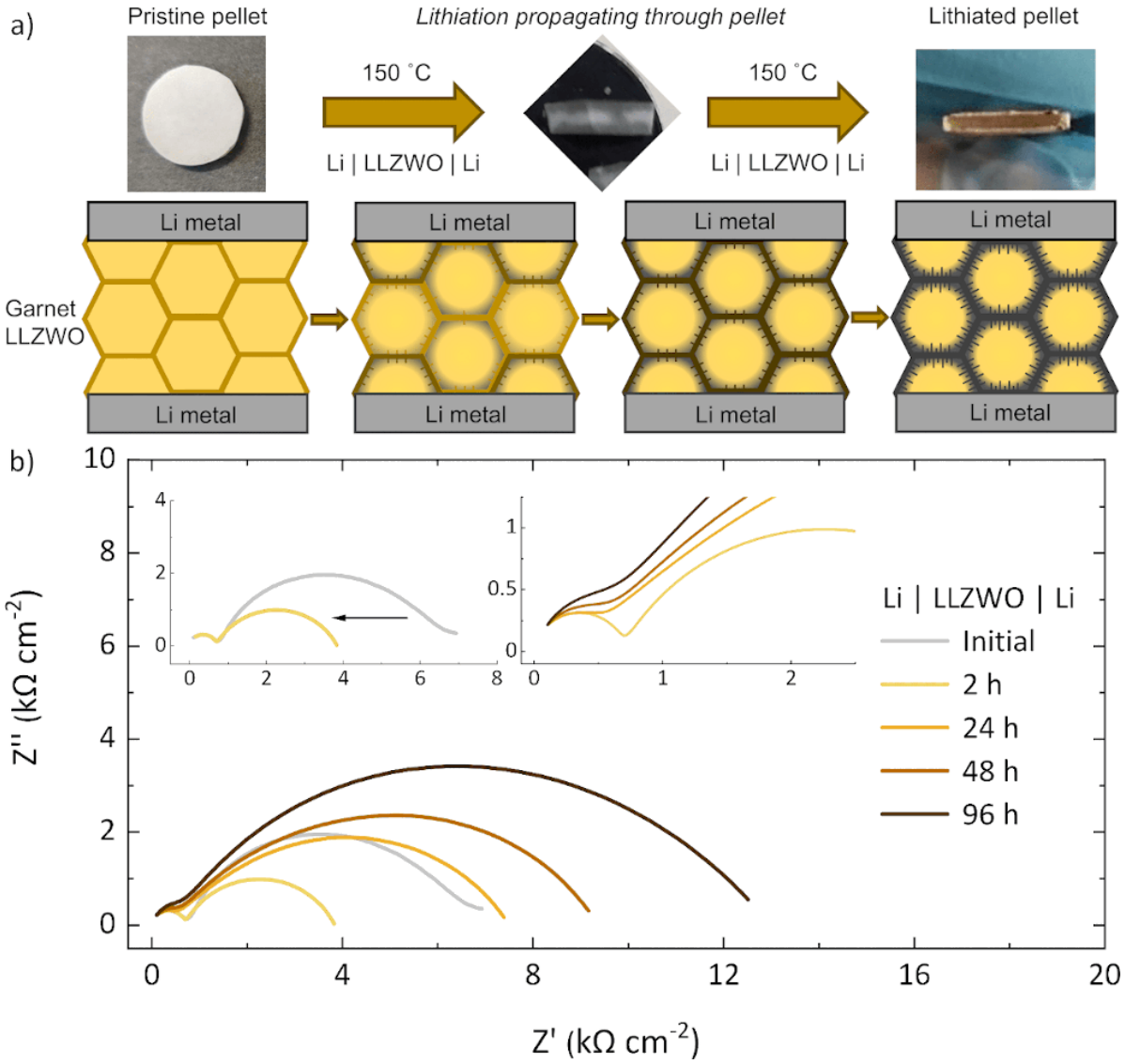

Figure 5.3: (a) Schematic outlining the procession of an interfacial reaction between Li metal and garnet LLZWO. The lithium/LLZWO interfacial reaction is predicted to propagate through the grain surfaces of the material. This reaction can be accelerated at elevated temperature or in an electric field gradient: the former is employed in this study to produce a "lithiated" LLZWO sample, whereby the garnet is fully reacted with metallic lithium. This produces a colour change from white/grey to brown/black throughout the pellet. (b) Experiment wherein a symmetric Li/LLZWO/Li cell was heated to 150 °C for varying time periods, cooled to room temperature, and the impedance spectrum measured. Only the spectra fits are shown here, data with fits are shown in Figure S5.11. The insets in (b) show the magnification of the spectra corresponding to i) the initial reduction of the interfacial resistance (upper left) and ii) the reduction of the resistance of the pellet due to separation of bulk and grain-boundary resistances (upper right).

In this model, a surface modification (called "lithiation" henceforth) of the grains is proposed to describe the interface propagation in LLZWO. In the proposed mechanism, Li^+ is picked up by the W^{6+} centres to drive the surface lithiation of the grains. As shown in Figure 5.3a, contact

between Li and LLZWO initiates a lithiation of the surface grains, promoting good contact between Li metal and LLZWO, and an initial drop of the interfacial resistance (also seen in Figure 5.2c). However, upon full propagation of this surface reaction through the pellet, Li^+ transport between grains is forced to pass through lithiated interfaces, which appear more resistive than the pristine interfaces, and consequently result in an overall build-up of the resistance. It is expected that volume changes associated with the lithiation of the grain surfaces will lead to partial loss of the particle-particle contact (Figure S5.9) and will contribute to the build-up of resistance (which accounts for the brittleness of lithiated pellets). To validate the model in Figure 5.3a, and to confirm the formation of resistive interphases in Li/LLZWO systems, a "lithiated" LLZWO sample was produced from heating a Li/LLWZO/Li cell and was investigated by muon spectroscopy (μSR), XAS, and XPS.

μSR can be applied as a volume-averaged, non-destructive probe to investigate the Li^+ dynamics and internal characteristics [61, 62] of LLZWO before and after lithiation. Longitudinal and transverse fields were applied in the temperature range 150 – 400 K (−123 – 127 °C): the fitting procedures are described in the Supporting Information (Equations S5.1 – S5.4), while plots of fitted data at 317 K (44 °C) are shown in Figure 5.4. Transverse field runs were conducted at 100 Gauss, much higher than the expected internal nuclear field distribution, and thus almost all muon spins are expected to precess in the direction of the applied field. Visually, the pristine sample displays an expected behaviour for a lithium-ion conductor [63]; there is a small relaxation in the envelope of the asymmetry signal likely due to the motion of Li^+ ions. Conversely, the lithiated sample appears to show multiple beating frequencies, indicating two distinct contributions to the signal. Consequently, pristine LLZWO was found to model well to one Gaussian oscillation function (Equation S5.1), whereas post-lithiation two oscillation functions were required (Equation S5.2).

The distinct signals in lithiated LLZWO, displayed in Table 5.1, can be roughly correlated to the bulk and surface regions of the grains, respectively (see Figure 5.4a for a visual interpretation). Muon implantation is volume-averaged (and dependent on density): the signal amplitudes therefore represent the relative volume fraction of each muon environment. Only one symmetrically equivalent oxygen site is known for garnet materials [64], and lithiated LLZWO was confirmed as garnet phase by X-ray diffraction (Figure S5.10), which suggests the dual signal arises from two magnetically distinct volumes rather than two discrete stopping sites with independent magnetic distributions within the unit cell [65]. The amplitudes do not change significantly with temperature (Figure S5.13), implying no significant magnetic ordering in the measured temperature region.

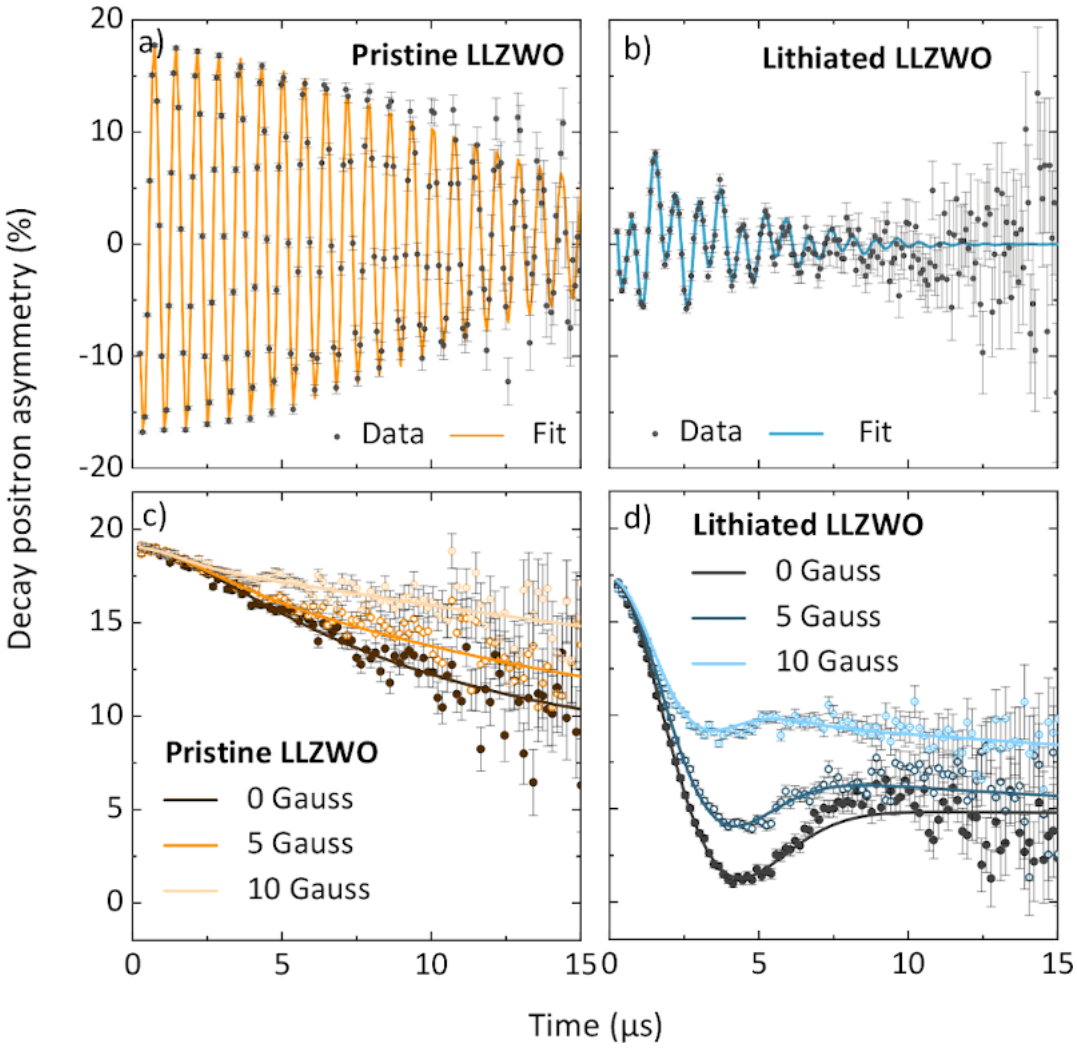

Figure 5.4: Fitted μSR measurements at 317 K (44 °C) of (a) pristine LLZWO in a 100 Gauss transverse field, (b) lithiated LLZWO in a 100 Gauss transverse field, (c) pristine LLZWO in 0, 5, and 10 Gauss applied longitudinal fields, and (d) lithiated LLZWO in 0, 5, and 10 Gauss applied longitudinal fields. The data show highly modified behaviour after LLZWO lithiation, with two precession frequencies visualised in (b) and a quasi-static Li^+ environment evident in (d).

The muon precession frequency in Gaussian oscillation 1 (predicted as the grain surface region) is lowered from the expected Larmor precession in a 100 G applied field (~1.35 MHz), while the relaxation rate (σ) is significantly increased. The nuclear magnetic fields present [66] are insufficiently strong to produce this frequency of oscillation (0.564 MHz) [67], meaning it is likely an electronic effect. Muonium formation (μ^+e^- [68]) upon implantation is well known for insulating and semiconducting materials [62, 69] and can undergo variable strengths of hyperfine coupling. Intercalated Li^+ (linked with reduced W) adds competing electron density and hence some implanted muons will not chemically bind with oxygen as expected, but will instead form muonium states [68]. Muonium associated with concentrated electron centres (similar to shallow donor states [70]) in oxygen vacancies, postulated to cause the interphase discolouration, would have a lower hyperfine coupling energy and cause the oscillation frequency shift to 0.564 (2) MHz. Furthermore, muonium states not associated with electron centres will have a large hyperfine

coupling [71] and thus will undergo a rapid spin relaxation, causing the loss of signal amplitude observed for the lithiated sample.

Table 5.1: Fitting results for a 100 Gauss transverse field measurement at 317 K (44 °C).

Material	Function	Gaussian Amplitude	Relaxation rate, σ (μs^{-1})	Frequency (MHz)	Phase, Φ	Flat Background	χ^2
Pristine LLZWO	Gaussian Oscillation	0.1794 (4)	0.0704 (9)	1.3939 (2)	0.035 (3)	0.0058 (2)	1.07
Lithiated LLZWO	Gaussian Oscillation 1	0.0463 (6)	0.283 (6)	0.564 (2)	0.26 (2)	0.0051 (3)	1.22
	Gaussian Oscillation 2	0.0711 (5)	0.159 (3)	1.350 (7)	-0.041 (9)		

To elucidate the rate of Li^+ ion diffusion and characteristic nuclear magnetic environment, longitudinal fields were applied. As electronic fields are generally stronger than nuclear fields, weak longitudinal fields can distinguish between the two [72, 73]. A 10 Gauss applied field was sufficient to largely decouple the nuclear dipole interaction of the muons, indicating a relatively weak characteristic nuclear magnetic environment in LLZWO. Data for pristine LLZWO were fitted using a Dynamic Kubo-Toyabe function [72] (Equation S5.3), while the evidence of a dual muon environment predicated an additional Gaussian relaxation for lithiated LLZWO (Equation S5.4). At 317 K, pristine LLZWO exhibits a slow relaxation rate, indicating fast Li^+ dynamics. Conversely, lithiated LLZWO appears to follow the form of the static Kubo-Toyabe function, whereby a fast relaxation is followed by a return to around 1/3 of initial asymmetry [72]. However, a gradual decrease in asymmetry at longer time scales ($\geq$8 μs) indicate the presence of dynamical Li^+, albeit at a lesser rate than observed for pristine LLZWO.

The field fluctuation rate, ν, was obtained *via* longitudinal field fitting and provides a direct analogy to the lithium hopping rate [74]. At low temperature, most Li^+ cannot overcome motional barriers; the onset of diffusion is observed to occur at around 250 K (−23 °C) for both samples, above which ν increases exponentially. Given the crystal structure remains similar (Figure S5.10), ν can be compared directly. There is an order of magnitude difference in ν between pristine and lithiated LLZWO (Figure 5.5), informing that Li^+ diffusion occurs far more rapidly pre-lithiation, in agreement with the formation of resistive interphases upon lithiation as found *via* EIS. An activation energy for Li^+ diffusion in pristine LLZWO was found *via* an Arrhenius analysis as 120 (3) meV, comparable to other values reported for solid electrolyte materials using μSR [4, 69]. This is lower than that measured by EIS due to the relative lack of grain boundary/surface influences on muons as a local probe.

The temperature evolution of the width of the static internal field distribution (Δ), which is dependent on proximity and size of nearby nuclear dipole moments, is shown in Figure 5.5b. The abundance of isotopes with significant nuclear moments is very low for Zr, W, and O (11, 14, and 0.04% for ^{91}Zr, ^{183}W, and ^{17}O respectively); Li and La will have the greatest influence on Δ [66]. Given no structural contraction is observed (Figure S5.10), the large rise in Δ displayed in Figure 5.5b must be a result of the additional nuclear moments from penetrated Li which act to increase the average field distribution width over the unit cell. Dipolar field calculations

indicate that increased Li occupancy alone cannot account for this large change in Δ, and thus the increased Li content and/or reduction of W likely alters the preferred muon stopping site in the grain surface region. The form of Δ is similar for both samples, indicating similar diffusion processes. The smooth decrease at higher temperatures is similar to previous reports [4, 75–77], signalling a motional narrowing effect caused by Li^+ diffusion.

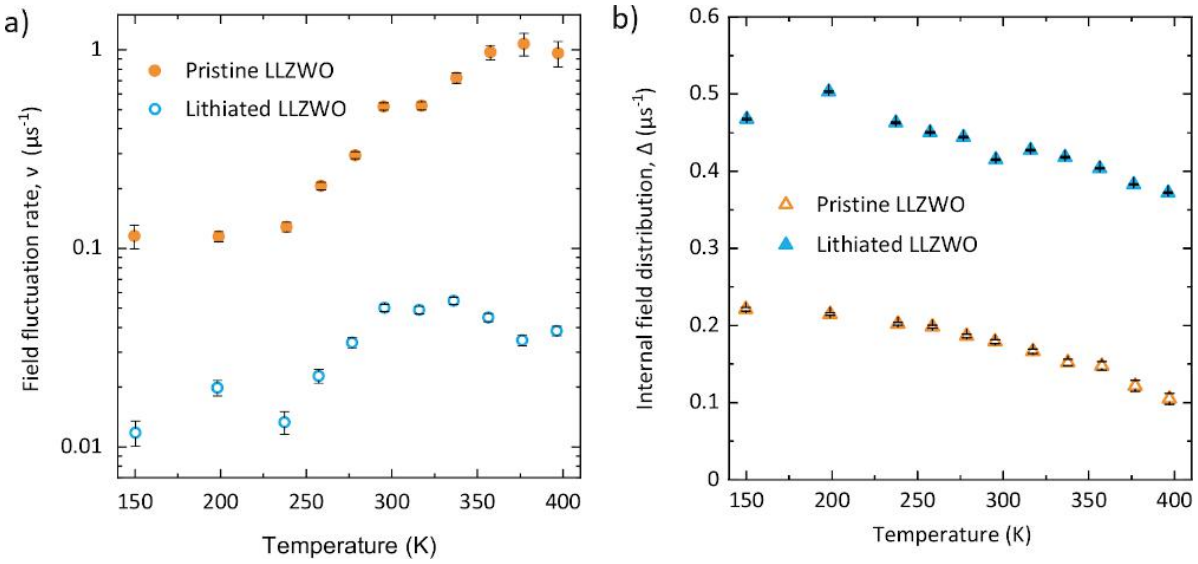

Figure 5.5: (a) The temperature dependence of the field fluctuation rate, ν, which is analogous to the lithium hopping rate. Lithiated LLZWO displays values of ν around an order of magnitude lower than pristine. (b) The temperature dependence of the static internal field distribution width. Δ is a measure of the width of the magnetic field distribution experienced by an implanted muon, governed primarily by the nuclear moment and distance of nearby nuclei. The large increase for lithiated LLZWO strongly suggests a higher Li content.

The diffusion coefficient of Li^+, D_{Li}, was determined as $5.6(5)\times10^{-11}$ cm^2 s^{-1} at 317 K (44 °C) for pristine LLZWO using Equation S5.5, concurring with the fast conductivity observed *via* EIS, and in excellent agreement to other garnet materials studied using μSR [4, 78]. A large reduction in D_{Li} after lithiation is obvious, due to the direct relationship with ν and similar structural parameters. The spatial distribution of ions in the cubic symmetry of garnets permits rapid Li^+ diffusion. Thus, increased Li content rationalises the reduction in ν, as blocked pathways hinder diffusion rates, somewhat resembling conductivity in the tetragonal phase [16, 79]. Chemical reduction of W^{6+} to W^{4+} may also decrease diffusional bottleneck sizes due to the ionic radii increase from 60 to 66 pm and lengthening of the W-O bond [41, 80]. Given the inhomogeneous muon environment and uncertainty over precise Li content it was deemed inappropriate to report a single activation energy or diffusion coefficient for lithiated LLZWO. Indeed, it suffices that the diffusion coefficient is predicted as at least an order of magnitude lower after lithiation. This matches well with galvanostatic cycling experiments (Figure 5.2d) which outline the resistive rise due to the propagation of the interfacial reaction. Under high applied current densities, the Li^+ diffusion coefficient is a limiting factor [81], and thus with the propagation of Li/W reduction the resistive growth rate will increase.

To justify the predicted reduction of W caused by lithiation of the grain surfaces, transmission

mode X-ray Absorption Spectroscopy (XAS) measurements of lithiated LLZWO were collected on the W L_3 edge. Normalized absorption spectra are shown in Figure 5.6 for pristine and lithiated LLZWO, as well as $Li_3Nd_3W_2O_{12}$ (LNWO) as a W^{6+} standard and WO_2 as a W^{4+} standard. LNWO is a low lithium content garnet material which may be used as a low voltage insertion anode due to the well-established reducibility of W^{6+} to W^{4+} under cycling conditions below 1.0 V [57–59]. In this instance it acts as an ideal W^{6+} standard due to the reliability of W^{6+} states in the pristine form and the identical local coordination environment. This is shown experimentally in Figure 5.6, as LNWO matches the edge position and line shape. The split peaks observed for the W^{6+} samples are indicative of the ligand field splitting of $5d$ electron states, generally only distinguishable for octahedrally coordinated W units [82]. WO_2 was employed as a pure W^{4+} standard and displays a smaller, broad peak, with no splitting and a small shift in peak position to a lower energy [83]. The peak intensity of lithiated LLZWO is observed midway between the W^{6+} and W^{4+} standards, while the splitting is dampened somewhat, and a minor but clear peak shift to lower energy is evident. Hence, XAS measurements confirm that partial W reduction has occurred during LLZWO lithiation, producing a mixed $W^{6+/4+}$ oxidation state.

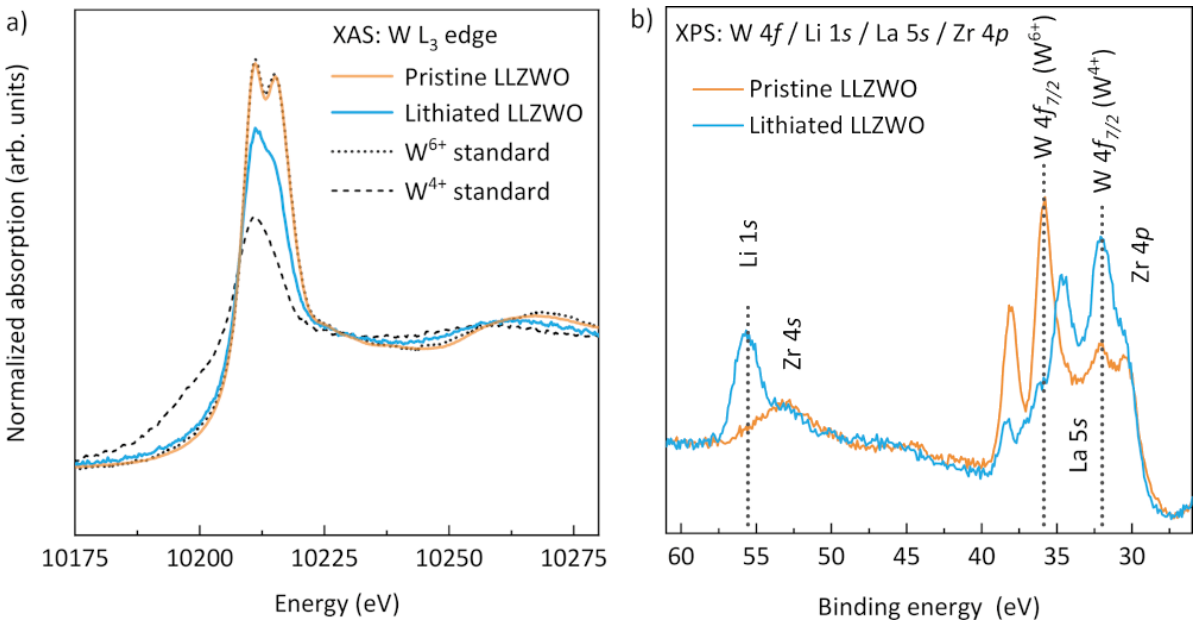

Figure 5.6: X-ray Absorption Spectroscopy (XAS) measurements of the W L_3 edge for pristine and lithiated LLZWO samples, as well as W^{6+} standard $Li_3Nd_3W_2O_{12}$ (LNWO) and W^{4+} standard WO_2. (b) X-ray photoelectron spectroscopy (XPS) spectrum covering the W $4f$ / Li $1s$ / La $5s$ / Zr $4p$ core level spectra. The spectra were normalized to the Zr $3d_{5/2}$ peak area for the respective samples.

This observation is further confirmed by X-ray photoelectron spectroscopy (XPS). Survey spectra for both samples are included in the Supporting Information and show all expected core and Auger lines. The La and Zr core level spectra (Figures S5.17) show only minute changes before and after lithiation and occur at binding energies commensurate with oxide environments. Figure 5.6b shows the binding energy region covering the W $4f$ and Li $1s$ core levels as well as the Zr $4s/4p$ and La $5s$ core levels. A clear increase in the Li $1s$ signal is observed after lithiation.

In parallel, a clear change in tungsten oxidation state occurs from W^{6+} before lithiation to W^{4+} after lithiation. Although it is not possible to determine the quantitative ratio of the two oxidation states due to the complex overall spectra caused by overlap with the Zr and La core levels, the main W $4f_{7/2}$ lines provide clear evidence for the partial reduction also observed in XAS. The W $4d$ spectra (Figures S5.17) displays the same behaviour as the W $4f$ core level and further confirms the partial reduction.

Conclusions

Investigation of buried interfaces in battery materials is a challenging prospect; here we find the LLZWO garnet an excellent candidate for studying the influence of a "reducible" dopant on the electrochemical properties of the Li/garnet interface through a combination of impedance analysis with local structural and dynamic tools. We have successfully followed the propagation of the Li/LLZWO surface reaction throughout the material where an initial decrease in the Li/garnet interfacial resistance indicates good contact between the Li metal and the LLZWO surface. This is followed by a developing large resistance as Li^+ mobility is progressively impeded. Insights from impedance spectroscopy reveal no change in the bulk resistance and a clear evolution of the grain-boundary/interfacial resistances, indicating that a modification is occurring at the grain surfaces. Muon spin relaxation reveals that two distinct environments in LLZWO exist after contact with Li; one of which is characterised by an increased electronic field component and intercalated Li, whose presence is confirmed *via* nuclear magnetic field distribution analysis. Meanwhile, Li^+ diffusion within this region is greatly hindered and contributes to the large resistance observed in the material after lithiation. These results propose a surface lithiation of the garnet grains that produces thick interphases easily detected by muon spectroscopy. Surface lithiation is driven by the high mobility of Li^+ in the system and is believed to occur *via* partial reduction of W^{6+} to W^{4+}, as evidenced by XAS and XPS. This combination of local and bulk characterisation methods has uncovered the role and behaviour of reducible dopants within the Li/garnet interphase, insights which are increasingly important in guiding control over these interfaces for improvements in performance.

Acknowledgements

The authors thank the ISIS Neutron and Muon facility, through the award of beamtime (DOI: 10.5286/ISIS.E.RB1920550), a Facility Development Studentship for IMC, and Josef Lewis Nutter for enabling the experiment. We also thank the Diamond Light Source for the award of beamtime as part of the Energy Materials Block Allocation Group SP14239. This work was supported by the ICSF Faraday Challenge project SOLBAT [Grant FIRG007].

References

[1] V. Thangadurai, S. Narayanan, and D. Pinzaru. Garnet-type solid-state fast Li ion conductors for Li batteries: Critical review. *Chem. Soc. Rev.*, 43:4714–4727, 2014.

[2] M. Pasta, D. Armstrong, Z. L. Brown, J. Bu, M. R. Castell, P. Chen, A. Cocks, S. A. Corr, E. J. Cussen, E. Darnbrough, V. Deshpande, C. Doerrer, M. S. Dyer, H. El-Shinawi, N. Fleck, P. Grant, G. L. Gregory, C. Grovenor, L. J. Hardwick, J. T. S. Irvine, H. J. Lee, G. Li, E. Liberti, I. McClelland, C. Monroe, P. D. Nellist, P. R. Shearing, E. Shoko, W. Song, D. S. Jolly, C. I. Thomas, S. J. Turrell, M. Vestli, C. K. Williams, Y. Zhou, and P. G. Bruce. 2020 roadmap on solid-state batteries. *J. Phys. Energy*, 2:032008, 2020.

[3] T. K Schwietert, V. A. Arszelewska, C. Wang, C. Yu, A. Vasileiadis, N. J. J. de Klerk, J. Hageman, T. Hupfer, I. Kerkamm, Y. Xu, E. van der Maas, E. M. Kelder, S. Ganapathy, and M. Wagemaker. Clarifying the relationship between redox activity and electrochemical stability in solid electrolytes. *Nat. Mater.*, 19:428–435, 2020.

[4] M. Amores, T. E. Ashton, P. J. Baker, E. J. Cussen, and S. A. Corr. Fast microwave-assisted synthesis of Li-stuffed garnets and insights into Li diffusion from muon spin spectroscopy. *J. Mater. Chem. A*, 4:1729–1736, 2016.

[5] H. El-Shinawi and J. Janek. Stabilization of cubic lithium-stuffed garnets of the type "$Li_7La_3Zr_2O_{12}$" by addition of gallium. *J. Power Sources*, 225:5296–5303, 2013.

[6] Z. Hu, H. Liu, H. Ruan, R. Hu, Y. Su, and L. Zhang. High Li-ion conductivity of Al-doped $Li_7La_3Zr_2O_{12}$ synthesized by solid-state reaction. *Ceram. Int.*, 42:12156–12160, 2016.

[7] Y. Li, Z. Wang, Y. Cao, F. Du, C. Chen, Z. Cui, and X. Guo. W-Doped $Li_7La_3Zr_2O_{12}$ Ceramic Electrolytes for Solid State Li-ion Batteries. *Electrochimica Acta*, 180:37–42, 2015.

[8] Q. Liu, Z. Geng, C. Han, Y. Fu, S. Li, Y. He, F. Kang, and B. Li. Challenges and perspectives of garnet solid electrolytes for all solid-state lithium batteries. *J. Power Sources*, 389:120–134, 2018.

[9] E. Rangasamy, J. Wolfenstine, and J. Sakamoto. The role of Al and Li concentration on the formation of cubic garnet solid electrolyte of nominal composition $Li_7La_3Zr_2O_{12}$. *Solid State Ion.*, 206:28–32, 2012.

[10] C. Li, Y. Liu, J. He, and K. S. Brinkman. Ga-substituted $Li_7La_3Zr_2O_{12}$: An investigation based on grain coarsening in garnet-type lithium ion conductors. *J. Alloys Compd.*, 695:3744–3752, 2017.

[11] Y. Zhang, F. Chen, R. Tu, Q. Shen, and L. Zhang. Field assisted sintering of dense Al-substituted cubic phase $Li_7La_3Zr_2O_{12}$ solid electrolytes. *J. Power Sources*, 268:960–964, 2014.

[12] R. Hongahally Basappa, T. Ito, T. Morimura, R. Bekarevich, K. Mitsuishi, and H. Yamada. Grain boundary modification to suppress lithium penetration through garnet-type solid electrolyte. *J. Power Sources*, 363:145–152, 2017.

[13] H. Yamada, T. Ito, and R. Hongahally Basappa. Sintering Mechanisms of High-Performance Garnet-type Solid Electrolyte Densified by Spark Plasma Sintering. *Electrochimica Acta*, 222:648–656, 2016.

[14] S. Afyon, , F. Krumeich, and Jennifer J. L. M. Rupp. A shortcut to garnet-type fast Li-ion conductors for all-solid state batteries. *J. Mater. Chem. A*, 3:18636–18648, 2015.

[15] C. A. Geiger, E. Alekseev, B. Lazic, M. Fisch, T. Armbruster, R. Langner, M. Fechtelkord, N. Kim, T. Pettke, and W. Weppner. Crystal Chemistry and Stability of "$Li_7La_3Zr_2O_{12}$" Garnet: A Fast Lithium-Ion Conductor. *Inorg. Chem*, 50:1089–1097, 2011.

[16] M. Klenk and W. Lai. Local structure and dynamics of lithium garnet ionic conductors: tetragonal and cubic $Li_7La_3Zr_2O_{12}$. *Phys. Chem. Chem. Phys.*, 17:8758–8768, 2015.

[17] S. Song, D. Sheptyakov, A. M. Korsunsky, H. M. Duong, and L. Lu. High Li ion conductivity in a garnet-type solid electrolyte via unusual site occupation of the doping Ca ions. *Mater. Des.*, 93:232–237, 2016.

[18] D. Rettenwander, C. A. Geiger, and G. Amthauer. Synthesis and Crystal Chemistry of the Fast Li-Ion Conductor $Li_7La_3Zr_2O_{12}$ Doped with Fe. *Inorg. Chem*, 52:8005–8009, 2013.

[19] A. Düvel, A. Kuhn, L. Robben, M. Wilkening, and P. Heitjans. Mechanosynthesis of Solid Electrolytes: Preparation, Characterization, and Li Ion Transport Properties of Garnet-Type Al-Doped $Li_7La_3Zr_2O_{12}$ Crystallizing with Cubic Symmetry. *J. Phys Chem. C*, 116:15192–15202, 2012.

[20] A. Kuhn, J. Choi, L. Robben, F. Tietz, M. Wilkening, and P. Heitjans. Li Ion Dynamics in Al-Doped Garnet-Type $Li_7La_3Zr_2O_{12}$ Crystallizing with Cubic Symmetry. *Z. Phys. Chem*, 226:525–537, 2012.

[21] J. Gai, E. Zhao, F. Ma, D. Sun, X. Ma, Y. Jin, Q. Wu, and Y. Cui. Improving the Li-ion conductivity and air stability of cubic $Li_7La_3Zr_2O_{12}$ by the co-doping of Nb, Y on the Zr site. *J. Eur. Ceram. Soc.*, 38:1673–1678, 2018.

[22] Xiaoning Ma, Youlong Xu, Baofeng Zhang, Xu Xue, Chao Wang, Shengnan He, Jun Lin, and Liu Yang. Garnet Si–$Li_7La_3Zr_2O_{12}$ electrolyte with a durable, low resistance interface layer for all-solid-state lithium metal batteries. *J. Power Sources*, 453:227881, 2020.

[23] S. Song, B. Chen, Y. Ruan, J. Sun, L. Yu, Y. Wang, and J. Thokchom. Gd-doped $Li_7La_3Zr_2O_{12}$ garnet-type solid electrolytes for all-solid-state Li-Ion batteries. *Electrochim. Acta*, 270:501–508, 2018.

[24] R. H. Brugge, J. A. Kilner, and A. Aguadero. Germanium as a donor dopant in garnet electrolytes. *Solid State Ion.*, 337:154–160, 2019.

[25] C. Liu, K. Rui, C. Shen, M. E. Badding, G. Zhang, and Z. Wen. Reversible ion exchange and structural stability of garnet-type Nb-doped $Li_7La_3Zr_2O_{12}$ in water for applications in lithium batteries. *J. Power Sources*, 282:286–293, 2015.

[26] Y. Ji, C. Zhou, F. Lin, B. Li, F. Yang, H. Zhu, J. Duan, and Z. Chen. Submicron-Sized Nb-Doped Lithium Garnet for High Ionic Conductivity Solid Electrolyte and Performance of Quasi-Solid-State Lithium Battery. *Materials*, 13:560, 2020.

[27] S. Adams and R. Prasada Rao. Ion transport and phase transition in $Li_{7-x}La_3(Zr_{2-x}M_x)O_{12}$ ($M = Ta^{5+}$, Nb^{5+}, $x = 0, 0.25$). *J. Mater. Chem.*, 22:1426–1434, 2012.

[28] T. Thompson, J. Wolfenstine, J. L. Allen, M. Johannes, A. Huq, I. N. David, and J. Sakamoto. Tetragonal vs. cubic phase stability in Al-free Ta doped $Li_7La_3Zr_2O_{12}$ (LLZO). *J. Mater. Chem. A*, 2:13431–13436, 2014.

[29] X. Chen, T. Cao, M. Xue, H. Lv, B. Li, and C. Zhang. Improved room temperature ionic conductivity of Ta and Ca doped $Li_7La_3Zr_2O_{12}$ via a modified solution method. *Solid State Ion.*, 314:92–97, 2018.

[30] T. Yang, Y. Li, W. Wu, Z. Cao, W. He, Y. Gao, J. Liu, and G. Li. The synergistic effect of dual substitution of Al and Sb on structure and ionic conductivity of $Li_7La_3Zr_2O_{12}$ ceramic. *Ceram. Int.*, 44:1538–1544, 2018.

[31] S. Ramakumar, L. Satyanarayana, S. V. Manorama, and Ramaswamy R. Murugan. Structure and Li+ dynamics of Sb-doped $Li_7La_3Zr_2O_{12}$ fast lithium ion conductors. *Phys. Chem. Chem. Phys.*, 15:11327–11338, 2013.

[32] Y. Luo, X. Li, H. Chen, and L. Guo. Influence of sintering aid on the microstructure and conductivity of the garnet-type W-doped $Li_7La_3Zr_2O_{12}$ ceramic electrolyte. *J. Mater. Sci.: Mater. Electron.*, 30:17195–17201, 2019.

[33] C. Deviannapoorani, L. Dhivya, S. Ramakumar, and R. Murugan. Lithium ion transport properties of high conductive tellurium substituted $Li_7La_3Zr_2O_{12}$ cubic lithium garnets. *J. Power Sources*, 240:18–25, 2013.

[34] L. J. Miara, W. D. Richards, Y. E. Wang, and G. Ceder. First-Principles Studies on Cation Dopants and Electrolyte |Cathode Interphases for Lithium Garnets. *Chem. Mater.*, 27:4040–4047, 2015.

[35] J. Wolfenstine, J. L. Allen, J. Read, and J. Sakamoto. Chemical stability of cubic $Li_7La_3Zr_2O_{12}$ with molten lithium at elevated temperature. *J. Mater. Sci.*, 48:5846–5851, 2013.

[36] Y. Zhu, J. G. Connell, S. Tepavcevic, P. Zapol, R. Garcia-Mendez, N. J. Taylor, J. Sakamoto, B. J. Ingram, L. A. Curtiss, J. W. Freeland, D. D. Fong, and N. M. Markovic. Dopant-Dependent Stability of Garnet Solid Electrolyte Interfaces with Lithium Metal. *Adv. Energy Mater.*, 9:1803440, 2019.

[37] C. Ma, Y. Cheng, K. Yin, J. Luo, A. Sharafi, J. Sakamoto, J. Li, K. More, N. J. Dudney, and M. Chi. Interfacial Stability of Li Metal-Solid Electrolyte Elucidated via in Situ Electron Microscopy. *Nano Lett.*, 16:7030–7036, 2016.

[38] T. Famprikis, P. Canepa, J. A. Dawson, M. S. Islam, and C. Masquelier. Fundamentals of inorganic solid-state electrolytes for batteries. *Nat. Mater.*, 18:1278–1291, 2019.

[39] H. Nemori, Y. Matsuda, S. Mitsuoka, M. Matsui, O. Yamamoto, Y. Takeda, and N. Imanishi. Stability of garnet-type solid electrolyte $Li_xLa_3A_{2-y}$ (A = Nb or Ta, B= Sc or Zr). *Solid State Ion.*, 282:7–12, 2015.

[40] D. Rettenwander, R. Wagner, A. Reyer, M. Bonta, L. Cheng, M. M. Doeff, A. Limbeck, M. Wilkening, and G. Amthauer. Interface Instability of Fe-Stabilized $Li_7La_3Zr_2O_{12}$ versus Li metal. *J. Phys. Chem.*, 122:3780–3785, 2018.

[41] J. Zhu, X. Li, C. Wu, J. Gao, H. Xu, Y. Li, X. Guo, H. Li, and W. Zhou. A Multilayer Ceramic Electrolyte for All-Solid-State Li Batteries. *Angew.*, 60:3781–3790, 2021.

[42] T. Thompson, A. Sharafi, M. D. Johannes, A. Huq, J. L. Allen, J. Wolfenstine, and J. Sakamoto. A Tale of Two Sites: On Defining the Carrier Concentration in Garnet-Based Ionic Conductors for Advanced Li Batteries. *Adv. Energy Mater.*, 5:1500096, 2015.

[43] Y. Kim, A. Yoo, R. Schmidt, A. Sharafi, H. Lee, J. Wolfenstine, and J. Sakamoto. Electrochemical Stability of $Li_{6.5}La_3Zr_{1.5}M_{0.5}O_{12}$ (M = Nb or Ta) against Metallic Lithium. *Front. Energy Res.*, 4:20, 2016.

[44] K. Ishiguro, Y. Nakata, M. Matsui, I Uechi, Y. Takeda, O. Yamamoto, and N. Imanishi. Stability of Nb-Doped $Li_7La_3Zr_2O_{12}$ with Lithium Metal. *J. Electrochem. Soc.*, 160:A1690–A1693, 2013.

[45] K. Fu, Y. Gong, B. Liu, Y. Zhu, S. Xu, Y. Yao, W. Luo, C. Wang, S. D. Lacey, J. Dai, Y. Chen, Y. Mo, E. Wachsman, and L. Hu. Toward garnet electrolyte–based Li metal batteries: An ultrathin, highly effective, artificial solid-state electrolyte/metallic Li interface. *Sci. Adv.*, 3:1–12, 2017.

[46] X. Han, Y. Gong, K. Fu, X. He, G. T. Hitz, J. Dai, A. Pearse, B. Liu, H. Wang, G. Rubloff, Y. Mo, V. Thangadurai, E. D. Wachsman, and L. Hu. Negating interfacial impedance in garnet-based solid-state Li metal batteries. *Nat. Mater.*, 16:572–579, 2017.

[47] W. Luo, Y. Gong, Y. Zhu, Y. Li, Y. Yao, Y. Zhang, K. Fu, G. Pastel, C. Lin, Y. Mo, E. D. Wachsman, and L. Hu. Reducing Interfacial Resistance between Garnet-Structured Solid-State Electrolyte and Li-Metal Anode by a Germanium Layer. *Adv. Mater.*, 29:1606042, 2017.

[48] C. L. Tsai, V. Roddatis, C. V. Chandran, Q. Ma, S. Uhlenbruck, M. Bram, P. Heitjans, and O. Guillon. $Li_7La_3Zr_2O_{12}$ Interface Modification for Li Dendrite Prevention. *ACS Appl. Mater. Interfaces*, 8:10617–10626, 2016.

[49] Y. Shao, H. Wang, Z. Gong, D. Wang, B. Zheng, J. Zhu, Y. Lu, Y. S. Hu, H. Li, X. Huang, Y. Yang, C. W. Nan, and L. Chen. Drawing a Soft Interface: An Effective Interfacial Modification Strategy for Garnet- Type Solid-State Li Batteries. *ACS Energy Lett.*, 3:1212–1218, 2018.

[50] W. Feng, X. Dong, X. Zhang, Z. Lai, P. Li, C. Wang, Y. Wand, and Y. Xia. Li/Garnet Interface Stabilization by Thermal-Decomposition Vapor Deposition of an Amorphous Carbon Layer. *Angew. Chem. Int. Ed.*, 59:5346–5349, 2020.

[51] M. Amores, H. El-Shinawi, I. McClelland, S. R. Yeandel, P. J. Baker, R. I. Smith, H. Y. Playford, P. Goddard, E. J. Cussen, and S. A. Corr. $Li_{1.5}La_{1.5}MO_6$ (M = W^{6+}, Te^{6+}) as a new series of lithium-rich double perovskites for all-solid-state lithium-ion batteries. *Nat. Comm.*, 11:6392, 2020.

[52] K. Momma and F. Izumi. VESTA 3 for three-dimensional visualization of crystal, volumetric and morphology data. *J. Appl. Cryst.*, 44:1272–1276, 2010.

[53] O. Arnold, J. C. Bilheux, J. M. Borreguero, A. Buts, S. I. Campbell, L. Chapon, M. Doucet, N. Draper, R. Ferraz Leal, M. A. Gigg, V. E. Lynch, A. Markvardsen, D.J. Mikkelson, R. L. Mikkelson, R. Miller, K. Palmen, P. Parker, G. Passos, T. G. Perring, P. F. Peterson, S. Ren, M. A. Reuter, A. T. Savici, J. W. Taylor, R. J. Taylor, R. Tolchenov, W. Zhou, and J. Zikovsky. Nuclear Instruments and Methods in Physics Research Section A: Accelerators, Spectrometers, Detectors and Associated Equipment. *Nucl. Instrum. Meth. A*, 764:156–166, 2014.

[54] B. Ravel and M. Newville. ATHENA, ARTEMIS, HEPHAESTUS: data analysis for X-ray absorption spectroscopy using IFEFFIT. *J. Synchrotron Rad.*, 12:537–541, 2005.

[55] J. T. S. Irvine, D. C. Sinclair, and A. R. West. Electroceramics: Characterization by Impedance Spectroscopy. *Adv. Mater.*, 2:132–138, 1990.

[56] H. El-Shinawi, G. W. Paterson, D. A. MacLaren, E. J. Cussen, and S. A. Corr. Low-temperature densification of Al-doped $Li_7La_3Zr_2O_{12}$" a reliable and controllable synthesis of fast-ion conducting garnets. *J. Mater. Chem. A*, 5:319–329, 2017.

[57] H. Xie, K. Park, J. Song, and J. B. Goodenough. Reversible lithium insertion in the garnet framework of $Li_3Nd_3W_2O_{12}$. *Electrochem. Commun.*, 19:135–137, 2012.

[58] R. Satish, V. Aravindan, W. C. Ling, J. B. Goodenough, and S. Madhavi. Carbon-Coated $Li_3Nd_3W_2O_{12}$: A High Power and Low-Voltage Insertion Anode with Exceptional Cycleability for Li-Ion Batteries. *Adv. Energy. Mater.*, 4:1301715, 2014.

[59] M. Luo, H. Yu, X. Cheng, W. Ye, H. Zhu, T. Liu, N. Peng, M. Shui, and J. Shu. Sol-Gel Synthesis and in Situ X-ray Diffraction Study of $Li_3Nd_3W_2O_{12}$ as a Lithium Container. *ACS. Appl. Mater. Interfaces*, 10:12716–12721, 2018.

[60] A. Sharafi H. M. Meyer, J. Nanda, J. Wolfenstine, and J. Sakamoto. Characterizing the Li-$Li_7La_3Zr_2O_{12}$ interface stability and kinetics as a function of temperature and current density. *J. Power Sources*, 302:135–139, 2016.

[61] I. McClelland, B. Johnston, P. J. Baker, M. Amores, E. J. Cussen, and S. A. Corr. Muon Spectroscopy for Investigating Diffusion in Energy Storage Materials. *Annu. Rev. Mater. Res.*, 50:1–15, 2020.

[62] S. J. Blundell. Spin-polarized muons in condensed matter physics. *Contemporary Physics*, 40:175–192, 1999.

[63] J. Sugiyama, H. Nozaki, I. Umegaki, K. Mukai, K. Miwa, S. Shiraki, T. Hitosugi, A. Suter, T. Prokscha, Z. Salman, J. S. Lord, and M. Månsson. Li-ion diffusion in $Li_4Ti_5O_{12}$ and $LiTi_2O_4$ battery materials detected by muon spin spectroscopy. *Phys. Rev. B*, 92:014417, 2015.

[64] H. Buschmann, J. Dölle, S. Berendts, A. Kuhn, P. Bottke, M. Wilkening, P. Heitjans, A. Senyshyn, H. Ehrenberg, A. Lotnyk, V. Duppel, L. Kienle, and J. Janek. Structure and dynamics of the fast lithium ion conductor "$Li_7La_3Zr_2O_{12}$". *Phys. Chem. Chem. Phys.*, 13:19378–19392, 2011.

[65] P. Dalmas De Réotier and A. Yaouanc. Muon spin rotation and relaxation in magnetic materials. *J. Phys. Condens. Matter*, 9:9113–9166, 1997.

[66] N. J. Stone. Table of nuclear magnetic dipole and electric quadrupole moments. *At. Data Nucl. Data Tables*, 90:75—176, 2005.

[67] J. H. Brewer, K. M. Crowe, F. N. Gygax, R. F. Johnson, B. D. Patterson, D. G. Fleming, and A. Schenck. Anomalous μ^+ p Precession in Silicon. *Phys. Rev. Lett.*, 31:143–146, 1973.

[68] S. J. Blundell. Muon-spin rotation studies of electronic properties of molecular conductors and superconductors. *Chem. Rev.*, 104:5717–5735, 2004.

[69] J. Sugiyama, H. Nozaki, I. Umegaki, K. Mukai, S. P. Cottrell, S. Shiraki, T. Hitosugi, Y. Sassa, A. Suter, Z. Salman, T. Prokscha, and M. Månsson. μ^+ SR Study on Li Ionic Conductors. *JPS Conf. Proc.*, 21:14–17, 2018.

[70] S. F. J. Cox, E. A. Davis, S. P. Cottrell, P. J. C. King, J. S. Lord, J. M. Gil, H. V. Alberto, R. C. Vil ao, J. Piroto Duarte, N. Ayres de Campos, A. Weidinger, R. L. Lichti, and S. J. C. Irvine. Experimental Confirmation of the Predicted Shallow Donor Hydrogen State in Zinc Oxide. *Phys. Rev. Lett*, 86:2601–2604, 2001.

[71] S. F. J. Cox. Implanted muon studies in condensed matter science. *J. Phys. C: Solid state Phys.*, 20:3187–3319, 1987.

[72] R. S. Hayano, Y. J. Uemura, J. Imazato, N. Nishida, T. Yamazaki, and R. Kubo. Zero- and low-field spin relaxation studied by positive muons. *Phys. Rev. B*, 20:850–859, 1979.

[73] M. Månsson and J. Sugiyama. Muon-spin relaxation study on Li- and Na-diffusion in solids. *Phys. Scr.*, 88:068509, 2013.

[74] J. Sugiyama, K. Mukai, Y. Ikedo, H. Nozaki, M. Månsson, and I. Watanabe. Li diffusion in Li_xCoO_2 probed by Muon-Spin spectroscopy. *Phys. Rev. Lett.*, 103:147601, 2009.

[75] T. E. Ashton, P. J. Baker, D. Bauer A. R. Groves C. Sotelo-Vazquez T. Kamiyama, T. Matsukawa, K. M. Kojima, and J. A. Darr. Multiple diffusion pathways in $Li_xNi_{0.77}Co_{0.14}Al_{0.09}O_2$ (NCA) Li-ion battery cathodes. *J. Mater. Chem. A*, 8:11545–11552, 2020.

[76] T. E. Ashton, J. V. Laveda, D. A. Maclaren, P. J. Baker, A. Porch, M. O. Jones, and S. A. Corr. Muon studies of Li^+ diffusion in $LiFePO_4$ nanoparticles of different polymorphs. *J. Mater. Chem. A*, 2:6238–6245, 2014.

[77] J. V. Laveda, B. Johnston, G. W. Paterson, P. J. Baker, M. G. Tucker, H. Y. Playford, K. M. Ø. Jensen, S. J. L. Billinge, and S. A. Corr. Structure-property insights into nanostructured electrodes for Li-ion batteries from local structural and diffusional probes. *J. Mater. Chem. A*, 6:127–137, 2018.

[78] H. Nozaki, M. Harada, S. Ohta, I. Watanabe, Y. Miyake, Y. Ikedo, N. H. Jalarvo, E. Mamontov, and J. Sugiyama. Li diffusive behavior of garnet-type oxides studied by muon-spin relaxation and QENS. *Solid State Ion.*, 262:585–588, 2014.

[79] J. Awaka, N. Kijima, H. Hayakawa, and J. Akimoto. Synthesis and structure analysis of tetragonal $Li_7La_3Zr_2O_{12}$ with the garnet-related type structure. *J. Solid State Chem.*, 182:2046–2052, 2009.

[80] A. Balerna, E. Bernieri, and E. Burattini. XANES studies of MeO_{3-x} (Me = W, Re, Ir) crystalline and amorphous oxides. *Nucl. Instrum. Methods. Phys. Res. A*, 308:240–242, 1991.

[81] F. Flatscher, M. Philipp, S. Ganschow, H. Martin R. Wilkening, and D. Rettenwander. The natural critical current density limit for $Li_7La_3Zr_2O_{12}$ garnets. *J. Mater. Chem. A*, 8:15782–15788, 2020.

[82] S. Yamazoe, Y. Hitomi, T. Shishido, and T. Tanaka. XAFS Study of Tungsten L_1- and L_3-Edges: Structural Analysis of WO_3 Species Loaded on TiO_2 as a Catalyst for Photooxidation of NH_3. *J. Phys. Chem. C*, 112:6869–6879, 2008.

[83] U. Jayarathne, P. Chandrasekaran, A. F. Greene, J. T. Mague, S. DeBeer, K. M. Lancaster, S. Sproules, and J. P. Donahue. X-ray Absorption Spectroscopy Systematics at the Tungsten L-Edge. *Inorg. Chem.*, 53:8230–8241, 2014.

Supporting Information

The Role of the Reducible Dopant in Solid Electrolyte-Lithium Metal Interfaces

Innes McClelland [1,2,3]‡, Hany El-Shinawi [3,4]‡, Samuel G. Booth [1,3], Anna Regoutz [5], Jasmin Clough [3,6], Sebastian Altus [3,6], Edmund J. Cussen [3,6], Peter J. Baker [2,3], and Serena A. Cussen [3,6]*

[1] Department of Chemical and Biological Engineering, The University of Sheffield, Sheffield, S1 3JD, UK

[2] ISIS Neutron and Muon Source, Science and Technology Facilities Council, Rutherford Appleton Laboratory, Harwell Campus, Didcot, OX11 0QX

[3] The Faraday Institution, Quad One, Harwell Campus, OX11 0RA, UK

[4] Chemistry Department, Faculty of Science, Mansoura University, Mansoura, 35516, Egypt

[5] Department of Chemistry, University College London, London, WC1H 0AJ, UK

[6] Department of Materials Science and Engineering, The University of Sheffield, Sheffield, S1 3JD, UK

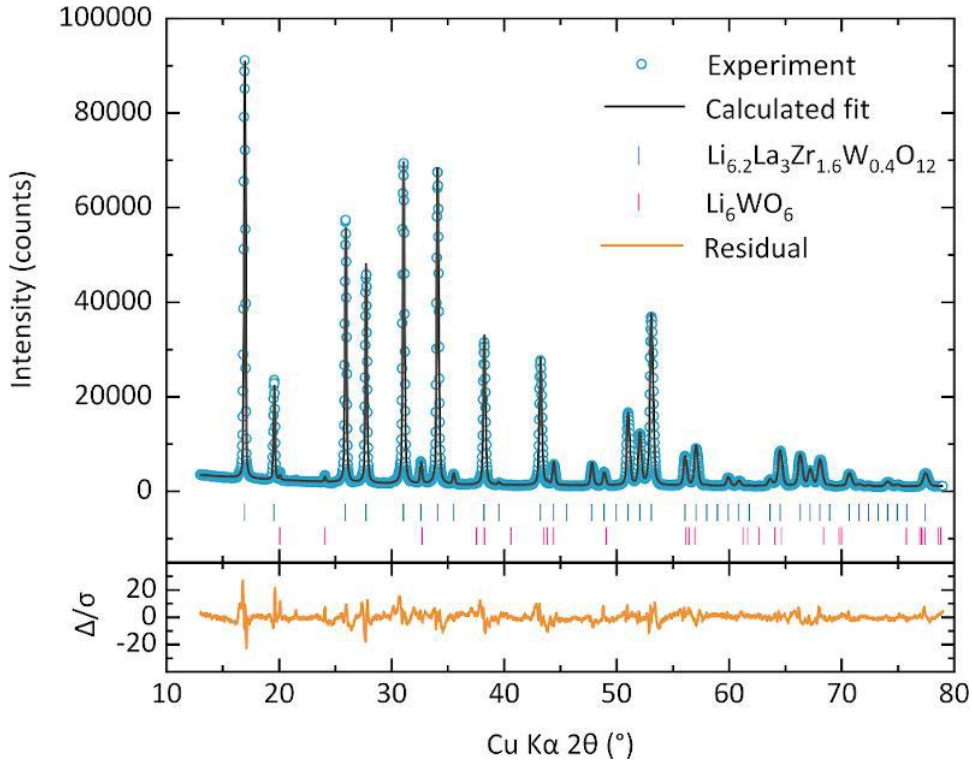

Figure S5.1. Rietveld refinement of as-synthesized $Li_{6.2}La_3Zr_{1.6}W_{0.4}O_{12}$ to a cubic garnet structure (space group *Ia-3d)*. A small Li_6WO_6 impurity phase was found, although this is removed following SPS treatment. R_{wp} = 5.83 %.

Table S5.1. Structural parameters obtained by Rietveld refinement of the sol-gel synthesised W-doped LLZO garnet. The Rietveld refinement from which these parameters were obtained is shown in Figure S5.1. Thermal parameters were not refined.

$Li_{6.2}La_3Zr_{1.6}W_{0.4}O_{12}$ Sol-gel	
Phase	Cubic
Space Group	*Ia-3d*
a* = *b* =*c	12.9294 (4)
α, ß, γ (˚)	90
Volume	2161.4 (2)
Weight fraction (%)	98.5 (2)
R_{wp} (%)	5.83
χ^2	3.57

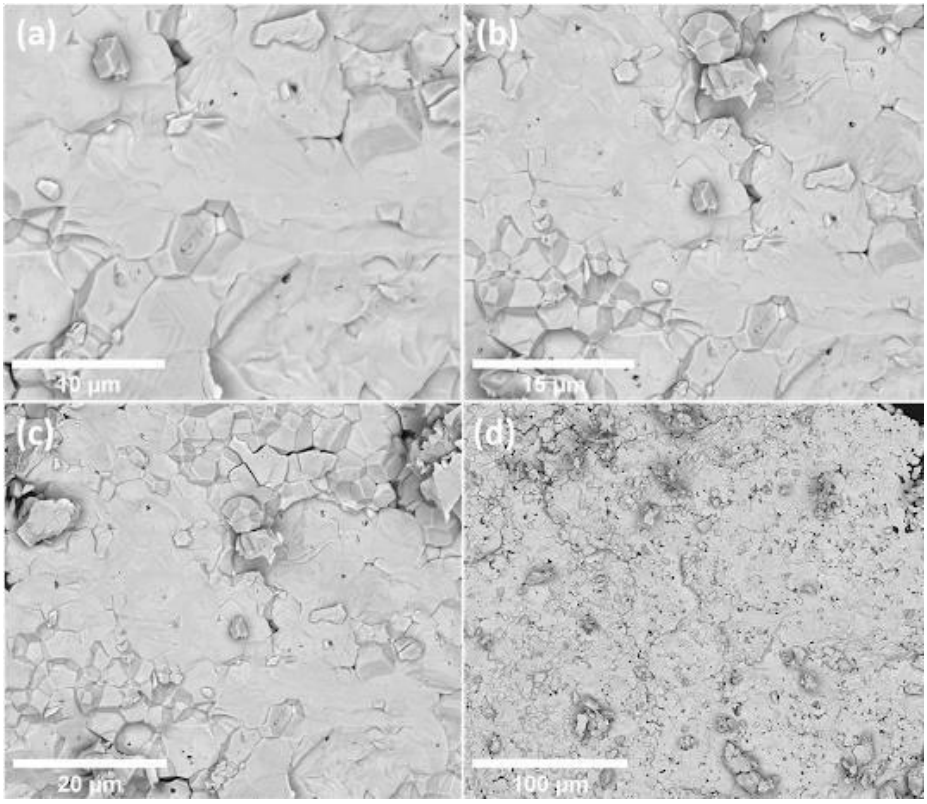

Figure S5.2. Scanning electron micrographs at different magnifications using a backscattered electron detector. Images were taken on the cross-sectional area of a spark plasma sintered (SPS) LLZWO pellet. Samples processed *via* SPS showed densities >94% of theoretical when measured using He gas pycnometry.

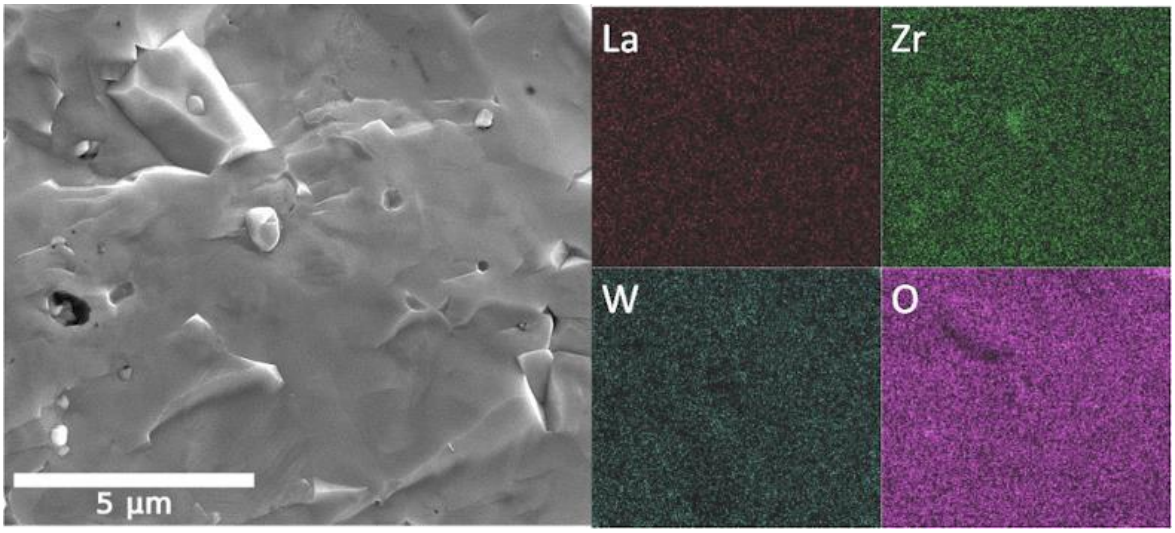

Figure S5.3. Energy dispersive X-ray spectroscopy of the cross-sectional area of an SPS LLZWO pellet. The SEM image which was used in shown on the left. Tungsten is uniformly dispersed across the cross-section, as expected from the single phase XRD shown in Figure 5.1a.

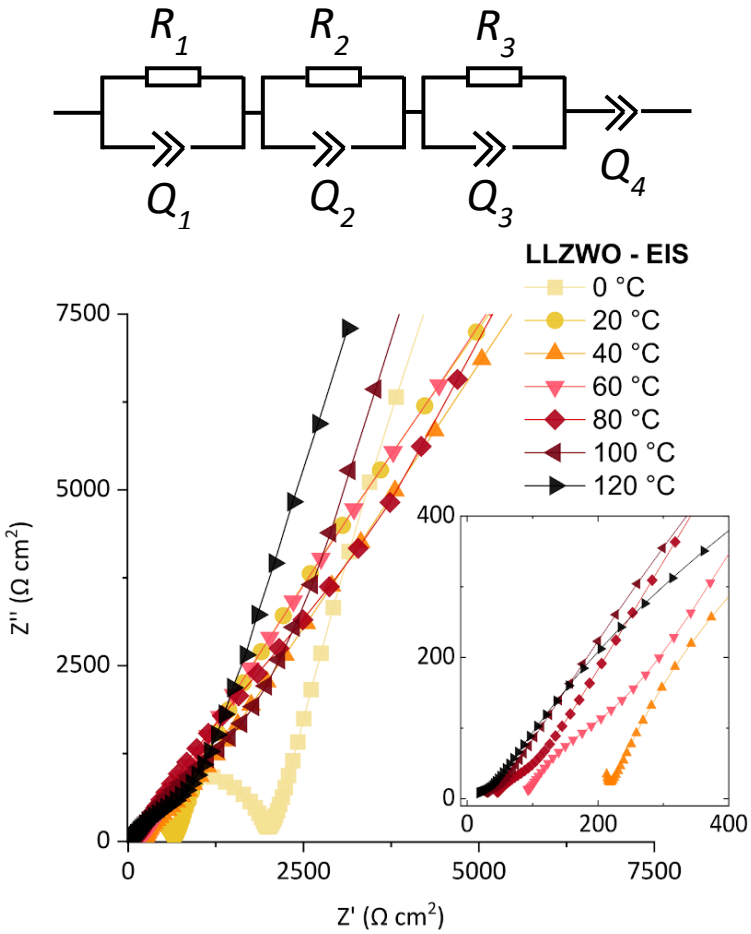

Figure S5.4. Temperature dependent EIS spectrum for LLZWO with blocking Au electrodes in the range 0 – 120 ˚C. The equivalent circuit used to fit these data, to extract conducitivty values at each temperature, is given above the figure. The 0 ˚C spectrum is shown the main text in Figure 5.2a. Spectra were collected between 1 MHz to 1 Hz. The lack of a high frequency semi-circular component at high temperature is due to the upper frequency limit of the equipment used, however the beginning of the tail is observed at all temperatures. The total conductivity of LLZWO was determined as ~3 × 10^{-4} S cm^{-1} at 20 ˚C, as well as an activation energy for ionic migration of ~400 meV.

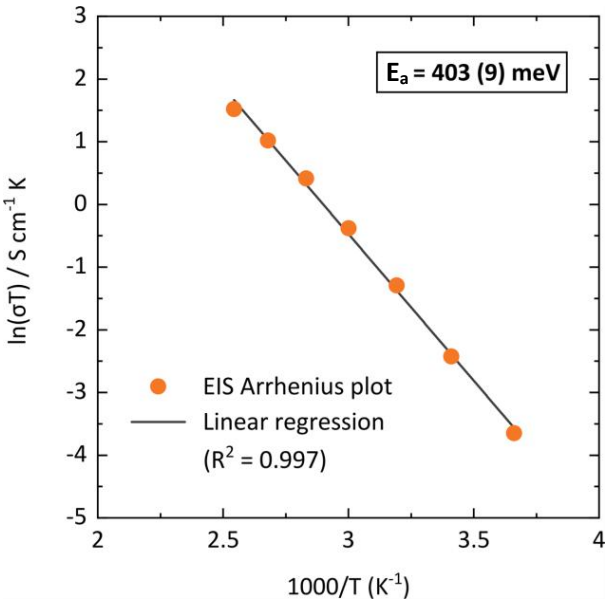

Figure S5.5. An Arrhenius analysis performed using the data from EIS in Figure S5.4. An activation energy for the migration of Li^+ movement in LLZWO was determined as 403 (9) meV using electrochemical impedance spectroscopy.

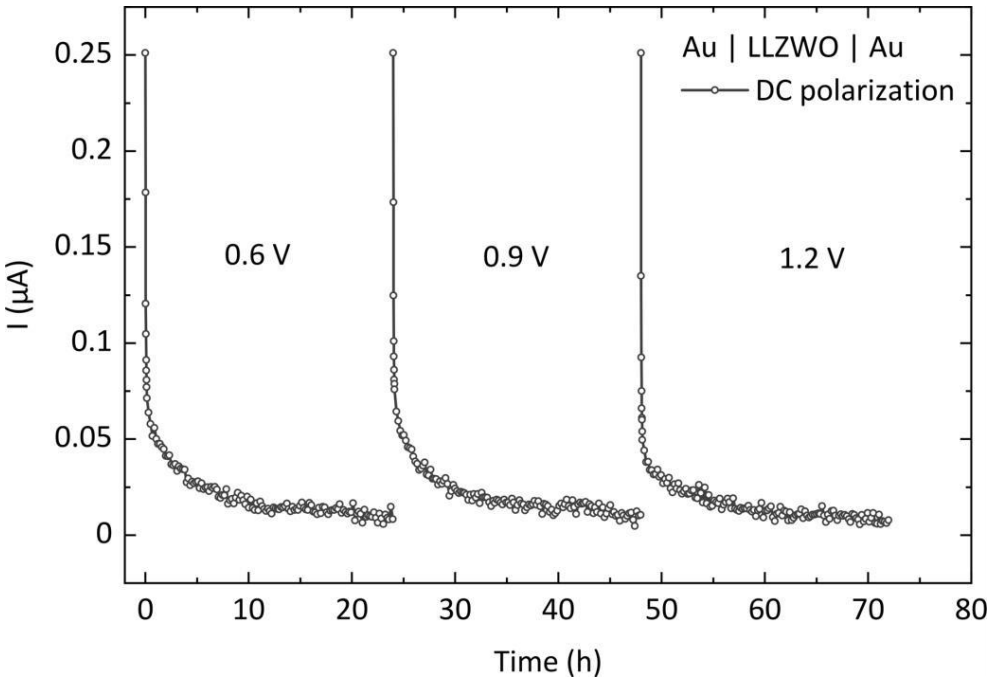

Figure S5.6. DC polarization experiment using LLZWO sandwiched by Au blocking electrodes. Three potentials of 0.6, 0.9, and 1.2 V were applied across the cell for 24 h each to polarize charge carriers. A rapid drop in current is observed before a gradual flattening in each instance. The conductivity was determined as around 5 (1) × 10^{-10} S cm^{-1} at room temperature. This is significantly lower than the conductivity calculated *via* EIS (~3 × 10^{-4} S cm^{-1}) and thus the primary charge carrier in LLZWO is Li^+. Electronic conductivity in pristine LLZWO is very low.

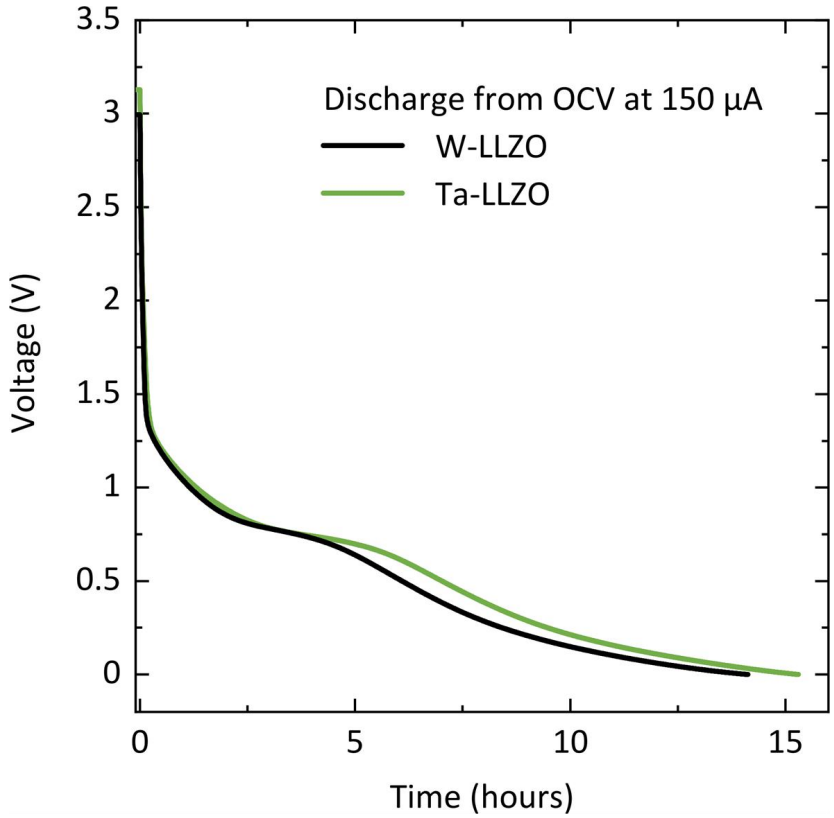

Figure S5.7. Discharge experiment using Ta- and W-doped LLZO garnets. The powders were mixed with amorphous carbon black in a 70:30 wt.% ratio to supply adequate electronic conductivity. 15 mg of LLZ*M*O/C (*M* = Ta, W) mixed powder was pressed at 1 ton in a 10 mm diameter pellet and transferred to a Swagelok cell. Metallic lithium was used as the counter electrode and 1M $LiPF_6$ (in 1:1 EC/DMC) as the electrolyte. Ta-LLZO is used as standard here as it is well known to be electrochemically inactive [1]. The discharge profile indicates no redox activity for either garnet sample, dissimilar to other studies involving W compounds such as that of low lithium content garnet $Li_3Nd_3W_2O_{12}$ [2, 3, 4] and perovskite $Li_{1.5}La_{1.5}WO_6$ [5]. W is known to be redox active in these materials and will chemically reduce from W^{6+} to W^{4+}, allowing the reversible intercalation of lithium below 1 V. $Li_3Nd_3W_2O_{12}$ is well known as a reversible lithium container due to the variable $W^{6+/4+}$ oxidation state [2, 3, 4]. Conversely, the redox stability displayed in Figure S5.7 can be attributed to the discontinuity of centres in LLZWO, meaning Li is not easily intercalated under applied current. The identical redox activity of Ta- and W-LLZO confirm W is not reduced.

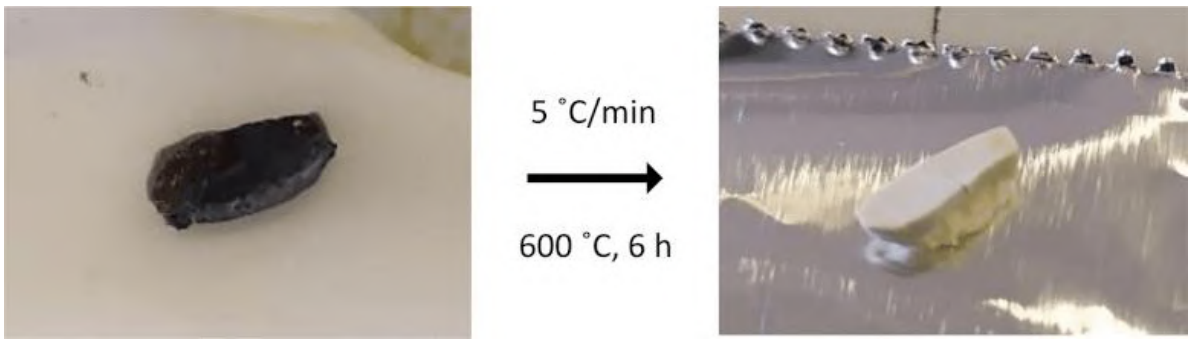

Figure S5.8. A small piece of lithiated LLZWO (black, left) was converted back to its pre-lithiation colour (white, right) *via* application of a heat treatment in air. This agrees well with previous studies of doped garnets [6, 7]. Wolfenstein *et al*. propose that the colour change during lithiation in LLZO in contact with Li is caused by trapped electrons at oxygen vacancies. The added electron density is a result of Li penetration into the material, which will chemically reduce the dopant species. In this case, LLZWO was found to obey similar behaviour under a heat treatment of 600 ˚C for 6 h, suggesting W^{6+} has been reduced during the lithiation treatment and can be re-oxidized by heating in air.

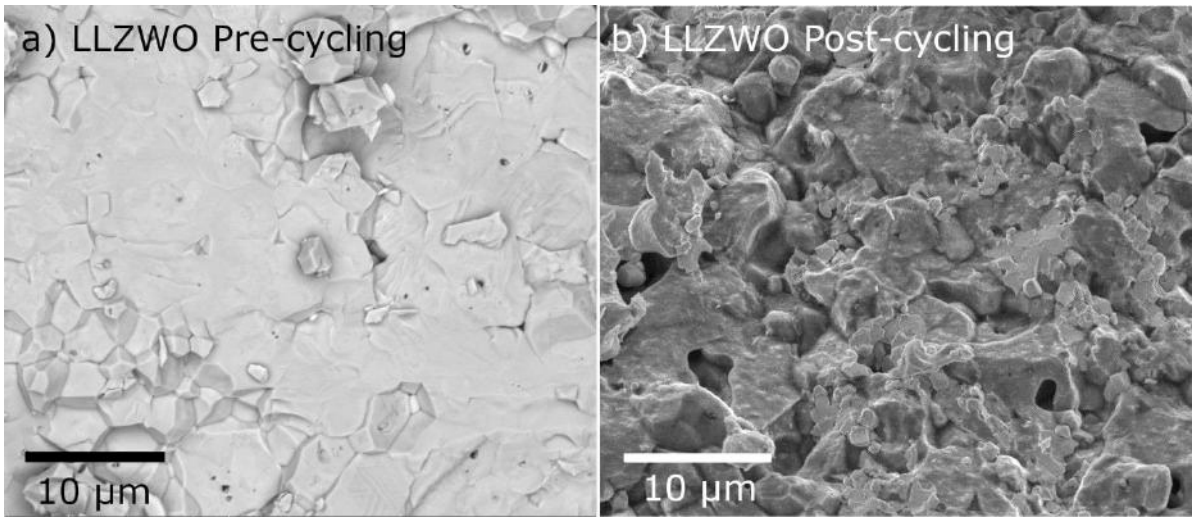

Figure S5.9. SEM cross-sectional images of LLZWO before and after galvanostatic cycling in a symmetric Li | LLZWO | Li cell. After cycling there is an observed particle breakdown, which corresponds to a reduced density and decreased contact between particles.

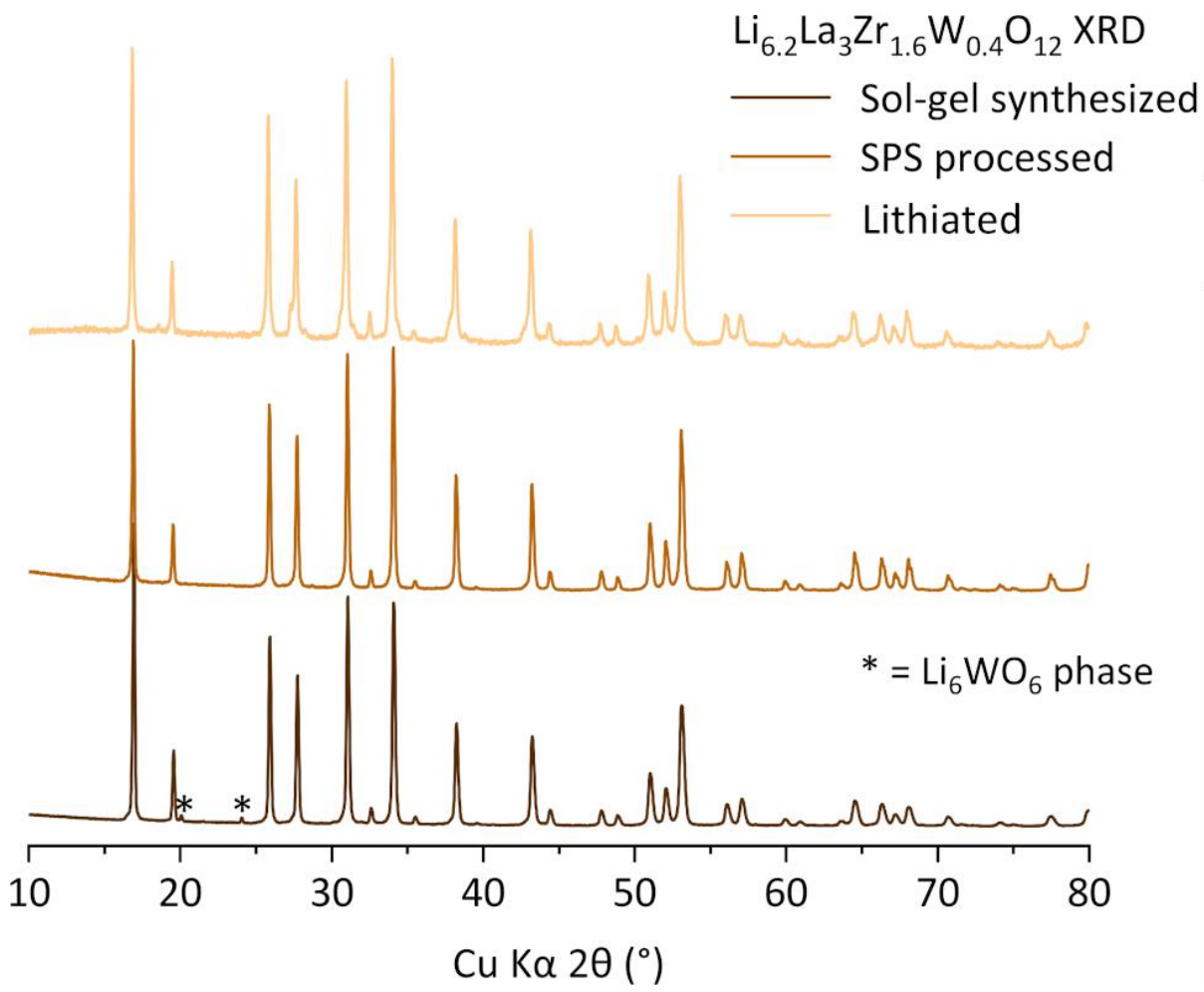

Figure S5.10. Powder X-ray diffraction patterns of sol-gel synthesised $Li_{6.2}La_3Zr_{1.6}W_{0.4}O_{12}$ before and after spark plasma sintering, and of lithiated LLZWO formed after heating a pellet in contact with Li on either side for 24 h at 175 ˚C. This heat treatment accelerates the interfacial reaction between LLZWO and Li, which eventually propagates the brown/black reacted area across the full pellet. The lithiated sample was cleared of Li and ground before measurement in an air sensitive sample holder.

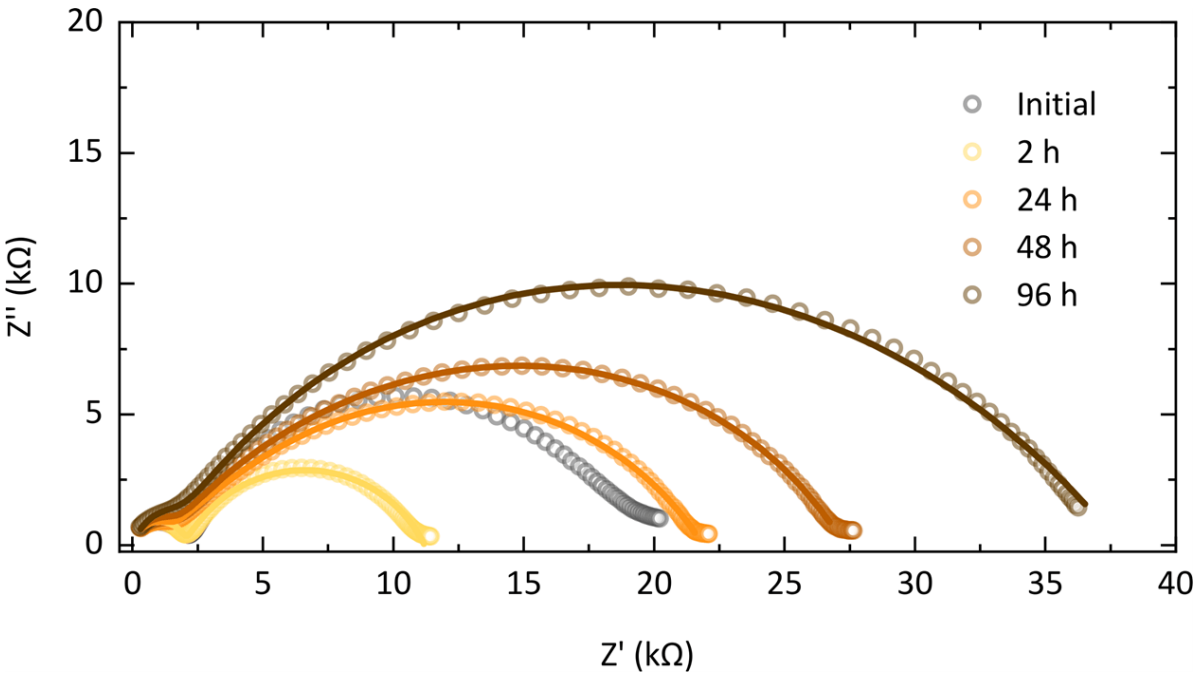

Figure S5.11. The electrochemical impedance spectroscopy data to accompany the fits show in the main text Figure 5.3b. Data is shown and hollow circles with the corresponding fits as solid lines.

A symmetric Li | LLZWO | Li cell was prepared and heated under vacuum (to prevent air contamination) at 150 ˚C for set time periods. The cell was allowed to cool to room temperature before impedance measurements were taken. Fitting of a two component $[R_1Q_1][R_2Q_2]$ equivalent circuit was found adequate for the 2 h heating period, whereafter three components $[R_1Q_1][R_2Q_2][R_3Q_3]$ were required to fit the spectra. The fitted plots are shown in Figure S5.11 and fitting results are given in Table S5.2.

Table S5.2. Fit parameter results from the fitting of R_xQ_x equivalent circuit components to the impedance spectra of a Li | LLZWO | Li heated at 150 ˚C for set times. All measurements were conducted at room temperature.

Heating time (h)	Q_1 **(F)**	A_1	R_1 **(Ω)**	Q_2 **(F)**	A_2	R_2 **(Ω)**	Q_3 **(F)**	A_3	R_3 **(Ω)**
2	1.22×10^{-10}	0.931	2458	1.70×10^{-7}	0.712	11193	-	-	-
24	6.55×10^{-11}	0.991	1251	1.07×10^{-7}	0.648	19348	1.09×10^{-7}	0.686	1265
48	6.85×10^{-11}	1	1225	1.06×10^{-7}	0.672	17178	1.61×10^{-7}	0.601	8890
96	8.96×10^{-11}	1	1200	2.90×10^{-8}	0.696	24755	5.82×10^{-7}	0.537	11893

Muon Spin Relaxation Measurements

Transverse field measurements

Muon measurements on both the pristine and lithiated LLZWO samples were completed within a bespoke cell holder on the EMU beamline at ISIS Neutron and Muon Source. The custom holder was used to test electrochemical measurements on the beamline, although none are presented here. Transverse field measurements (at 100 G) of the pristine sample were fitted in the temperature range 150 – 400 K using a flat background (A_{bg}) and an oscillating Gaussian function (P_{Go}) described by

$$A_0P(t) = A_{bg} + A_GP_{Go}(\sigma, f), \tag{S5.1}$$

where f is the frequency of muon precession and σ is the muon spin relaxation rate. A_G is the amplitude of the oscillating Gaussian P_{Go}.

This fitting function was inadequate to fit the lithiated sample transverse field data, and thus an additional oscillating Gaussian function was added. This fitting function is then described as:

$$A_0P(t) = A_{bg} + A_GP_{Go}(\sigma, f) + A_GP_{Go}(\sigma, f). \tag{S5.2}$$

That a second oscillation was required to fit the lithiated sample well is evident by a visual analysis of the data (shown in Figure 5.4b). The pattern shows an irregular beating pattern which indicates separate relaxation rates from multiple magnetically inequivalent sites.

Longitudinal field measurements

Longitudinal fields in parallel to the direction of initial muon spin polarization were applied in strengths of 0, 5, and 10 Gauss to gradually decouple the muon from its nuclear magnetic environment. The same temperature range of 150 – 400 K was used. Pristine LLZWO modelled well to a flat background and a dynamic Kubo-Toyabe function described by:

$$A_0P(t) = A_{bg} + A_{KT}P_{KT}(\Delta, \nu, t), \tag{S5.3}$$

where Δ is the static field distribution width felt by the muons, ν is the field fluctuation rate due to diffusion lithium ions [8], and t is time. P_{KT} represents the dynamic Kubo-Toyabe function. The lack of any paramagnetic ions in pristine LLZWO, as seen by the low relaxation rate within transverse field measurements (Figure S5.13), meant that no additional or multiplicative exponential relaxation component was required.

An additional Gaussian relaxation component was added to account for the inhomogeneous muon stopping environment for lithiated LLZWO. Thus, the fitting function can be described as:

$$A_0P(t) = A_{bg} + A_{KT}P_{KT}(\Delta, \nu, t) + A_GP_G(\sigma, t). \quad \text{(S5.4)}$$

P_G is a Gaussian relaxation function which takes the form of a Gaussian decay with relaxation rate σ over time t.

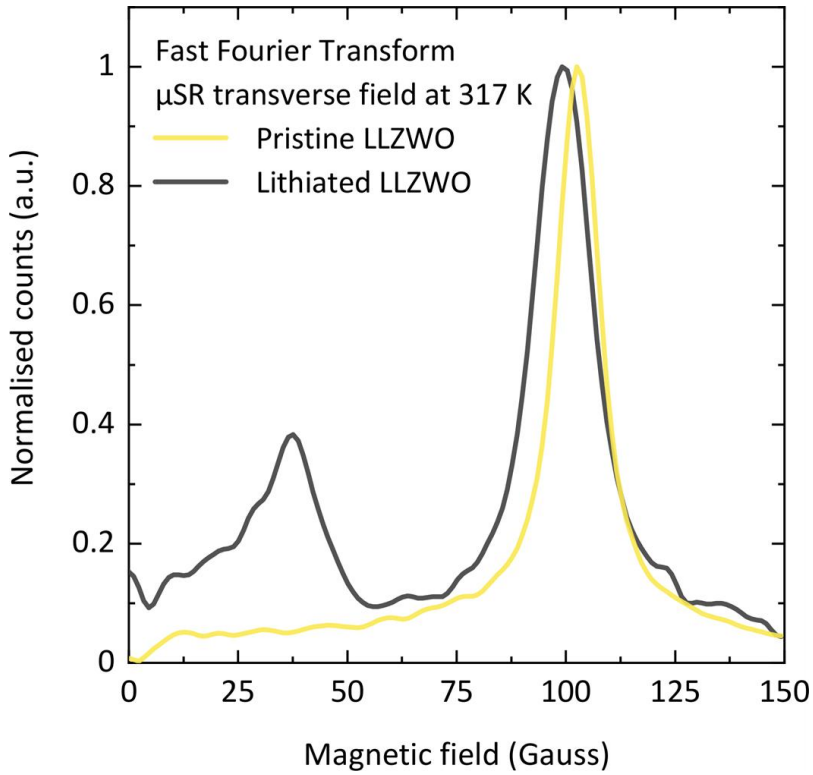

Figure S5.12. A frequency domain analysis using a Fast Fourier Transform (FFT) method to qualitatively show the dominant precession frequencies for both LLZWO samples. The x-axis has been converted into magnetic field and the y-axis is the normalised transform modulus of the FFT. The inhomogeneity of muon stopping environment in Lithiated LLZWO is immediately evident. The peak at 100 Gauss is caused by the applied transverse field: most muons will align with and precess around the 100 Gauss external field. The smaller, broader, peak at around 37 Gauss for the lithiated sample must be caused by the sample itself. The frequency of this component is much higher than the oscillation of a muon in the presence of a weak local nuclear field [9], and the peak is therefore believed to arise as an electronic effect. Additional electron density from intercalated Li ions may cause some muons to undergo hyperfine coupling to a loose electron instead of chemically bonding to an oxygen atom. As a result, the precession frequency of the hyperfine coupled muons is altered.

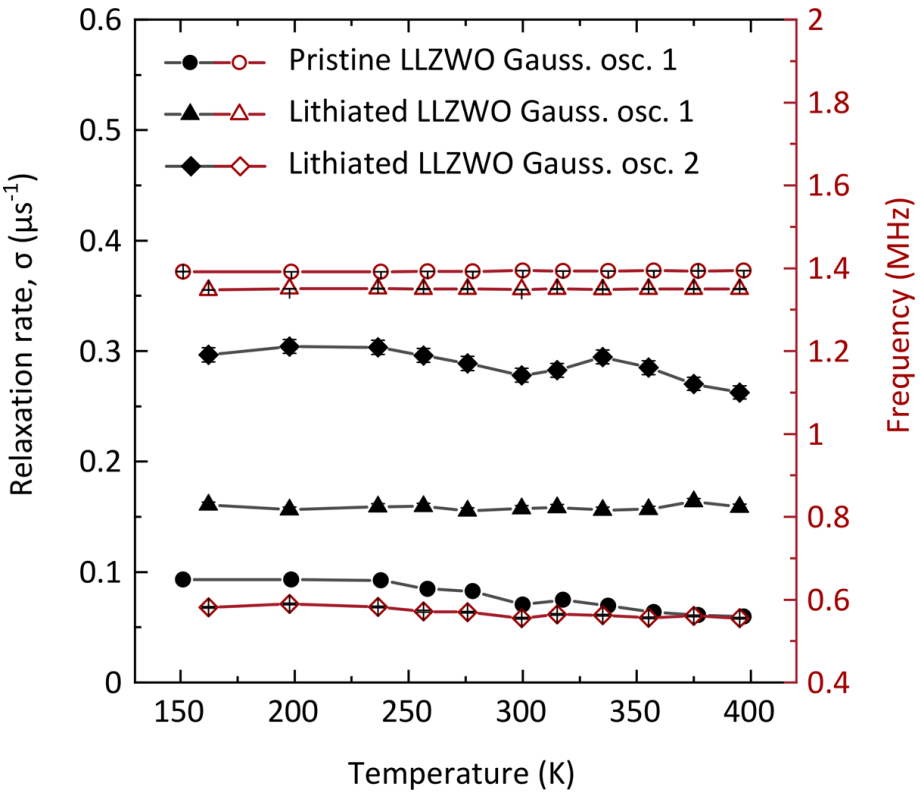

Figure S5.13. The evolution of transverse field muon fitting parameters with temperature for both the pristine and lithiated LLZWO samples, fitted data for which is shown in Figure 5.4 at 317 K. One Gaussian oscillation was required to fit the pristine sample and two were required for the lithiated sample. The black symbols correspond to the relaxation rate, σ, and the red symbols to the frequency. The first oscillation term for both samples is observed to match well, whereas the second oscillation term for lithiated LLZWO a much lower frequency. This frequency component is the same shown by the smaller peak in Figure S5.12. The increased relaxation rate for this component indicates a larger electronic field effect.

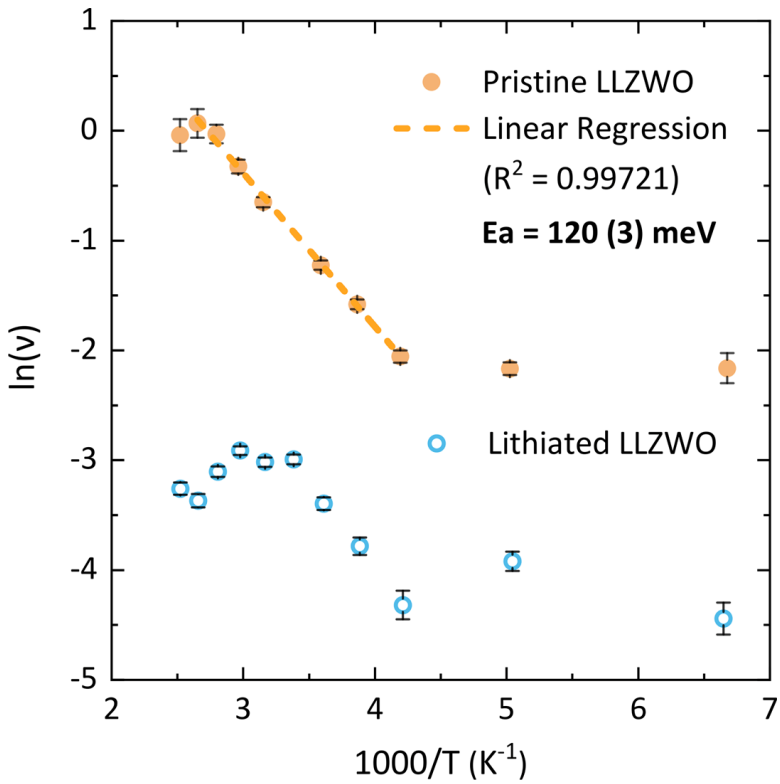

Figure S5.14. An Arrhenius plot of the natural logarithm of the field fluctuation rate, ν, against reciprocal temperature for both the pristine and lithiated LLZWO samples. A linear regression was fitted to the thermally activated region of the pristine sample, yielding an activation energy of 120 (3) meV. Only the points covered by the dotted line were used to fit the linear regression. Given the dual muon environment discovered *via* transverse field fitting, it was deemed inappropriate to report a single activation energy for lithiated LLZWO. However, the similar slope of the thermally activated region (>250 K) indicates that similar diffusion pathways exist.

Diffusion Coefficient Determination

Equation S5.5 was used to estimate the temperature dependent self-diffusion coefficient, D_{Li}, which is an intrinsic material property.

$$D_{Li} = \sum_{i=1}^{n} \left(\frac{1}{N_i}\right) Z_{v,i}\, s_i^2 \nu_{Li} \quad \text{(S5.5)}$$

N_i is the number of Li sites in the i^{th} path, $Z_{v,i}$ is the vacancy fraction of the i^{th} Li site, s_i is the hopping distance to the i^{th} site, and ν_{Li} is the field fluctuation rate as obtained *via* longitudinal field fitting μSR.

There are two Li sites within the garnet structure: the tetrahedrally coordinated 24*d* site Li(1) and a double Li(2) site, both on *96h* sites sandwiching an octahedrally coordinated 48*h* site [3]. Li^+ diffusion occurs through a 3D pathway, generally from Li(1)-Li(2)-Li(2)-Li(1), and can be visualised using Figures 5.1b and S5.15. The octahedral Li(2) site has a higher occupancy and acts as a bridging site between the Li(1) sites. It is therefore crucial to diffusion rates. Higher Li site occupancy, as is predicted for lithiated LLZWO, may fill the Li(2) site and culminate in an increased difficulty of Li^+ diffusion, as is the case for tetragonal LLZO which has full occupancy of Li(2) sites.

Fractional occupancies ($Z_{v,i}$) of 0.322 and 0.436 were estimated for the Li(1) and Li(2) sites respectively, using a small extrapolation of Li content from the detailed study of $Li_{6.75}La_3Zr_{1.75}Ta_{0.25}O_{12}$ by Adams et al [10], which also provided the jump distances (s_i). This involved scaling to the slightly lower Li content in LLZWO (6.2 p.f.u.) by a linear reduction in occupancy for each site. Given the common site preference and similar Li content of the Ta or W doped compounds only minor variation on site occupancies are expected from Ta-LLZO to W-LLZO. Nonetheless, the reported diffusion coefficient is an estimation.

To calculate the diffusion coefficient, three distinct jumps were considered: Li(1) to Li(2), Li(2) to Li(2), and Li(2) to Li(1). The vacancy fraction used was unity minus the occupation fraction. D_{Li} was estimated as 5.6 (5) × 10^{-11} cm^2 s^{-1} at 317 K for pristine LLZWO. A single D_{Li} value is not reported for LLZWO due to the uncertainty over accurate diffusion rates in separate bulk/grain surface environments and accurate estimations of Li site occupancies. However, $\nu_{lithiated}$ is observed as around an order of magnitude lower than $\nu_{pristine}$ (0.049 vs. 0.51 μs^{-1}, respectively) at 317 K, and thus D_{Li} is predicted as at least an order of magnitude lower (~10^{-12} cm^2 s^{-1}) for lithiated LLZWO. Given the suspected increase in lithium content, $Z_{v,i}$ would be of a lower value for lithiated LLZWO and consequently decrease D_{Li} as well. The increased Li

occupancy, especially of Li(2), is expected to be the main contributing factor to the decreased value of $v_{lithiated}$, as sites available for diffusion become full and a bottleneck occurs.

D_{Li} is reported at 317 K, rather than 300 K, because of a suspected readback problem from the thermocouple. For this reason, the 300 K point is also left out of the activation energy calculation shown in Figure S5.14. This readback problem is not expected to have affected any other measurements.

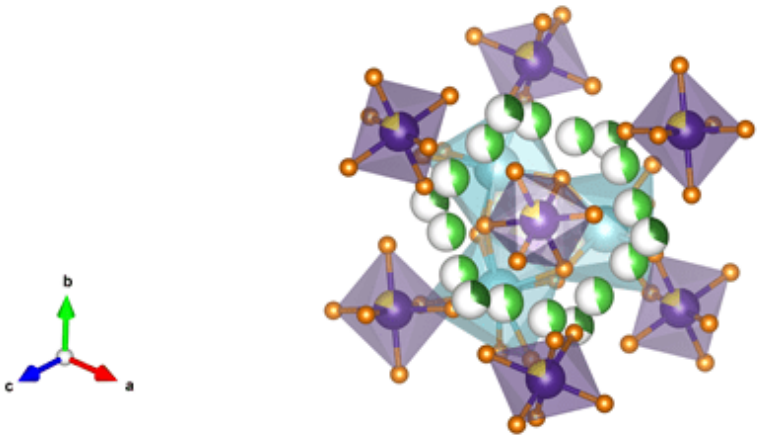

Figure S5.15. Alternative view of the cubic garnet configuration in LLZWO. La is turquoise, Zr/W are purple/yellow respectively, O is orange, Li(1) is dark green, and Li(2) is light green. Li^+ diffusion occurs through a Li(1)-Li(2)-Li(2)-Li(1) pathway, where the Li(1) to Li(2) step is believed to be rate limiting [10].

Pure Li metal

The possibility of metallic Li dendrites [11] as the source of the second muon precession frequency was considered. To validate this possibility, the muon spin relaxation properties of pure lithium were measured. Li metal was stuffed inside a Ti powder holder and measured at room temperature under high vacuum. The results from fitting a flat background plus a dynamic Kubo-Toyabe function to zero/longitudinal field data and a Gaussian relaxation to transverse field data are shown in Table S5.3 below.

Table S5.3. Muon fitting parameters for Li metal at room temperature in both the zero/longitudinal field and transverse field configuration.

Zero field + 10 G longitudinal field						
Temp (K)	**Background Amplitude**	**Dynamic KT Amplitude**	**Δ (μs^{-1})**	**ν (μs^{-1})**		**χ^2**
299.87	0.0110 (3)	0.24261	0.080 (6)	1.2 (2)		0.89
100 G Transverse field						
Temp (K)	**Background amplitude**	**Gaussian Oscillation Amplitude**	**σ (μs^{-1})**	**Frequency (MHz)**	**Φ**	**χ^2**
299.87	0.0110 (3)	0.2286 (5)	0.008 (6)	1.3878 (2)	0.029 (3)	0.94

Nuclear motion in Li metal appears highly dynamic as ν>>Δ. The low value of Δ displayed is likely a result of significant motional narrowing and thus this data is appropriate for comparison purposes only: fitted signals in other samples cannot be attributed to Li metal. This excludes the possibility that one component of the signal observed in the lithiated LLZWO sample is due to muons stopped in agglomerated Li metal within the material or on the surface.

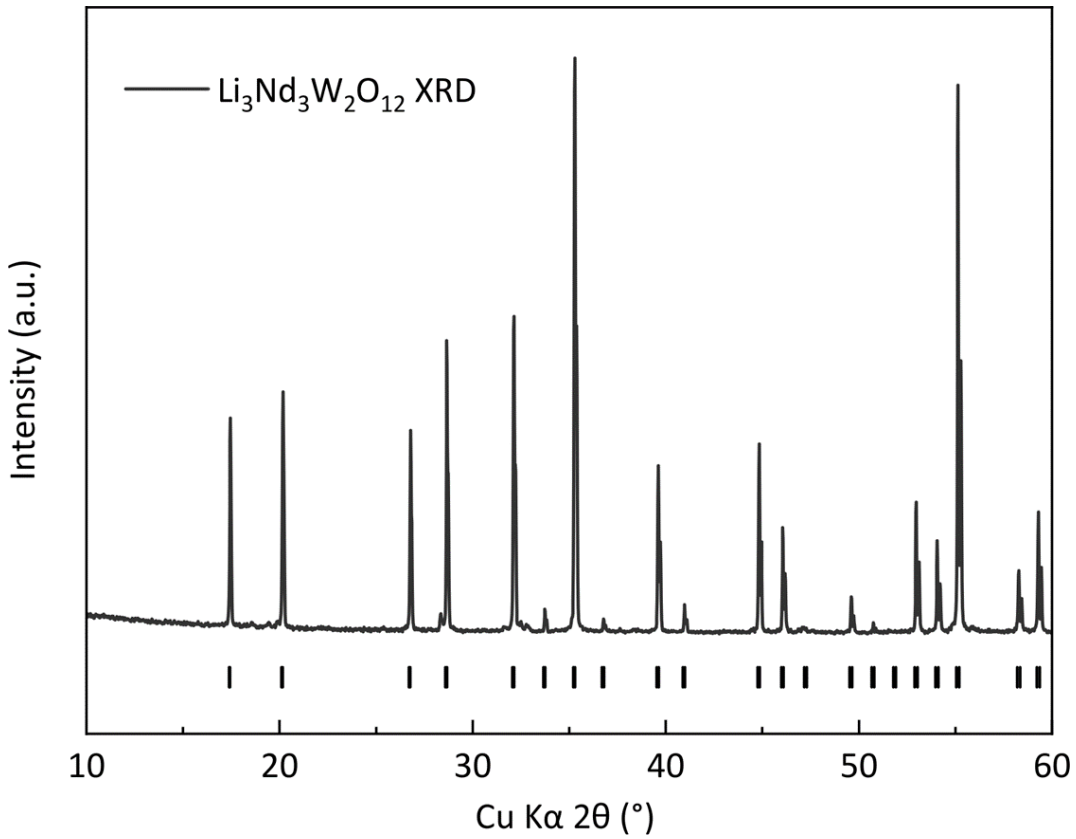

Figure S5.16. A powder X-ray diffraction pattern collected for $Li_3Nd_3W_2O_{12}$ (LNWO), which was used as a W^{6+} standard for X-ray absorption experiments. LNWO was synthesized *via* sol-gel reaction. Allowed reflections are indicated by markers underneath the data.

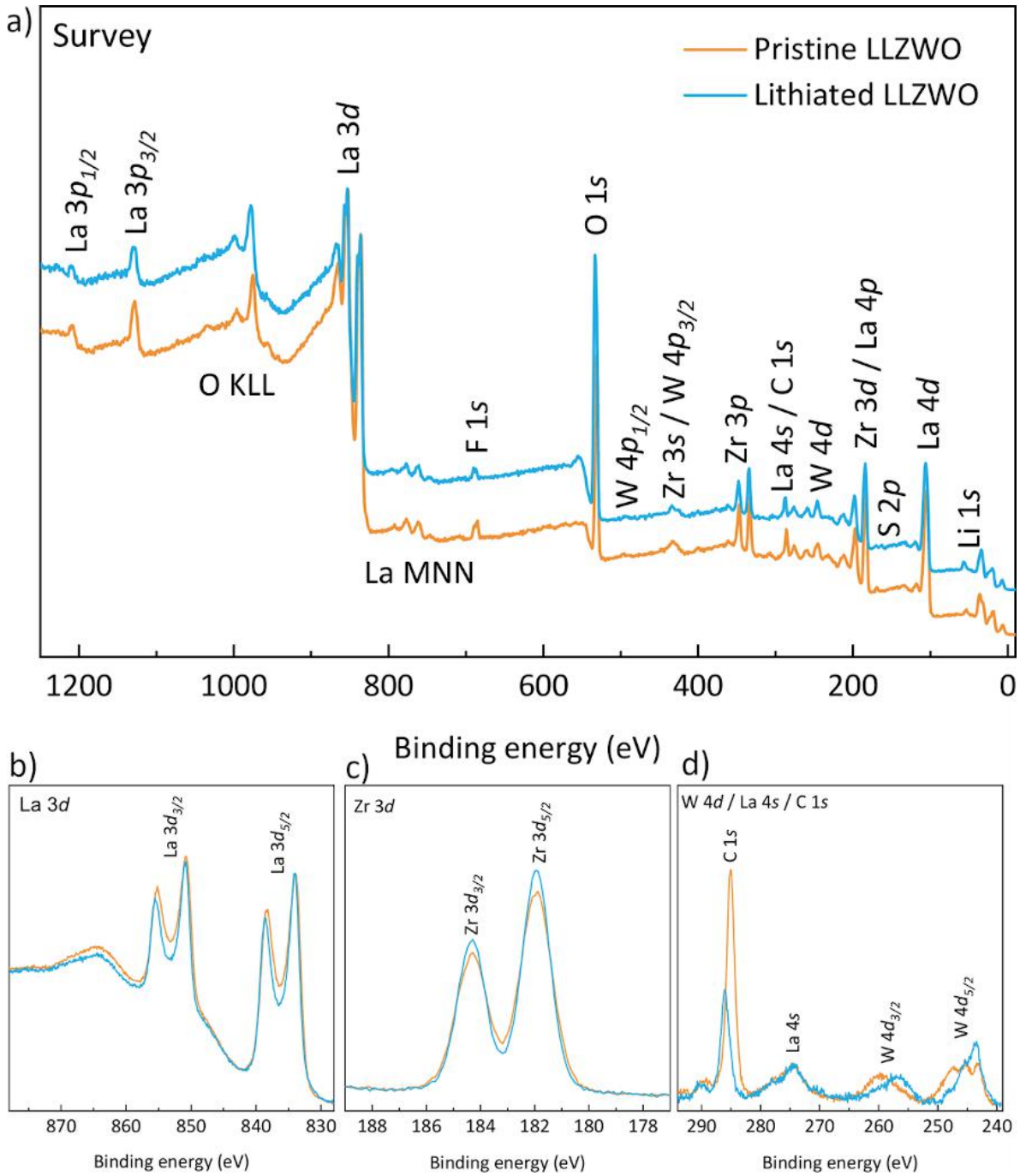

Figure S5.17. (a) XPS survey spectra of the pristine and lithiated LLZWO with all major core and Auger lines indicated. XPS core level spectra of the pristine and lithiated LLZWO, including (b) La 3*d*, (c) Zr 3*d*, and (d) W4*d* / La 4*s* / C1*s*.

Supporting Information References

[1] Y. Zhu, J. G. Connell, S. Tepavcevic, P. Zapol, R. Garcia-Mendez, N. J. Taylor, J. Sakamoto, B. J. Ingram, L. A. Curtiss, J. W. Freeland, D. D. Fong, and N. M. Markovic. Dopant-Dependent Stability of Garnet Solid Electrolyte Interfaces with Lithium Metal. *Adv. Energy Mater*., 9:1803440, 2019.

[2] H. Xie, K. Park, J. Song, J. B. Goodenough. Reversible lithium insertion in the garnet framework of $Li_3Nd_3W_2O_{12}$. *Electrochem. Commun*., 19:135-137, 2012.

[3] R. Satish, V. Aravindan, W. C. Ling, J. B. Goodenough, S. Madhavi. Carbon-Coated $Li_3Nd_3W_2O_{12}$: A High Power and Low-Voltage Insertion Anode with Exceptional Cycleability for Li-Ion Batteries. *Adv. Energy Mater*., 4:1301715, 2014.

[4] M. Luo, H. Yu, X. Cheng, W. Ye, H. Zhu, T. Liu, N. Peng, M. Shui, J. Shu. Sol-gel Synthesis and *in Situ* X-ray Diffraction Study of $Li_3Nd_3W_2O_{12}$ as a Lithium Container. *ACS Appl. Mater. Interfaces*., 10:12716-12721, 2018.

[5] M. Amores, H. El-Shinawi, I. McClelland, S. R. Yeandel, P. J. Baker, R. I. Smith, H. Y. Playford, P. Goddard, S. A. Cussen, E. J. Cussen. $Li_{1.5}La_{1.5}MO_6$ (M = W^{6+}, Te^{6+}) as a new series of lithium-rich double perovskites for all-solid-state lithium-ion batteries. *Nat. Comm.*, 11:6392, 2020.

[6] J. Wolfenstine, J. L. Allen, J. Read, and J. Sakamoto. Chemical stability of cubic $Li_7La_3Zr_2O_{12}$ with molten lithium at elevated temperature. *J. Mater. Sci*., 48:5846– 5851, 2013.

[7] Y. Kim, A. Yoo, R. Schmidt, A. Sharafi, H. Lee, J. Wolfenstine, and J. Sakamoto. Electrochemical Stability of $Li_{6.5}La_3Zr_{1.5}M_{0.5}O_{12}$ (M = Nb or Ta) against Metallic Lithium. *Front. Energy Res.*, 4:20, 2016.

[8] J. Sugiyama, K. Mukai, Y. Ikedo, H. Nozaki, M. Månsson, I. Watanabe. Li Diffusion in Li_xCoO_2 Probed by Muon-Spin Spectroscopy. *Phys. Rev. Lett*., 103:147601, 2009.

[9] J. H. Brewer, K. M. Crowe, F. N. Gygax, R. F. Johnson, B. D. Patterson, D. G. Fleming, and A. Schenck. Anomalous μ^+ Precession in Silicon. *Phys. Rev. Lett.*, 31:143–146, 1973.

[10] S. Adams and R. Prasada Rao. Ion transport and phase transition in $Li_{7-x}La_3(Zr_{2-x}M_x)O_{12}$ (M = Ta^{5+}, Nb^{5+}, x = 0, 0.25). *J. Mater. Chem.*, 22:1426-1434, 2012.

[11] C. Tsai, V. Roddatis, C. Vinod Chandran, Q. Ma, S. Uhlenbruck, M. Bram, P. Heitjans, and O. Guillon. $Li_7La_3Zr_2O_{12}$ Interface Modification for Li Dendrite Prevention. *ACS Appl. Mater. Interfaces,* 8:10617−10626, 2016.

Technical Report

The BAM Cell: An Electrochemical Device for *Operando* Ionic Diffusion Measurements using Muon Spectroscopy

Innes McClelland, Samuel G. Booth, Beth I. J. Johnston, Laurence Middlemiss, Edmund J. Cussen, Peter J. Baker, Serena A. Cussen

[I. McClelland, S. G. Booth, B. I. J. Johnston, L. Middlemiss, E. J. Cussen, P. J. Baker, and S. A. Cussen. The BAM Cell: An Electrochemical Device for *Operando* Ionic Diffusion Measurements using Muon Spectroscopy. *Not yet submitted*]

Abstract

An electrochemical cell is presented for ionic diffusion measurements using muon spectroscopy (μSR) on the EMU beamline at the ISIS Neutron and Muon Source. Such experiments elucidate the rate of atomic-scale ionic motion using implanted spin-polarized muons, which can provide fundamental information on active material behaviour during charge/discharge cycles. Consequently, key areas of change or failure in operating battery systems can be determined. The Battery Analysis by Muon (BAM) cell is described here as an electrochemically reliable device, versatile towards a variety of chemistries. Galvanostatic cycling and impedance spectroscopy experiments using both solid- and liquid-based electrolytes are found not to compromise the electrochemical performance of the BAM cell in comparison to commercially available cell types. The cell enables data collection at high counting rates from the component of interest. Its suitability is outlined by a previous *operando* experiment, and a range of future applications remain available for exploration.

Introduction

The continuously increasing worldwide demand for electrochemical storage devices such as lithium-ion batteries has recently facilitated a global research effort to investigate new, high performance materials [1]. The introduction of new materials poses fresh challenges, with stringent performance requirements, such as a high rate capability and minimal degradation over a long cycle life, imperative for successful commercial implementation. The dynamical process which underpins battery operation is the speed of ionic transfer during cycling; a microscopically occurring process which significantly influences macroscopic performance properties, including conductivity and long-term cyclability [2, 3]. Ionic mobility is fundamentally affected by the material phenomena which occur during the charge/discharge processes, such as changes in structural parameters [4], site vacancies/defects, and degradation mechanisms [5]. Thus, advanced characterisation of the diffusional properties of new materials necessitates direct and non-invasive techniques which can be applied during charging/discharging.

The simultaneous application of an experimental techniques to an operating battery, often called "*operando*" measurements, are now well established in battery research [6, 7]. Demonstrations to date include spectroscopic (i.e., X-ray absorption spectroscopy [8, 9]), structural (i.e., X-ray/neutron diffraction [10]), and electrochemical (i.e., impedance spectroscopy [11]) examples. Such experiments afford reliable, high precision, and detailed information [12] which can identify subtle phenomena while avoiding sample contamination or the user error concerns of *ex situ* measurements [7]. The development of μSR to accurately characterise ionic diffusion processes during cycling therefore poses a valuable opportunity to obtain complementary information to other established *operando* methodologies. A custom-built cell to satisfy the requirements of the technique is highly beneficial; the design, performance, and applications of such a cell are described for *operando* μSR experiments herein.

Muon spectroscopy for battery research

Muon spectroscopy (μSR) has been used to quantify intrinsic material properties previously [13–22]; the self-diffusion coefficient and activation energy of ionic hopping can be readily determined [23]. The promise of applying μSR in an *operando* environment offers a unique probe into how these properties change in relation to state of charge. While previous studies elucidate the fundamental energy barriers for ionic diffusion in pristine materials, they often do not consider the dominant diffusion pathways during battery operation, which only become influential during the charge/discharge process as site vacancies emerge. *Operando* experiments offer a greatly increased level of detail from standard measurements; detail which is more representative of realistic operating conditions. Advantageously, the non-invasive character of the technique means it can study electrochemical systems without significant interference [24]. The diffusivity range probed by μSR is between 10^{-8} – 10^{-13} cm^2 s^{-1}, appropriate to assess the self-diffusion rates of various ionic species in electrode materials, and crucially, outside the range of Li-based liquid electrolytes ($\geq 10^{-7}$ cm^2 s^{-1} [25]). Therefore, the dynamic contribution from other constituents in a battery, such as electrolyte, carbon, and binder, is minimal. A controllable penetration range

of implanted muons permits the study of either electrode individually, provided an appropriate active material mass loading is used (generally $\geq$50 mg cm^{-2}). *Operando* capabilities also present the opportunity to discover how degradation mechanisms, which often manifest over multiple cycles or at extreme potentials, can affect ionic dynamics.

The Battery Analysis by Muon (BAM) Cell

Design

To date, no other electrochemical cells exist for ionic diffusion experiments using μSR, excluding adaptations of commercially available cells, as previously shown by our group [26]. The BAM cell was designed primarily to increase the data quality from such cell adaptations. To ensure its functional reliability, it must fulfil the requirements for both electrochemical performance and the μSR technique. Very similar electrochemical performances to off-the-shelf equipment, such as coin or Swagelok cells, is imperative for experimental validity. The scale-up from standard active material mass loading ($\sim$1 – 10 mg cm^{-2}) represents an electrochemical challenge. However, various methodologies exist for the preparation of thick electrodes (generally possessing a mass loading of $\sim$30 – 100 mg cm^{-2}) [27–29], which have been found to perform comparably to standard cells.

A brief description of the experimental requirements for the BAM cell is given in Table 6.1, alongside the design solution to counteract these. To maximise the amplitude of signal from the sample, an 18 mm diameter circular inspection window was implemented to suit the beam spot size on EMU, which is a Gaussian profile of around 25×10 mm^2 when uncollimated. All cell components are non-magnetic to ensure little interfere with any muons which miss the target material; this is especially important for the current collectors which act as windows. The current collectors are thin enough to allow most muons to pass through ($\lesssim$100 μm for stainless steel), while thick enough to retain a flat, robust contact to the electrodes, especially under high vacuum. The cell is designed to be fully reversible, meaning it can be flipped to study either electrode, or a solid electrolyte, individually (Figure 6.1). The BAM cell is also suitable for experiments on the HiFi spectrometer at ISIS, enabling potential for high field experiments and a versatility towards alternative research avenues, and is adaptable to other muon instruments.

Table 6.1: Brief outline of the BAM cell requirements for μSR experiments of ionic diffusion, and the design solution to satisfy them.

Cell Requirement	**Solution**
Low background count	Wide inspection window (18 mm diameter)
Non-magnetic materials	Austenitic 316L grade steel cell body
Muons reach sample	Current collector $\leq$100 μm thick
Positron escape	Compact cell body
Adequate muon implantation in active material	High active material mass loading
Representative electrochemistry	Gasket compressibility; cell testing

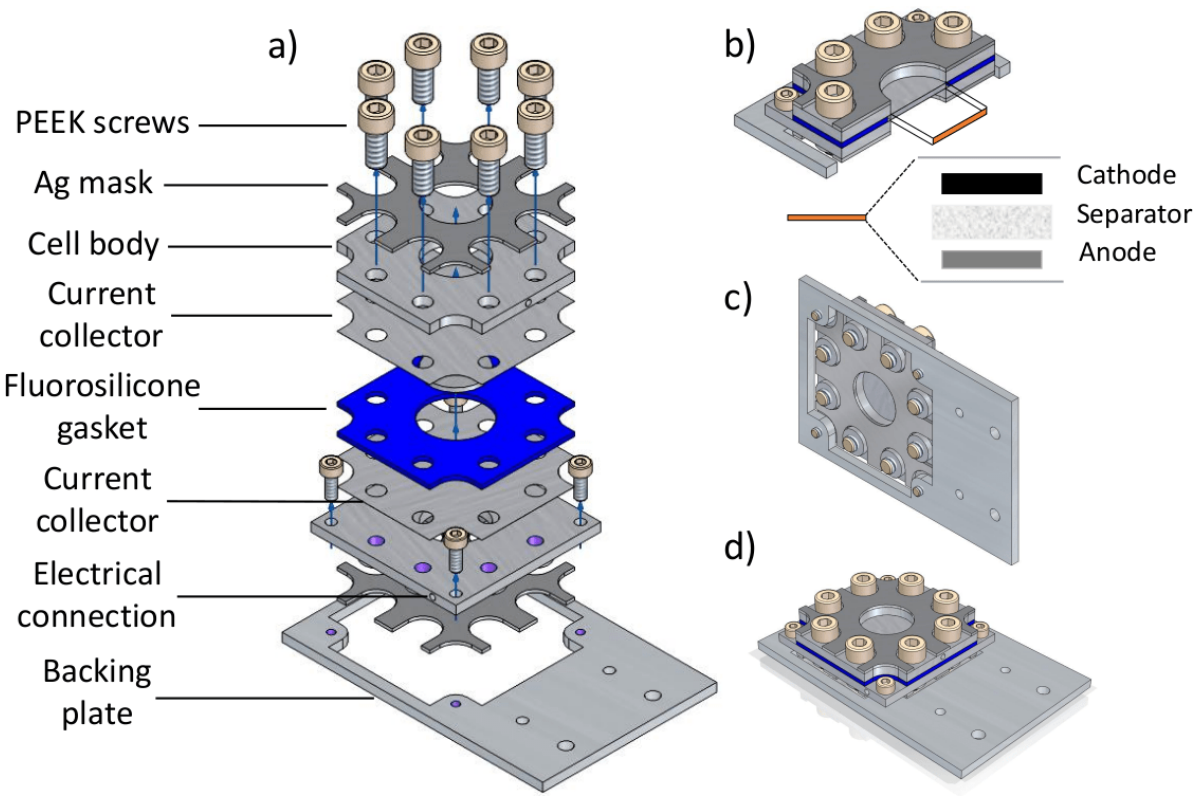

Figure 6.1: The Battery Analysis by Muon (BAM) cell for *operando* μSR measurements of ionic diffusion. (a) An exploded view showing all of the cell components. (b) Cross-section of an assembled cell, with the orange area between current collectors depicting where the battery constituents are assembled. (c), (d) A view of the cell as attached to the backing plate from alternate angles.

Cell Body

The cell body is composed of square stainless steel plates of length 50 mm and thickness 3 mm. PEEK screws are used to tighten the cell shut whilst maintaining electrical isolation between the terminals. Eight screws are sufficient to provide a lasting hermetic seal, given appropriate gasket compression, including under high vacuum. Four small screws are used to tighten the cell onto a backing plate which can be attached to the beamline (Figure 6.2). Electrical banana clip connections are inserted into the side of the cell and are run through to a potentiostat outside the beamline. A silver mask is placed in front of the cell to stop any wayward muons which do not pass through the inspection window. The nuclear magnetic moment of silver is negligible and thus the spin of any muons which stop in the mask will not relax significantly, meaning the contribution to the asymmetry signal can easily be subtracted as background in the data analysis.

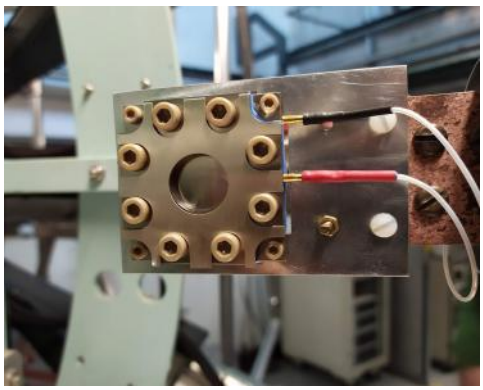

Figure 6.2: A picture of an assembled BAM cell attached to the EMU spectrometer at the ISIS Neutron and Muon Source. The silver mask can be taped to the cell if required.

Window/current collector

Thin stainless steel sheets of austenitic grade 316L are used as current collectors on either side of the cell. Thicknesses between 50 – 100 μm can be used; thinner current collectors offer deeper muon penetration inside the cell, while thicker provides a more rigid foil which can improve contact with the electrode. The muon penetration depth can be controlled somewhat by choice of current collector thickness, although adequate electrochemical testing under vacuum is recommended prior to usage. Alternative current collector materials can be used if necessary (i.e., for Na-ion batteries).

Gasket

A fluorosilicone rubber gasket is used to electrically isolate the cell terminals. The compressibility of the gasket is crucial to provide an air-tight seal after assembly. The battery constituents are assembled inside the cavity of the gasket (on top of a current collector). A range of gasket thicknesses are available, from 0.4 – 1.5 mm, and they can be stacked to suit a range of sample thicknesses with retention of an air seal. As such, the cell thickness can be easily controlled to suit custom configurations. The choice of an appropriate gasket thickness is important to ensure both the sample integrity and a robust electrical contact from the current collector to the electrode.

Experimental Details

Garnet samples of doped-LLZO ($Li_7La_3Zr_2O_{12}$) were prepared using a sol-gel technique followed by densification *via* spark plasma sintering (described in Chapter 5). Au electrodes were deposited using an Agar manual sputter coater for a time of 200 s on each side of the pellet. Measurements were completed in cells assembled under an Ar atmosphere. Electrochemical impedance spectroscopy measurements were collected using both a VMP-300 potentiostat between 7 MHz to 1 Hz and a VSP potentiostat between 0.6 MHz to 10 Hz. In both instances, a perturbation voltage amplitude of 10 mV was used.

NMC811 ($LiNi_{0.8}Mn_{0.1}Co_{0.1}O_2$) was synthesised *via* co-precipitation as described in Chapter 7, while NMC622 ($LiNi_{0.6}Mn_{0.2}Co_{0.2}O_2$) was purchased from Targray (SNMC 03001). The active material was mixed thoroughly in an agate mortar inside the glovebox with conductive carbon and PTFE binder in the wt.% ratio 70:20:10, respectively. The powder cathode cell preparation methodologies are also described in Chapter 7. Thick film electrodes were prepared by forming a slurry of active material, carbon, and binder (96:2:2 wt.%, respectively) in N-methyl-2-pyrrolidone solvent and casting onto Al foil using a doctor blade, before drying in a vacuum oven. Lithium ribbon (99.9% trace metals basis, Sigma) was polished and punched into discs for use as a counter electrode. 1.0 M $LiPF_6$ in ethylene carbonate/diethyl carbonate (50/50: v/v, Sigma) was used as electrolyte. Galvanostatic cycling data were collected between 3.0–4.4 V using a Biologic VSP potentiostat.

Muon spin relaxation measurements are used from the studies outlined in Chapters 4, 5, and 7. All measurements described were taken at 300 K. The data fitting procedures are described elsewhere (Chapters 4, 5, 7), and were completed using Mantid [30].

Performance

Electrochemical

The electrochemical reliability of the BAM cell is imperative if the results from *operando* μSR experiments are to be related to real systems. To validate this, various materials were tested in both BAM and Swagelok cells. Figure 6.3 displays electrochemical impedance spectroscopy (EIS) measurements of two solid electrolyte pellets: W- and Ta-doped LLZO ($Li_7La_3Zr_2O_{12}$). Each pellet was measured in both cells consecutively, and all measurements were taken at room temperature.

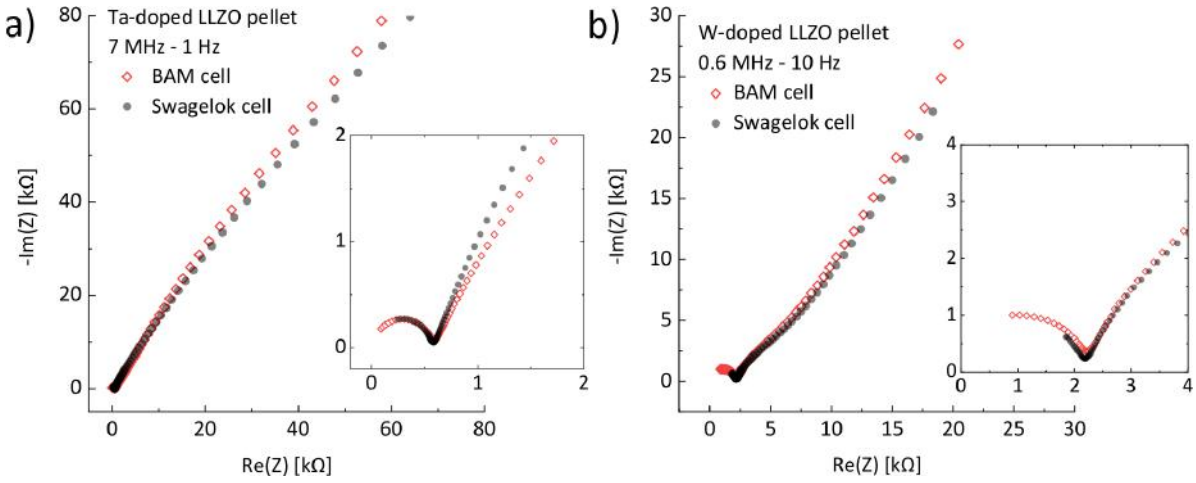

Figure 6.3: Electrochemical impedance spectroscopy measurements of two samples: (a) Ta- and (b) W-doped LLZO pellets. Each pellet was measured in both cells consecutively. Both samples used Au as symmetrical Li^+ blocking electrodes.

The semi-circle component at high frequency (shown in Figure 6.3 insets), represents the total pellet resistance (bulk and grain boundary). The pellet impedance does not change for

either garnet sample between the two cells, clearly indicating there is no resistance added by the BAM cell. Interestingly, the high frequency response appears more detailed for the BAM cell than a Swagelok cell, likely a consequence of the altered cell body geometry. The low frequency tails are also very comparable. Note that, during cell assembly of highly dense pellet samples, the gasket thickness must be chosen wisely to maintain a flat contact area between sample and current collector. These results outline the reliability of EIS measurements and solid electrolyte testing in the BAM cell.

To investigate the charge/discharge cycling performance of liquid electrolyte chemistry in the BAM cell, charge/discharge tests were conducted using both $LiNi_{0.8}Mn_{0.1}Co_{0.1}O_2$ (NMC811) and $LiNi_{0.6}Mn_{0.2}Co_{0.2}O_2$ (NMC622) cathode materials. Figure 6.4 displays the difference in electrochemical performance between a 10 mg cathode (an active material loading of 6.2 mg cm^{-2}) in a Swagelok cell, a 30 mg cathode (10.5 mg cm^{-2}) in a BAM cell, and a 200 mg cathode (70 mg cm^{-2}) in a BAM cell. The cells were subject to consecutive charge/discharge cycles at C/20, C/10, and C/5 (based on a practical capacity of 200 mA h g^{-1} for NMC811 and 175 mA h g^{-1} for NMC622) to determine the capacity fade and effect on the differential capacity (dQ/dV) plot.

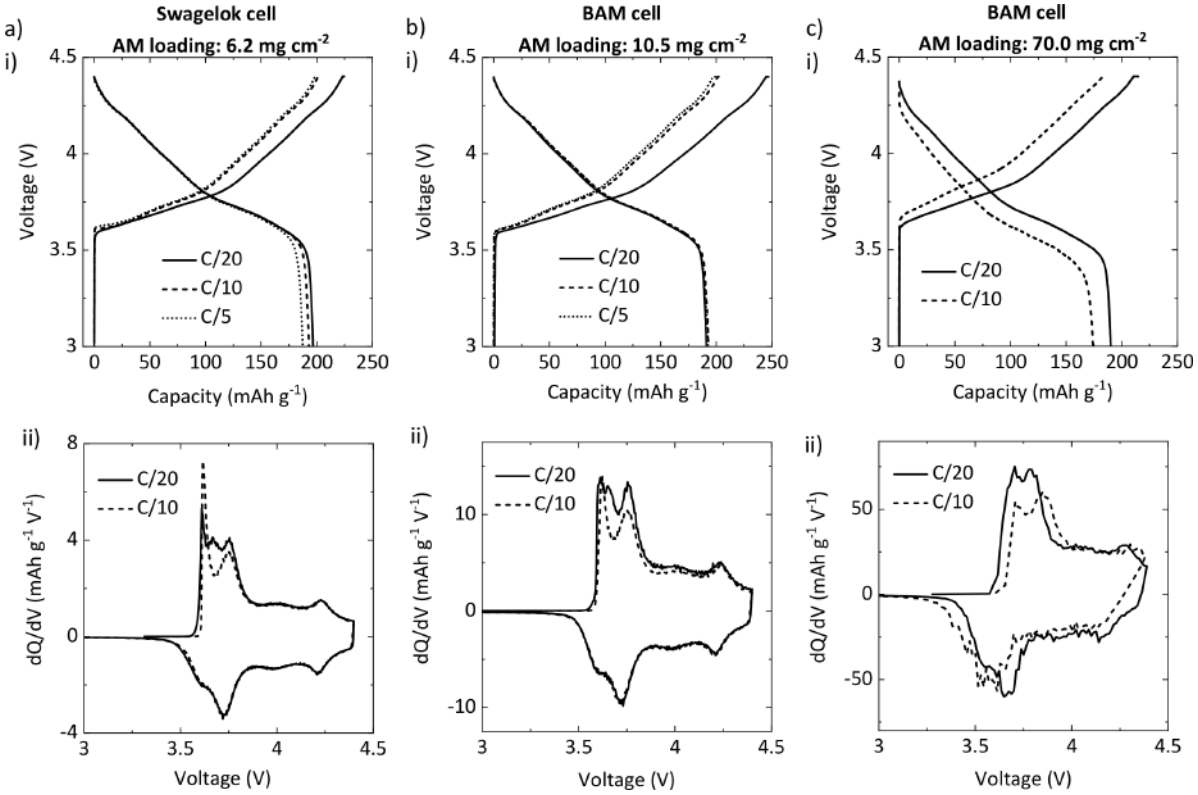

Figure 6.4: Discharge cycles of Li | NMC811 cells in: (a) a Swagelok configuration with an active material (AM) loading of 6.2 mg cm^{-2}, (b) a BAM configuration with an AM loading of 10.5 mg cm^{-2}, and (c) a BAM configuration with an AM loading of 70.0 mg cm^{-2}. Differential capacity (dQ/dV) plots are shown for each cell in part ii).

The low cathode mass loading configurations in both cells (Figure 6.4a, b) display very similar cycling performances, with discharge capacities close to 200 mAh g^{-1} (typical for NMC811 using this voltage window [31]) and little capacity fade at a cycling rate up to C/5. The high mass

loading BAM cell (70 mg cm^{-2}, Figure 6.4c), suitable for *operando* μSR experiments, shows a very comparable first cycle performance at C/20 to the low mass loading cells and a good performance at C/10. The cell did not manage the high current rate (≥2.5 mA cm^{-2}) required at C/5. The dQ/dV plots shown in Figure 6.4ii provide reasoning for this, with a voltage shift evident in both charge and discharge peaks at C/10 which is not observed in either low mass loading cell. This effect is often caused by an increase in internal impedance of the cell [32], common for thick electrodes [28]. The high resistance through the cathode leads to a kinetic limitation on charge transport, culminating in an overpotential in redox activity [4, 28]. This effect is accentuated at higher cycling rates and directly contributes to the capacity fade observed. However, the high mass loading cell is seen to be highly representative of the electrochemistry shown in low mass loading configurations, especially at lower cycling rates (∼C/20). The mass loading and C-rate should be chosen to optimise the balance between electrochemical performance and μSR data collection rate. While higher C-rates are useful for accelerating degradation mechanisms, the experimenter must take care during operando measurements to choose the rate such that the μSR data collection period for one point (generally, grouped runs at three field strengths) does not cover too wide a voltage range, otherwise subtle changes in dynamics may be obscured.

To validate other thick electrode preparation methodologies, Li | NMC622 half cells were cycled in three configurations. A Swagelok cell with an active material loading of 6.2 mg cm^{-2} was used as a benchmark, alongside an 80.0 mg cm^{-2} powder cathode in the BAM cell, and a 44.6 mg cm^{-2} mass loading cast electrode film in the BAM cell (Figure 6.5a-c, respectively). One advantage of the electrode film, which is more similar to standard cathodes albeit much thicker [27, 28], is the reduced quantity of electrolyte required (∼100 μL vs. ∼400 μL). This will improve the ratio of μSR signal gained from the active material. All cells in Figure 6.5 achieved excellent first cycle discharge capacities of ∼175 mAh g^{-1}, which is expected for NMC622 [31]. It is clear that high mass loading cells are more susceptible to capacity fade, especially at faster cycling rates, similar to NMC811 (Figure 6.4). The initial voltage decline during discharge at C/5 in Figure 6.5c indicates an incomplete redox activity during charging, caused by kinetic limitations across the thick cathode film at high applied current. The capacity fade is worsened for the cathode film, which may be a consequence of the lower carbon content, which struggles to transport electrons from the bulk. Overall, the electrochemical performance of the BAM cell is found to be reliable and, while high mass loading cells display good performances at a low C-rate, the cycling conditions must be managed to suit the experimental objectives.

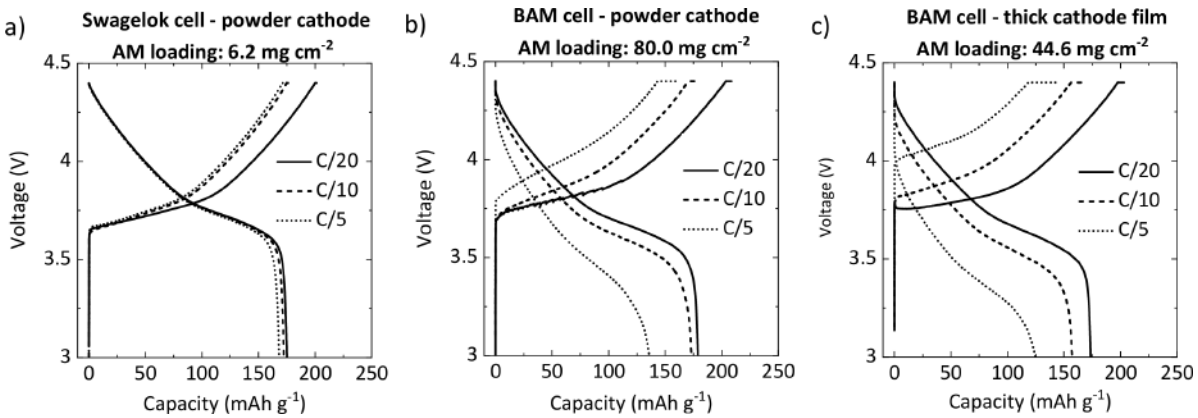

Figure 6.5: Three charge/discharge cycles of Li | NMC622 cells: (a) Swagelok cell with an active material (AM) loading of 6.2 mg cm^{-2}, (b) BAM cell with an AM loading of 80.0 mg cm^{-2}, and (c) a cathode film in the BAM cell with an AM loading of 44.6 mg cm^{-2}.

Muon Spin Relaxation

To explore how the BAM cell influences μSR measurements, data from previous studies (Chapter 4,5, and 7) were examined to see how the background/dynamic signal ratio differs between sample environments (given in Table 6.2). A comparison between two powdered samples and two pellet samples is shown, and the background amplitude is observed to be similar between the BAM cell and a standard Ti-holder (2 mm deep sample well, 24 mm diameter inspection window, 30 μm window thickness). The BAM cell does not appear to compromise on the collection of the dynamic signal from pristine samples (i.e., isolated materials, not functioning cells). Two *operando* cell environments are also shown [26], which provide much higher background rates because of the other cell components present. The larger inspection window of the BAM cell (18 mm diameter), in comparison with the commercially available coin cell (10 mm diameter), permits a lower background ratio. Further improvements in the optimisation of cell preparation methods will enable another improvement in this regard. Note that the coin cell experiment used a solid-state battery configuration, which is much more likely to provide a better signal/background ratio due to the absence of liquid electrolyte. Therefore, there is a large improvement in data quality seen for the BAM cell.

Table 6.2: A comparison of how the signal amplitudes vary for a variety of single material (i.e., powder/pellet) studies in the BAM cell and standard Ti sample holders, as well as in two *operando* cell configurations. The fractional background is the background amplitude normalized by the expected signal amplitude for a pure Ag plate ($A_0 = 0.232$).

Sample form	Sample Holder	Material	Flat Background Amp.	Dynamic KT Amp.	Gaus/Exp. Decay Amp.	Fractional Background
Powder	Ti-holder	NMC811	0.1392 (6)	0.1071 (6)	-	0.600 (3)
Powder	Ti-holder	Ti-doped LLZO	0.094 (1)	0.1563 (9)	-	0.405 (4)
Pellet	BAM cell	W-doped LLZO	0.0567 (2)	0.131 (1)	-	0.2444 (9)
Pellet	BAM cell	LNWO	0.0645 (4)	0.1674 (8)	0.0045 (8)	0.278 (2)
***Operando* cell**	Coin cell	NASICON Solid-state battery [26]	0.172 (1)	0.032 (2)	-	0.741 (4)
***Operando* cell**	BAM cell	Li|NMC811 liquid electrolyte battery	0.1592 (2)	0.034 (4)	0.013 (1)	0.6862 (9)

To understand how the μSR signal obtained from an *operando* experiment differs from a standard powder measurement, NMC811 was analysed as a powder in a Ti-holder and as a cathode in an operating BAM cell. The cell prepared was the subject of the study in Chapter 7 and displayed very similar cycling data to that given in Figure 6.4c. The comparison is detailed in Figure 6.6, which shows the two configurations of NMC811 at 300 K using 0, 5, and 10 Gauss longitudinally applied fields.

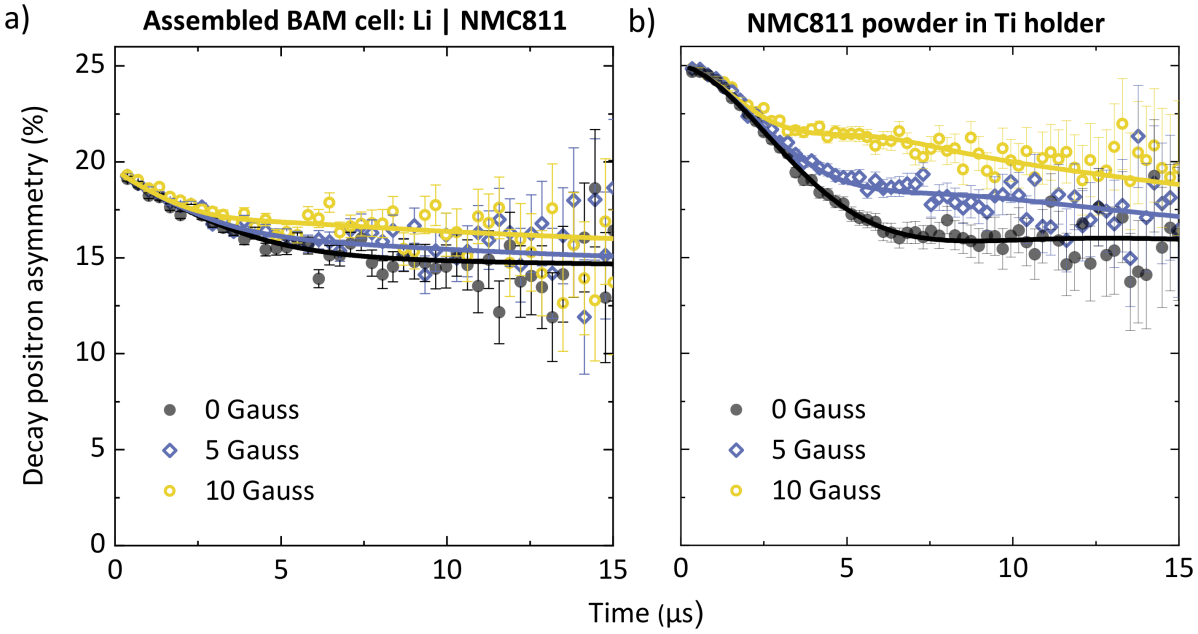

Figure 6.6: A comparison of the cathode material NMC811 in (a) a working *operando* BAM cell and (b) in a standard Ti-holder. Measurements show the relaxation in asymmetry at 300 K using 0, 5, and 10 Gauss longitudinally applied fields. Fit curves are shown as full lines.

As there is a large quantity of other components in the *operando* cell, such as liquid electrolyte, the BAM cell has a higher background signal and a loss in asymmetry. This point is illustrated by the decrease in muon decoupling strength using weak longitudinal fields in Figure 6.6a, compared with the powder sample in Figure 6.6b; muons that stop in a region which will either rapidly depolarise its spin (i.e., muonium formed in the electrolyte) or not depolarize it at all (i.e., silver mask) will be unaffected by the applied field (Table 6.3). The decreased decoupling by the applied field reflects the smaller proportion of muons stopped in the active material. The other constituents of the cell, such as carbon and binder, will contribute to the signal relaxation but should display a minimal dynamic contribution. The different muon stopping environment is also reflected by the low time behaviour of the two data-sets, where the initial relaxation ($\leq$1 μs) takes a slightly different form in the *operando* cell. An additional exponential relaxation term was used in the fitting function for the BAM cell experiment to account for this and the inhomogeneous muon stopping environment. The longer timescale of relaxation is broadly similar for both samples, indicating a dynamical signal is indeed measured from the active material.

Table 6.3: Table providing the general effect of different cell components on a typical μSR asymmetry profile. The specifics depend on the material used.

Cell component	**Expected μSR signal**
Silver mask	Non-relaxing background contribution
Steel body	Mostly background contribution
Active material	Ionic motion causes relaxing signal contribution
Liquid electrolyte	Little contribution to dynamic relaxing signal but loss of asymmetry likely
Conductive carbon	Low dynamic contribution
Binder (PTFE/PVDF)	No dynamic contribution but possible F–μ–F bonds

A quantitative analysis of the data shown in Figure 6.6 is given in Table 6.4, which shows the fitting parameters for both configurations of NMC811. Slight differences in fitting parameters between the samples are expected given the different synthesis techniques (see Experimental section). The decreased amplitude of the dynamic Kubo-Toyabe is expected for the BAM cell configuration, however, the χ^2 values indicate the applied function describes the data well in both cases. The larger errors in fitting parameters seen for the BAM cell are indicative of the lower amplitude of the dynamical signal; increasing the proportion of active material in the cathode would improve the obtained data quality.

The value of the static field distribution width, Δ, is very similar for both configurations and validates that the Kubo-Toyabe signal arises from NMC811 itself. Any Δ value arising from the Li anode, or carbon additive, would be expected to take a different value [33]. The field fluctuation rate, ν, is seen to be slightly different but within reason for both configurations. The similarity of these important parameters, Δ and ν, gives confidence to the described *operando* methodologies and justifies that the measurements from the BAM cell are representative of pristine material investigations. As such, the changes in fitting parameters during an *operando* experiment can be assumed to reflect real changes in the active material under investigation.

Table 6.4: A comparison of a powder sample of cathode material NMC811 inside a standard Ti sample holder, and an NMC811 cathode (before charge/discharge has begun) inside an operational BAM cell.

Environment	**B.G. Amp.**	**Dyn. KT Amp.**	Δ (μs^{-1})	ν(μs^{-1})	**Exp. Decay Amp.**	λ (μs^{-1})	χ^2
NMC811 powder in Ti-Holder	0.1392 (6)	0.1071 (6)	0.296 (3)	0.288 (9)	-	-	0.987
NMC811 cathode in BAM cell	0.159 (2)	0.034 (4)	0.28 (1)	0.37 (4)	0.013 (1)	0.71 (3)	0.994

Applications

The reliability of μSR and electrochemical data collected using the BAM cell opens the possibility of previously inaccessible *operando* μSR experiments. Such experiments afford the opportunity

to access the diffusion properties of a wide range of battery materials under chosen conditions, including cycle number and high state of charge. The BAM cell is suitable to a wide range of chemistries, using either solid- and liquid-based electrolyte configurations, while *operando* measurements of Na^+ or Mg^{2+} motion remain unstudied to date. Indeed, μSR is suitable to study the motion of many other ions such as ^{27}Al, ^{25}Mg [34], ^{39}K [35], ^{51}V, and ^{127}I [18]. Control over both the inspection window thickness and beam degraders permits the possibility to study any cell component. Although the current experimental methodology involves the preparation of thick electrodes to ensure adequate muon implantation, the selection of low momentum muons at continuous sources is possible to reduce the range width of implantation and permit the study of thin electrodes, with the caveat of slower collection rates. Furthermore, *operando* elemental analyses using negative muons would build on the studies by Umegaki *et al.* [36], with applications toward a wide range of electrochemical phenomena possible.

Meanwhile, the development of computational muon site modelling for battery materials during cycling will realise a sound comparison between experiment and theory. The necessity to understand how the structural changes during charge/discharge affect the muon site underpin the data analysis and will allow greater detail to be extracted from *operando* measurements. The collaboration of *operando* μSR with complementary experimental techniques, for example with impedance spectroscopy, remains an exciting prospect. Furthermore, spectroscopic techniques such as X-ray absorption yield crucial information on oxidation state and local structure, the influence of which on ionic diffusion at an atomic level is fundamental to battery operation and would prove a valuable comparison. *Operando* μSR investigations are presented here as a developing battery characterisation technique with a wide range of potential applications.

Conclusions

An easily assembled electrochemical cell is presented for *operando* μSR measurements of batteries on the EMU beamline at the ISIS Neutron and Muon Source, suitable for the study of various ionic species. Such experiments offer the opportunity to directly track ionic dynamics under specific electrochemical conditions and elucidate the effect of material degradation processes on diffusion rates. The cell is bench-marked against cathode and solid electrolyte materials in commercially available cells and displays very similar electrochemical performances in cycling and impedance experiments, with low noise and a negligible resistance. The existing methodology requires a high active material mass loading, which is found to be representative of control experiments at low mass loading during initial charge/discharge cycles at a rate of C/20. The μSR results outline a low background signal contribution when using the cell for standard samples, while measurements of a working cell are seen to be representative of the active material. As such, the BAM cell displays functional reliability in both electrochemical and μSR data collection. There is a wide range of scientific applications towards the use of *operando* μSR for the study of various electrochemical phenomena. The BAM cell is available for use on the EMU and HiFi spectrometers by the ISIS user community and can be adapted to other muon instruments.

References

[1] R. Marom, S. F. Amalraj, N. Leifer, D. Jacob, and D. Aurbach. A review of advanced and practical lithium battery materials. *J. Mater. Chem.*, 21:9938–9954, 2011.

[2] T. Famprikis, P. Canepa, J. A. Dawson, M. S. Islam, and C. Masquelier. Fundamentals of inorganic solid-state electrolytes for batteries. *Nature Materials*, 18:1278–1291, 2019.

[3] J. Sugiyama, K. Mukai, M. Harada, H. Nozaki, K. Miwa, T. Shiotsuki, Y. Shindo, S. R. Giblin, and J. S. Lord. Reactive surface area of the $Li_x(Co_{1/3}Ni_{1/3}Mn_{1/3})O_2$ electrode determined by μ^+SR and electrochemical measurements. *Phys. Chem. Chem. Phys.*, 15:10402, 2013.

[4] K. Märker, P. J. Reeves, C. Xu, K. J. Griffith, and C. P. Grey. Evolution of Structure and Lithium Dynamics in $LiNi_{0.8}Mn_{0.1}Co_{0.1}O_2$ (NMC811) Cathodes during Electrochemical Cycling. *Chem. Mater.*, 31:2545–2554, 2019.

[5] X. Bai, T. Li, and Y. J. Bai. Capacity degradation of $Li_4Ti_5O_{12}$ during long-term cycling in terms of composition and structure. *Dalton Trans.*, 49:10004–10010, 2020.

[6] P. P. R. M. L. Harks, F. M. Mulder, and P. H. L. Notten. In situ methods for Li-ion battery research: A review of recent developments. *J. Power Sources*, 288:92–105, 2015.

[7] X. Li, H-Y. Wang, H. Yang, W. Cai, S. Liu, and B. Liu. In situ/operando characterization techniques to probe the electrochemical reactions for energy conversion. *Small Methods*, 2:1700395, 2018.

[8] O. J. Borkiewicz, K. M. Wiaderek, P. J. Chupas, and K. W. Chapman. Best Practices for Operando Battery Experiments: Influences of X-ray Experiment Design on Observed Electrochemical Reactivity. *J. Phys. Chem. Lett.*, 6:2081–2085, 2015.

[9] O. J. Borkiewicz, B. Shyam, K. M. Wiaderek, C. Kurtz, P. J. Chupas, and K. W. Chapman. The AMPIX electrochemical cell: a versatile apparatus for *in situ* X-ray scattering and spectroscopic measurements. *J. Appl. Cryst.*, 45:2081–2085, 2012.

[10] S. Taminato, M. Yonemura, S. Shiotani, T. Kamiyama, S. Torii, M. Nagao, Y. Ishikawa, K. Mori, T. Fukunaga, Y. Onodera, T. Naka, M. Morishima, Y. Ukyo, D. Sulistyanintyas Adipranoto, H. Arai, Y. Uchimoto, Z. Ogumi, K. Suzuki, M. Hirayama, and R. Kanno. Real-time observations of lithium battery reactions—operando neutron diffraction analysis during practical operation. *Sci. Rep.*, 6:28843, 2016.

[11] V. Charbonneau, A. Lasia, and G. Brisard. Impedance studies of Li^+ diffusion in nickel manganese cobalt oxide (NMC) during charge/discharge cycles. *J. Electroanal. Chem*, 875:113944, 2020.

[12] A. J. Merryweather, C. Schnedermann, Q. Jacquet, C. P. Grey, and A. Rao. Operando optical tracking of single-particle ion dynamics in batteries Imaging lithium-ion transport in LCO. *Nature*, 594:522–528, 2021.

[13] P. J. Baker, I. Franke, F. L. Pratt, T. Lancaster, D. Prabhakaran, W. Hayes, and S. J. Blundell. Probing magnetic order in LiMPO$_4$ (M = Ni, Co, Fe) and lithium diffusion in Li$_x$FePO$_4$. *Phys. Rev. B*, 84:174403, 2011.

[14] T. E. Ashton, J. V. Laveda, D. A. Maclaren, P. J. Baker, A. Porch, M. O. Jones, and S. A. Corr. Muon studies of Li^+ diffusion in LiFePO$_4$ nanoparticles of different polymorphs. *J. Mater. Chem. A*, 2:6238–6245, 2014.

[15] D. Z. C. Martin, A. R. Haworth, W. L. Schmidt, P. J. Baker, R. Boston, K. E. Johnston, and N. Reeves-McLaren. Evaluating lithium diffusion mechanisms in the complex spinel Li$_2$NiGe$_3$O$_8$. *Phys. Chem. Chem. Phys.*, 21:23111–23118, 2019.

[16] J. V. Laveda, B. Johnston, G. W. Paterson, P. J. Baker, M. G. Tucker, H. Y. Playford, K. M. Ø. Jensen, S. J. L. Billinge, and S. A. Corr. Structure–property insights into nanostructured electrodes for Li-ion batteries from local structural and diffusional probes. *J. Mater. Chem. A*, 6:127–137, 2018.

[17] I. D. Johnson, T. E. Ashton, E. Blagovidova, G. J. Smales, M. Lübke, P. J. Baker, S. A. Corr, and J. A. Darr. Mechanistic insights of Li^+ diffusion within doped LiFePO$_4$ from Muon Spectroscopy. *Sci. Rep.*, 8:4114, 2018.

[18] D. W. Ferdani, S. R. Pering, D. Ghosh, P. Kubiak, A. B. Walker, S. E. Lewis, A. L. Johnson, P. J. Baker, M. S. Islam, and P. J. Cameron. Partial cation substitution reduces iodide ion transport in lead iodide perovskite solar cells. *Energy Environ. Sci.*, 12:2264–2272, 2019.

[19] M. Amores, P. J. Baker, E. J. Cussen, and S. A. Corr. Na$_{1.5}$La$_{1.5}$TeO$_6$:Na^+ conduction in a novel Na-rich double perovskite. *Chem. Commun.*, 54:10040–10043, 2018.

[20] M. Amores, T. E. Ashton, P. J. Baker, E. J. Cussen, and S. A. Corr. Fast microwave-assisted synthesis of Li-stuffed garnets and insights into Li diffusion from muon spin spectroscopy. *J. Mater. Chem. A*, 4:1729–1736, 2016.

[21] J. Sugiyama, K. Mukai, Y. Ikedo, H. Nozaki, M. Månsson, and I. Watanabe. Li Diffusion in Li$_x$CoO$_2$ Probed by Muon-Spin Spectroscopy. *Phys. Rev. Lett.*, 103:147601, 2009.

[22] A. S. Powell, J. S. Lord, D. H. Gregory, and J. J. Titman. Muon Spin Relaxation Studies of Lithium Nitridometallate Battery Materials: Muon Trapping and Lithium Ion Diffusion. *J. Phys. Chem. C*, 113:20758–20763, 2009.

[23] I. McClelland, B. Johnston, P. J. Baker, M. Amores, E. J. Cussen, and S. A. Corr. Muon Spectroscopy for Investigating Diffusion in Energy Storage Materials. *Annu. Rev. Mater. Res.*, 50:1–15, 2020.

[24] S. J. Blundell. Spin-polarized muons in condensed matter physics. *Contemp. Phys.*, 40:175–192, 1999.

[25] L. Yang, A. Xiao, and B. L. Lucht. Investigation of solvation in lithium ion battery electrolytes by NMR spectroscopy. *J. Mol. Liq.*, 154:131–133, 2010.

[26] I. McClelland, S. G. Booth, H. El-Shinawi, B. I. J. Johnston, J. Clough, W. Guo, E. J. Cussen, P. J. Baker, and S. A. Corr. In Situ Diffusion Measurements of a NASICON-Structured All-Solid-State Battery Using Muon Spin Relaxation. *ACS. Appl. Energy. Mater.*, 4:1527–1536, 2021.

[27] T. Danner, M. Singh, S. Hein, J. Kaiser, H. Hahn, and A. Latz. Thick electrodes for Li-ion batteries: A model based analysis. *J. Power Sources*, 334:191–201, 2016.

[28] H. Zheng, J. Li, X. Song, G. liu, and V. S. Battaglia. A comprehensive understanding of electrode thickness effects on the electrochemical performances of Li-ion battery cathodes. *Electrochim. Acta*, 71:258–265, 2012.

[29] R. Elango, A. Demortieére, V. De Andrade, M. Morcrette, and V. Seznec. Thick Binder-Free Electrodes for Li–Ion Battery Fabricated Using Templating Approach and Spark Plasma Sintering Reveals High Areal Capacity. *Adv. Energy Mater.*, 8:1703031, 2018.

[30] O. Arnold, J. C. Bilheux, J. M. Borreguero, A. Buts, S. I. Campbell, L. Chapon, M. Doucet, N. Draper, R. Ferraz Leal, M. A. Gigg, V. E. Lynch, A. Markvardsen, D.J. Mikkelson, R. L. Mikkelson, R. Miller, K. Palmen, P. Parker, G. Passos, T. G. Perring, P. F. Peterson, S. Ren, M. A. Reuter, A. T. Savici, J. W. Taylor, R. J. Taylor, R. Tolchenov, W. Zhou, and J. Zikovsky. Mantid - Data analysis and visualization package for neutron scattering and μSR experiments. *Nucl. Instrum. Meth. A*, 764:156–166, 2014.

[31] R. Jung, M. Metzger, F. Maglia, C. Stinner, and H. A. Gasteiger. Oxygen Release and Its Effect on the Cycling Stability of $LiNi_xMn_yCo_zO_2$ (NMC) Cathode Materials for Li-Ion Batteries. *J. Electrochem. Soc.*, 164:A1261–A1377, 2017.

[32] B.-C. Park, H.-B Kim, S.-T. Myung, K. Amine, I. Belharouak, S.-M Lee, and Y.-K. Sun. Improvement of structural and electrochemical properties of AlF_3-coated $Li[Ni_{1/3}Co_{1/3}Mn_{1/3}]O_2$ cathode materials on high voltage region. *J. Power Sources*, 178:826–831, 2008.

[33] N. J. Stone. Table of nuclear magnetic dipole and electric quadrupole moments. *At. Data Nucl. Data Tables*, 90:75—176, 2005.

[34] R. D. Bayliss, B. Key, G. Sai Gautam, P. Canepa, B. Jin Kwon, S. H. Lapidus, F. Dogan, A. A. Adil, A. S. Lipton, P. J. Baker, G. Ceder, J. T. Vaughey, and J. Cabana. Probing Mg Migration in Spinel Oxides. *Chem. Mater.*, 32:663–670, 2020.

[35] N. Matsubara, E. Nocerino, O. K. Forslund, A. Zubayer, P. Gratrex, and et. al. Magnetism and ion diffusion in honeycomb layered oxide $K_2Ni_2TeO_6$. *Sci. Rep.*, 10:18305, 2020.

[36] I. Umegaki, Y. Higuchi, Y. Kondo, K. Ninomiya, S. Takeshita, M. Tampo, H. Nakano, H. Oka, J. Sugiyama, M. K. Kubo, and Y. Miyake. Nondestructive high-sensitivity detections of metallic lithium deposited on a battery anode using muonic x-rays. *Anal. Chem.*, 92:8194–8200, 2020.

Research Article

Direct Observation of the Dynamic Lithium Diffusion Properties in the First Cycle of $LiNi_{0.8}Mn_{0.1}Co_{0.1}O_2$ (NMC811) using *Operando* Muon Spectroscopy

Innes McClelland, Samuel G. Booth, Nirmalesh Anthonisamy, Laurence Middlemiss, Gabriel E. Pérez, Edmund J. Cussen, Peter J. Baker, Serena A. Cussen

[I. McClelland, S. G. Booth, N. Anthonisamy, L. Middlemiss, Gabriel E. Pérez, E. J. Cussen, P. J. Baker, and S. A. Cussen. Direct Observation of the Dynamic Lithium Diffusion Properties in the First Cycle of $LiNi_{0.8}Mn_{0.1}Co_{0.1}O_2$ (NMC811) using *Operando* Muon Spectroscopy. *Under peer review.*]

Abstract

Ni-rich layered oxide cathode materials such as $LiNi_{0.8}Mn_{0.1}Co_{0.1}O_2$ (NMC811) provide a higher capacity than their lower Ni-content analogues, although they suffer a far more pronounced performance fade, especially when cycled above 4.2 V. In this study, we apply *operando* muon spectroscopy (μSR), for the first time, to investigate how the local (∼Å length scale) diffusional and internal field properties change in NMC811 during the first cycle. The measurements are largely unaffected by interface/surface effects, providing a specific characterisation of the fundamental bulk properties. Li^+ dynamics in the first cycle of NMC811 are found to increase most rapidly at the beginning of charge before decreasing above 75% state of charge (SOC). This fits well with previously reported models for lithium diffusion in NMC811 and correlates with the *c* lattice contraction observed by X-ray diffraction. Complementary electrochemical impedance spectroscopy (EIS) measurements show a minimum charge transfer resistance at around 50% SOC, before a large resistive

increase above 70% SOC. The combination of *operando* μSR and EIS enables the elucidation of the limiting factors on charge transport, which for NMC811 appears to be the particle surface regions at high SOC.

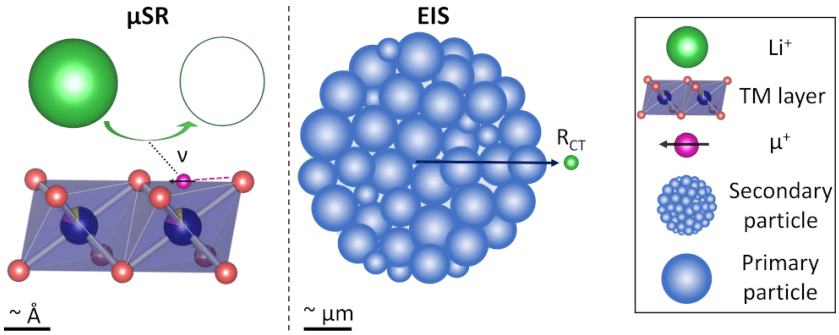

Graphical abstract. The different mechanisms of probing ionic diffusion using muon spin relaxation spectroscopy and electrochemical impedance spectroscopy.

Introduction

The promise of higher capacity offered by the Ni-rich layered oxide cathode material $LiNi_{0.8}Mn_{0.1}Co_{0.1}O_2$ (NMC811, practical capacity ≥200 mAh g^{-1}) is somewhat dampened by significant and irreversible capacity loss over the first cycle [1]. Such irreversibility is not as pronounced for lower Ni-content NMCs [1, 2], meaning its origin remains under active investigation. Numerous material degradation processes exist for NMC811, including Li/Ni mixing [3, 4], surface layer reconstruction [5, 6], particle cracking [7], decomposition reactions with the electrolyte [8, 9], and sluggish Li^+ diffusion kinetics [10, 11]. Charging beyond 4.2 V vs. Li^+/Li in NMC811 is highly detrimental to capacity retention, correlating with the high voltage event, observed as a small peak at 4.2 V in the differential capacity plot [12]. Such limitation to high voltage cycling provides an ongoing research challenge as it threatens to dampen much of the practical capacity increase offered by high Ni-content compositions. While previously thought as the consequence of a two-phase O3-O1 transition, similar to the debilitating process observed for $LiNiO_2$ [13], multiple studies have now observed no phase change at high voltage for NMC811 [12, 14]. The high voltage event (≥4.2 V) is, however, heavily linked to a rapid *c*-axis contraction [15]. The increased Ni-content in NMC811 strengthens the *M*-O bond at highly delithiated states, therefore decreasing the repulsion between O^{2-} layers and contributing to layer collapse [16, 17].

It is important to consider, and distinguish, the degradation processes from both bulk and surface effects in NMC811 [5, 18]. Surface layers such as spinel and/or rock-salt structures, far more prevalent in high Ni-content NMCs [19, 20], are formed from the aggressive reduction of highly reactive Ni^{4+} to Ni^{3+} by the electrolyte and are a significant factor in the first cycle capacity fade [21]. The rock-salt layer has been reported as between 5 – 15 nm thick using TEM and OEMS [1, 22]. Although limited in thickness, the surface Li^+ ion mobility properties are significantly lowered compared to the bulk [23], and hence it can act as a bottleneck for Li^+

transport between particles. Furthermore, lattice mismatch between the bulk and the surface rock-salt at high SOC (because of the lattice contraction) has been reported as the primary cause of fatigue degradation in the bulk [5].

A high-rate capability is increasingly paramount for fast charging battery applications such as electric vehicles. Such capabilities depend on many cell characteristics [24], including mass transport, percolating Li^+ ion pathways, adhesion to the current collector, and solid-electrolyte interface formation, but the fundamental performance limitations rely on the lithium diffusion coefficient (D_{Li}) within the electrode materials [25]. Kinetic limitations are pertinent within cathode materials [26]; sluggish Li^+ diffusion has been proposed as a cause of overpotential growth, resulting in reduced cathode utilisation [10, 27]. A direct observation of dynamical mechanisms, such as ionic diffusion, is therefore crucial for material development [28, 29]. For this, a precise characterisation of electrochemical phenomena which occur during cycling (i.e., *operando* measurements) is highly desirable, as some subtle effects may be hidden for *ex situ* measurements on relaxed cells. Although for many techniques this is non-trivial [30], it is the logical next step to afford an improved understanding of battery operation under realistic conditions.

Previous studies of NMC811 have employed the enhanced capabilities of *operando* techniques to study its structural [13], diffusional [26], and spectroscopic [31] properties to excellent effect. Muon spectroscopy (μSR) has become a well-established local probe of diffusion barriers, suitable for mobile ions including Li^+, Na^+, K^+ and Mg^{2+} [32–35]. To date, most μSR studies of ionic diffusion have focused on pristine, as-prepared materials. Such studies provide useful fundamental properties, although it is important to remember they often refer to fully lithiated cathode compounds, where ionic hopping occurs *via* interstitial sites or neighbouring defects. In contrast, the diffusional properties during cycling depend heavily on the vacancies within available pathways, site blocking, and layer spacing. While EIS or galvanostatic intermittent titration technique (GITT) can provide D_{Li} as a function of SOC, such measurements cover the entire cell and are not direct measurements of local diffusivity within a material. The development of an *operando* approach to μSR, as reported here, enables characterisation of the variation in material properties during charge/discharge cycles. One relevant advantage of μSR is the isolation of Li^+ transport in the electrode material from within the electrolyte, since diffusion rates in liquid electrolytes ($\sim 10^{-6}$ – 10^{-7} cm^2 s^{-1} [36]) are outside the motional range probed by the muon lifetime ($\sim 10^{-8}$ – 10^{-13} cm^2 s^{-1} [35]).

Herein, we describe an *operando* μSR study of the first cycle of cathode material NMC811. μSR is proposed as a detailed probe to link both the diffusional properties and the highly correlated structural changes within the unit cell. Analysis of μSR measurements was guided by complementary X-ray diffraction (XRD) and electrochemical impedance spectroscopy (EIS) results. An *operando* cell is presented as a working electrochemical device which can be used for a variety of future μSR experiments.

Experimental

Materials and Synthesis

The hydroxide precursor $Ni_{0.8}Mn_{0.1}Co_{0.1}(OH)_2$ was prepared using a co-precipitation method inside a controlled stirred tank reactor at pH 11. Stoichiometric quantities of $NiSO_4{\cdot}6H_2O$ (>98%, Sigma), $MnSO_4{\cdot}xH_2O$ (>98%, Sigma), and $CoSO_4{\cdot}7H_2O$ (>99%, Sigma) were weighed and dissolved in a solution of NH_4OH and deoxygenated water. The reaction was completed overnight under continuous agitation and N_2 gas flow inside the vessel, which was held at 60 °C. The mixture was allowed to settle before being washed using deoxygenated water. This process was repeated multiple times before the mixture was dried well in an oven under air to yield the brown precursor powder. To lithiate the hydroxide precursor, stoichiometric amounts of $Ni_{0.8}Mn_{0.1}Co_{0.1}(OH)_2$ and $LiOH{\cdot}H_2O$ were weighed and ground together thoroughly for 30 minutes in an agate mortar. A 10% weight excess of $LiOH{\cdot}H_2O$ was used to account for losses during calcination. Calcination was performed in two steps: first 450 °C for 12 hours, followed by 30 minutes grinding in an Ar-filled glovebox, and secondly 850 °C for 12 hours, before immediate transfer to the glovebox while hot to minimise air exposure. Both steps were completed in a tube furnace under an O_2 atmosphere with a ramp rate of 4 °C/min.

Characterisation

X-ray diffraction measurements were performed using a Rigaku Miniflex with a Cu K_α X-ray source with wavelength 1.5406 Å. *Operando* X-ray diffraction was performed using an ECC-Opto-Std test cell (EL-cell) at a rate of C/50 (based on a practical capacity of 200 mAh g^{-1}, using a 5 × 10 mm Kapton window which was transparent to X-rays. The EL-cell was assembled using a freshly cut lithium disk covered by a glass microfibre separator and then an NMC811 composite cathode deposited on a mesh aluminium current collector. Electrolyte was added using a syringe. Sequential Pawley fits were employed to determine lattice parameters. SEM measurements were conducted using an FEI Inspect F50 high resolution electron microscope using an accelerating voltage of 5 kV.

For all electrochemical measurements, the active material, NMC811, was mixed thoroughly in an agate mortar with conductive carbon and PTFE binder in the wt.% ratio 70:20:10, respectively. *In situ* impedance measurements were collected using a Biologic VMP-300 potentiostat, while *operando* electrochemistry was conducted using a Biologic VSP potentiostat. For the *in situ* EIS experiment a 17 mg cm^{-2} cathode powder was used in a Swagelok type cell and cycled at a rate of C/20. The cyclic voltammetry experiment used an identical cell set-up to the EIS experiment, with a scan rate of 0.1 mV s^{-1}.

Muon spin relaxation measurements were conducted on the EMU spectrometer at the ISIS Neutron and Muon Source in a specifically designed BAM (Battery Analysis by Muon) cell [37]. A description of ionic diffusion using μSR has been given previously by our group [35]. The cell was assembled within a Ar-filled glovebox with cross-tightened PEEK screws to ensure even pressure. The current collectors used were 100 μm thick 306L grade austenitic steel. This grade

is non-magnetic and thin enough to not interfere significantly with the muon signal. Within the half-cells, pre-cut Li discs (16 mm diameter and 0.25 mm thick, PI-KEM, UK) were used as the anode material, with approximately 400 μL of electrolyte ($LiPF_6$ in ethylene carbonate: ethyl methyl carbonate [50:50 v/v] with 2% vinylene carbonate additive [Solvionic, France]). A thick cathode was necessary to ensure adequate muon implantation in the region of interest. Therefore, the cell was prepared with a cathode loading of around 100 mg cm^{-2} (area ∼2 cm^2), with additional separators and electrolyte used to ensure appropriate wetting. Continuous μSR measurements were taken to 20 million positron detection events in the order of: 0, 10, 20 Gauss longitudinally applied fields during (de)lithiation. These three field measurements were grouped to form one distinct measurement in this experiment, allowing the collection of 71 points over the first cycle (at C/20). Each point required around 35 minutes of measurement time. A rate of C/20 was used (current density of 10 mA g^{-1}), and two pauses were necessary due to muon beam outages. All measurements were conducted at 300 K. MantidPlot was used for all μSR data analysis [38].

Results and Discussion

A pH-controlled stirred tank reaction was used to produce a hydroxide precursor, which was thoroughly mixed with $LiOH{\cdot}H_2O$ and calcined under oxygen flow to yield the cathode material, $LiNi_{0.8}Mn_{0.1}Co_{0.2}O_2$ (NMC811). An X-ray powder diffraction pattern of the resultant NMC811 is shown in Figure 7.1a, confirming a single phase $R\bar{3}m$ structure with a (003)/(104) peak ratio of ∼1.7, indicating low cation mixing [39]. Rietveld refinement (Figure S7.1) was performed to validate the quality of the sample and determine lattice parameters of $a = b = 2.87376$ (8) and $c = 14.2099$ (3) Å. Scanning electron micrographs, displayed in Figure 7.1(b, c) depict spherical secondary particles between 5 – 10 μm consisting of primary particles which are several hundred nanometres in diameter. This is typical of polycrystalline NMC811 synthesised through co-precipitation.

To enable *operando* muon measurements on the EMU spectrometer at ISIS Neutron and Muon Source, an electrochemical cell was developed. Figure 7.2(a, b, c) shows the assembled BAM (Battery Analysis by Muon) cell, which possesses a stainless-steel inspection window of diameter 18 mm to allow ample beam penetration area. The 100 μm thick steel current collector was thin enough to allow most muons to pass through and implant in the cathode. The cell components are expanded to show the constituents (Figure 7.2d) and the experimental set-up (Figure 7.2e). Further details on cell assembly are given in the Supporting Information.

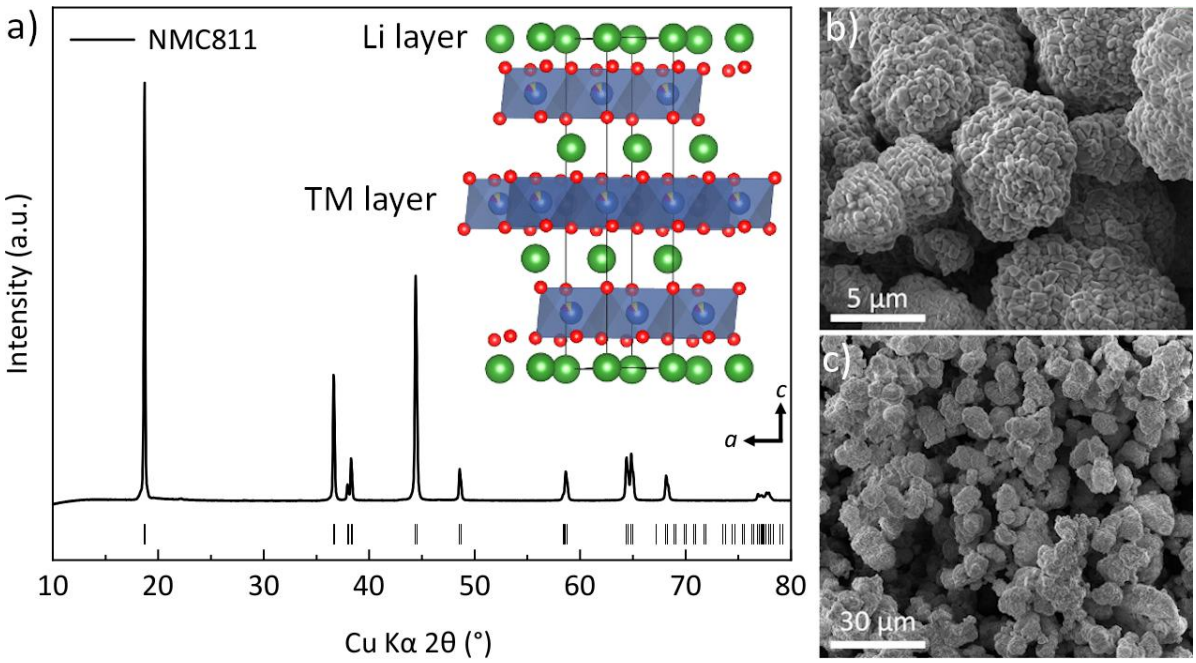

Figure 7.1: (a) X-ray diffraction pattern of synthesized $LiNi_{0.8}Mn_{0.1}Co_{0.1}O_2$ (NMC811) for which a Rietveld refinement can be found in Figure S7.1. The layered Li and transition metal (TM) structure is shown, with the unit cell outlined. (b), (c) Scanning electron micrographs at different magnifications, showing spherical secondary particles.

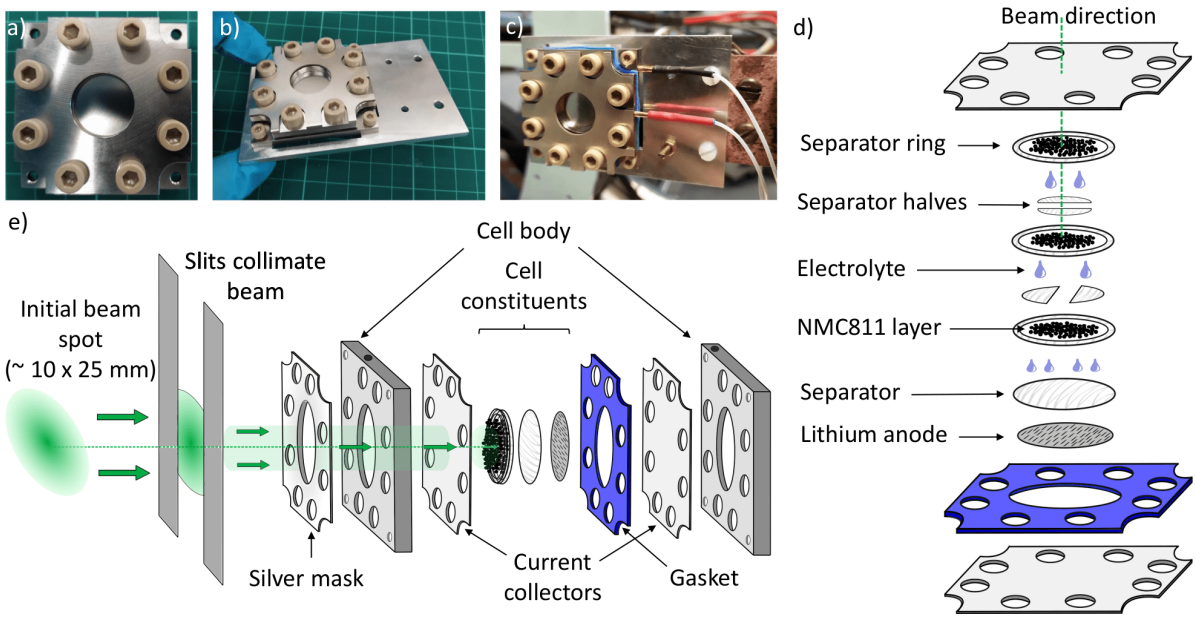

Figure 7.2: (a), (b) Pictures showing the BAM (Battery Analysis by Muon) cell. (c) The cell fixed on the EMU spectrometer at the ISIS Neutron and Muon Source. (d) Schematic showing how the cell was assembled in this study, using layers of cathode with separator rings and halves to hold sufficient electrolyte to fully wet the cathode active material loading of 70 mg cm^{-2}. (e) Experimental schematic showing the beam penetration into the cathode.

To evaluate the dynamic lithium diffusion properties of NMC811, the first charge/discharge cycle was examined through *operando* μSR. The voltage window was extended slightly to follow the high voltage behaviour of the material, cycling between 3.0 and 4.4 V vs. Li/Li^+ at C/20.

Utilising the *operando* cell, we achieved a first charge capacity of 222 mAh g^{-1} and a first discharge capacity of 198 mAh g^{-1} (Figure 7.3c). Although a large cathode mass was used, muons unavoidably implant into everything they encounter within the cell. Consequently, the relaxing signal coming from the cathode material, A_{KT}, accounts for only $\sim 1/6^{th}$ of the expected initial amplitude, A_0 (Equation 7.1). Li^+ transport *via* the electrolyte is too fast to be detectable within the muon lifetime [40], and Li^+ surface sorption through the cathode additives is unlikely to significantly influence the signal, meaning its contribution to the muon spin relaxation is minimal. Therefore, A_{KT} can be confidently assumed to arise from Li^+ transport within the NMC811 crystal structure. Any inhomogeneities across the thick electrode are expected to be averaged out in the obtained signal.

Continuous zero and longitudinal fields were collected to follow the Li^+ dynamics during the first charge/discharge cycle. The data were fit in the time domain (t) 0.1 – 25 μs using a composite function containing a flat background, a dynamic Kubo-Toyabe function, and an exponential relaxation described as:

$$A_0 P(t) = A_{bg} + A_{KT} P_{KT}(\Delta, \nu, t) + A_{exp} P_{exp}(\lambda, t). \tag{7.1}$$

The component amplitudes (A) and the relaxation rate (λ) were held as fixed global parameters, while the field fluctuation rate (ν) and the static field distribution (Δ) were allowed to fluctuate (shown in Table S7.3). CCCV (constant current constant voltage) cycling was applied to compensate for the kinetic limitations expected when using a high mass loading [41], and to provide sufficient time for a measurement at 4.4 V.

To illustrate how the muon signal changes during charging, zero-field fits are shown in Figure 7.3a. The signal relaxation decreases gradually towards 4.3 V before increasing between 4.3 and 4.4 V. In general, the form of the relaxation will vary depending on the ratio ν/Δ [42]; Figure 7.3a thus suggests that the rate of ionic hopping tends to increase over the first charge until high SOC, where it slows down. The trend appears to reverse over the course of the discharge, with a large change evident below 3.7 V, likely indicating poor Li^+ ion dynamics in this low voltage region. A visual interpretation of all three fields at the beginning of the first charge (3.6 V), the top of the first charge (4.4 V), and the end of the first discharge (3.5 V) is given in Figure 7.3d (also shown separately in Figure S7.4), and clearly indicates faster Li^+ ion diffusion at high SOC. The form of the asymmetry does not return to its initial state after discharge, with the deviation clear at longer timescales ($\geq$6 μs). This suggests a change in diffusional properties after the first cycle, which aligns with the loss of capacity between charge and discharge as Li sites are not fully reoccupied after one cycle.

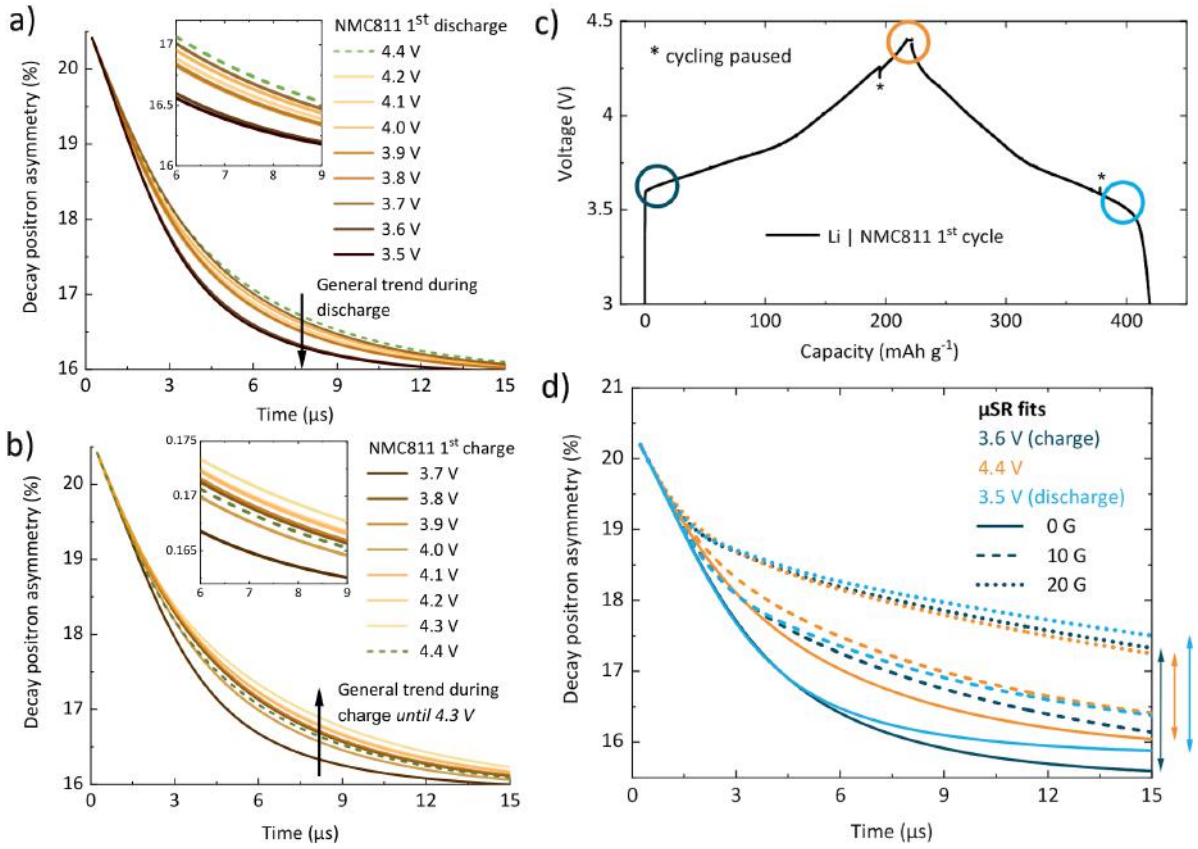

Figure 7.3: (a), (b) *Operando* μSR data comparing zero field (0 G) fit curves across the first charge/discharge cycle of NMC811, which is shown in (c). (d) 0, 10, and 20 G longitudinal fields at the beginning (3.6 V), the top (4.4 V), and the end (3.5 V) of the first charge/discharge cycle.

Fitting Equation 7.1 to the data collected during cycling yields the evolution of two important parameters: the field fluctuation rate (ν) and the static field distribution width (Δ). As a Li^+ ion diffuses past an implanted muon, its nuclear moment causes a change in local magnetic field which acts to flip the muon spin. As such, field fluctuation rate is analogous to the ionic hopping rate [34]; to analyse the variation in Li^+ ion mobility during cycling, ν was plotted against voltage (Figure 7.4). The data shows a rapid rise from 0.4 to 0.6 μs^{-1} at the beginning of the first charge as the voltage rises to ~3.6 V and starts to plateau. At OCV, with close-to full Li occupancy in the cathode, the fluctuation rate is at its lowest due to the difficulty of Li^+ ion diffusion to a vacant site. As the battery is charged and Li^+ ions begin to leave the cathode, the hopping rate increases steadily to 0.8 μs^{-1} at around $x = 0.4$ (x in $Li_{1-x}Ni_{0.8}Mn_{0.1}Co_{0.1}O_2$) due to the gradual increase in the Li layer spacing, which acts to decrease the activation energy for ionic hopping [12, 43]. The beginning of charge sees the fastest rate of increase, agreeing with NMR [12], GITT [31], and EIS [43]. ν continues to climb steadily at a slower pace until around $x = 0.75$, where it reaches a maximum and begins to fall, correlated with the high voltage event seen in the dQ/dV plot. This is a consequence of the collapse in the Li layer spacing, causing a reduction in unit cell volume as observed by X-ray diffraction (Figure S7.3). This tightening of diffusion pathways will counteract the activation energy decrease for Li^+ hopping due to an increased vacancy fraction.

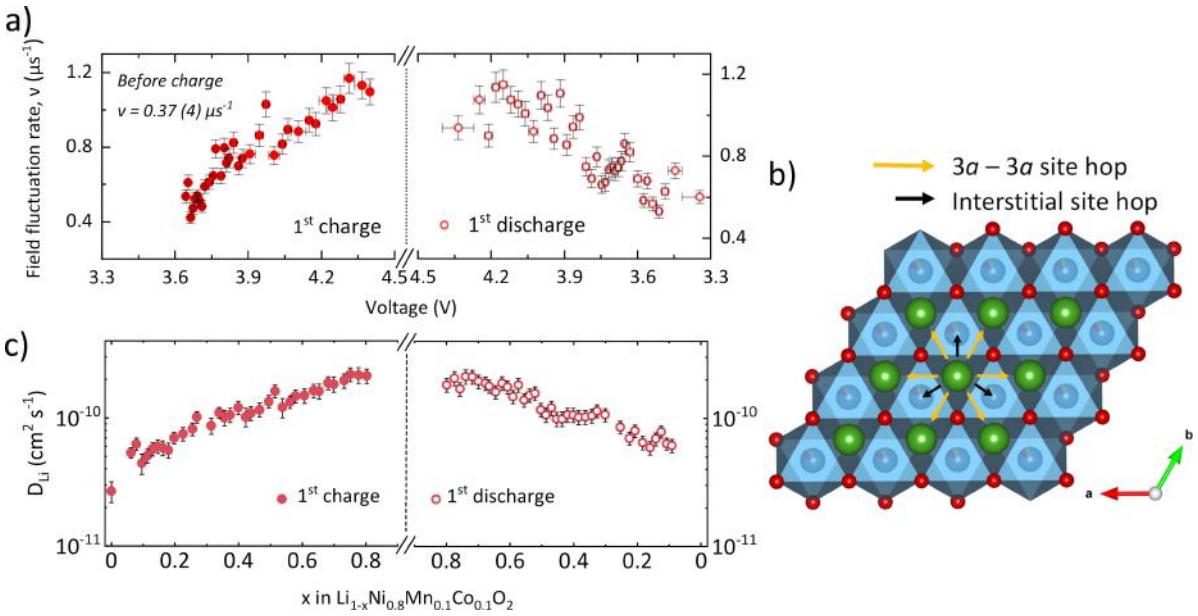

Figure 7.4: (a) The field fluctuation rate, ν, which is analogous to the ionic hopping rate in NMC811, during the first charge/discharge of a Li | NMC811 cell. (b) Projection looking down the *c*-axis to visualise the two possible Li hops: direct site and interstitial hopping. (c) The diffusion coefficient, D_{Li}, as a function of Li content in NMC811 from μSR.

The diffusion rate coefficient, D_{Li}, is an important parameter to evaluate and was determined using Equation S7.1. In NMC811, there are two available pathways for Li^+ diffusion (Figure 7.4b): directly from 3*a* to 3*a* sites, or through interstitial sites. At full Li site occupancy (i.e., 0% SOC), the 3*a* to 3*a* pathway is unavailable as there are no vacant sites available for diffusion, and hence the interstitial pathway is dominant. As charging begins and Li^+ is extracted from the cathode structure, 3*a* vacancies appear and site-site hopping becomes increasingly influential. Therefore, D_{Li} steadily increases during charging until $x = 0.75$ (Figure 7.4c) when it is hindered by structural parameters, similarly to the trend in ν. D_{Li} is observed to span around an order of magnitude depending on the NMC811 SOC.

Upon discharge, the trend is largely reversed; D_{Li} increases slightly at the beginning of the discharge as the *c*-axis rapidly expands again upon initial re-intercalation of Li^+, reaching a maximum at around $x = 0.75$. As Li^+ is re-inserted the vacancy fraction decreases and acts to reduce the available pathways for diffusion, consequently lowering the diffusion coefficient steadily. A plateau in D_{Li} is then seen between $x = 0.5$ to 0.3, as the material hits a balance between Li content and hopping rate. Interesting, ν does not return to the same level as before charging ($\sim$0.4 μs^{-1}) when discharged fully. This is likely correlated to the first cycle irreversible capacity loss; Li sites do not return to fully occupied after one cycle and thus the diffusion rate remains higher due to the availability of both diffusion pathways. That the material does not return to its initial state after a single cycle agrees with the study by Hong *et al.* [43], who describe how D_{Li} is higher at the beginning of the second cycle than the first, and consequently show that the NMC811 cathode does return to its original structure after the first cycle.

The diffusion coefficient from μSR provides a useful comparison to electrochemical measurements such as GITT [2, 12] and EIS [44]. μSR shows a maximum for Li^+ mobility at around

$x = 0.75$, while electrochemical analysis techniques have placed the peak in Li-diffusion rate at around $x = 0.5$, before noting a decrease in diffusion rate at low Li content. N.B. the chemical diffusion coefficient (from electrochemical techniques) is related to the diffusion coefficient (from μSR) *via* a thermodynamic factor which is not constant over cycling [45]. Nonetheless, the difference between the trends in diffusivity are inherent to the technique used; as stated in the introduction, muon implantation is volume averaged, meaning that limiting factors for overall ionic migration such as large resistances at the particle surfaces [6] are largely ignored. With current estimates of the surface rock-salt layer between 5 – 15 nm (secondary particle size 5 – 10 μm), this is expected to have little influence on the μSR signal. As such, the reported D_{Li} here outlines the diffusion coefficient from a local level (i.e., site-site hopping) inside the bulk NMC811 particles, while electrochemical techniques probe the long-range transport properties. This highlights the importance of combining both surface and bulk sensitive techniques for effective characterisation.

To evaluate how charge transfer proceeded on a longer length scale than μSR, *in situ* impedance spectroscopy was employed. A Li/NMC811 half-cell was prepared and cycled at a rate of C/20, with EIS measurements taken at regular intervals (Figure 7.5a). The collected spectra were fit using an equivalent circuit consisting of two $[RQ]$ elements (a resistor, R, and constant phase element, Q, in parallel) in series with another resistor and a Warburg element. This model is very similar to that previously used for NMC cells [43, 44, 46] and described the data well (Figure S7.8). The first resistor represents the solution resistance, while the first RQ element, visible as the first semi-circle in Figure 7.5b, describes the cathode-electrolyte interface (CEI) effects present in the cell. The third component is assigned to the resistance of charge transfer through the NMC particles themselves (R_{CT}). Figure 7.5b shows the change in the Nyquist plot over Li^+ (de)intercalation, while Figure 7.5c displays the trend in the fit values of the two resistance components.

R_{CEI} is found to initially drop as charging begins, likely due to the removal of adventitious lithium carbonate impurities [12], before reducing steadily during charge. The reverse is true upon discharge although the value does not climb back to its initial value. R_{CT} reaches a minimum around $x = 0.5$ where the second semi-circle at lower frequency disappears, which agrees well with other electrochemical analyses of NMC811 by GITT and EIS [2, 43]. Above $x = 0.7$, R_{CT} rises rapidly, and the second semi-circle reappears in the Nyquist plot; this effect is well correlated with the contraction of the c-axis (Figure S7.3) [12, 41]. Indeed, interfacial mismatch between the bulk and surface rock-salt phases as a result of lattice expansion and contraction during cycling has been touted as a primary cause of fatigue degradation in the bulk [5, 13, 18], which evidently increases R_{CT}. At the end of the first cycle, R_{CT} returns to a high value which is less than at $x = 0$ (before charge). This agrees excellently with D_{Li} found *via* μSR after one cycle, which also does not decrease to its initial value because of the remaining availability of the direct site-site hopping pathway caused by the capacity loss.

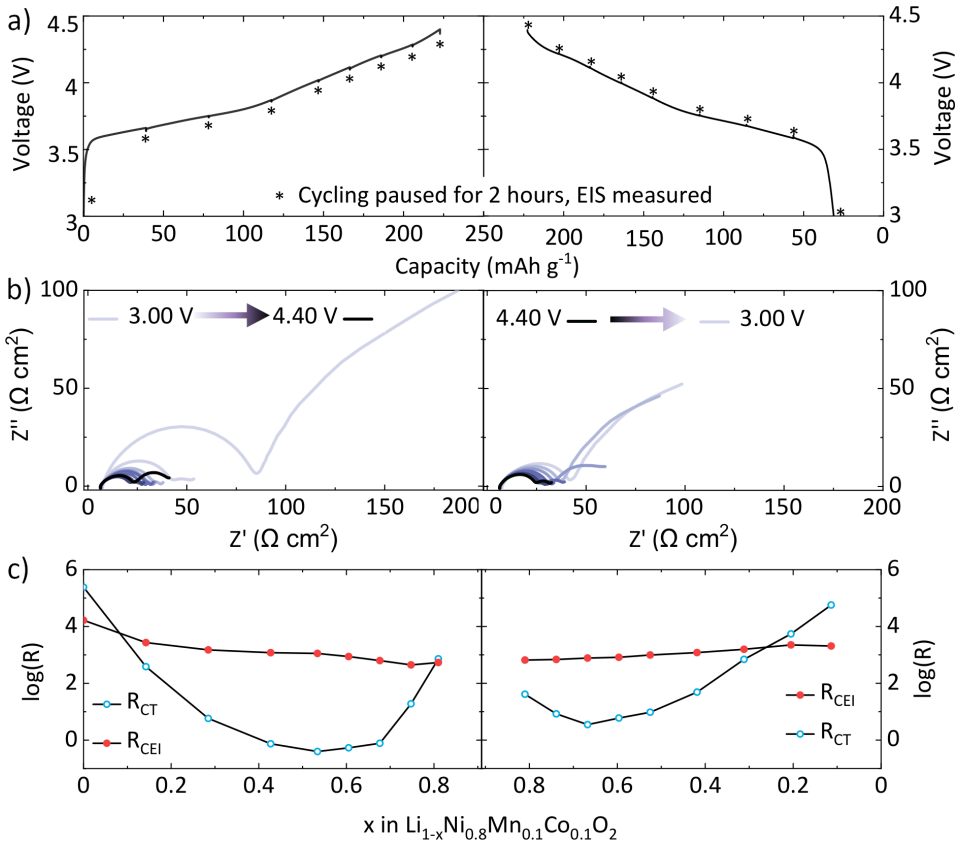

Figure 7.5: Electrochemical impedance spectroscopy (EIS) measurement of Li/NMC811 within a Swagelok cell. (a) The charge/discharge cycle (C/20), with asterisks marking the points where EIS measurements were taken. (b) Nyquist plots over charge and discharge. (c) The change in resistance of the charge transfer (R_{CT}) and cathode-electrolyte interface (R_{CEI}) components as obtained by equivalent circuit fitting (Figure S7.8).

The diminished reduction in the ionic hopping rate from μSR above 70% SOC (Figure 7.4), in comparison to EIS highlights the subtleties between different measurement techniques. The nature of μSR as a local probe means it reflects the diffusion rates at specific sites and from a site-to-site basis, in contrast with EIS which provides information on resistive interfaces and long-range charge transfer. By such a comparison, it can be concluded that Li^+ site hopping through the bulk is not quite so affected by cycling to high voltages, while long-range charge transfer appears significantly hindered as a consequence of Li^+ mobility between different crystal structures or between particles through surface layers. This hindrance of surface transport can facilitate a bottleneck for diffusion in the bulk, which is thus detected at high SOC by μSR.

The static field distribution width, Δ, was obtained *via* μSR and represents the proximity and strength of nuclear magnetic moments near the muon site (nuclear moments and abundances of the relevant isotopes for NMC811 are given in Table S7.4.) Figure 7.6a displays the fluctuation in Δ during the first charge/discharge process. Muons prefer to reside near the electronegative oxygen ions, forming a weak O-μ bond of length ∼1 Å [35], and Δ provides a sense of the local environment near this site. For NMC811, the effect of Ni and O on Δ is negligible, while Li, Co, and Mn have a much greater influence, although Co and Mn have a lower occupancy (see Table S7.4). Given this, Δ would be expected to decline over the first charge as Li^+ leaves the cathode

structure. Curiously, this effect is not seen experimentally, and Δ appears dependent on the lithiation state. To validate these results, the stopping site of the muon must be understood.

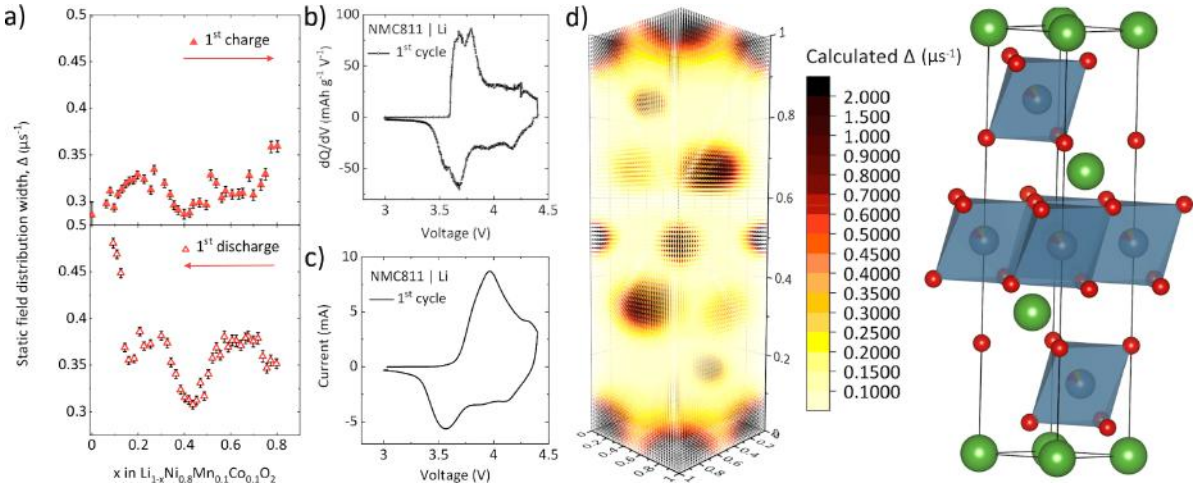

Figure 7.6: (a) The static field distribution width, Δ, as a function of lithiation state of NMC811. (b) The differential capacity plot from the *operando* muon study and (c) a cyclic voltammogram (scan rate 0.1 mV s^{-1}) recorded for a single cycle of the NMC811 material within a Swagelok cell. (d) A map of Δ values in the unit cell at full Li occupancy as predicted by dipolar field calculations. Visually evident is the greater influence of Li on Δ than the transition metals. The muon stopping site is likely in the transition metal layer [47]. The black regions at atomic sites correspond to Δ values $\gg 2$ μs^{-1}.

To narrow down the possible muon sites, dipolar field calculations (Equation S7.2) were performed at varying SOC and compared to experimental values, which is discussed in the Supporting Information. While many muon sites are plausible at full Li occupancy, to match with the experimentally determined Δ our calculations strongly suggest the muon prefers to reside in the transition metal (TM) layer. This explains the lack of reduction in Δ during the charge process (Figure 7.6a); although it may be expected that the reduced Li occupancy would lower the field distribution width experienced by the muon, the preferred muon site indicates a stronger sensitivity to changes within the TM layer. Indeed, Forslund *et al.* used DFT calculations to determine the muon site in $NaNiO_2$ as within the NiO_2 plane, and subsequently extended the applicability of this result to other layered oxide materials [47].

The features in Δ clearly follow the peaks in the dQ/dV plot (Figures S7.5, S7.6, 7.6), with a broad feature seen during charging around 30% SOC, and a sharp increase in Δ above 70% SOC. Such correlation strongly suggests that Δ is sensitive to the TM redox activities and the resultant TM-O bond length changes. Such correlation is likely caused by the movement of the muon site relative to its surround nuclear moments. Indeed, the broad feature at low %SOC is likely associated with the $Ni^{2+}/Ni^{3+}/Ni^{4+}$ oxidation process. Meanwhile, the sharp increase above 70% SOC initially appears to be associated with the *c*-axis contraction observed *via* XRD, however, this effect is not reversible upon discharge, unlike the axis length. Dipolar field calculations reveal the change in *c* lattice parameter has only a small effect on Δ (Table S7.5). The irreversibility of this feature in Δ then suggests this is an irreversible event in the structure, which may then be related to an increase in Li/TM disorder. Any such rearrangement

near the muon site would increase Δ due to the large nuclear moment of Li (+3.26 for ^{7}Li), and has the repositioning of Li^+ to Ni^{4+} sites has previously been reported at high % SOC [48]. The trend of the data appears to be largely reversible upon discharge, barring deviations at high and low SOC. The higher average value of Δ during discharge may also be correlated with the increased presence of Ni^{3+}, which has increased in abundance due to the irreversible capacity loss [49]. Without detailed structural information it is difficult to concretely assign features in the experimental Δ values to specific events, however, the clear correlation between the trend in dQ/dV, CV, and Δ warrants further investigation. This work presents an opportunity for future studies to use various complementary techniques to explore how the muon may be used as a structural probe in operating electrochemical systems.

Conclusions

Operando μSR measurements of ionic diffusion have been used to correlate structural and diffusional changes of an NMC811 cathode during cycling. A working electrochemical cell for usage on the EMU beamline at ISIS Neutron and Muon Source is presented which achieves similar performances to conventional cells. Within the BAM cell, background signal was easily subtracted, and a high level of detail was achieved over one cycle due to the speed of measurement. The Li^+ hopping rate through the bulk of NMC811 is seen to increase rapidly between 0-30% SOC, before slowing to a steady increase during delithiation and finally dropping off after 75% SOC. This reduction in diffusivity is well correlated with the collapse of the Li interlayer spacing as seen by XRD. A pronounced increase in charge transfer resistance is observed above 70% using EIS, likely a result of lattice mismatch between the formed rock-salt surface phase and bulk particle during the lattice contraction at high voltage. The differences between EIS and μSR highlight the benefit of employing both surface and bulk sensitive techniques; at high % SOC, long range Li^+ transport is limited by surface diffusion resistance rather than individual site hopping. Surprisingly, the trends in nuclear field distribution width of the implanted muons follow the peaks in the differential capacity and cyclic voltammetry plots. As such, μSR can excellently complement electrochemical and spectroscopic data and is presented here as an emerging tool for advanced *operando* battery characterisation.

Acknowledgements

This project was funded through the ISCF Faraday Challenge projects FutureCat (FIRG017), Degradation (FIRG001) and SOLBAT (FIRG007). Dexmet is thanked for the donation of the aluminium mesh current collectors. The authors thank the ISIS Neutron and Muon Source for the award of beamtime (10.5286/ISIS.E.RB2010364). IM gratefully acknowledges the ISIS Neutron and Muon facility for a Facility Development Studentship. We acknowledge the valuable contributions of Jamie Nutter, Colin Offer, Maksim Schastny, and Jason Chandler: the STFC Engineering team.

References

[1] R. Jung, M. Metzger, F. Maglia, C. Stinner, and H. A. Gasteiger. Oxygen Release and Its Effect on the Cycling Stability of $LiNi_xMn_yCo_zO_2$ (NMC) Cathode Materials for Li-Ion Batteries. *J. Electrochem. Soc.*, 164:A1261–A1377, 2017.

[2] H. J. Noh, S. Youn, C. S. Yoon, and Y. K. Sun. Comparison of the structural and electrochemical properties of layered $Li[Ni_xCo_yMn_z]O_2$ (x = 1/3, 0.5, 0.6, 0.7, 0.8 and 0.85) cathode material for lithium-ion batteries. *J. Power Sources*, 233:121–130, 2013.

[3] Y. J. Gu, Q. G. Zhang, Y. B. Chen, H. Q. Liu, J. X. Ding, Y. M. Wang, H. F. Wang, L. Chen, M. Wang, S. W. Fan, Q. F. Zang, and X. L. Yang. Reduction of the lithium and nickel site substitution in $Li_{1+x}Ni_{0.5}Co_{0.2}$ $Mn_{0.3}O_2$ with Li excess as a cathode electrode material for Li-ion batteries. *J. Alloys Compd.*, 630:316–322, 2015.

[4] R. V. Chebiam, F. Prado, and A. Manthiram. Structural Instability of Delithiated $Li_{1-x}Ni_{1-y}Co_yO_2$ Cathodes. *J. Electrochem. Soc.*, 148:A49–A53, 2001.

[5] C. Xu, K. Märker, J. Lee, A. Mahadevegowda, P. J. Reeves, S. J. Day, M. F. Groh, S. P. Emge, C. Ducati, B. L. Mehdi, C. C. Tang, and C. P. Grey. Bulk fatigue induced by surface reconstruction in layered Ni-rich cathodes for Li-ion batteries. *Nat. Mater.*, 20:84–92, 2021.

[6] A. Ghosh, J. M. Foster, G. Offer, and M. Marinescu. A Shrinking-Core Model for the Degradation of High-Nickel Cathodes (NMC811) in Li-Ion Batteries: Passivation Layer Growth and Oxygen Evolution. *J. Electrochem. Soc.*, 168:020509, 2021.

[7] R. Ruess, S. Schweidler, H. Hemmelmann, G. Conforto, A. Bielefeld, D. A. Weber, M. T. Elm, and J. Janek. Influence of NCM Particle Cracking on Kinetics of Lithium-Ion Batteries with Liquid or Solid Electrolyte. *J. Electrochem. Soc.*, 167:100532, 2020.

[8] Q. Huang, L. Ma, A. Liu, X. Ma, J. Li, J. Wang, and J. R. Dahn. The reactivity of charged positive $Li_{1-n}[Ni_xMn_yCo_z]O_2$ electrodes with electrolyte at elevated temperatures using accelerating rate calorimetry. *J. Power Sources*, 390:78–86, 2018.

[9] H. Rong, M. Xu, L. Xing, and W. Li. Enhanced cyclability of $LiNi_{0.5}Mn_{1.5}O_4$ cathode in carbonate based electrolyte with incorporation of tris(trimethylsilyl)phosphate (TMSP). *J. Power Sources*, 261:148–155, 2014.

[10] M. D. Radin, S. Hy, M. Sina, C. Fang, H. Liu, J. Vinckeviciute, M. Zhang, M. S. Whittingham, Y. S. Meng, and A. Van der Ven. Narrowing the Gap between Theoretical and Practical Capacities in Li-Ion Layered Oxide Cathode Materials. *Adv. Energy Mater.*, 7:1602888, 2017.

[11] S. Kang, D. P. Abraham, W. Yoon, K. Nam, and X. Yang. First-cycle irreversibility of layered Li-Ni-Co-Mn oxide cathode in Li-ion batteries. *Electrochim. Acta*, 54:684–689, 2008.

[12] K. Märker, P. J. Reeves, C. Xu, K. J. Griffith, and C. P. Grey. Evolution of Structure and Lithium Dynamics in $LiNi_{0.8}Mn_{0.1}Co_{0.1}O_2$ (NMC811) Cathodes during Electrochemical Cycling. *Chem. Mater.*, 31:2545–2554, 2019.

[13] C. Xu, P. J. Reeves, Q. Jacquet, and C. P. Grey. Phase Behavior during Electrochemical Cycling of Ni-Rich Cathode Materials for Li-Ion Batteries. *Adv. Energy Mater.*, 11:2003404, 2020.

[14] A. O. Kondrakov, A. Schmidt, J. Xu, H. Geßwein, R. Mönig, P. Hartmann, H. Sommer, T. Brezesinski, and J. Jürgen. Anisotropic Lattice Strain and Mechanical Degradation of High- and Low-Nickel NCM Cathode Materials for Li-Ion Batteries. *J. Phys. Chem. C*, 121:3286–3294, 2017.

[15] D. Goonetilleke, N. Sharma, W. Kong, V. K. Peterson, R. Petibon, J. Li, and J. R. Dahn. Structural Evolution and High-Voltage Structural Stability of $Li(Ni_xMn_yCo_z)O_2$ Electrodes. *Chem. Mater*, 31:44, 2019.

[16] S. Laubach, S. Laubach, P. C. Schmidt, D. Ensling, S. Schmid, W. Jaegermann, A. Thißen, K. Nikolowski, and H. Ehrenberg. Changes in the crystal and electronic structure of $LiCoO_2$ and $LiNiO_2$ upon Li intercalation and de-intercalation. *Phys. Chem. Chem. Phys.*, 11:3278–3289, 2009.

[17] N. Yabuuchi, Y. Makimura, and T. Ohzuku. Solid-State Chemistry and Electrochemistry of $LiNi_{1/3}Mn_{1/3}Co_{1/3}O_2$ for Advanced Lithium-Ion Batteries: III. Rechargeable Capacity and Cycleability. *J. Electrochem. Soc.*, 154:A314–A321, 2007.

[18] H. H. Ryu, K. J. Park, C. S. Yoon, and Y. K. Sun. Capacity Fading of Ni-Rich $Li[Ni_xCo_yMn_{1-x-y}]O_2$ ($0.6 \leq x \leq 0.95$) Cathodes for High-Energy-Density Lithium-Ion Batteries: Bulk or Surface Degradation? *Chem. Mater.*, 30:1155–1163, 2018.

[19] F. Lin, I. M. Markus, D. Nordlund, T. Weng, M. D. Asta, H. L. Xin, and M. M. Doeff. Surface reconstruction and chemical evolution of stoichiometric layered cathode materials for lithium-ion batteries. *Nat. Commun.*, 5:1–9, 2014.

[20] P. Xiao, T. Shi, W. Huang, and G. Ceder. Understanding Surface Densified Phases in Ni-Rich Layered Compounds. *ACS Energy Lett.*, 4:811–818, 2019.

[21] P. Hou, H. Zhang, Z. Zi, L. Zhang, and X. Xu. Core-shell and concentration-gradient cathodes prepared via co-precipitation reaction for advanced lithium-ion batteries. *J. Mater. Chem. A*, 5:4254–4279, 2017.

[22] J. Li, H. Liu, J. Xia, A. R. Cameron, M. Nie, G. A. Botton, and J. R. Dahn. The Impact of Electrolyte Additives and Upper Cut-off Voltage on the Formation of a Rocksalt Surface Layer in $LiNi_{0.8}Mn_{0.1}Co_{0.1}O_2$ Electrodes . *J. Electrochem. Soc.*, 164:A655–A665, 2017.

[23] S. S. Zhang. Problems and their origins of Ni-rich layered oxide cathode materials. *Energy Storage Mater.*, 24:247–254, 2020.

[24] S. Wu, W. Zhang, X. Song, A. K. Shukla, G. Liu, V. Battaglia, and V. Srinivasan. High Rate Capability of $Li(Ni_{1/3}Mn_{1/3}Co_{1/3})O_2$ Electrode for Li-Ion Batteries. *J. Electrochem. Soc.*, 159:438–444, 2012.

[25] S. Wang, M. Yan, Y. Li, C. Vinado, and J. Yang. Separating electronic and ionic conductivity in mix-conducting layered lithium transition-metal oxides. *J. Power Sources*, 393:75–82, 2018.

[26] A. J. Merryweather, C. Schnedermann, Q. Jacquet, C. P. Grey, and A. Rao. Operando optical tracking of single-particle ion dynamics in batteries Imaging lithium-ion transport in LCO. *Nature*, 594:522–528, 2021.

[27] E. Trevisanello, R. Ruess, G. Conforto, F. H. Richter, and J. Janek. Polycrystalline and Single Crystalline NCM Cathode Materials—Quantifying Particle Cracking, Active Surface Area, and Lithium Diffusion. *Adv. Energy Mater.*, 11:2003400, 2021.

[28] O. J. Borkiewicz, K. M. Wiaderek, P. J. Chupas, and K. W. Chapman. Best Practices for Operando Battery Experiments: Influences of X-ray Experiment Design on Observed Electrochemical Reactivity. *J. Phys. Chem. Lett.*, 6:2081–2085, 2015.

[29] T. Famprikis, P. Canepa, J. A. Dawson, M. S. Islam, and C. Masquelier. Fundamentals of inorganic solid-state electrolytes for batteries. *Nature Materials*, 18:1278–1291, 2019.

[30] P. P. R. M. L. Harks, F. M. Mulder, and P. H. L. Notten. In situ methods for Li-ion battery research: A review of recent developments. *J. Power Sources*, 288:92–105, 2015.

[31] K. Märker, C. Xu, and C. P. Grey. Operando NMR of NMC811/Graphite Lithium-Ion Batteries: Structure, Dynamics, and Lithium Metal Deposition. *J. Am. Chem. Soc*, 142:17447–17456, 2020.

[32] M. Amores, T. E. Ashton, P. J. Baker, E. J. Cussen, and S. A. Corr. Fast microwave-assisted synthesis of Li-stuffed garnets and insights into Li diffusion from muon spin spectroscopy. *J. Mater. Chem. A*, 4:1729–1736, 2016.

[33] I. D. Johnson, T. E. Ashton, E. Blagovidova, G. J. Smales, M. Lübke, P. J. Baker, S. A. Corr, and J. A. Darr. Mechanistic insights of Li^+ diffusion within doped $LiFePO_4$ from Muon Spectroscopy. *Sci. Rep.*, 8:4114, 2018.

[34] J. Sugiyama, K. Mukai, Y. Ikedo, H. Nozaki, M. Månsson, and I. Watanabe. Li Diffusion in Li_xCoO_2 Probed by Muon-Spin Spectroscopy. *Phys. Rev. Lett.*, 103:147601, 2009.

[35] I. McClelland, B. Johnston, P. J. Baker, M. Amores, E. J. Cussen, and S. A. Corr. Muon Spectroscopy for Investigating Diffusion in Energy Storage Materials. *Annu. Rev. Mater. Res.*, 50:1–15, 2020.

[36] L. Yang, A. Xiao, and B. L. Lucht. Investigation of solvation in lithium ion battery electrolytes by NMR spectroscopy. *J. Mol. Liq.*, 154:131–133, 2010.

[37] S. G. Booth, A. J. Nedoma, N. N. Anthonisamy, P. J. Baker, R. Boston, H. Bronstein, S. J. Clarke, E. J. Cussen, V. Daramalla, M. De Volder, S. E. Dutton, V. Falkowski, N. A. Fleck, H. S. Geddes, N. Gollapally, A. L. Goodwin, J. M. Griffin, A. R. Haworth, M. A. Hayward, S. Hull, B. J. Inkson, B. J. Johnston, Z. Lu, J. L. MacManus-Driscoll, X. Martínez De Irujo Labalde, I. McClelland, K. McCombie, B. Murdock, D. Nayak, S. Park, G. E. Pérez, C. J. Pickard, L. F. J. Piper, H. Y. Playford, S. Price, D. O. Scanlon, J. C. Stallard, N. Tapia-Ruiz, A. R. West, L. Wheatcroft, M. Wilson, L. Zhang, X. Zhi, B. Zhu, and S. A. Cussen. Perspectives for next generation lithium-ion battery cathode materials. *APL Mater.*, 9:109201, 2021.

[38] O. Arnold, J. C. Bilheux, J. M. Borreguero, A. Buts, S. I. Campbell, L. Chapon, M. Doucet, N. Draper, R. Ferraz Leal, M. A. Gigg, V. E. Lynch, A. Markvardsen, D.J. Mikkelson, R. L. Mikkelson, R. Miller, K. Palmen, P. Parker, G. Passos, T. G. Perring, P. F. Peterson, S. Ren, M. A. Reuter, A. T. Savici, J. W. Taylor, R. J. Taylor, R. Tolchenov, W. Zhou, and J. Zikovsky. Mantid - Data analysis and visualization package for neutron scattering and μSR experiments. *Nucl. Instrum. Meth. A*, 764:156–166, 2014.

[39] T. Ohzuku, A. Ueda, M. Nagayama, Y. Iwakoshi, and H. Komori. Comparative Study of $LiCoO_2$, $LiNi_{1/2}Co_{1/2}O_2$ and $LiNiO_2$ for 4 Volt Secondary Lithium Cells. *Electrochim. Acta*, 38:1159–1167, 1993.

[40] M. Månsson and J. Sugiyama. Muon-spin relaxation study on Li- and Na-diffusion in solids. *Phys. Scr.*, 88:068509, 2013.

[41] H. Liu, S. Kazemiabnavi, A. Grenier, G. Vaughan, M. Di Michiel, B. J. Polzin, K. Thornton, K. W. Chapman, and P. J. Chupas. Quantifying Reaction and Rate Heterogeneity in Battery Electrodes in 3D through Operando X-ray Diffraction Computed Tomography. *ACS Appl. Mater. Interfaces*, 11:18386–18394, 2019.

[42] S. J. Blundell. Spin-polarized muons in condensed matter physics. *Contemp. Phys.*, 40:175–192, 1999.

[43] C. Hong, Q. Leng, J. Zhu, S. Zheng, H. He, Y. Li, R. Liu, J. Wan, and Y. Yang. Revealing the correlation between structural evolution and Li^+ diffusion kinetics of nickel-rich cathode materials in Li-ion batteries. *J. Mater. Chem. A*, 8:8540–8547, 2020.

[44] V. Charbonneau, A. Lasia, and G. Brisard. Impedance studies of Li^+ diffusion in nickel manganese cobalt oxide (NMC) during charge/discharge cycles. *J. Electroanal. Chem*, 875:113944, 2020.

[45] J. Sugiyama, K. Mukai, M. Harada, H. Nozaki, K. Miwa, T. Shiotsuki, Y. Shindo, S. R. Giblin, and J. S. Lord. Reactive surface area of the $Li_x(Co_{1/3}Ni_{1/3}Mn_{1/3})O_2$ electrode determined by μ^+SR and electrochemical measurements. *Phys. Chem. Chem. Phys.*, 15:10402, 2013.

[46] T. Li, X. Z. Yuan, L. Zhang, D. Song, K. Shi, and C. Bock. Degradation Mechanisms and Mitigation Strategies of Nickel-Rich NMC-Based Lithium-Ion Batteries. *Electrochem. Energy Rev.*, 3:43–80, 2020.

[47] O. K. Forslund, H. Ohta, K. Kamazawa, S. L. Stubbs, O. Ofer, M. Månsson, C. Michioka, K. Yoshimura, B. Hitti, D. Arseneau, G. D. Morris, E. J. Ansaldo, J. H. Brewer, and J. Sugiyama. Revisiting the *A*-type antiferromagnet $NaNiO_2$ with muon spin rotation measurements and density functional theory calculations. *Phy. Rev. B*, 102:184412, 2020.

[48] H. Liu, C. Zhao, Q. Qiu, B. Hu, F. Geng, J. Li, W. Tong, B. Hu, and C. Li. What Triggers the Voltage Hysteresis Variation beyond the First Cycle in Li-Rich 3d Layered Oxides with Reversible Cation Migration? *J. Phys. Chem. Lett.*, 12:8740–8748, 2021.

[49] Y.Yu, P. Karayaylali, L. Giordano, J. Corchado-García, J. Hwang, D. Sokaras, F. Maglia, R. Jung, F. S. Gittleson, and Y. Shao-Horn. Probing Depth-Dependent Transition-Metal Redox of Lithium Nickel, Manganese, and Cobalt Oxides in Li-Ion Batteries. *ACS Appl. Mater. Interfaces*, 12:55865–55875, 2020.

Supporting Information

Direct Observation of the Dynamic Lithium Diffusion Properties in the First Cycle of $LiNi_{0.8}Mn_{0.1}Co_{0.1}O_2$ (NMC811) Using *Operando* Muon Spectroscopy

Innes McClelland,[1,2,3] Samuel G. Booth,[1,2] Nirmalesh Anthonisamy,[1,2] Laurence Middlemiss,[1,2] Gabriel E. Pérez,[2,3] Edmund J. Cussen,[2,4] Peter J. Baker,[2,3] and Serena A. Cussen*[2,4]

[1] Department of Chemical and Biological Engineering, The University of Sheffield, Sheffield, S1 3JD, UK

[2] The Faraday Institution, Quad One, Harwell Campus, OX11 0RA, UK

[3] ISIS Neutron and Muon Source, Science and Technology Facilities Council, Rutherford Appleton Laboratory, Harwell Campus, Didcot, OX11 0QX

[4] Department of Materials Science and Engineering, The University of Sheffield, Sheffield, S1 3JD, UK

Rietveld refinement of as-synthesized NMC811

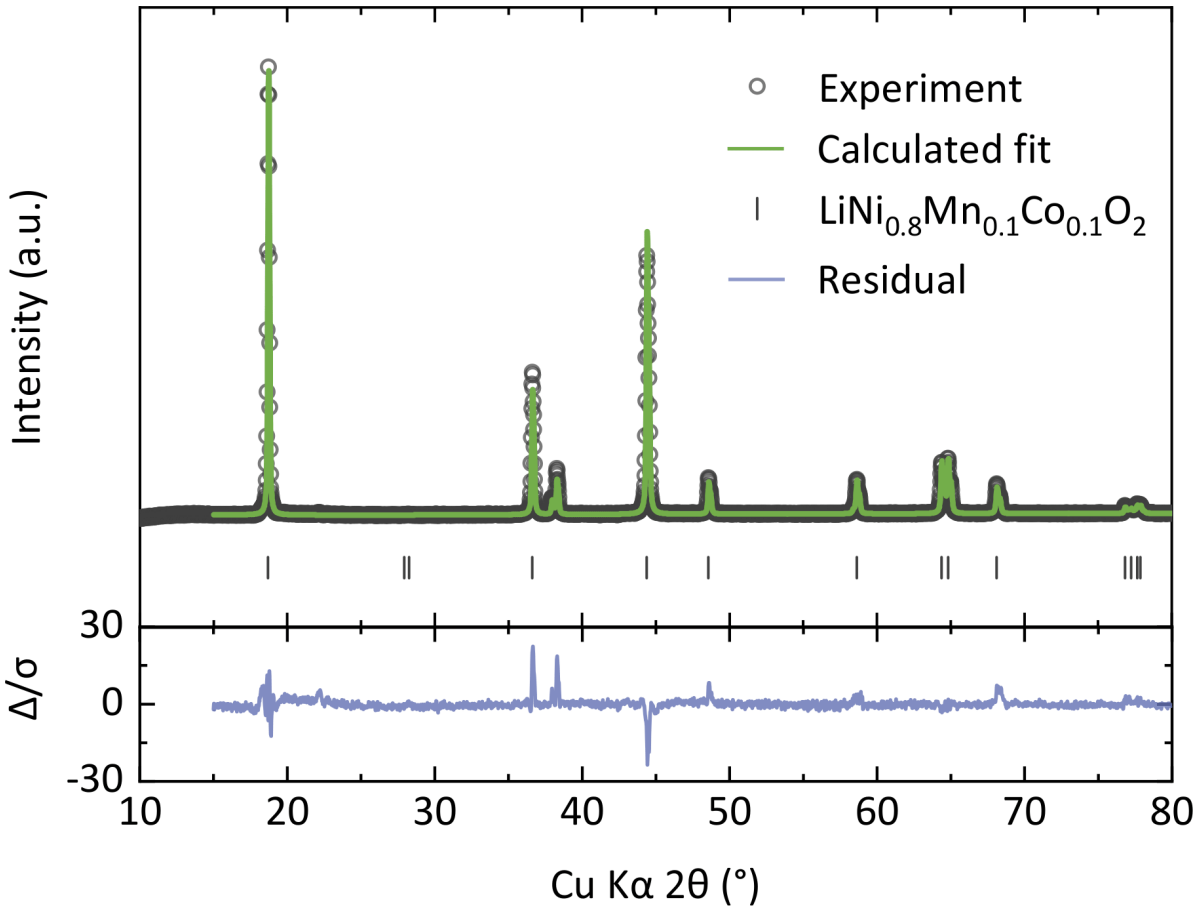

Figure S7.1. Rietveld refinement of as-synthesized $LiNi_{0.8}Mn_{0.1}Co_{0.1}O_2$ to a $R\bar{3}m$ layered oxide crystal structure after calcination at 850 ˚C for 12 h in an O_2 atmosphere. A weighted residual of 1.81% is found.

Table S7.1. Various structural parameters obtained by a Rietveld refinement of the as-synthesized NMC811 sample. Thermal parameters and atomic coordinates were not refined.

Rietveld Refinement (from Figure S7.1)	
Material	$LiNi_{0.8}Mn_{0.1}Co_{0.1}O_2$
Space Group	$R\bar{3}m$
a, *b*	2.87376 (8) Å
c	14.2099 (3) Å
α, ß, γ	90˚, 90˚, 120˚
Volume	101.630 (5) $Å^3$
R_{WP}	1.81%

BAM (Battery Analysis by Muon) *operando* cell assembly

To achieve a reasonable signal during the *operando* experiment, a significant mass of active material (≥100 mg) was required to ensure adequate muon implantation. The carbon content of the prepared cathode powders (70:20:10, NMC811:C:PTFE wt.%) was high to ensure sufficient electronic conduction across the large area/mass. The devised methodology for this experiment involved the usage of ~50 mg of cathode powder in layers, packed down using a spatula. Small glass-microfibre separator semicircles were used alongside separator rings to hold additional electrolyte within the cell to fully wet all cathode particles and enable high-rate cycling, although large contact areas between cathode layers were retained. This cell assembly procedure was found to display comparable performances to standard low mass loading coin/Swagelok type cell configurations over the first few cycles (i.e., ~200 mAh g^{-1} first discharge capacity) and produced consistent cycling results.

***Operando* XRD experiment**

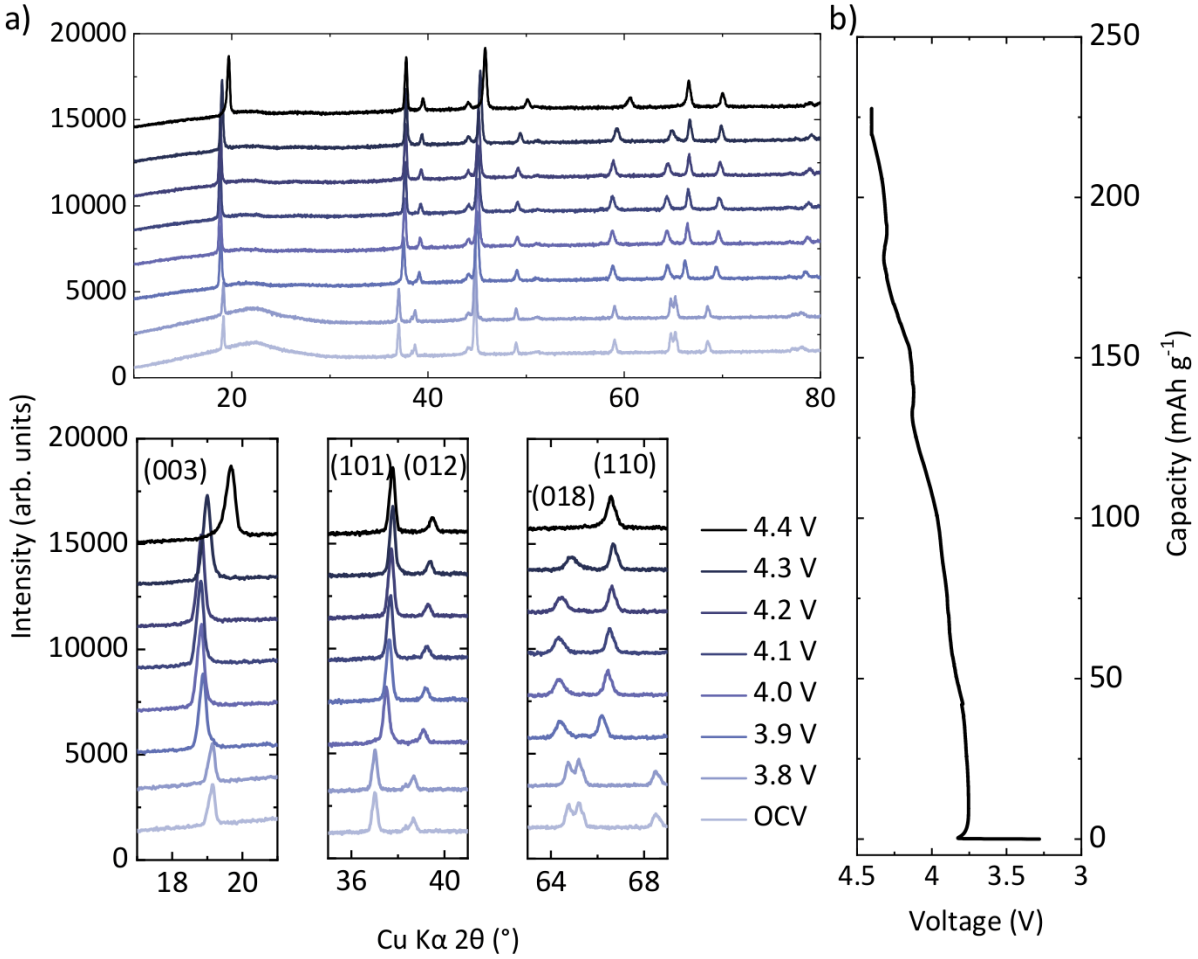

Figure S7.2. (a) An *operando* X-ray diffraction experiment performed using an EL-cell on a Li/NMC811 cell. The XRD pattern before charging is shown at open circuit voltage (OCV). Initially upon charging the (003) peak shifts to lower angles up to around 4.2 V, where it moves rapidly to higher angles. This suggests a contraction of the *c*-axis. The (101) peaks gradually shifts to higher angles during charging, indicating a steady contraction of the *a* axis. No splitting of the (101) peak is observed indicating no distinct two-phase transition occurs. Meanwhile, the (018) and (110) peaks clearly split around 3.9 V noting a material phase transformation. (b) The first charge of the *operando* XRD cell from the results shown in (a). An initial overpotential is seen, likely due to electrode surface impurities from potential air exposure and is not predicted to significantly affect any obtained XRD patterns. The EL-cell was cycled at C/50 and achieved a charge capacity of 227 mAh g^{-1}.

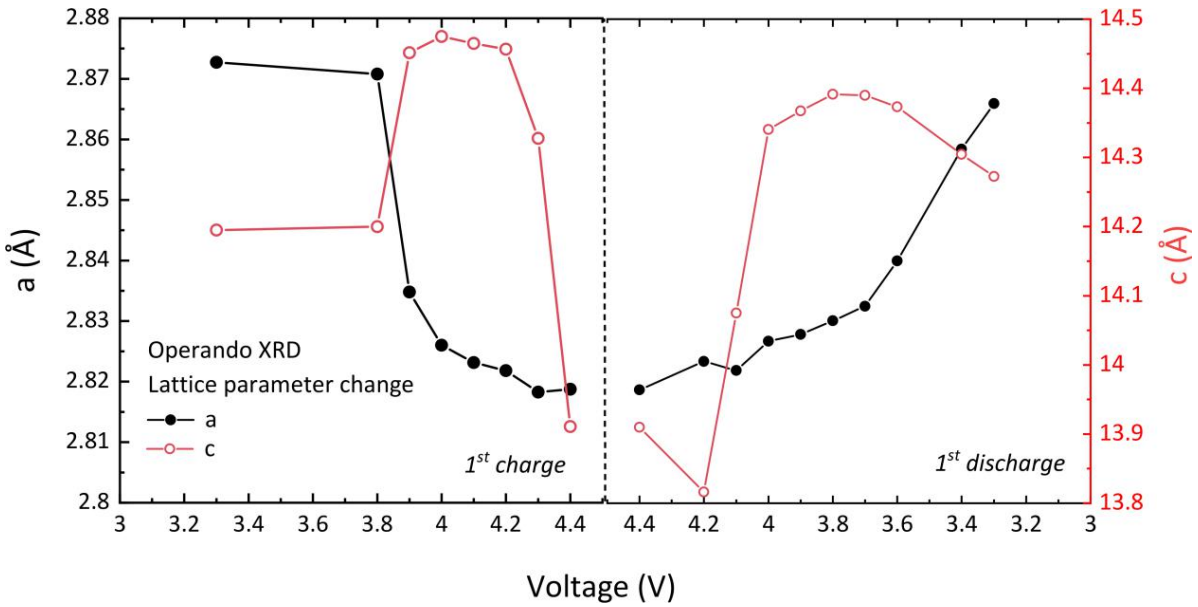

Figure S7.3. Lattice parameters obtained through an *operando* X-ray diffraction experiment performed using an EL-cell on a Li/NMC811 cell. Sequential Pawley fits were performed to refine the structure at each voltage point. The *c*-axis length is observed to initially expand before contracting rapidly above 4.2 V, similar to other reports [1, 2]. Meanwhile, the *a*- and *b*-axes undergo a much smaller contraction during charging, followed by a steady expansion during discharging.

Table S7.2. Table displaying the lattice parameter trends obtained by *operando* XRD as shown in Figure S7.2 & S7.3.

Voltage (V)	***a*, *b* (Å)**	***c* (Å)**
1st charge		
3.3	2.8727 (1)	14.1940 (9)
3.8	2.8708 (1)	14.1988 (9)
3.9	2.8348 (1)	14.450 (1)
4.0	2.8260 (1)	14.474 (1)
4.1	2.8231 (1)	14.464 (1)
4.2	2.8218 (1)	14.455 (1)
4.3	2.8183 (1)	14.327 (1)
4.4	2.8187 (2)	13.910 (1)
1st discharge		
4.4	2.8188 (2)	13.910 (1)
4.2	2.8235 (2)	13.816 (1)
4.1	2.8219 (2)	14.075 (2)
4.0	2.8268 (1)	14.341 (1)
3.9	2.8279 (1)	14.367 (1)
3.8	2.8302 (1)	14.391 (1)
3.7	2.8326 (1)	14.390 (1)
3.6	2.8401 (1)	14.3730 (9)
3.4	2.8584 (1)	14.3044 (8)
3.2	2.8661 (1)	14.2725 (8)

Fitted asymmetry μSR data across the first cycle of NMC811

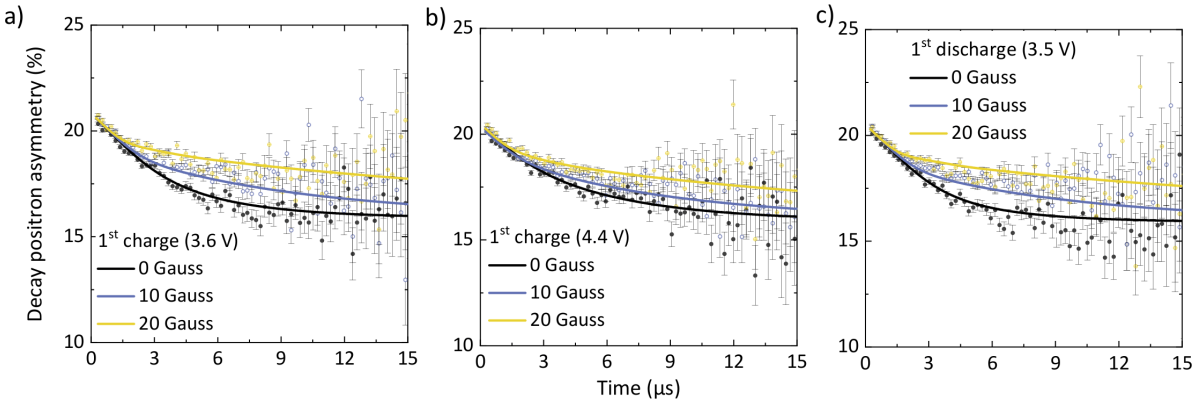

Figure S7.4. Fitted 0, 5, and 10 Gauss applied field strengths for an Li | NMC811 cell at (a) the beginning of the first charge (~3.6 V), (b) the top of the first charge (~4.4 V), and (c) the end of the first discharge (~3.5 V). At all voltages a high background is seen, caused by the large amount of material in the cathode which is not NMC811, such as carbon, PTFE, and liquid electrolyte, within which muons will stop. Given the detectable timeframe for ionic diffusion seen by muons (10^{-5} - 10^{-8} s), ionic motion in the electrolyte is too fast to be detectable by μSR. An exponential relaxation with a fixed relaxation rate was added to the fitting function to account for these other stopping environments. From the start of the charge plateau (3.6 V) to the top (4.4 V) there is a clear increase in muon spin relaxation which suggests motional narrowing, indicative of a faster dynamical environment. This effect is largely reversed upon discharge to 3.5 V.

Muon Spin Relaxation Measurements

Muon measurements were fitted using Equation 7.1. The exponential term was added to account for the other materials contained within the *operando* cell (carbon, binder, electrolyte, *etc*.), which some muons will undoubtedly stop within. Due to the low volume fraction of active material, the flat background was found to be a large value of 0.159 (2). A relatively low Kubo-Toyabe amplitude of 0.034 (2) was obtained (these are displayed in Table S7.3), which is around 17% of the total measured amplitude. The fitting function was constrained to three separate runs, grouped as consecutive 0, 10, 20 G measurements, to form a single 'point'. All unfixed parameters were fitted globally at each point. The voltage change during the μSR measurement period was averaged out across the time duration of the measurement. This model provided nicely fitted data across the cycle, with χ^2 values largely below 1.10.

Table S7.3. Fitting parameters for Equation 7.1 to fit the *operando* muon data of an Li/NMC811 half-cell. The amplitudes of the three components were refined and then fixed globally across the final fits. The relaxation rate λ was found for each point and fixed to an average value. Δ and ν were allowed to fluctuate freely for each point. Only selected runs are shown for brevity. Figures 7.4a and 7.6a show the trends in ν and Δ over the first cycle.

μSR fits using Equation 7.1							
Voltage	A_{bg}	A_{KT}	**Δ (μs^{-1})**	**ν (μs^{-1})**	A_{exp}	**λ (μs^{-1})**	χ^2
OCV	0.159 (2)	0.034 (2)	0.325 (4)	0.40 (3)	0.0130 (1)	0.713 (2)	1.10
3.64			0.297 (4)	0.53 (4)			0.99
…			…	…			…
4.40			0.359 (6)	1.10 (7)			0.99
...			…	…			…

Diffusion Coefficient Calculation

To calculate the diffusion coefficient, D_{Li}, the following equation was used:

$$D_{Li} = \sum_{i=1}^{n} \left(\frac{1}{N_i}\right) Z_{\nu,i} s_i^2 \nu_{Li} \quad \text{(S7.1)}$$

In Equation S7.1, N_i is the number of possible Li sites for diffusion in the i^{th} path, Z is defined as the vacancy fraction (i.e., 1 – Li occupancy) for the i^{th} site, s_i is the site-site hopping distance and ν is the field fluctuation rate obtained *via* μSR data fitting. In NMC811, there are two diffusion pathways for Li^+ hopping through the material (n = 2). These are shown graphically in Figure 7.4c: Li can either hop directly from 3*a*-3*a* site, or through an interstitial site. A hop from site 3a-3a will be of length a, while to an interstitial site will be of length $a/\sqrt{3}$ [3]. The number of accessible sites in the 3*a*-3*a* pathway is 6, as can be seen from Figure 7.4c, while for the interstitial hop N = 3. We will assume that the vacancy fraction of the interstitial sites is always 1 and in the initial discharged state Z = 0 for the 3*a*-3*a* pathway. Values for the hopping distances were taken from the *operando* XRD experiment as shown in Figure S7.3.

Comparison between Δ and d*Q*/d*V*

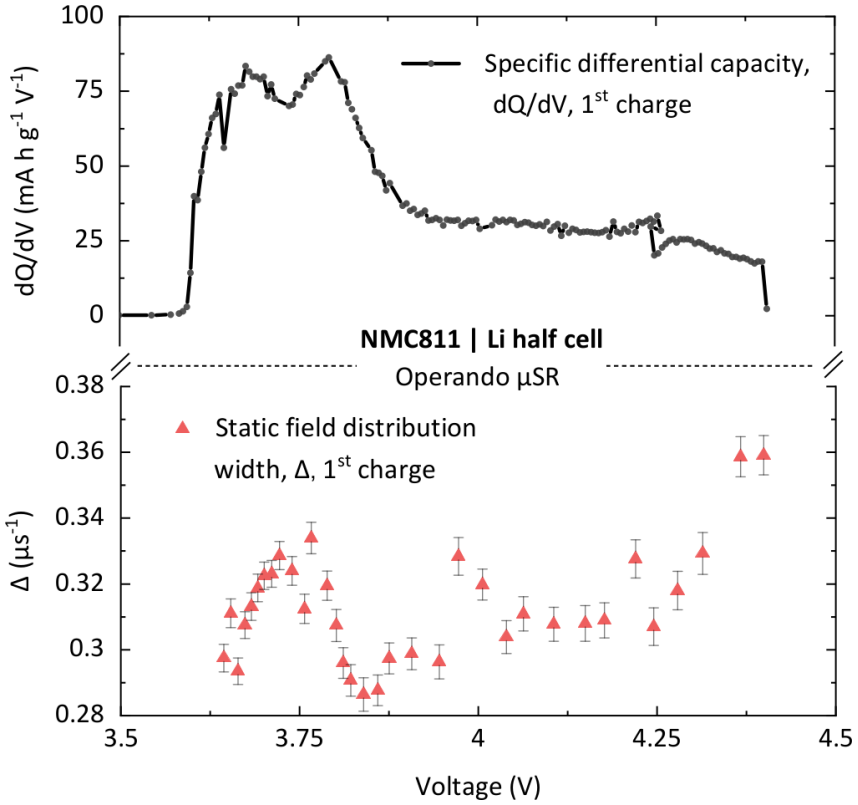

Figure S7.5. The static field distribution data seen in Figure 7.6a as compared to the *dQ*/*dV* data of the *operando* μSR cell for the charge process only. The two data sets appear to correlate well, with the main redox/phase processes indicated by the *dQ*/*dV* reflected as features in Δ. Although Δ is a measure of nuclear moments nearby the muon site, this is clearly heavily influenced by the redox processes during cycling, which induce M-O/M-M bond length and interlayer spacing changes. The muon is thus a sensitive probe of electrochemical processes during cycling.

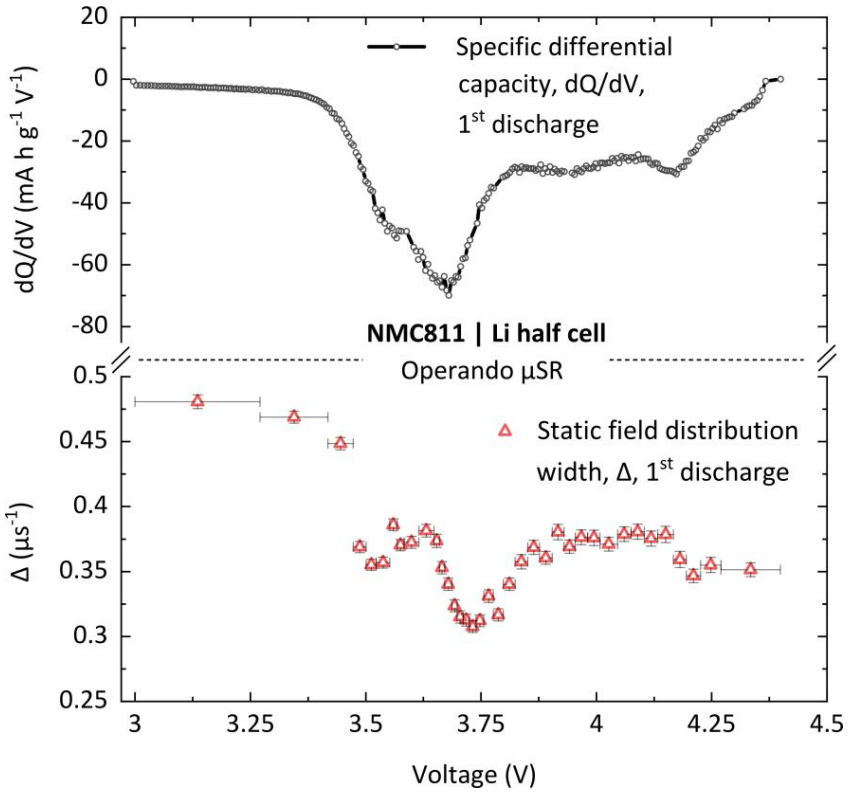

Figure S7.6. Similar to Figure S7.5 but for the discharge process only. Again, Δ is seen to follow the *dQ*/*dV* data well.

Dipolar Field Calculations and Muon Site Discussion

To better understand the muon stopping site in NMC811, dipolar field calculations were performed to compare theoretical with experimental Δ values. These were completed in a similar manner to the method previously used by our group [4], using Equation S7.2 [5]. The unit cell size of $z \leq 0.5$ from our previous study was increased to $z \leq 1.0$ for these calculations.

$$\Delta^2 = \frac{2}{3}\mu_0^2\gamma_\mu^2\hbar^2\sum_i \frac{I_i(I_i+1)\gamma_i^2}{r_i^6} \qquad \text{(S7.2)}$$

In Equation S7.2, γ_μ is the muon's gyromagnetic ratio, I_i and γ_i are the spin and the nuclear gyromagnetic ratio of the i^{th} nucleus, respectively, and r_i is the distance between the i^{th} nucleus and the muon site. This was calculated over the full unit cell for NMC811. The muon is predicted as roughly 1 Å away from any oxygen atom in the structure.

Table S7.4. The isotopes of the elements present in NMC811 which will have an influence on Δ [6]. Isotopes with no significant nuclear moment are not shown. Li is predicted to have a large effect on Δ, with Ni not so much. Although both Mn and Co have isotopes with large nuclear moments and 100% abundance, these are only 0.1 per formula unit and hence have limited influence. O will have very little influence due to the low abundance of any isotope with a non-zero moment. However, the influence of any element is dependent on the specific stopping site of the muon.

$LiNi_{0.8}Mn_{0.1}Co_{0.1}O_2$			
Isotope	**Nuclear spin (*I*)**	**Magnetic moment (μ/μ_N)**	**Relative abundance**
^{6}Li	1	0.822	7.6 %
^{7}Li	3/2	3.26	92.4 %
^{59}Co	7/2	4.627	100 %
^{61}Ni	3/2	−0.75	1.1 %
^{55}Mn	5/2	3.45	100 %
^{17}O	5.2	−1.89	0.04 %

To enable firm comparisons between calculated and experimental Δ values, an understanding of the muon site is imperative. Δ calculations were thus performed as function of lithium content (i.e., during cycling), where the Li content and the lattice parameters from the *operando* XRD experiment (Figures S7.2, S7.3) were used. A range of ≥150 sites across the unit cell which had a Δ value between 0.29 - 0.31 μs^{-1} at OCV were chosen as possible sites due to their similarity to the experimental value of 0.3 ± 0.01 μs^{-1} before cycling. Potential muon stopping sites were chosen as ~1 Å from an O atom. The Δ values for the same sites were then calculated at different lithium contents to compare with experimental values.

Figure S7.7b shows the Δ value at these selected sites using the lattice parameters and Li content at $x = 0.6$ (~4.1 V). Near the Li sites in the structure, Δ is at a low value in comparison to the OCV value of ~0.3 μs^{-1} before cycling, while in contrast, the sites close to transition metal ions remain much closer to the experimental value of Δ, strongly indicating that muons prefer to reside within the TM layers.

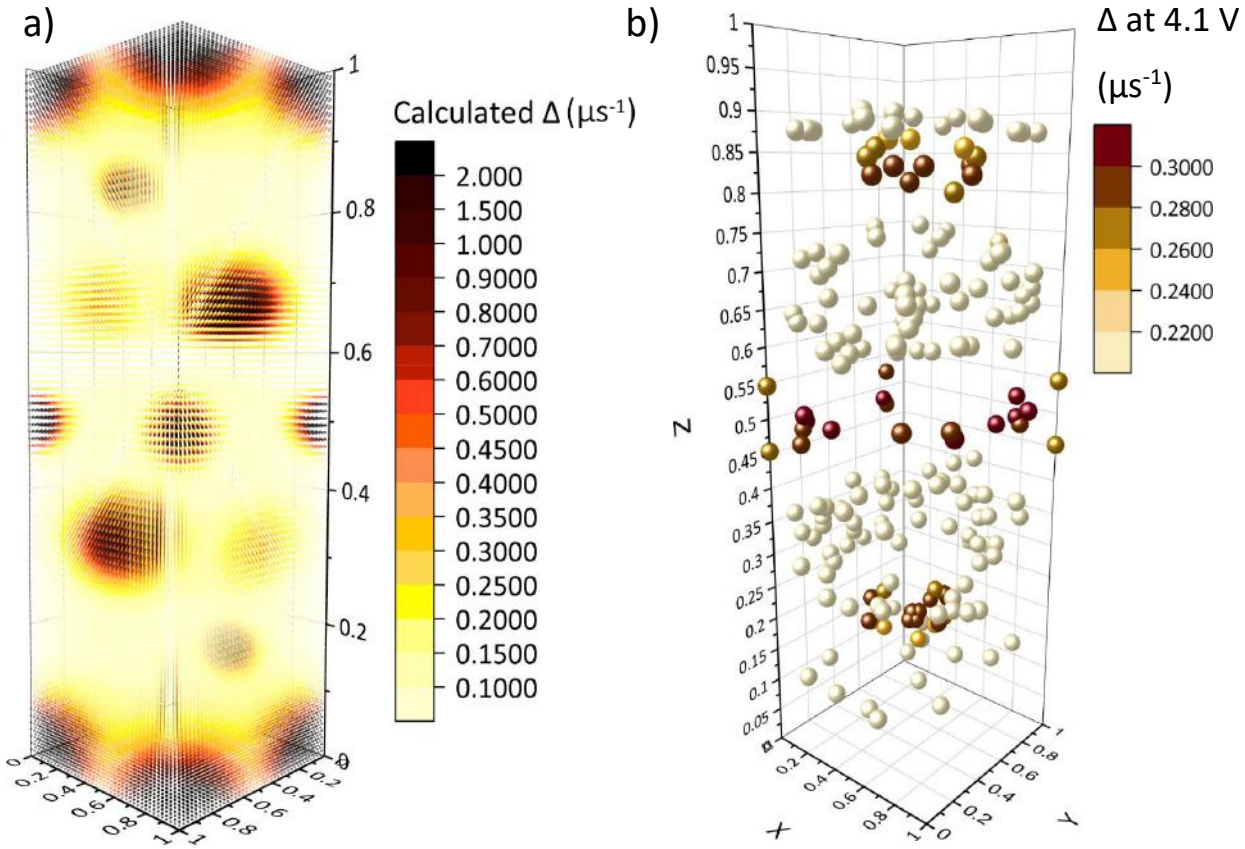

Figure S7.7. (a) Visual depiction of Δ across the unit cell of NMC811 at full Li occupancy. The Li layer is at $z = 0$ and $z = 1$, while the TM layer is at $z = 0.5$. As Δ^2 is inversely proportional to r^6, near any atomic sites Δ scales rapidly to values >> 2 (shown in black). To match with experimental values, predicted muon sites are within the orange regions. (b) Δ values at 4.1 V (0.4 Li p/f.u.) for muon sites chosen as matching the experimental Δ at OCV (full Li occupancy). It is obvious that for most sites, Δ is far lower than what would be expected from experiment (~0.31 μs^{-1} at 4.1 V). This is perhaps expected due to the lower Li content. Only near the transition metal ions does Δ reflect the experimental observations. This indicates that the muon stopping site is likely within the TM layer and is not heavily influenced by Li content. This agrees well with DFT predictions of the muon site in other layered materials [7].

Table S7.5. Calculated Δ values during charging as partially shown in Figure S7.7b. Sites at OCV which were ~1 Å from an O atom and had a Δ value of between 0.29 - 0.31 μs^{-1}, matching experimentally obtained values. Δ retains its value during charging much better for sites in the TM layer. Δ is not predicted to be too heavily influenced by the contraction of the *c*-axis at high voltage. Selected sites are shown for brevity.

Layer	***x***	***y***	***z***	**Δ at OCV (μs^{-1})**	**Δ at 4.1 V (μs^{-1})**	**Δ at 4.4 V (μs^{-1})**
Li	0.6	0.725	0.113	0.294	0.186	0.144
Li	0.15	0.225	0.124	0.297	0.183	0.143
Li	0.2	0.6	0.134	0.295	0.247	0.249
TM	0.45	0.875	0.155	0.294	0.275	0.271
TM	0.225	0.45	0.165	0.295	0.284	0.279
TM	0.525	0.675	0.165	0.295	0.284	0.279
TM	0.45	0.575	0.175	0.297	0.289	0.287
TM	0.425	0.875	0.175	0.297	0.289	0.287
TM	0.15	0.55	0.186	0.292	0.281	0.286
TM	0.425	0.575	0.186	0.299	0.288	0.293
TM	0.45	0.6	0.186	0.292	0.281	0.285
TM	0.425	0.85	0.186	0.299	0.288	0.293
TM	0.2	0.6	0.196	0.294	0.275	0.290
Li	0.8	0.325	0.247	0.295	0.179	0.137
Li	0.75	0.6	0.258	0.304	0.188	0.145
Li	0.8	0.775	0.289	0.299	0.194	0.142
Li	0.675	0.275	0.423	0.290	0.176	0.139
TM	1	1	0.454	0.294	0.271	0.302
TM	0.2	0.025	0.474	0.297	0.296	0.306
TM	0.775	0.975	0.485	0.299	0.305	0.309
TM	0.225	0.025	0.515	0.299	0.305	0.309
TM	0.975	0.2	0.515	0.299	0.305	0.309
TM	0.775	0.975	0.515	0.299	0.305	0.309
TM	0.825	0.025	0.526	0.297	0.296	0.306
TM	0.975	0.175	0.526	0.297	0.296	0.306
TM	0.025	0.825	0.526	0.297	0.296	0.306
TM	0	0	0.546	0.294	0.271	0.302
Li	0.975	0.625	0.608	0.299	0.191	0.143
Li	0.6	0.4	0.660	0.291	0.194	0.138
Li	0.9	0.25	0.701	0.296	0.195	0.141
Li	0.225	0.525	0.753	0.300	0.182	0.143
TM	0.8	0.4	0.804	0.294	0.275	0.290
TM	0.55	0.4	0.814	0.292	0.281	0.286

TM	0.575	0.125	0.825	0.297	0.289	0.287
TM	0.875	0.425	0.825	0.297	0.289	0.287
TM	0.675	0.15	0.835	0.295	0.284	0.279
TM	0.775	0.225	0.835	0.295	0.284	0.279
TM	0.775	0.55	0.835	0.295	0.284	0.279
TM	0.55	0.125	0.845	0.294	0.275	0.271
TM	0.875	0.45	0.845	0.294	0.275	0.271

***In situ* EIS experiment**

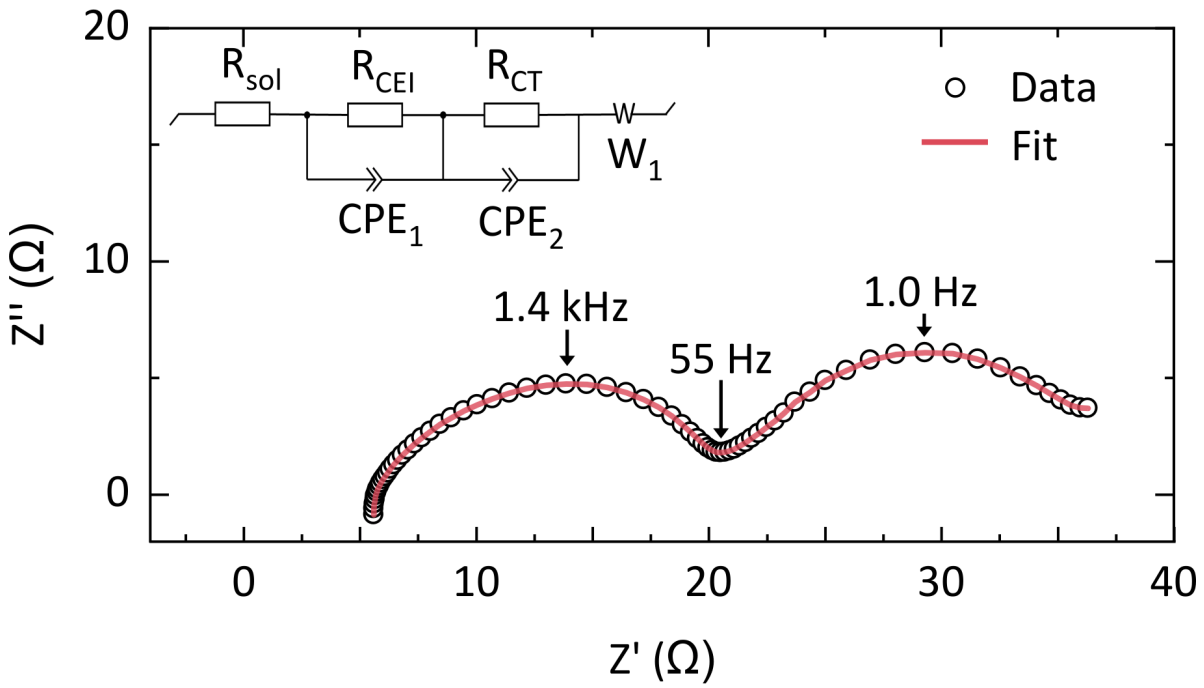

Figure S7.8. Example of the fitted impedance spectra at 4.4 V for the data shown in Figure 7.5. An [R_{sol} + R_{CEI}/CPE_1 + R_{CT}/CPE_2 + W_1] equivalent circuit was used, as it common for impedance fitting of NMC half cells [8]. R_{sol} is defined as the solution resistance (between 0 Ω and first semi-circle), R_{CEI} as the cathode/electrolyte interface resistance, and R_{CT} as the charge transfer resistance through NMC secondary particles.

Table S7.6. Fitted values of resistance and capacitance for the equivalent circuit displayed in Figure S7.8 across the first cycle of an Li/NMC811 half-cell. These data are presented graphically in Figure 7.5. The smaller capacitance of $C1$ (~10^{-6} F) suggests this arises from phenomena at the sample-electrode interface or a passivation layer on the particle surfaces, known as the cathode electrolyte interface (CEI) [9].

Voltage	R_{sol}	R_{CEI}	R_{CT}	**Capacitance 1 (µF)**	**Capacitance 2 (mF)**
1st Charge					
OCV (before charge)	6.557	68.03	217.6	1.92	7.62
3.64	6.069	30.94	13.27	2.70	19.2
3.74	5.979	23.91	2.143	3.41	7.68
3.86	5.917	21.71	0.878	3.88	16.7
4.01	5.868	21.13	0.669	4.12	25.1
4.10	5.669	18.94	0.762	4.40	19.1
4.19	5.589	16.45	0.8949	6.23	0.0122
4.27	5.52	14.12	3.591	4.46	7.24
4.38	5.604	17.49	17.49	3.81	9.54
1st Discharge					
4.40	5.566	16.72	5.019	23.6	5.38
4.23	5.604	17.06	2.519	2.73	7.72
4.12	5.64	17.95	1.721	81.8	3.11
4.05	5.671	18.43	2.172	32.7	5.69
3.89	5.717	19.96	2.666	24.2	6.70
3.76	5.74	21.76	5.41	3.63	8.51
3.69	5.799	24.48	17.15	17.7	11.6
3.61	5.84	28.52	42.06	6.27	24.8
3.0	5.826	27.44	116.1	9.16	14.1

Supporting Information References

[1] K. Märker, P. J. Reeves, C. Xu, K. J. Griffith, and C. P. Grey. Evolution of Structure and Lithium Dynamics in $LiNi_{0.8}Mn_{0.1}Co_{0.1}O_2$ (NMC811) Cathodes during Electrochemical Cycling. *Chem. Mater.*, 31:2545–2554, 2019.

[2] J. Li, L. E. Downie, L. Ma, W. Qiu and J. R. Dahn. Study of the Failure Mechanisms of $LiNi_{0.8}MnCo_{0.1}O_2$ Cathode Material for Lithium Ion Batteries. *J. Electrochem. Soc*., 162:A1401−A1408, 2015.

[3] J. Sugiyama, K. Mukai, Y. Ikedo, H. Nozaki, M. Månsson, and I. Watanabe. Li Diffusion in Li_xCoO_2 Probed by Muon-Spin Spectroscopy. *Phys. Rev. Lett*., 103:147601, 2009

[4] I. McClelland, S. G. Booth, H. El-Shinawi, B. I. J. Johnston, J. Clough, W. Guo, E. J. Cussen, P. J. Baker, and S. A. Corr. *In Situ* Diffusion Measurements of a NASICON-Structured All-Solid-State Battery Using Muon Spin Relaxation. *ACS Appl. Energy Mater.*, 4:1527-1536, 2021.

[5] R. S. Hayano, Y. J. Uemura, J. Imazato, N. Nishida, T. Yamazaki, R. Kubo, R. Zero and low-field spin relaxation studied by positive muons. *Phys. Rev. B*, 20:850– 859, 1979.

[6] N. J. Stone. Table of nuclear magnetic dipole and electric quadrupole moments. *At. Data Nucl. Data Tables*, 90:75– 176, 2005.

[7] O. K. Forslund, H. Ohta, K. Kamazawa, S. L. Stubbs, O. Ofer, M. Månsson, C. Michioka, K. Yoshimura, B. Hitti, D. Arseneau, G. D. Morris, E. J. Ansaldo, J. H. Brewer, and J. Sugiyama. Revisiting the A-type antiferromagnet $NaNiO_2$ with muon spin rotation measurements and density functional theory calculations. *Phys. Rev. B*, 102:184412, 2020.

[8] T. Li and X. Z. Yuan and L. Zhang and D. Song and K. Shi and C. Bock. Degradation Mechanisms and Mitigation Strategies of Nickel-Rich NMC-Based Lithium-Ion Batteries. *Electrochem. Energy Rev.,* 3:43-80, 2020.

[9] J. T. S. Irvine, D. C. Sinclair, and A. R. West. Electroceramics: Characterization by Impedance Spectroscopy. *Adv. Mater.*, 2:132–138, 1990.

8 Conclusions and Future Work

8.1 Conclusions

The purpose of this thesis has been to advance the use of muon spectroscopy towards the *operando* characterisation of ionic diffusion in operating Li-ion batteries. The methodologies to conduct such experiments have evolved from an *in situ* study of an all-solid-state battery (Chapter 4), which permitted six measurement points during one discharge, to an *operando* study of a liquid-based battery system using a custom-built cell (Chapter 7), which afforded more than 70 measurement points doing a full charge/discharge cycle. As such, *operando* experiments have been realised, and the opportunity for further development is promising. The secondary aim of this work was to obtain useful knowledge on battery materials of scientific interest. This has been achieved through application of multiple experimental techniques on NASICON solid electrolytes, garnet solid electrolytes, and high voltage layered cathode materials.

In Chapter 4, a commercially available coin cell was employed to conduct *in situ* μSR measurements on an all-solid-state NASICON-structured system. The cell contained a metallic Li anode with a NASICON LZP electrolyte and an LTP cathode, with the similarly structured materials integrated to aid diffusive pathways across the electrolyte-cathode interface. The pristine materials, LZP and LTP, both showed a low activation energy for ionic self-diffusion alongside fast-ion transport. However, in the all-solid-state battery configuration, the Li-electrolyte interface displayed a large resistance which increased during cycling. Such an effect is a common problem with solid electrolyte materials (further investigated in Chapter 5). Employing *in situ* μSR, the ionic dynamics within the electrolyte LZP were found to decrease suddenly below 1.2 V by around 1/3. Such voltage instability seriously hampers the reversible capacity which can be extracted from the system. This effect was likely caused by a structural contraction on diffusion channels, as predicted by the trend in the static field distribution width.

To obtain higher quality μSR data than was possible in the experiment described in Chapter 4, a custom cell holder was designed and built, primarily offering a much larger inspection area. This permitted much faster data collection and a lower background ratio, greatly improving both the speed and quality of measurements. The BAM cell was first tested using a garnet solid electrolyte pellet with a reducible tungsten dopant (Chapter 5). The reaction between garnets with reducible dopants and metallic lithium is difficult to quantify accurately due to the thin and buried nature of the resultant interphase. Employing a combination of μSR and EIS to investigate this reaction from beneath the surface, Li^+ was found to penetrate from the electrode into the garnet structure, partially reducing W^{6+} to W^{4+} to maintain charge balance. Upon initial contact between Li metal and the garnet electrolyte, the interfacial reaction reduces the

area specific resistance as the interphase merges the two solids to create a larger contact surface area, improving cyclability. However, as the reaction proceeds, the interphase propagates unbounded through the electrolyte, and this greatly increases the pellet's overall resistance. Impedance spectroscopy elucidates that this reaction proceeds through the grain surfaces, forcing Li^+ to travel through the resistive grain surface regions when the interphase is fully propagated. Meanwhile, μSR uncovers the magnetically distinct environments of the grain and grain surface, which reveal an increased Li^+ content and slower diffusion rates in the grain surface regions. This model of surface grain lithiation has wide implications for the usage of garnet solid electrolytes with a reducible dopant, and future materials may be designed to reflect this.

To validate the performance of the BAM cell, both for μSR and electrochemical experiments, it was evaluated using a range of example systems in Chapter 6. The design and implementation of the BAM cell is provided, alongside the motivation for such *operando* experiments. The cell is found to display low background counts from μSR and electrochemistry data representative of commercially available cells. The desirability of thick electrodes for *operando* μSR experiments at ISIS is explained, describing an example methodology. Thick electrodes generally lead to a faster capacity fade than generic configurations, meaning thorough testing of new materials in the BAM cell is recommended. Alterations in cell components to improve the quality of data collection are presented. A working methodology for *operando* μSR experiments is described, and the versatility of the BAM cell opens the opportunity for a host of further experiments.

The first example of such an applied experiment is given in Chapter 7, which presents the diffusional properties of topical cathode material $LiNi_{0.8}Mn_{0.1}Co_{0.1}O_2$ during its first cycle. Utilising the BAM cell, the rate of Li^+ diffusion in the cathode was found to increase rapidly at the beginning of charge, before gradually slowing and dropping at a high state of cathode delithiation. This conclusion is reinforced by an impedance spectroscopy experiment which outlines a large charge transfer resistance above 70% state of charge as a result of the lattice mismatch between the particle surface and bulk. Such kinetic limitations act to decrease the usable lifetime of the material during long-term cycling to high voltage. This study highlights the strength of employing both bulk and surface sensitive techniques to study ionic transport. Indeed, the combination of μSR and impedance spectroscopy makes for a prosperous relationship which is utilised throughout this work. The interplay between Δ and the structural properties of the cathode unit cell is interesting and displays a profile that is not solely dependent on the Li content or the lattice parameter fluctuations. The level of detail in Δ throughout cycling is surprising and deserves further investigation in similar materials.

8.2 Future Work

The development of an *operando* methodology for μSR affords a broad range of prospects for future experiments. The most obvious is perhaps the study of alternative ions to Li^+, such as Na^+ and Mg^{2+}. The study of Na^+ diffusion in particular is straightforward using μSR due to the ion's large nuclear moment. However, these larger ions complicate the use of thick electrodes in the BAM cell (or any other *operando* cell developed for μSR) as the kinetic limitations on mass transport generally promote large capacity losses, especially at high cycling rates. A consistent replication of representative electrochemistry is thus more difficult than for thick electrode Li^+ cells, although this is a challenge which will yield valuable information. Work is underway to develop these methodologies for Na^+ cells. Moreover, any ion with a nuclear magnetic moment is a potential candidate. For example, future energy storage technologies such as Al-ion [1] or K-ion [2] may be studied. Applications beyond battery technology, such as solar or fuel cells, are also achievable, although outside the scope of this discussion.

The BAM cell, presented in Chapter 6, can be used to study a wide range of electrochemically active materials, having already been demonstrated on solid-state and liquid electrolyte chemistries. Development in solid-state measurements is straightforward due to the large mass available to implant muons inside and the lack of interfering materials. Of particular interest is the performance at extreme potentials and of interfacial reactions. The ionic diffusion kinetics at extreme potentials are highly influential to a cell's cyclability, as demonstrated in Chapter 4. Higher detail *operando* studies thus represent an enticing chance to follow the degradation processes of all-solid-state batteries at extreme potentials. As explained in Chapter 5, understanding the interfacial reaction (and its products) between a solid electrolyte and lithium metal is crucial to advance the design of future SSBs.

Electrochemical and structural characterisation options are open to further expand the work done on solid electrolyte-lithium interfaces in Chapters 4 and 5. Particularly for garnet electrolytes, the reducibility of the dopant is clearly an influential factor for the interfacial properties. Future experiments may be designed to use this to an advantage. For example, the investigation of bi-layer or tri-layer garnets is planned to control the interaction between the electrolyte and lithium. This can enable a low area specific resistance at the interface but block the growth of the interphase, along with Li^+ penetration, from propagating across a full pellet. Such a configuration could permit stable high current cycling due to the fast ionic motion through the bulk and interfacial stability. An experiment to investigate the variation in electrochemical cycling performance for different relative thicknesses of the bi-layer is planned. A tri-layer could potentially allow for improved incorporation with a cathode material for an all-solid-state system. However, the challenge lies in a consistent preparation methodology to allow reproducible

processing to high relative densities with a low garnet-garnet resistance.

For solid electrolyte interfaces, effects such as Li creep, Li dendrites, interphase formation, and electrolyte decomposition are all important to understand, and all lie within the grasp of μSR. The non-invasive nature of the muon as a local probe provides a big advantage in this regard. For example, Li deposition has already been observed using negative muon spectroscopy [3]: an area with obvious *operando* opportunities. Furthermore, the depth progression of the interfacial reaction is hugely important and something that it is possible to observe using low energy muons. Low energy muons allow the experimenter to possess an improved depth penetration control, however, the inefficiency in production of low energy muons means that the experimental counting rate is much lower. Thus, pulsed beams are generally preferable for ionic diffusion studies while low energy muons may have specific applications.

The opportunities to study liquid electrolyte-based technologies with μSR are also wide-ranging. Tweaking the cell assembly procedures can permit a higher signal to be obtained from the region of interest, improving the quality of experimental data. Further testing will no doubt improve the electrochemical reliability of the cell, and optimisation of cathode preparation procedures will bring the capacity retention of thick electrodes closer to that of traditional thin electrodes. Planned improvements in the facilities at ISIS (a new instrument called Super-MuSR is planned which will greatly increase the counting rate and time resolution) will add to the potential for highly detailed experiments and improve the chance to study longer term degradation effects.

The suitability of μSR for materials containing magnetic ions means that most electrode materials are suitable. The successful investigation of cathode material NMC811 at high voltage (Chapter 7), has motivated the planning for a subsequent *operando* experiment on similar material $LiNiO_2$ (LNO). This should allow for a direct transfer of cell assembly procedures to enable a rapid follow-up investigation. LNO undergoes many interesting structural transitions during cycling for which diffusional and structural data will be valuable. Crucially, this material is chosen because of its simple transition metal composition, as opposed to NMC, which will disentangle the analysis of the static field distribution width (Δ) data. The detailed trends in Δ during Chapter 7 are perhaps the most open-ended dataset in this thesis. LNO thus represents the ideal material with which to compare the existing NMC811 study and, if a robust model of the muon site during cycling is made, has the potential to unlock the use of the implanted muon as a probe of structural phase transitions during cycling. Advanced data analysis techniques could yield such information provided adequate structural information is known. *Operando* XAS and neutron experiments are planned to correlate the data in Δ with the site occupancies and M-O bond length changes; this will allow a detailed analysis of the diffusion mechanisms and their influences. While understanding Δ in high detail is non-trivial and very sample specific, the prize of utilising the muon as a structural and

diffusional probe offers an enticing opportunity to further advance the μSR technique for energy materials.

References

[1] G. A. Elia, K. V. Kravchyk, M. V. Kovalenko, J. Chacón, A. Holland, and R. G. A. Wills. An overview and perspective on Al and Al-ion battery technologies. *J. Power Sources*, 481:228870, 2021.

[2] N. Matsubara, E. Nocerino, O. K. Forslund, A. Zubayer, K. Papadopoulos D. Andreica, J. Sugiyama, R. Palm, Z. Guguchia, S. P. Cottrell, T. Kamiyama, T. Saito, A. Kalaboukhov, Y. Sassa, T. Masese, and M. Månsson. Magnetism and ion diffusion in honeycomb layered oxide $K_2Ni_2TeO_6$. *Sci. Rep.*, 10:18305, 2020.

[3] I. Umegaki, Y. Higuchi, Y. Kondo, K. Ninomiya, S. Takeshita, M. Tampo, H. Nakano, H. Oka, J. Sugiyama, M. K. Kubo, and Y. Miyake. Nondestructive High-Sensitivity Detections of Metallic Lithium Deposited on a Battery Anode Using Muonic X-rays. *Anal. Chem.*, 92:8194–8200, 2020.

List of publications and conferences presented at

Publications

- I. McClelland, B. Johnston, P. J. Baker, M. Amores, E. J. Cussen, S. A. Corr. Muon spectroscopy for investigating diffusion in energy storage materials. *Annu. Rev. Mater. Res.*, 50:371–393, 2020.

- M. Pasta, D. Armstrong, Z. L. Brown, J. Bu, M. R. Castell, P. Chen, A. Cocks, S. A. Corr, E. J. Cussen, E. Darnbrough, V. Deshpande, C. Doerrer, M. S. Dyer, H. El-Shinawi, N. Fleck, P. Grant, G. L. Gregory, C. Grovenor, L. J. Hardwick, J. T. S. Irvine, H. J. Lee, G. Li, E. Liberti, I. McClelland, C. Monroe, P. D. Nellist, P. R. Shearing, E. Shoko, W. Song, D. S. Jolly, C. I. Thomas, S. J. Turrell, M. Vestli, C. K. Williams, Y. Zhou, P. G. Bruce. 2020 Roadmap on solid-state batteries. *J. Phys. Energy*, 2:032008, 2020.

- M. Amores, H. El-Shinawi, I. McClelland, S. R. Yeandel, P. J. Baker, R. I. Smith, H. Y. Playford, P. Goddard, S. A. Corr, E. J. Cussen. $Li_{1.5}La_{1.5}MO_6$ ($M = W^{6+}$, Te^{6+}) as a new series of lithium-rich double perovskites for all-solid-state lithium-ion batteries. *Nat. Comm.*, 11:1–12, 2020.

- I. McClelland, S. G. Booth, H. El-Shinawi, B. I. J. Johnston, J. Clough, W. Guo, E. J. Cussen, P. J. Baker, S. A. Corr. *In Situ* Diffusion Measurements of a NASICON-Structured All-Solid-State Battery Using Muon Spin Relaxation. *ACS Appl. Energy. Mat.*, 4:1527–1536, 2021.

- S. G. Booth, A. J. Nedoma, N. N. Anthonisamy, P. J. Baker, R. Boston, H. Bronstein, S. J. Clarke, E. J. Cussen, V. Daramalla, M. De Volder, S. E. Dutton, V. Falkowski, N. A. Fleck, H. S. Geddes, N. Gollapally, A. L. Goodwin, J. M. Griffin, A. R. Haworth, M. A. Hayward, S. Hull, B. J. Inkson, B. J. Johnston, Z. Lu, J. L. MacManus-Driscoll, X. Martínez De Irujo Labalde, I. McClelland, K. McCombie, B. Murdock, D. Nayak, S. Park, G. E. Pérez, C. J. Pickard, L. F. J. Piper, H. Y. Playford, S. Price, D. O. Scanlon, J. C. Stallard, N. Tapia-Ruiz, A. R. West, L. Wheatcroft, M. Wilson, L. Zhang, X. Zhi, B. Zhu, S. A Cussen. Perspectives for next-generation lithium-ion battery cathode materials. *APL Mater.*, 9:109201, 2021.

- I. McClelland, H. El-Shinawi, S. G. Booth, J. Clough, S. Altus, A. Regoutz, E. J. Cussen, P. J. Baker, S. A. Corr. The Role of the Reducible Dopant in Electrolyte–Lithium Metal Interfaces. *Chem Mater. Accepted Manuscript*, 2022.

Conference Presentations

Below is a list of the conferences presented (both oral and poster presentations) during this doctorate program. Note that both domestic and overseas conference attendance was limited by the COVID-19 pandemic.

Oral Presentations

- **ISIS Neutron and Muon User Meeting,** University of Warwick, April 2019
- **EUROMAT,** Stockholm, September 2019
- **ISIS Neutron and Muon Student Meeting,** Milton Hill House, October 2019
- **Solid State Chemistry Christmas Meeting,** University of Liverpool, 2019
- **ISIS Neutron and Muon Student Meeting,** STFC Harwell campus, October 2021
- **ISIS Muon User Meeting,** STFC Harwell campus, December 2021
- **Energy Materials Research Network,** STFC Harwell campus, November 2021
- **MuSR Science Day,** STFC Harwell campus, December 2021

Poster Presentations

- **ISIS Neutron and Muon User Meeting,** Milton Hill House, October 2018
- **Solid State Chemistry Christmas Meeting,** University College London, December 2018
- **Electrochemistry Northwest** Manchester Metropolitan University, July 2019
- **Advanced Characterisation of Energy Materials** University of Sheffield, April 2021